

Multifunctional Hybrid Nanomaterials for Energy Storage

Lead Guest Editor: Zhengping Zhou

Guest Editors: Jiawei Gong, Yichen Guo, and Linqin Mu





Multifunctional Hybrid Nanomaterials for Energy Storage

Multifunctional Hybrid Nanomaterials for Energy Storage

Lead Guest Editor: Zhengping Zhou

Guest Editors: Jiawei Gong, Yichen Guo, and Linqin Mu



Copyright © 2019 Hindawi. All rights reserved.

This is a special issue published in "Journal of Nanomaterials." All articles are open access articles distributed under the Creative Commons Attribution License, which permits unrestricted use, distribution, and reproduction in any medium, provided the original work is properly cited.

Editorial Board

- Domenico Acierno, Italy
Katerina Aifantis, USA
Nageh K. Allam, USA
Margarida Amaral, Portugal
Martin Andersson, Sweden
Raul Arenal, Spain
Ilaria Armentano, Italy
Vincenzo Baglio, Italy
Lavinia Balan, France
Thierry Baron, France
Andrew R. Barron, USA
Stefano Bellucci, Italy
Enrico Bergamaschi, Italy
Debes Bhattacharyya, New Zealand
Sergio Bietti, Italy
Giovanni Bongiovanni, Italy
Mohamed Bououdina, Bahrain
Victor M. Castaño, Mexico
Albano Cavaleiro, Portugal
Bhanu P. S. Chauhan, USA
Shafiq Chowdhury, USA
Yu-Lun Chueh, Taiwan
Elisabetta Comini, Italy
Giuseppe Compagnini, Italy
David Cornu, France
Miguel A. Correa-Duarte, Spain
P. Davide Cozzoli, Italy
Anuja Datta, USA
Loretta L. Del Mercato, Italy
Yong Ding, USA
Yu Dong, Australia
Zehra Durmus, Turkey
Joydeep Dutta, Oman
Ovidiu Ersen, France
Ana Espinosa, France
Claude Estournès, France
Giuliana Faggio, Italy
Andrea Falqui, Saudi Arabia
Matteo Ferroni, Italy
Ilaria Fratoddi, Italy
Siddhartha Ghosh, Singapore
Filippo Giubileo, Italy
Fabien Gasset, Japan
Jean M. Greneche, France
- Kimberly Hamad-Schifferli, USA
Simo-Pekka Hannula, Finland
Michael Harris, USA
Yasuhiko Hayashi, Japan
Michael Z. Hu, USA
Nay Ming Huang, Malaysia
Zafar Iqbal, USA
Balachandran Jeyadevan, Japan
Jeong-won Kang, Republic of Korea
Hassan Karimi-Maleh, Iran
Antonios Kelarakis, UK
Alireza Khataee, Iran
Ali Khorsand Zak, Iran
Philippe Knauth, France
Prashant Kumar, UK
Eric Le Bourhis, France
Jun Li, Singapore
Meiyong Liao, Japan
Shijun Liao, China
Silvia Licoccia, Italy
Nathan C. Lindquist, USA
Zainovia Lockman, Malaysia
Jim Low, Australia
Gaurav Mago, USA
Muhamamd A. Malik, UK
Francesco Marotti de Sciarra, Italy
Ivan Marri, Italy
Laura Martinez Maestro, UK
Sanjay R. Mathur, Germany
Tony McNally, UK
Yogendra Mishra, Germany
Paulo Cesar Morais, Brazil
Paul Munroe, Australia
J.-M. Myoung, Republic of Korea
Rajesh R. Naik, USA
Albert Nasibulin, Russia
Toshiaki Natsuki, Japan
Hiromasa Nishikiori, Japan
Natalia Noginova, USA
Sherine Obare, USA
Won-Chun Oh, Republic of Korea
Abdelwahab Omri, Canada
Ungyu Paik, Republic of Korea
Edward A. Payzant, USA
- Alessandro Pegoretti, Italy
Oscar Perales-Pérez, Puerto Rico
Jorge Pérez-Juste, Spain
Alexey P. Popov, Finland
Thathan Premkumar, Republic of Korea
Helena Prima-García, Spain
Alexander Pyatenko, Japan
Haisheng Qian, China
You Qiang, USA
Philip D. Rack, USA
Mohammad Rahimi-Gorji, Belgium
Peter Reiss, France
Ilker S. Bayer, Italy
Lucien Saviot, France
Sudipta Seal, USA
Shu Seki, Japan
Donglu Shi, USA
Bhanu P. Singh, India
Surinder Singh, USA
Vladimir Sivakov, Germany
Adolfo Speghini, Italy
Marinella Striccoli, Italy
Fengqiang Sun, China
Ashok K. Sundramoorthy, India
Angelo Taglietti, Italy
Bo Tan, Canada
Leander Tapfer, Italy
Valeri P. Tolstoy, Russia
Muhammet S. Toprak, Sweden
R. Torrecillas, Spain
Achim Trampert, Germany
Takuya Tsuzuki, Australia
Tamer Uyar, Turkey
Luca Valentini, Italy
Antonio Vassallo, Italy
Ester Vazquez, Spain
Ajayan Vinu, Australia
Ruibing Wang, Macau
Shiren Wang, USA
Yong Wang, USA
Magnus Willander, Sweden
Ping Xiao, UK
Zhi Li Xiao, USA
Yingchao Yang, USA



Yoke K. Yap, USA
Dong Kee Yi, Republic of Korea

Jianbo Yin, China
William Yu, USA

Michele Zappalorto, Italy
Renyun Zhang, Sweden

Contents

Multifunctional Hybrid Nanomaterials for Energy Storage

Zhengping Zhou , Jiawei Gong , Yichen Guo , and Linqin Mu 
Editorial (2 pages), Article ID 3013594, Volume 2019 (2019)

Study on the Relationship between Electrical Tree Development and Partial Discharge of XLPE Cables

Chaofei Gao , Yanlong Yu, Zan Wang, Wei Wang, Liwei Zheng, and Jian Du
Research Article (10 pages), Article ID 8932312, Volume 2019 (2019)

Bandgap Engineering of Bilayer Ge/CdS Thin Films via Interlayer Diffusion under Different Annealing Temperatures

Faheem Amin , Syedah Afsheen Zahra, Muhammad Sultan, Sajjad Hussain Mirza, and Fahad Azad
Research Article (10 pages), Article ID 8384794, Volume 2019 (2019)

Improving Electrochemical Activity in a Semi-V-I Redox Flow Battery by Using a C-TiO₂-Pd Composite Electrode

Tsung-Sheng Chen, Shu-Ling Huang , Mei-Ling Chen, Tz-Jiun Tsai, and Yung-Sheng Lin 
Research Article (11 pages), Article ID 7460856, Volume 2019 (2019)

Mesoporous Nickel-Based Zeolite Capsule Complex with Fe₃O₄ as Electrode for Advanced Supercapacitor

Lili Song, Yinghui Han , Feng Guo, Yunpeng Jiao, Yujuan Li, Yunpeng Liu , and Feng Gao
Research Article (13 pages), Article ID 9813203, Volume 2018 (2019)

Study of a Microbistable Piezoelectric Energy Harvesting

Li Hua Chen , Shou Jie Cui , Shuo Yang , and Wei Zhang 
Research Article (8 pages), Article ID 7824685, Volume 2018 (2019)

The Effects of Power Levels/Time Periods for Sputtering Cobalt onto Carbon Nanotubes/Graphene Composites and Cobalt Annealed on the Characteristics of Anode Materials for Lithium-Ion Batteries

Chuen-Chang Lin , You-Lun Shen, and An-Na Wu
Research Article (11 pages), Article ID 9489042, Volume 2018 (2019)

Template-Free Electrochemical Preparation of Hexagonal CuSn Prism-Structural Electrode for Lithium-Ion Batteries

Xiaona Pan, Haiyan Zhang, Xiaoyu Wen, Jinqiu Zhang, Maozhong An, and Peixia Yang 
Research Article (5 pages), Article ID 1507985, Volume 2018 (2019)

UCNPs@Zn_{0.5}Cd_{0.5}S Core-Shell and Yolk-Shell Nanostructures: Selective Synthesis, Characterization, and Near-Infrared-Mediated Photocatalytic Reduction of Cr(VI)

Wan-Ni Wang, Wang Dong, Chen-Xi Huang, Bo Liu, Sheng Cheng , and Haisheng Qian 
Research Article (9 pages), Article ID 1293847, Volume 2018 (2019)

Effects of Biceramic AlN-SiC Microparticles on the Thermal Properties of Paraffin for Thermal Energy Storage

Arash Badakhsh, Kay-Hyeok An , Chan Woo Park , and Byung-Joo Kim 
Research Article (10 pages), Article ID 8632350, Volume 2018 (2019)

Editorial

Multifunctional Hybrid Nanomaterials for Energy Storage

Zhengping Zhou ^{1,2}, Jiawei Gong ³, Yichen Guo ⁴, and Linqin Mu ^{1,5}

¹Department of Chemistry, Virginia Tech, Blacksburg, VA 24061, USA

²Department of Mechanical Engineering, North Dakota State University, Fargo, ND 58108, USA

³Department of Mechanical Engineering, Penn State Behrend, Eire, PA 16563, USA

⁴Materials Science and Engineering, Stony Brook University, Stony Brook, NY 11794, USA

⁵Institute of Physics, Chinese Academy of Sciences, Beijing 100190, China

Correspondence should be addressed to Zhengping Zhou; zzhou85@vt.edu

Received 28 February 2019; Accepted 28 February 2019; Published 3 April 2019

Copyright © 2019 Zhengping Zhou et al. This is an open access article distributed under the Creative Commons Attribution License, which permits unrestricted use, distribution, and reproduction in any medium, provided the original work is properly cited.

Over the past few decades, nanomaterials have played a crucial role in the development of energy storage. A tremendous progress in the design and preparation of new nanomaterials has brought a large number of solutions to the existing challenges in energy storage systems, such as high energy and power densities, high efficiency, long-term stability, and low-cost processes. As an emerging material, multifunctional hybrid nanomaterials, usually integrating two or more disparate nanomaterials (e.g., polymeric, semiconductive, carbonaceous, and inorganic materials), have been considered a promising candidate to address these challenges. In particular, the hybridization of these nanomaterials can lead to unique superior multifunctions and thus offers the vast promise of applications in chemical and biological sensing, heterogeneous catalysis, energy conversion and storage, and environment and human health.

Currently, people are learning to integrate different types of nanomaterials to tailor the structures and improve the properties including but not limited to a high specific surface area, a well-controlled pore or particle size, a homogeneous distribution, and a strong attachment between nanomaterial interfacial surfaces. The ability to tailor the structures and properties of hybrid nanomaterials over broad length scales suggests that researches on hybrid nanomaterials will have a tremendous impact in the fields of polymer, carbon, nanotechnology, physical chemistry, and electrochemistry. However, the design and preparation of multifunctional hybrid nanomaterials remain challenging and their introduction

into practical applications is not yet satisfactory. Therefore, it is highly desirable to provide a breakthrough on the state-of-the-art nanomanufacturing and scale-up nanotechnology to design and synthesize advanced multifunctional hybrid nanomaterials with improved performance.

In this special issue, we present an elegant collection of high-quality reviews and original articles that illustrate the importance of developing multifunctional hybrid nanomaterials for energy storage and related applications. A deep understanding and relevant theoretical calculations for exploring the behaviors of integrated nanomaterials at their interface have also been obtained by fundamental investigations. The purpose of this editorial is to provide a brief introduction for each published or accepted paper and highlight their major findings and discoveries. In the following, we review all the articles in our special issue, and we believe this editorial will interest the broadest possible section of readership.

Traditional mesoporous metal oxide materials for supercapacitor electrodes undergo either high cost or performance limits (e.g., specific capacitance and cycle life). A new kind of cost-effective complex materials was designed and synthesized by L. Song et al. through an internal template method. This innovated material made of mesoporous nickel-based capsule complex with Fe_3O_4 was used as a supercapacitor electrode, exhibiting a high specific capacitance of 739.8 F/g at a current density of 1 A/g in a 6 M KOH electrolyte solution. They demonstrated a good capacitance retention of

72.8% after 1000 cycles of charge/discharge processes, indicating this new complex material as a promising electrode material for use in supercapacitors. The work by T.-S. Chen et al. presented a C-TiO₂-Pd composite electrode for use in a semivanadium/iodine redox flow battery (semi-V-I RFB) system. The authors found out that the C-TiO₂-Pd electrodes enhanced the electrocatalytic activity of the designed semi-V-I RFB system and then led to an improved energy storage ability. A high energy efficiency of 81.23% was obtained. This excellent work could bring us a new design and assembly technology to further improve the overall efficiency of energy storage systems.

To break up the performance limits of anode materials in Li-ion batteries, C.-C. Lin et al. have designed and prepared carbon nanotubes/graphene deposited with cobalt. A good understanding on how the sputtering power levels/time periods influence the specific capacity of Li-ion batteries has been explored. This study tells us that a longer time period of cobalt sputtering will lead to a higher capacity. Differently, the specific capacity increased at the power level range of 50-100 W, but decreased at the range of 100-150 W. X. Pan et al. have reported a direct template-free electrodeposition method to synthesize hexagonal CuSn prism electrodes for Li-ion batteries. The batteries exhibited an initial discharge capacity of 345 mAh/g and still maintained a high capacity of 210 mAh/g after 10 cycles. When the electrodeposition time was increased, the diameter of CuSn prism increased, but the structure converted to be inhomogeneous and unsteady. Moreover, the size of CuSn prism strongly influenced the capacity and cycle performance of Li-ion batteries.

A study of a microbistable piezoelectric energy harvester is reported by L.H. Chen et al. Based on Hamilton's principles, they have established a nonlinear oscillation differential equation by investigating thermoelectromechanical coupling effect. With the size effect, the strain gradient theory is extended to the nonlinear problem of microbistable piezoelectric energy harvesting. When the ambient vibration frequency was increased, the microscale bistable energy harvester led to a snap-through phenomenon. Gao et al. have investigated the relationship between the electrical tree development and the partial discharges of cross-linked polyethylene cables. According to their calculation, an early warning caused by the defects in cable insulation can be detected, which helps to effectively monitor the cable conditions.

Paraffin wax has been proven to be a very promising phase-change material for the purpose of latent heat thermal storage. However, the low intrinsic thermal conductivity of paraffin restrains its performance. To improve the thermal conductivity, A. Badakhsh et al. produced a paraffin composite reinforced with the AlN-coated SiC ceramic powder (SiC@AlN). Due to the high affinity between AlN and paraffin, SiC@AlN powder can be evenly dispersed within the paraffin matrix, which creates the conductive networks to enhance the thermal conductivity of the composite. In addition, this paraffin composite is proven to be cost-effective and easily processable.

Another interesting research is reported in detail by W.-N. Wang et al., who explored a facile two-step solution

method for the synthesis of upconversion nanoparticles with Zn_{0.5}Cd_{0.5}S (UCNPs@Zn_{0.5}Cd_{0.5}S) core-shell and yolk-shell nanostructures. They demonstrated that the UCNPs@Zn_{0.5}Cd_{0.5}S core-shell nanostructures can be converted to the yolk-shell nanostructures through a calcination at 400°C. In addition, the UCNPs@Zn_{0.5}Cd_{0.5}S yolk-shell nanostructures substantially improved the photocatalytic activity for reduction of Cr(VI) under near-infrared light. The paper by Amin et al. investigated the band gap changes of Ge/CdS bilayer films under different annealing temperatures. At high temperatures, Ge diffused into a CdS layer, forming a mixed phase of CdGeS. It was found that the optical band gap of the bilayer has a linear relationship with the annealing temperature. Increasing the temperature led to a wide band gap. This finding proposed a practical method of engineering the band gap of Ge/CdS bilayer films, which paves a way to their applications in optoelectronic devices.

In view of the above review and discussion, we believe that the present special issue explored the latest research on multifunctional hybrid nanomaterials including fundamental theory and experiments together with reviews and articles. More efficient designs and synthesis processes, as well as the further understandings on the interfacial chemistry of integrated materials in energy storage systems, are needed.

Conflicts of Interest

The guest editors declare that this work was conducted in the absence of any commercial or financial relationships that could be construed as a potential conflict of interest.

Authors' Contributions

All the guest editors wrote the editorial and contributed to and approved the final editorial.

Zhengping Zhou
Jiawei Gong
Yichen Guo
Linqin Mu

Research Article

Study on the Relationship between Electrical Tree Development and Partial Discharge of XLPE Cables

Chaofei Gao¹, Yanlong Yu,² Zan Wang,^{1,3} Wei Wang,¹ Liwei Zheng,¹ and Jian Du¹

¹State Key Laboratory of Alternate Electrical Power System with Renewable Energy Sources, North China Electric Power University, Beijing 102206, China

²Hangzhou Power Supply Bureaus, Hangzhou 310052, China

³State Grid Economic and Technological Research Institute Co. Ltd., Beijing 102209, China

Correspondence should be addressed to Chaofei Gao; gao200401050208@126.com

Received 16 October 2018; Revised 10 January 2019; Accepted 20 February 2019; Published 1 April 2019

Guest Editor: Zhengping Zhou

Copyright © 2019 Chaofei Gao et al. This is an open access article distributed under the Creative Commons Attribution License, which permits unrestricted use, distribution, and reproduction in any medium, provided the original work is properly cited.

Based on the slice materials of 35 kV and 110 kV XLPE cables, an experimental platform is built to study the relationship between electrical tree and PDs in XLPE with different voltage levels. There are three significant statistical characteristics of the PDs during the growth of electrical trees. The analysis of the results shows that each growth stage has certain characteristics. Different features existed between the growth of the electrical trees and the PD in the insulation of the 35 and 110 kV cables. Evident characteristics such as large spans of time and frequency were present as the electrical trees grew violently in the equivalent time-frequency diagram at every stage. These results could provide criteria for the identification of the deterioration using PD to monitor cables in service at rated voltages. The results are important for the identification of defects in cable insulation in order to provide an early warning of insulation breakdown in the cables.

1. Introduction

The study on the electrical trees and partial discharge of cross-linked polyethylene (XLPE) cables has been a critical issue for achieving better properties of XLPE cables [1–3]. Further, predictive maintenance of power cables plays an important role in effectively detecting and discovering insulation defects so that power grid interruptions caused by sudden power cable failure can be avoided [4, 5].

Partial discharge (PD) detection is recognized as the most direct and effective method to evaluate the insulation conditions of the cables [6–8]. However, no research has been done on how to estimate and forecast the degree of insulation defects based on the PD. It is important to forecast the insulation conditions of cables in order to find a standard to evaluate the severity of cable insulation defects through partial discharge detection [9].

Most insulation faults occur in cable accessories [10, 11]. Partial discharge is more likely to occur in the cable accessories due to their complex structure, concentrated electric field

stress, and on-site construction. The breakdown of insulation in cable accessories is caused by lateral slip flash discharges between the stress cone and XLPE insulation [12, 13], as well as longitudinal dendritic discharge in XLPE insulation, which is the major form of discharge. These discharges initially develop from small PD [14–16]. Consequently, it necessitates more complete understanding of the relationship between electrical tree development and partial discharge of XLPE cables [17, 18]. It is of great importance for the online diagnosis of cable defects in PD detection to provide an early warning [19].

In this paper, the characteristics of PD during the electrical tree growth process in the insulations of 35 kV and 110 kV XLPE cables were studied by monitoring partial discharge and observing the growth of electrical trees using a digital microscope. The results can provide criteria for the identification of defects in the cable insulation in online monitoring of PD.

Although widely used in the study of electrical trees, the majority of microscopes are used to study the morphological

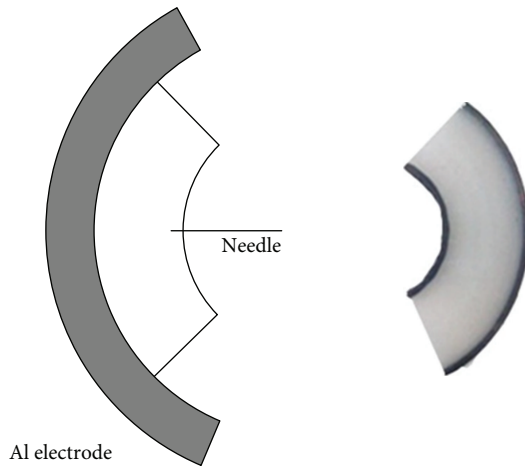


FIGURE 1: Sketch of the 35 kV XLPE cable slice and the needle-plate electrode.

growth of electrical trees at applied voltages. However, by combining the growth of electrical trees and the characteristics of PD in actual cable insulation, this paper studied the identification of defects in the insulation in order to provide an early warning of the breakdown of the cable insulation for the first time.

2. Experimental

2.1. Materials. Two kinds of test samples of the cable slices were used in the real-time monitoring system. One is 5 mm in thickness which was cut from 35 kV XLPE cable, and the other is 5 mm thick and were cut from 110 kV XLPE cable.

For the test samples of 35 kV cables shown in Figure 1, two semiconductive layers and XLPE insulation were kept on both sides. In order to collect clear images of the electrical trees, the surface of the translucent slices was sanded with sandpaper until it becomes glossy and smooth [20].

The electrode structure that was used to induce electrical trees was the typical needle-plate electrode. The ground electrode was made of aluminum and was close to the outer semiconductive layer. An austenitic stainless steel needle was used as the needle electrode on the high-voltage side [21, 22]. In order to narrow the difference between the induced electrical trees and the actual defects, the curvature radius of the needle tip should be as small as possible and was about $7 \pm 1 \mu\text{m}$. After being heated, the needle tip was inserted slowly from the inner semiconductive layer 1 mm into the insulation. Heating the needle tip prevented the formation of small air gaps in the insulation when the needle was removed. The thickness of the 35 kV XLPE cable insulation was 11 mm and was 1 mm for the semiconductive shield. The distance from the needle tip to the outer semiconductive shield was about 10 mm.

The test samples of 110 kV cables were shaped as in Figure 2 in order to avoid surface flashover between the needle tip and the aluminum electrode at the rated voltage of 110 kV [23, 24]. The XLPE barriers were 7 mm in height and 1 mm thick, and both sides were processed in the cable insulation to prevent the surface slip flash discharge along

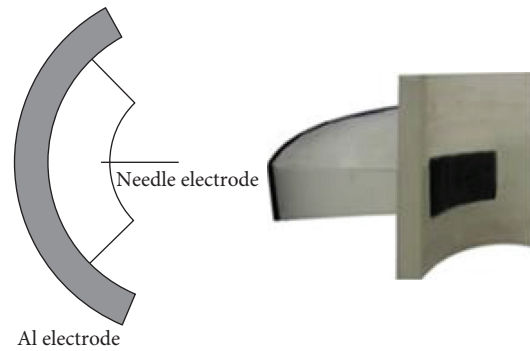


FIGURE 2: Sketch of the 110 kV XLPE cable slice and the needle-plate electrode.

the surface of the cable slices between the needle electrode and the ground electrode. The inner semiconductive layer, 5 mm wide and 1 mm thick, was reserved as shown. The thicknesses of the 110 kV XLPE cable insulation and the inner and outer semiconductive shields were 18 mm, 1.5 mm, and 1 mm, respectively. After being heated, the needle tip was inserted slowly from the inner semiconductive layer 2 mm into the insulation. The distance between the needle tips and the outer semiconductive shield was 16 mm.

2.2. Real-Time Monitoring System. The experimental system was made up of three parts. The first part was the equipment collecting the electrical tree images, which included the digital microscope, industrial control computer, and a cold light source. These images observed and collected using this part were updated four times per second in order to reflect the morphological growth of electrical trees in real time.

The second part was the PD detection system that included the testing transformer, detection sensor, oscilloscope, and industrial control computer. The detection impedance was connected to the ground loops of the samples of cable slices. The partial discharge signals detected by the impedance were magnified by the amplifier that had a magnification of 35 dB and a bandwidth of 3-40 MHz [25]. The VHF bandwidth is usually adopted in actual online monitoring.

The final part of the experimental setup was the sample of cable slices that were immersed in transformer oil and loaded in a transparent plexiglass tank. This prevents the creeping discharge and surface flashover between the needle ground electrodes. In order to collect clear and bright images of the electrical trees, the light emitted from the cold light must pass through the transparent plexiglass tank, the slice, and the transformer oil at the same time. The schematic illustration of the test system was shown in Figure 3.

2.3. Statistical PD Characteristics. The raw PD data in the growth processes of the electrical trees were sampled every two hours, and each sampling period collected 150 power frequency periods. The statistical characteristics of PD were chosen to characterize the deterioration process of the electrical trees in the XLPE cables [26, 27]. These characteristics are as follows:

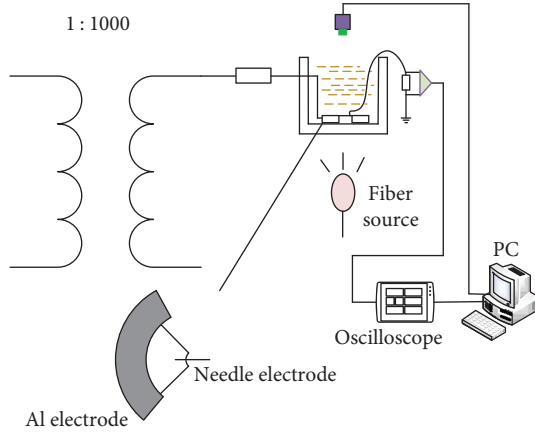


FIGURE 3: Schematic illustration of the test system.

q_m , the maximum discharge magnitude of PD signals in each sampling period;

q , the average discharge magnitude of PD signals in each sampling period;

U , the average discharge amplitude of PD signals in each power frequency period in each sampling period; and n , the average numbers of discharge of PD signals in each power frequency period in each sampling period.

2.4. Waveform Characteristics of PD. The equivalent time-frequency classification algorithm of the PD pulse was chosen to identify the deterioration degree. Different time-frequency features of PD waveforms at different deterioration stages provided a foundation for the identification of the deterioration degree of electrical trees [28, 29].

Considering the application in online monitoring, the feature extraction of pulse waveform should have the following characteristics: (1) real-time and fast calculations, (2) unrelated to the time record points, and (3) unrelated to the pulse amplitude and polarity. Accordingly, the data processing of a single-pulse waveform obtained from broadband detection was as follows:

$$p_j(t_i) = \begin{cases} m_0, m_1, \dots, m_i, \dots, m_{n-1}, \\ 0, \Delta t, \dots, \Delta t_{(i-1)}, \dots, \Delta t_{(n-1)}, \end{cases} \quad (1)$$

$$P_j(f_i) = \begin{cases} M_0, M_1, \dots, M_i, \dots, M_{(n/2)-1}, \\ 0, \Delta f, \dots, \Delta f_{(i-1)}, \dots, \Delta f_{((n/2)-1)}, \end{cases}$$

where p_j is the j -th pulse; P_j is the pulse p_j 's fast Fourier transform (FFT); n represents that the pulse waveform is composed of n points, and the FFT spectrum of the pulse waveform is composed of $n/2$ points; m_i is the amplitude of corresponding time domain waveform of i -th point; $\Delta t_{(i-1)}$ is the corresponding time points for the i -th point ($\Delta t = 1/f$, s is the sampling interval, f is the sampling rate, and $s = n\Delta f$); and $\Delta f_{(i-1)}$ is the frequency value of the i -th point.

In this paper, the time dispersing T and frequency dispersing F were selected to obtain the feature extraction of

the pulse waveform. The processing of the pulse $p_j(t_i)$ was as follows:

$$T_0^j = \frac{\sum_{i=0}^n t_i p_j(t_i)^2}{\sum_{i=0}^n p_j(t_i)^2},$$

$$F_0^j = \frac{\sum_{i=0}^{n/2} f_i P_j(f_i)^2}{\sum_{i=0}^{n/2} P_j(f_i)^2},$$

$$(T_j)^2 = \frac{\sum_{i=0}^n (t_i - T_0^j)^2 \cdot p_j^2(t_i)}{\sum_{i=0}^n p_j^2(t_i)},$$

$$(F_j)^2 = \frac{\sum_{i=0}^{n/2} (f_i - F_0^j)^2 \cdot P_j^2(f_i)}{\sum_{i=0}^{n/2} P_j^2(f_i)}.$$

In equation (2), the mean time of the pulse waveform signal T_0^j and mean frequency F_0^j were calculated. The strike time T_j and frequency spread F_j of the pulse waveform signal were, respectively, defined as equivalent time width and equivalent bandwidth.

The 150 pulse waveforms of the PD that were collected in each sampling period were collected at a sampling rate of 1 GHz. The sampling time for each PD pulse was $1 \mu s$ so that the true PD pulse information could be fully reflected in the data. Next, 150 points appeared on the T - F diagram after the equivalent time-frequency transformed, and each point represented the equivalent time and frequency of a PD pulse waveform. On the basis of the principle of fuzzy cluster analysis, T - F points of similar waveforms could achieve good clustering performance, so the deterioration stages can be characterized using the T - F diagram.

3. Results and Discussion

3.1. Growth Characteristics of Electrical Trees of 35 kV Cables.

The rated phase voltage of the 20.2 kV was evenly applied on the needle electrode and inserted into the insulation slice. The growth of electrical trees lasted about 49 hours from the starting of the electric branches to the breakdown of the entire insulation. The degradation process of the electrical trees was divided into five stages in chronological order: the early stage from 0 to the 10th hour, the early-middle stage from the 10th to 20th hour, the middle stage from the 20th to 30th hour, the middle-late stage from the 30th to 40th hour, and the late stage from the 40th to 49th hour.

The growth process of the electrical trees can be outlined as follows: the initial electrical trees expanded quickly at the early stage; stagnation-type electrical trees existed at early-middle stage; branches of electrical trees expanded quickly and developed into dendritic forms during the middle stage; the branched trees continued to expand throughout the entire insulation during the middle-late stage; at the late stage, the entire insulation was covered with electrical trees; and finally, the electric breakdown of the slice occurred. The typical states of the electrical trees from the beginning to breakdown are shown in Figure 4.

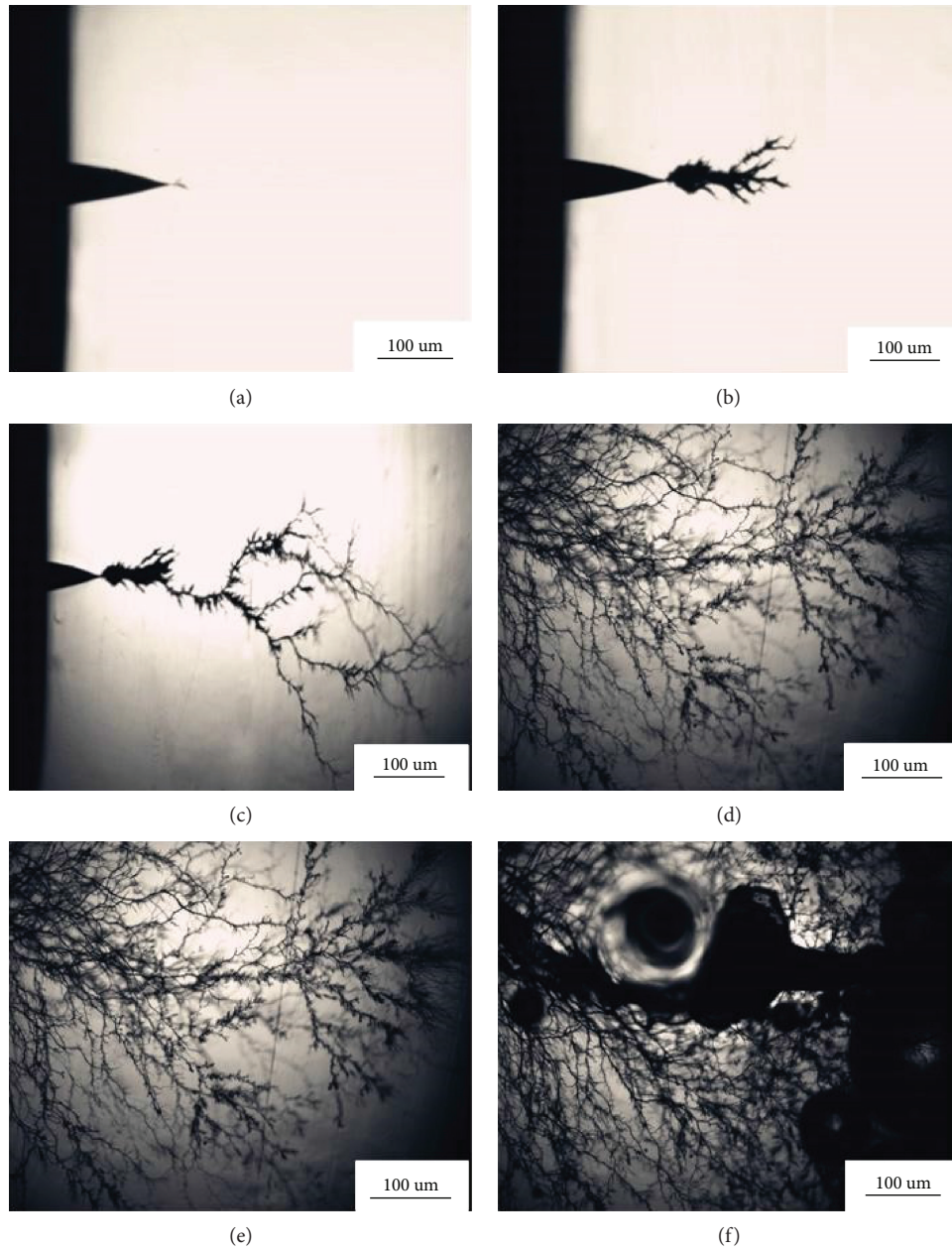


FIGURE 4: Deterioration process of the entire cable insulation of 35 kV cable: (a) starting, (b) 12 hours later, (c) 22 hours later, (d) 37 hours later, (e) 48 hours later, (f) breakdown.

3.2. Growth Characteristics of Electrical Trees of 110 kV Cables. The rated phase voltage of 63.5 kV was evenly applied on the needle electrode and inserted into the insulation slice. The growth of electrical trees lasted about 50 hours from the starting of the electrical trees to the breakdown of the entire insulation. The degradation process of the electrical trees was divided into five stages in chronological: the early stage from 0 to the 10th hour, the early-middle stage from the 10th to 20th hour, the middle stage from the 20th to 30th hour, the middle-late stage from the 30th to 40th hour, and the late stage from the 40th to 49th hour.

The growth process of the electrical trees in the 110 kV cable insulation was different from the 35 kV cable. The initial electrical trees grew out quickly during the early stage

and expanded into a bush-like structure when high voltage was applied. The branched electrical trees grew out at the front end of the bush structure in the late period of the early stage. At the early-middle stage, the growth of electrical trees did not stagnate, but the bush-like electrical trees continued to expand. The branched electrical trees at the front end of the bush structure gradually grew and became thicker, and more subtle electrical trees appeared around the branched electrical trees. During the middle stage, some branched electrical trees developed quickly and covered the insulation in fan shapes. At the middle-late stage, the branched electrical trees continued to expand and became thicker. During the late stage, the electrical trees covered the entire insulation and reached the outer semiconductive layer and the main

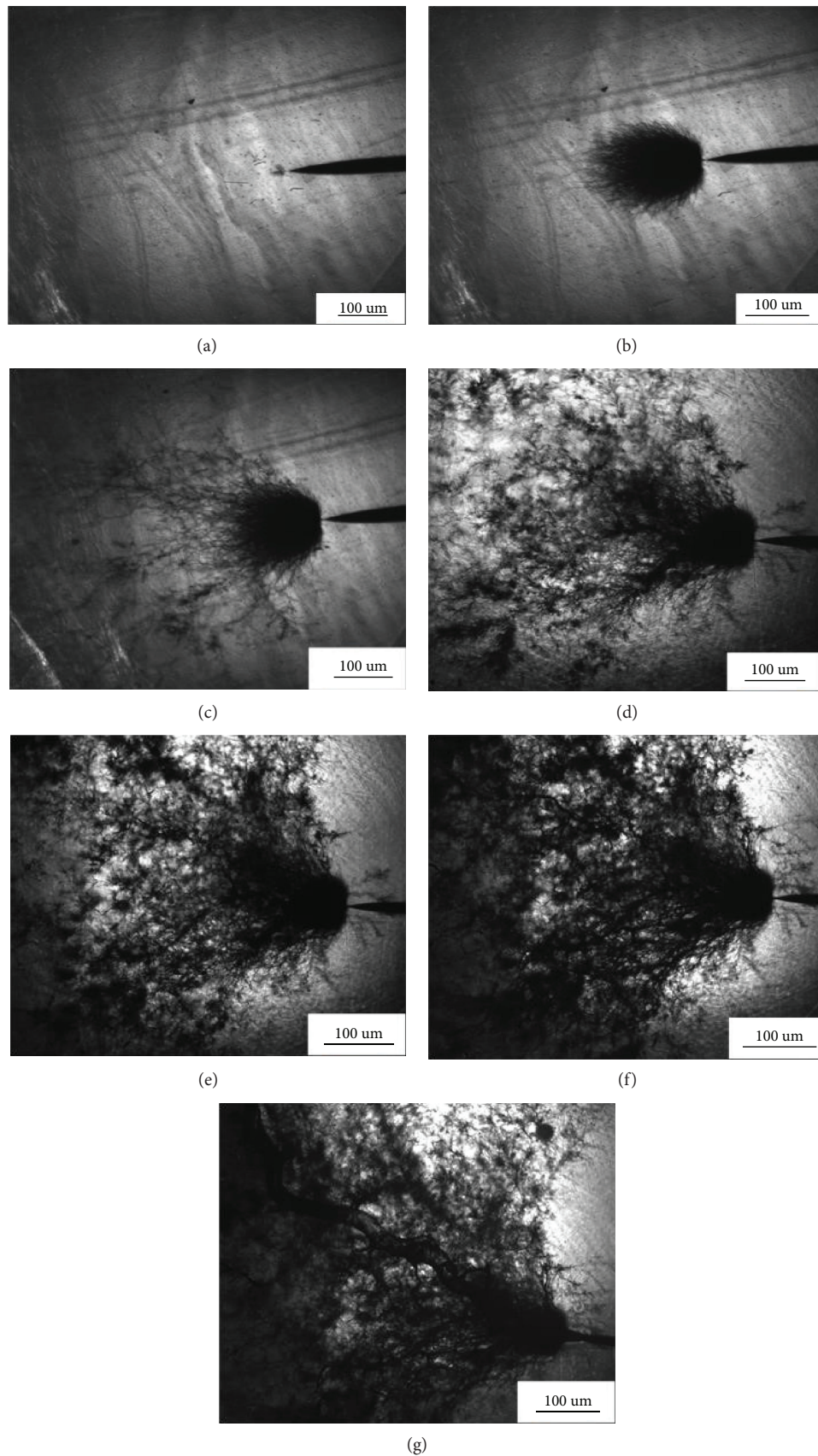


FIGURE 5: Deterioration process of the entire cable insulation of 110 kV cable: (a) starting, (b) 5 hours later, (c) 11 hours later, (d) 26 hours later, (e) 39 hours later, (f) 47 hours later, (g) breakdown.

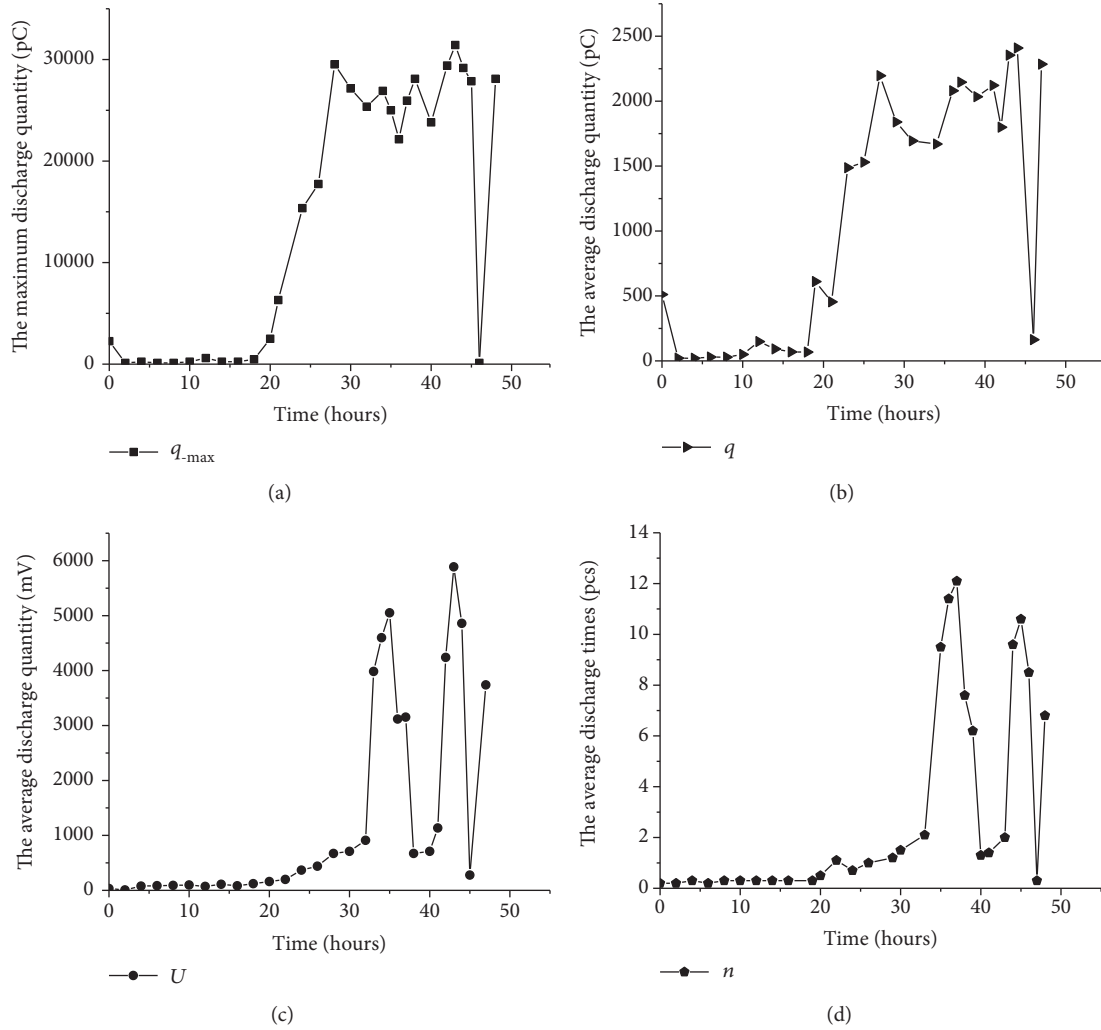


FIGURE 6: The changing trends of the statistical characteristics of PD in the growth process of electrical trees in 35 kV cable deterioration process of the whole cable insulation of 35 kV cable.

branches became thicker. At last, one of the main branching trees became a conductive channel and the insulation slice broke down. The typical states of the electrical trees from the beginning to breakdown are shown in Figure 5.

3.3. Statistical Characteristics of PD of 35 kV Cables. The trend graphs of q_m , q , U , and n during the entire degradation process of the electrical trees are shown in Figure 6. The q_m and q of the initial electrical trees at the early stage were larger than those of the stagnation-type electrical trees during the early-middle stage. The PD for the stagnation-type electrical trees was small and could hardly be detected. The q_m and q quickly rose during the middle stage and maintained a high and stable level before the breakdown which was far greater than at the early stage. However, U and n decreased dramatically near the 40th hour when the electrical trees reached the outer semiconductive layer. The PD had the special characteristics during this stage, with small and weak discharges, interspersed with the occasional large discharges. Additionally, the PD suddenly disappeared shortly before the breakdown and then increased rapidly for a short period before the breakdown.

3.4. Equivalent Time-Frequency Characteristics of PD Pulses at Different Deterioration Stages of 35 kV Cables. The equivalent time-frequency characteristics of the PD pulses at different deterioration stages can be summarized by quick growth of the electrical trees when the voltage was applied (Figure 7).

In the equivalent time-frequency diagram, discharges occurred in areas one and two and most were concentrated in area one, whose equivalent time width and equivalent bandwidth were from 120 to 260 ns and from 3 to 20 MHz, respectively. There were rare discharges in area two, whose equivalent time width and equivalent bandwidth were from 180 to 220 ns and from 27 to 40 MHz, respectively. Twelve hours later, the stagnation-type electrical trees occurred at the early-middle stage and all discharges were concentrated in area one, whose equivalent time width and bandwidth were from 100 to 200 ns and from 3 to 20 MHz, respectively.

Twenty-two hours later, branches of electrical trees expanded quickly and developed into a dendritic form. In the equivalent time-frequency diagram, there were discharges in both areas one and two and most of the discharges were concentrated in area two. The equivalent time widths and equivalent bandwidths of areas one and two were from

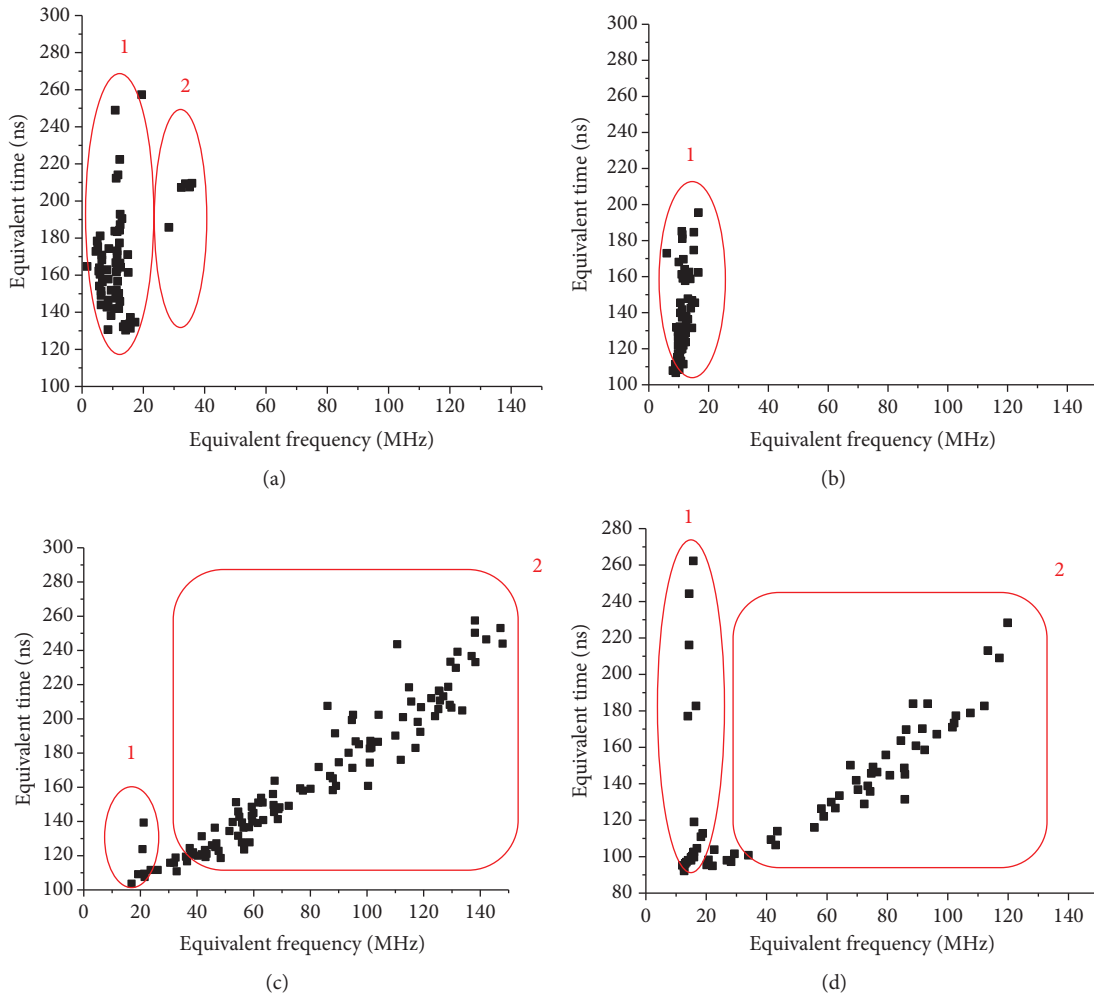


FIGURE 7: T - F clustering diagrams of PD pulse in the growth process of electrical trees in 35 kV cable: (a) starting, (b) 12 hours later, (c) 22 hours later, (d) 48 hours later.

100 to 140 ns and from 15 to 25 MHz and from 100 to 260 ns and from 25 to 150 MHz, respectively. Forty-eight hours later, the entire insulation was covered by electrical trees and almost all electrical tree clusters reached the outer semiconductive layer. At this point, the slice was about to breakdown. In the equivalent time-frequency diagram, there were discharges in both areas one and two and there were more discharges in area one than in area two. The equivalent time width and equivalent bandwidth of area one were from 90 to 260 ns and from 10 to 25 MHz, while those of area two were from 100 to 240 ns and from 25 to 125 MHz, respectively.

3.5. Statistical Characteristics of PD of 110 kV Cables. The trend graphs for the q_m , q , U , and n during the entire degradation process of the electrical trees are shown in Figure 8. The q_m and q of the initial electrical trees at the early stage were relatively large, but the discharges were small, and occasionally there were several large discharges during the early stage. The PD could not maintain a stable state during the early-middle and middle stages. Occasionally, the PD signals were small and could hardly be detected, but they were large at other times. Then, the PD maintained a stable state

during the middle-late stage. Four statistical characteristics maintained a high and stable level. The PD was weakened when the electrical trees reached the outer semiconductive layer during the late stage, but increased rapidly right before the breakdown.

3.6. Equivalent Time-Frequency Characteristics of PD Pulses at Different Deterioration Stages of 110 kV Cables. The equivalent time-frequency characteristics of PD pulses at different deterioration stages are summarized as in Figure 9.

The initial electrical trees branched out quickly and expanded into a bush-like structure at the early stage. There were discharges both in area one and two, and there were more discharges in area one than in area two. The equivalent time width and equivalent bandwidth of area one were from 430 to 540 ns and from 5 to 25 MHz, while those of area two were from 440 to 480 ns and from 25 to 40 MHz, respectively. Eleven hours later, the equivalent time width and equivalent bandwidth of area one were from 430 to 500 ns and from 10 to 25 MHz, while those of area two were from 430 to 520 ns and from 30 to 60 MHz, respectively. Twenty-six hours later, the electrical trees grew quickly. There were no discharges in

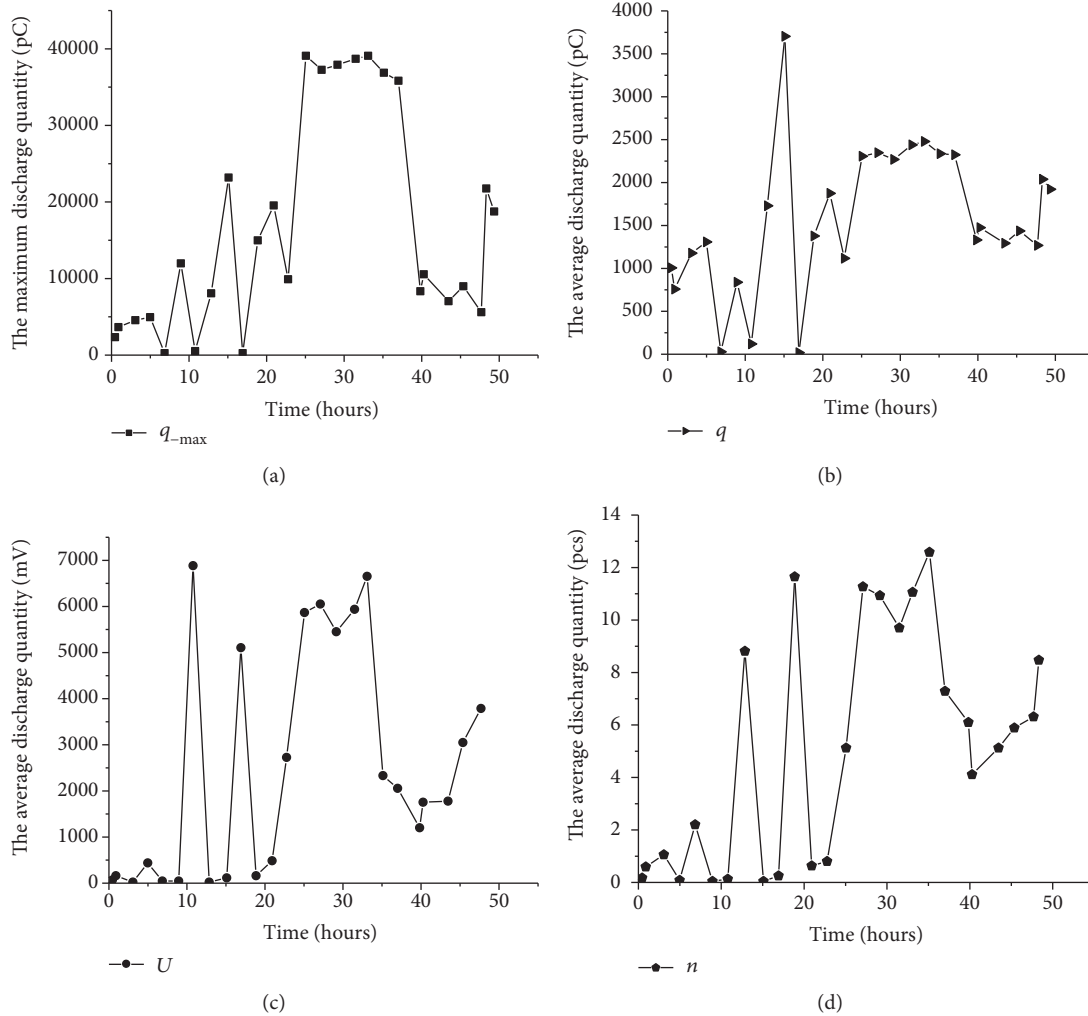


FIGURE 8: The changing trends of the statistical characteristics of PD in the growth process of electrical trees in 110 kV cable deterioration process of the whole cable insulation of 110 kV cable.

area one, but discharges were concentrated in area two, whose equivalent time width was from 400 to 560 ns and the equivalent bandwidth from 30 to 110 MHz as a result of the drastic growth of electrical trees. Forty-seven hours later, there were discharges in both areas one and two, but more discharges are concentrated in area two. The equivalent time width and equivalent bandwidth in area one were from 440 to 480 ns and from 10 to 35 MHz, while those in area two were from 450 to 560 ns and from 35 to 100 MHz, respectively.

4. Conclusion

In this paper, a real-time system using PDs was built to monitor the growth of electrical trees in the slices of 35 kV and 110 kV XLPE. The morphological development of the electrical trees and the characteristics of PD were studied at rated voltages. The following conclusions were drawn.

- (1) The morphological development was different between the electrical trees in the 35 kV and the 110 kV XLPE. The morphology of the electrical trees in the 35 kV cable insulation was dendritic, while that

in the 110 kV cable insulation contained both the bushes and the dendrites. Unlike the 35 kV, the growth of the electrical trees in the 110 kV cable insulation did not stagnate during the early-middle stage and the electrical trees reached the outer semiconductive layer well before the insulation was broken down in nearly 39 hours

- (2) There were three significant statistical characteristics of the PDs during the growth of electrical trees. The first feature was that the PDs were small and could hardly be detected during the early-middle stages, although they were large when the initial electrical trees grew out. Another feature was that after growing, the PDs maintained a high and stable level during the middle and middle-late stages. The third feature was that the PDs were weakened when the electrical trees reached the outer semiconductive layer and then increased rapidly until the breakdown
- (3) As shown in the equivalent time-frequency characteristics of the PD pulses, there were some similarities in the equivalent time-frequency diagram at every

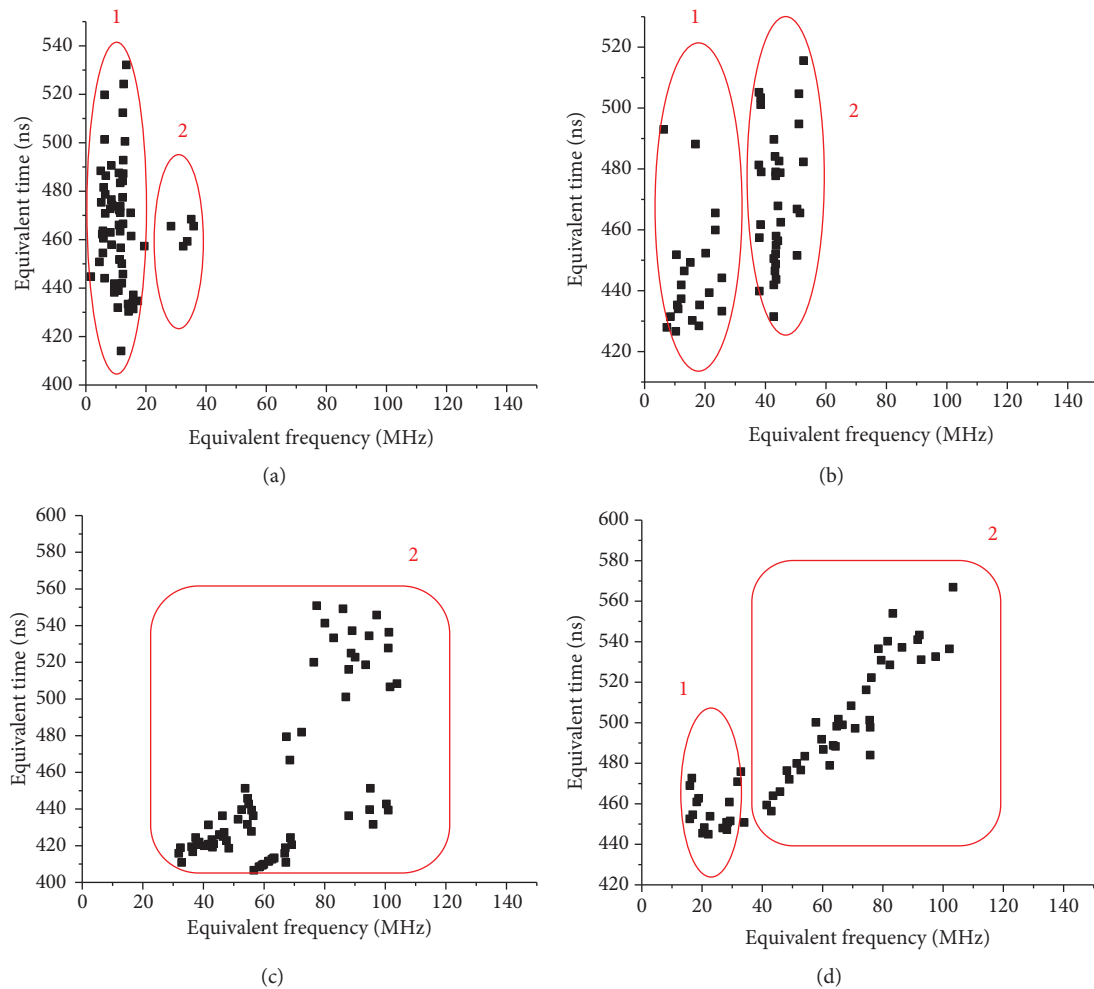


FIGURE 9: T - F clustering diagrams of PD pulse in the growth process of electrical trees in 110 kV cable: (a) starting, (b) 11 hours later, (c) 26 hours later, (d) 47 hours later.

stage in the insulation of the 35 kV and 110 kV cables. Evident characteristics such as large spans of time and frequency were present as the electrical trees grew violently in the equivalent time-frequency diagram at every stage. Such characteristics, if combined with the statistical characteristics of the PDs, could provide criteria for the identification of defects in cable insulation in order to provide an early warning of insulation breakdown in the cable

Data Availability

All authors can share the data that support the findings of the article by depositing them in a publicly available data repository wherever possible.

Conflicts of Interest

The authors declare that they have no conflicts of interest.

Acknowledgments

This research was funded by the National Basic Research Program of China (973 Program) (Grant 2009CB724506).

References

- [1] X. Chen, Y. Xu, X. Cao, and S. M. Gubanski, "On the conducting and non-conducting electrical trees in XLPE cable insulation specimens," *IEEE Transactions on Dielectrics and Electrical Insulation*, vol. 23, no. 1, pp. 95–103, 2016.
- [2] H. Sui, L. M. Shen, W. Wang, Y. L. Yu, Z. Wang, and C. F. Gao, "PD detecting during the growth of electrical trees in HV XLPE cable," in *2011 Asia-Pacific Power and Energy Engineering Conference*, pp. 1–4, Wuhan, China, March 2011.
- [3] Y. Wang, K. Xiao, C. Wang, L. Yang, and F. Wang, "Effect of nanoparticle surface modification and filling concentration on space charge characteristics in TiO_2/XLPE nanocomposites," *Journal of Nanomaterials*, vol. 2016, Article ID 2840410, 10 pages, 2016.
- [4] B. Quak, E. Gulski, F. J. Wester, and P. N. Seitz, "Advanced PD site location in distribution power cables," in *Proceedings of the*

- 7th International Conference on Properties and Applications of Dielectric Materials (Cat. No.03CH37417), pp. 183–186, Nagoya, Japan, 2003.
- [5] J. Kuffel and P. Kuffel, *High Voltage Engineering Fundamentals*, Elsevier, 2000.
- [6] N. Rouha and A. Beroual, “Modelling the treeing growth, currents and loss factor in solid electrical insulations with and without tree,” in *International Conference on Electrical Engineering, Electronics and Automatics ICREA*, pp. 135–138, Bejaia, Algeria, 2010.
- [7] C. Wang, Y. Wang, P. Fan, and R. Liao, “Space charge property of polyethylene/silica nanocomposites at different elongations,” *Journal of Nanomaterials*, vol. 2015, Article ID 963960, 14 pages, 2015.
- [8] X. L. Zhang, Z. H. Wang, Z. Y. Huang, and X. J. Han, “The design of high-voltage cable partial discharge on-line monitoring system software,” *Applied Mechanics and Materials*, vol. 672–674, pp. 810–813, 2014.
- [9] Y. Wang, Y. Wang, C. Wang, and H. Xu, “The partial discharge characteristic of typical XLPE cable insulation defects under damped oscillating voltage,” in *2014 IEEE Electrical Insulation Conference (EIC)*, pp. 290–293, Philadelphia, PA, USA, 2014.
- [10] A. H. A. Bakar, H. Mokhlis, H. A. Illias, and P. L. Chong, “The study of directional overcurrent relay and directional earth-fault protection application for 33 kV underground cable system in Malaysia,” *International Journal of Electrical Power & Energy Systems*, vol. 40, no. 1, pp. 113–119, 2012.
- [11] W. Zheng, Y. Qian, N. Yang, C. Huang, and X. Jiang, “Research on partial discharge localization in XLPE cable accessories using multi-sensor joint detection technology,” *Przegląd Elektrotechniczny*, vol. 87, no. 11, pp. 84–88, 2011.
- [12] J. G. Gao, H. Zhang, L. L. Li, J. Zhang, N. Guo, and X. H. Zhang, “Study on space charge of XLPE/O-MMT Nanocomposites,” *Acta Polymerica Sinica*, vol. 13, pp. 126–133, 2013.
- [13] X. Chen, Y. Xu, X. Cao, S. Dodd, and L. Dissado, “Effect of tree channel conductivity on electrical tree shape and breakdown in XLPE cable insulation samples,” *IEEE Transactions on Dielectrics and Electrical Insulation*, vol. 18, no. 3, pp. 847–860, 2011.
- [14] H. Wang, J. He, X. Zhang, Z. Li, L. Li, and G. Guan, “Electrical tree inception characteristics of XLPE insulation under power-frequency voltage and superimposed impulse voltage,” in *11th International Symposium on High-Voltage Engineering (ISH 99)*, pp. 320–323, London, UK, 1999.
- [15] M. Bao, X. Yin, and J. He, “Structure characteristics of electrical treeing in XLPE insulation under high frequencies,” *Physica B: Condensed Matter*, vol. 406, no. 14, pp. 2885–2890, 2011.
- [16] J. Yang, C. Liu, C. Zheng, H. Zhao, X. Wang, and M. Gao, “Effects of interfacial charge on the DC dielectric properties of nanocomposites,” *Journal of Nanomaterials*, vol. 2016, Article ID 2935202, 11 pages, 2016.
- [17] A. El-Zein, M. Talaat, and M. El Bahy, “A numerical model of electrical tree growth in solid insulation,” *IEEE Transactions on Dielectrics and Electrical Insulation*, vol. 16, no. 6, pp. 1724–1734, 2009.
- [18] Z. Jing, C. Li, H. Zhao, G. Zhang, and B. Han, “Doping effect of graphene nanoplatelets on electrical insulation properties of polyethylene: from macroscopic to molecular scale,” *Materials*, vol. 9, no. 8, p. 680, 2016.
- [19] F. Komori, D. Asai, Y. Suzuoki, and T. Kawahara, “Electrical tree in the crosslinked polyethylene with bowtie trees and the partial discharge occurrence phase angle distribution,” in *Proceedings of 2014 International Symposium on Electrical Insulating Materials*, pp. 176–179, Niigata City, Japan, 2014.
- [20] L. M. Yang, Z. E. Zhu, R. K. Yang, Y. Yang, and Y. Wang, “Insulation material and structure design of HVDC flexible cables,” *Automation of Electric Power Systems*, vol. 37, pp. 117–124, 2013.
- [21] M. Eesaee, E. David, N. R. Demarquette, and D. Fabiani, “Electrical breakdown properties of clay-based LDPE blends and nanocomposites,” *Journal of Nanomaterials*, vol. 2018, Article ID 7921725, 17 pages, 2018.
- [22] C. Laurent, F. Massines, and C. Mayoux, “Optical emission due to space charge effects in electrically stressed polymers,” *IEEE Transactions on Dielectrics and Electrical Insulation*, vol. 4, no. 5, pp. 585–603, 1997.
- [23] Suwarno, Y. Suzuoki, F. Komori, and T. Mizutani, “Partial discharges due to electrical treeing in polymers: phase-resolved and time-sequence observation and analysis,” *Journal of Physics D: Applied Physics*, vol. 29, no. 11, pp. 2922–2931, 1996.
- [24] W. Chang, C. Li, Q. Su, and Z. Ge, “Study on development of partial discharges at the defect caused by a needle damage to a cable joint,” *Zhongguo Dianji Gongcheng Xuebao*, vol. 33, no. 7, pp. 192–201, 2013.
- [25] Suwarno, “Partial discharge in high voltage insulating materials,” *International Journal on Electrical Engineering and Informatics*, vol. 8, no. 1, pp. 147–163, 2016.
- [26] T. Kumazawa, “Application of the AC superposition method to degradation diagnosis of 22/33-kV class XLPE cables,” *Electrical Engineering in Japan*, vol. 195, no. 1, pp. 32–39, 2016.
- [27] B. Jonuz, P. H. F. Morshuis, H. J. Van Breen, J. Pellis, and J. J. Smit, “Detection of water trees in medium voltage XLPE cables by return voltage measurements,” in *2000 Annual Report Conference on Electrical Insulation and Dielectric Phenomena (Cat. No.00CH37132)*, pp. 355–358, Victoria, BC, Canada, 2000.
- [28] J. Lin, J. Gui, S. Gao et al., “Propagation characteristics of partial discharge pulses in the cable,” *Journal of Power and Energy Engineering*, vol. 2, no. 9, pp. 112–116, 2014.
- [29] E. Ouatah, S. Megherfi, K. Haroun, and Y. Zebboudj, “Characteristics of partial discharge pulses propagation in shielded power cable,” *Electric Power Systems Research*, vol. 99, pp. 38–44, 2013.

Research Article

Bandgap Engineering of Bilayer Ge/CdS Thin Films via Interlayer Diffusion under Different Annealing Temperatures

Faheem Amin ¹, Syedah Afsheen Zahra,¹ Muhammad Sultan,² Sajjad Hussain Mirza,³ and Fahad Azad¹

¹Department of Physics, School of Natural Sciences, National University of Sciences and Technology, Islamabad, Pakistan

²National Center for Physics, Islamabad, Pakistan

³LINAC Project, PINSTECH, Nilore Islamabad, Pakistan

Correspondence should be addressed to Faheem Amin; faheem_phy@yahoo.com

Received 30 April 2018; Revised 6 November 2018; Accepted 23 December 2018; Published 24 March 2019

Guest Editor: Jiawei Gong

Copyright © 2019 Faheem Amin et al. This is an open access article distributed under the Creative Commons Attribution License, which permits unrestricted use, distribution, and reproduction in any medium, provided the original work is properly cited.

Bilayer thin films of Ge/CdS have been deposited on a glass substrate through thermal evaporation method. The obtained Ge/CdS samples were annealed at temperatures up to 400°C to observe the resulting effect on the structural changes in the film. The bandgap of the annealed films was found to increase with increasing annealing temperature which can be attributed to the increased interlayer diffusion. The interlayer diffusion was found to take effect above a temperature of 300°C which was confirmed by the Rutherford backscattering technique. Complementary XPS was done to investigate the surface stoichiometry of the bilayers.

1. Introduction

Multijunction solar cells are promising energy devices that are expected both to mitigate the imminent energy crisis and environmental menace [1–4]. However, for better understanding of the performance of these devices, a subtle knowledge of interfacial effects is required [5]. By carefully maneuvering the interface characteristics, the power conversion efficiency of the device can be enhanced. Moreover, the fact that theoretical efficiency is limited by the Shockley-Queisser limit exacerbated by the intrinsic losses makes the multijunction tandem solar cells with a tunable bandgap an ultimate choice [6, 7]. Multijunction solar cells on one hand can mitigate the thermal losses by utilizing several layers having different bandgap. On the other hand, the concatenation of absorber layers may enhance the efficiency of these solar cells significantly. For example, multijunction (III-V)/Ge semiconductor solar cells have been reported to manifest high efficiency of ~39% with up to four absorber layers [8]. The ability to engineer a bandgap of a multilayer thin-film solar cell is a technological milestone corroborated by the widespread research efforts over

the past few decades. Many efforts have been put by the scientists to develop cascaded structures of intrinsic (Si and Ge) and extrinsic semiconductor compounds (metal chalcogenides [9–11] and perovskites [12, 13]). However, II-VI semiconductors have been rather less explored and needed further attention. In fact, heterojunctions of Ge/CdS have been developed through chemical vapor deposition of single crystal CdS epitaxial layers on (111) *p*-Ge substrates by Paorici et al. [14]. However, their aim was to study various methods to grow CdS on a Ge substrate rather than studying the impact of interface properties on the grown structures. Cadmium sulfide is a widely used material in various applications, such as photovoltaics, biomedical imaging, catalysis, IR detector, and space technologies, due to its wide bandgap of around 2.4 eV [15–17]. In solar cells, CdS has been vastly used as a buffer layer [18, 19]. Ge, on the other hand, is an indirect bandgap material (0.66 eV) and is commonly used as a bottom layer in multijunction solar cells.

In this work, we endeavor to study the behavior of Ge/CdS bilayer system to understand the underpinned mechanism for expected bandgap change. The bandgap of CdS has been reported to be sensitive to the oxygen concentration while

Ge content has been observed to increase the bandgap of alloyed $\text{Cu}_2\text{ZnGe}_x\text{Sn}_{1-x}\text{Q}_4$ ($\text{Q} = \text{S}, \text{Se}$) [20, 21]. Therefore, we forecast a change in the bandgap of CdS upon alloying with Ge. The propitious alloying was achieved by the annealing of the bilayer films at various temperatures and diffusion of Ge into the CdS layer was observed. The interlayer diffusion is an important phenomenon as it results in the change in the thickness of layers and therefore the bandgap of materials. We specifically aimed at tailoring the thickness of the Ge layer as it has a relatively larger Bohr exciton radius (24.3 nm) [22] as compared to CdS (5.8 nm) [23].

2. Materials and Methods

All the reagents used in this study were of analytical grade. Powders of CdS (99.99%, M.Wt. $144.47 \text{ g}\cdot\text{mol}^{-1}$) and Ge (99.999%, M.Wt. $72.64 \text{ g}\cdot\text{mol}^{-1}$) were purchased from Sigma-Aldrich. The thin films were deposited on the soda lime glass substrate by thermally evaporating the precursors through resistive heating. The substrate was cleaned prior to deposition by sonicating at 70°C in dilute detergents for 10 minutes to avoid impurities that may cause defects in the films emanated due to contamination. The slides were then sonicated in deionized (DI) water for another 10 minutes to remove the detergent. Following this, the films were sonicated in pure ethanol for another 10 minutes. Finally, the slides were rinsed with DI water and blown dry with nitrogen.

For deposition, the vacuum level was maintained up to 1×10^{-5} mbar using diffusion pumps. The powders were melted in tungsten boats and evaporated to the slides. The substrates were held at room temperature and the substrate holder was rotated at 30 rpm for uniform deposition of the films. A 15 nm thick layer of Ge was deposited with an average deposition rate of 0.2 nm per second. After that, CdS was melted and evaporated to deposit a 20 nm thick layer on the Ge layer with an average deposition rate of 0.2 nm per second. The rate of deposition was monitored by the quartz crystal monitor placed inside the deposition chamber. The films were annealed in air at temperatures 100°C , 200°C , 300°C , 350°C , and 400°C inside a Muffle furnace for one hour before further use.

2.1. Structural Analysis

2.1.1. X-Ray Diffraction (XRD). X-ray diffraction (also called X-ray crystallography) was used to determine the structure of the prepared films. D8 Discover X-ray Diffractometer (Bruker AXS, Germany) was used with $\text{Cu-K}\alpha$ radiation as a source of X-rays. The analysis was done at a grazing angle of 1° .

2.1.2. Scanning Electron Microscopy (SEM). The surface morphology of the thin films was studied by a Hitachi S-4800 FEG scanning electron microscope. The microscope is equipped with a Horiba EMAX EDS detector having an EMAX energy software for the elemental analysis of the materials.

2.1.3. Atomic Force Microscopy (AFM). The topological features of the films were analysed by the AFM microscopy

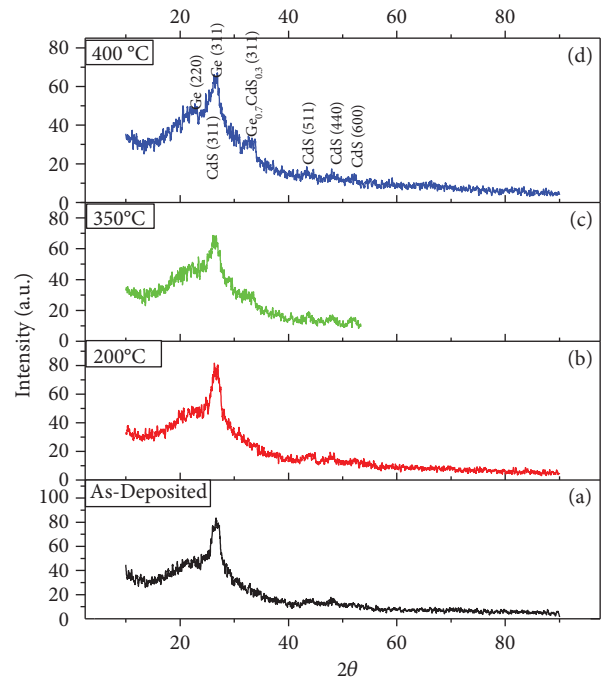


FIGURE 1: (a-d) Grazing incidence XRD pattern showing the peaks of various scatterings from the planes of Ge and CdS crystals. The spectra show the formation of FCC cubic structures of both Ge and CdS. The formation of a new mixed phase $\text{Cd}_{0.7}\text{Ge}_{0.3}\text{S}$ was also observed at high sintering temperature.

technique using Quesant Universal SPM (Ambios Technology) that can image a lateral resolution down to 1.5 nm and a vertical resolution down to 0.05 nm. The images were taken in contact mode by using silicon nitride tips. The scans were taken over $5.0 \times 5.0 \mu\text{m}$.

2.1.4. Rutherford Backscattering Spectroscopy (RBS). RBS depth profiling was done to determine the nonstoichiometric phases in the films. A beam of alpha particles of desired energy was generated by adjusting the voltage value of the beam accelerator, having a maximum capacity (5 MeV) of producing energetic He^{+2} particles, at an average energy of 2 MeV for alpha particle production. The samples were cut in pieces of size $1 \times 1 \text{ cm}^2$ and taped on the sample holder. The chamber was evacuated prior to measurement. The geometry of target and detector was measured using CORNELL. The time required for recording a spectrum depends upon the charge collection. SIMNRA was used for the simulation of RBS spectra. The simulated spectrum is overlapped on the experimental spectrum to extract information about the thickness and composition of each layer. Ag-Cu alloy monolayer (with known backscattered energies) deposited on a glass substrate was used for the energy to channel scale conversion prior to sample measurement. The calculated values for $\text{keV}(0)$ and keV/Ch were 56.820 keV and 1.1360, respectively. All of the subsequent simulations for the different samples were done using these values. After the successful channel to energy scale calibration, the expected target information was provided to the software and the simulation was run. The simulated spectrum thus generated was overlapped

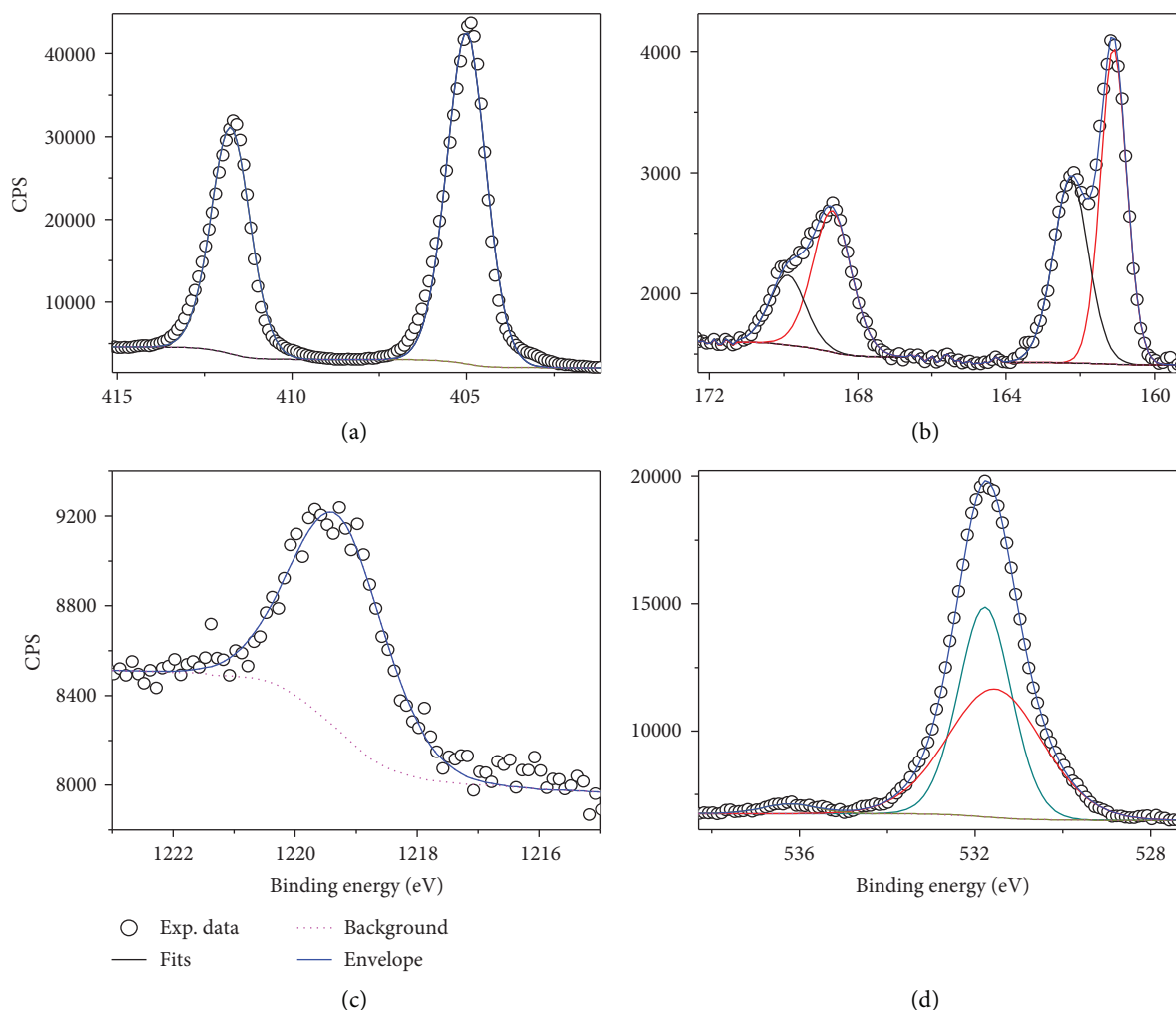


FIGURE 2: High resolution (a) Cd3d core level spectrum, (b) S2p XPS spectra of CdS film, and (c) Ge2p spectrum of underneath Ge spectrum. The surface oxides are shown in (d).

on the experimental spectrum and the thicknesses of layers were calculated.

2.2. Spectroscopic Analysis

2.2.1. UV-Visible Spectroscopy. The optical properties of the films were studied through the Labomed UV-visible spectrophotometer. The films were held perpendicular to the beam for the analysis. The obtained data was converted to transmittance and further analysed for the calculation of the band-gap via the Tauc plot.

2.2.2. Photoluminescence. A photoluminescence analysis was performed to determine the emission characteristics of the prepared thin films. The Kimmon 30 mW He-Cd laser (325 nm) was used as an excitation source. A photomultiplier (PMT), a focal length monochromator (500 mm), and the lock-in amplifier were used for the acquisition of the spectrum.

2.2.3. XPS Spectroscopy. The XPS spectroscopy was performed using a standard omicron system equipped with a

monochromatic Al K α 1486.7 eV X-ray source and the Argus hemispherical electron spectrometer with 128 channel MCP detector. The CasaXPS software was used for data analysis and curve fitting. C1s was used for the calibration of binding energies of all spectra.

3. Results and Discussion

Figures 1(a)–1(d) show the XRD patterns of the annealed films at various temperatures. X-rays were made incident at a grazing angle of 1° on the film to minimize the contribution from the underlying amorphous glass substrate. The broader hump at around 26° can be attributed to the superposition of the glass substrate and (311) contribution from Ge and CdS. A small spike at about 32.8° (not labeled) correspond to (400) in samples annealed at 350°C and 400°C . Moreover, the intensity of (311) the peak was found to lower for these samples. This can be probably due to the formation of a new mixed phase, CdGeS. A tiny spike before the main peak at about 21° corresponds to (200) plane in Ge. Further peaks at 43.2° , 48.1° , and 52.8° correspond to (511), (400), and

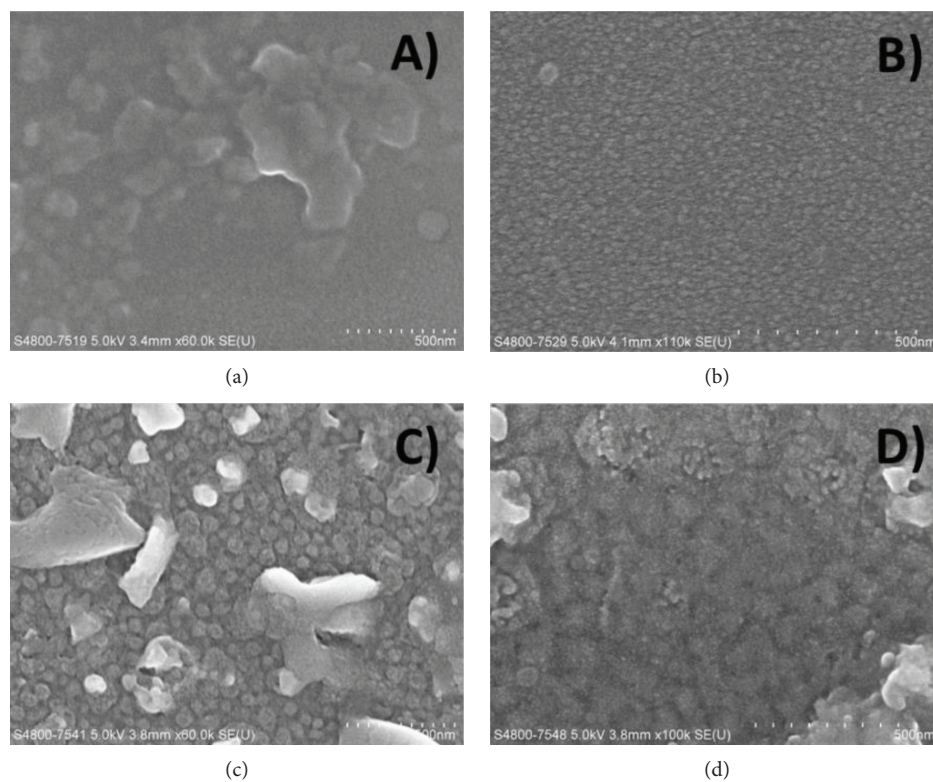


FIGURE 3: SEM images of sintered samples:(a) the as-deposited film, (b) film annealed at 200°C, (c) film annealed at 350°C, and (d) film annealed at 400°C. Different phases of materials are also developing with sintering temperature. The scale corresponding to (a) is 1 μm while to (b) and (c) is 300 nm.

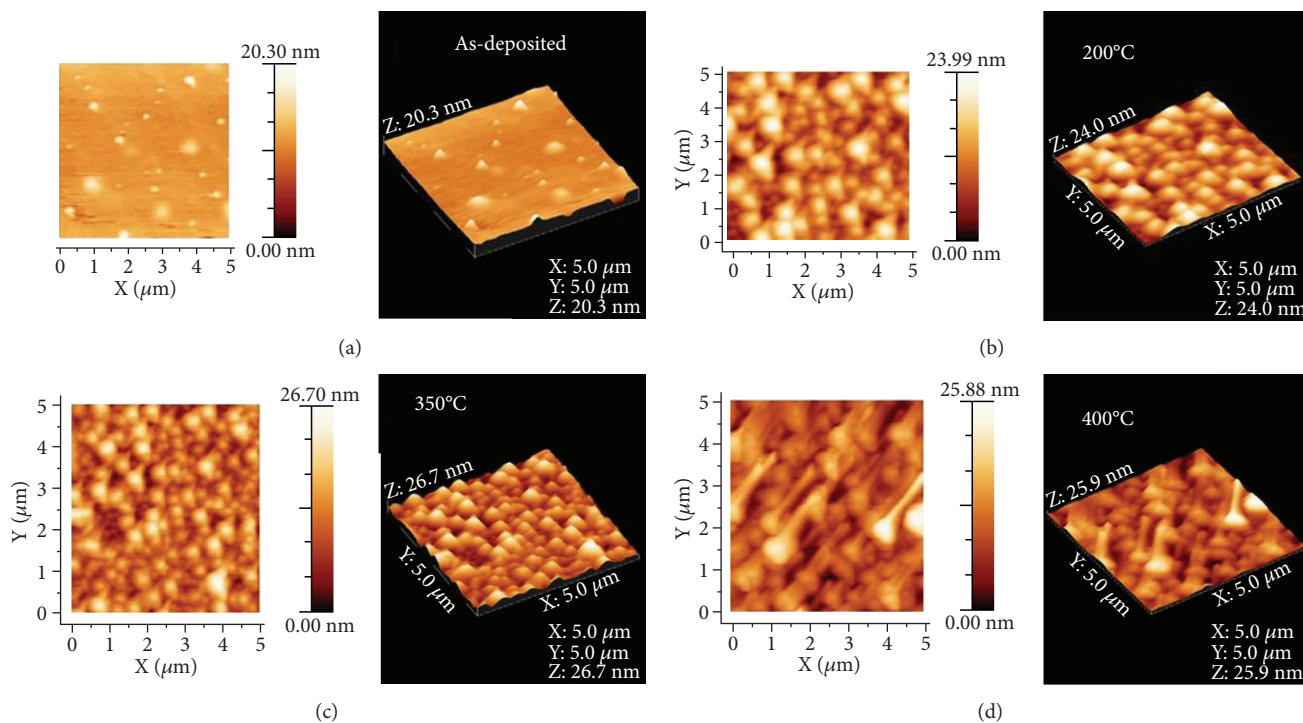


FIGURE 4: (a-d) AFM images of the annealed films. The samples annealed at the different temperatures show the increased roughness with the annealing temperature. The sample annealed at 400°C shows the associated oxides which can be confirmed by XPS.

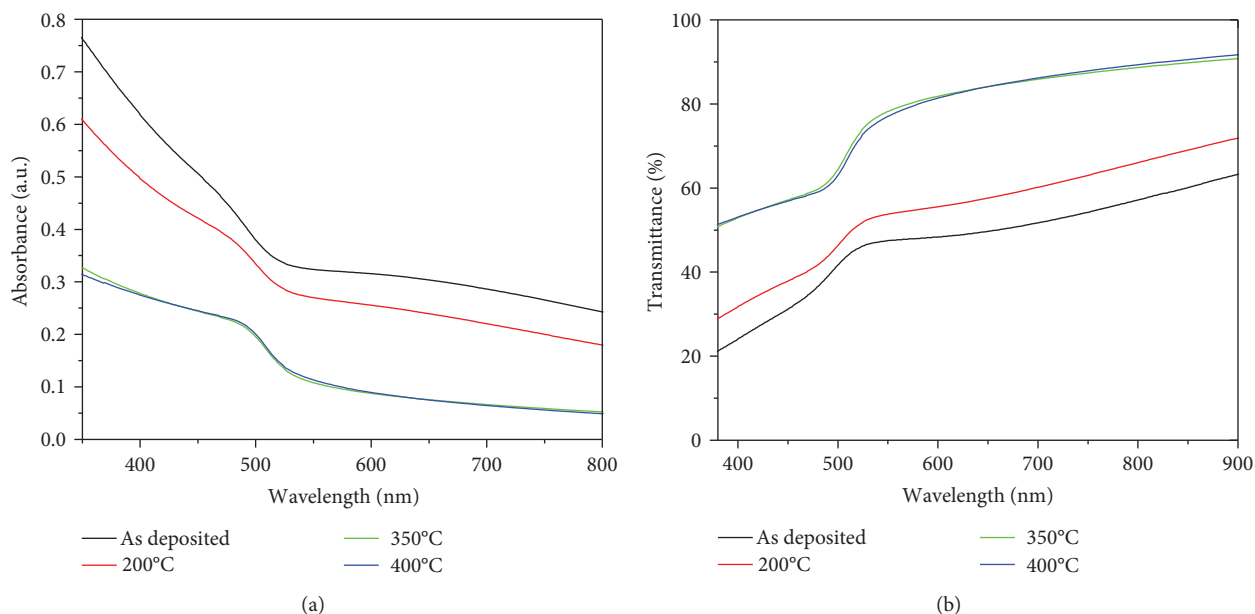


FIGURE 5: Absorbance (a) and transmittance (b) of the films annealed at the different temperatures.

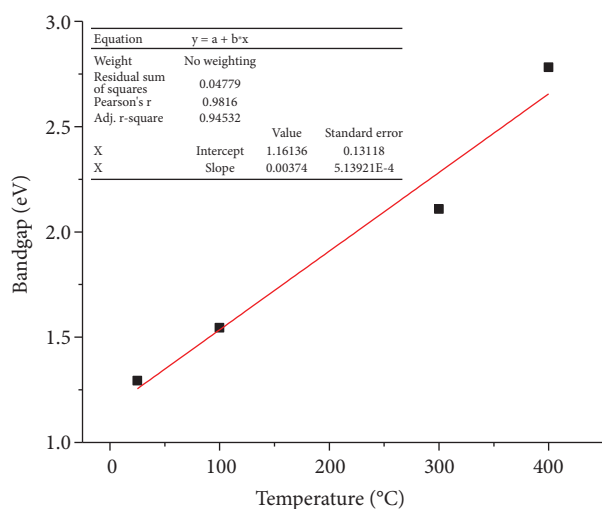


FIGURE 6: Optical bandgap as a function of sintering temperature. The Tauc plot was used for the determination of bandgap.

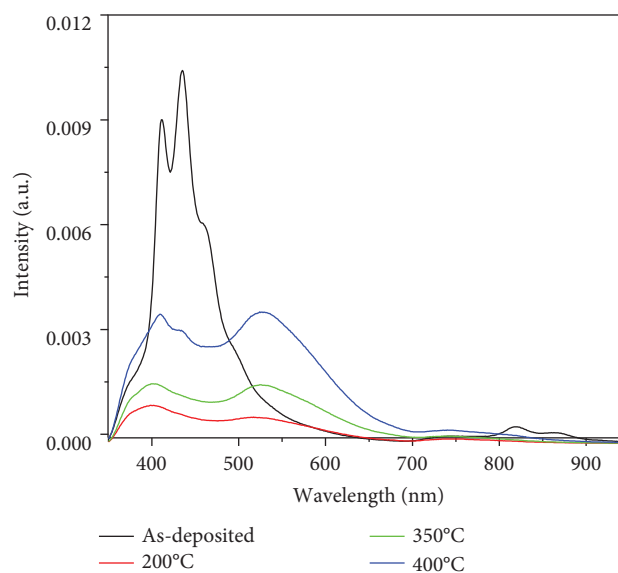


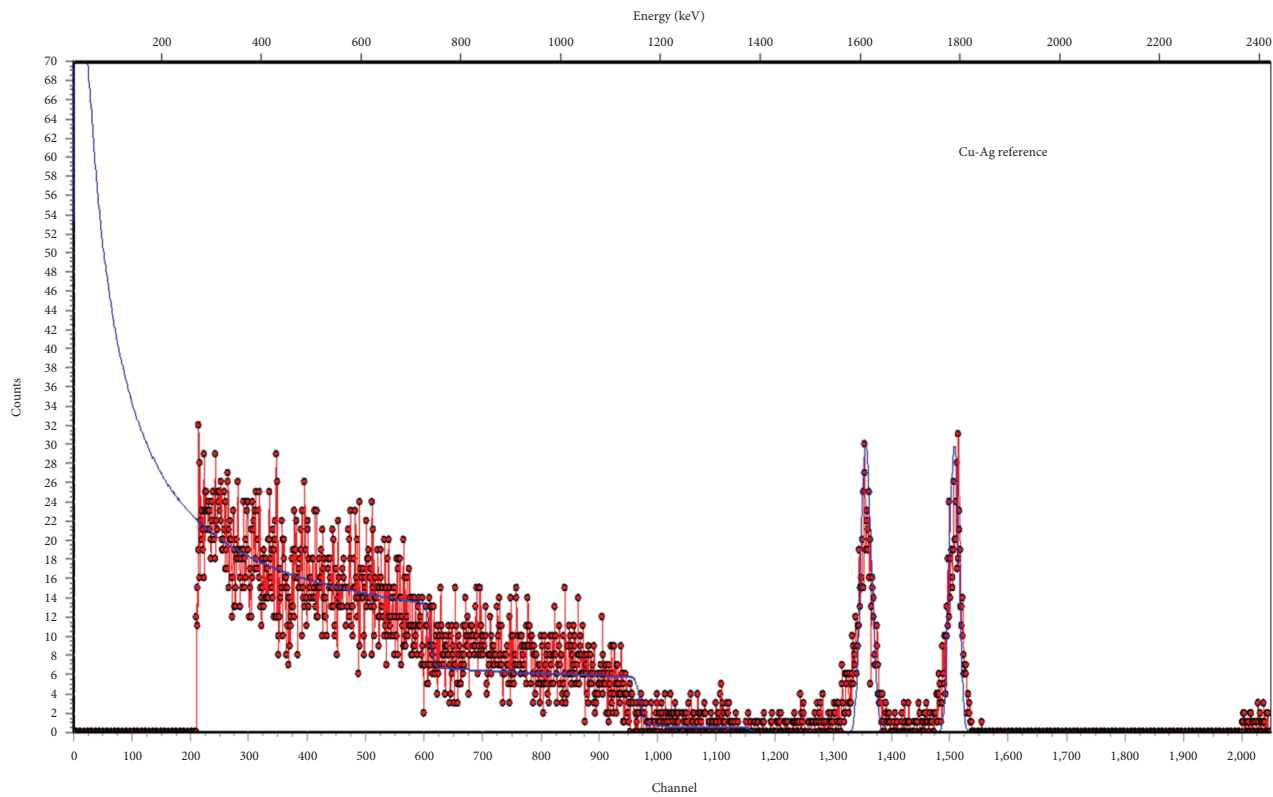
FIGURE 7: Photoluminescence spectra of annealed thin films.

(600) planes in CdS, respectively. From the XRD spectrum, it can be elucidated that FCC structured germanium with a space group of Fm-3m (225) and FCC structured CdS with a space group of F-43m (216) were developed on the films.

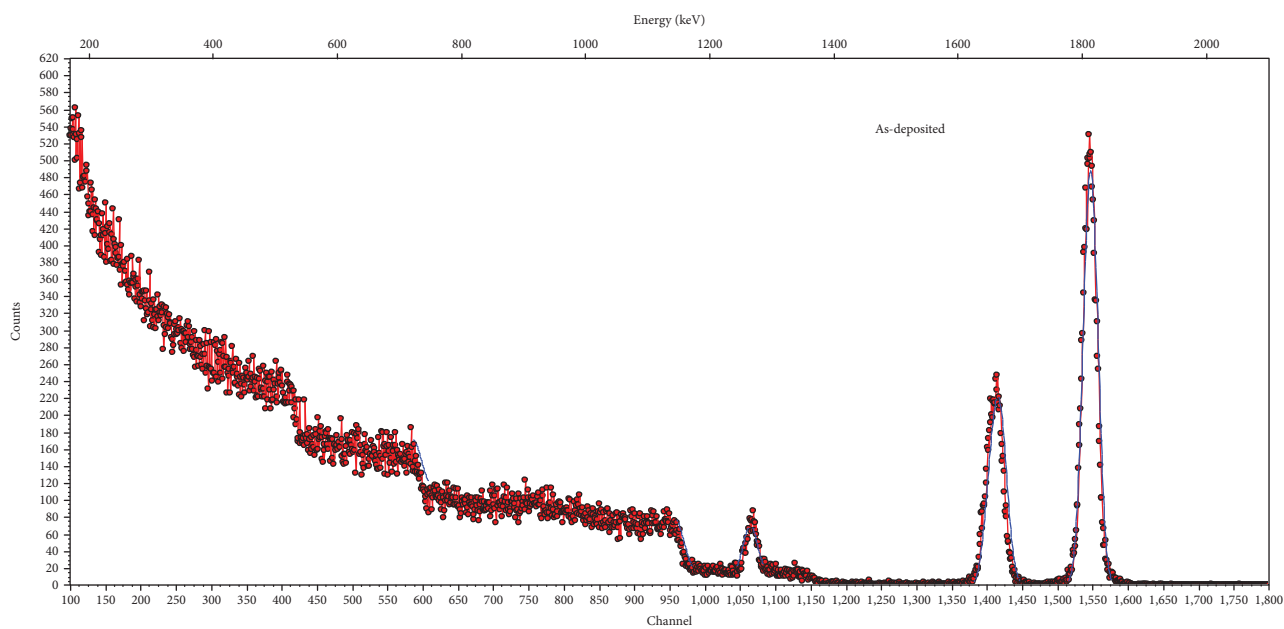
XPS analysis of the sample annealed at 400°C was done to get further insight of diffusion. Figure 2 shows the high resolution Cd3d, S2p, Ge2p, and O1s spectra of a CdS/Ge bilayer sample. All the high resolution spectra were fitted by the Voigt line shape using the Shirley background. The Cd3d line shape can be fitted by a single symmetric peak corresponding to CdS bonding. On the other hand, the S2p spectra can be fitted by two components consisting of the CdS bond along with one additional contribution at about 168.5 eV possibly

from the oxidation of sulfur to the sulphate group. Ge2p peak was also observable by XPS which indicates that the CdS layer is very thin so that one can see the underneath Ge layer. As seen in Figure 2(d), the O1s also shows two peaks, one mainly from the surface-adsorbed oxygen species and one additional contribution possibly from the oxidized surface of the substrate, i.e., SiO₂. The Ge signal was found at a depth of around 10 nm which indicates the diffusion of Ge into the CdS layer.

Figure 3 shows the SEM images of the (a) as-prepared film, (b) film annealed at 200°C, and (c) film annealed at 350°C. Annealing is found favourable for the grain growth and grain boundaries and increase more rapidly above 300°C.

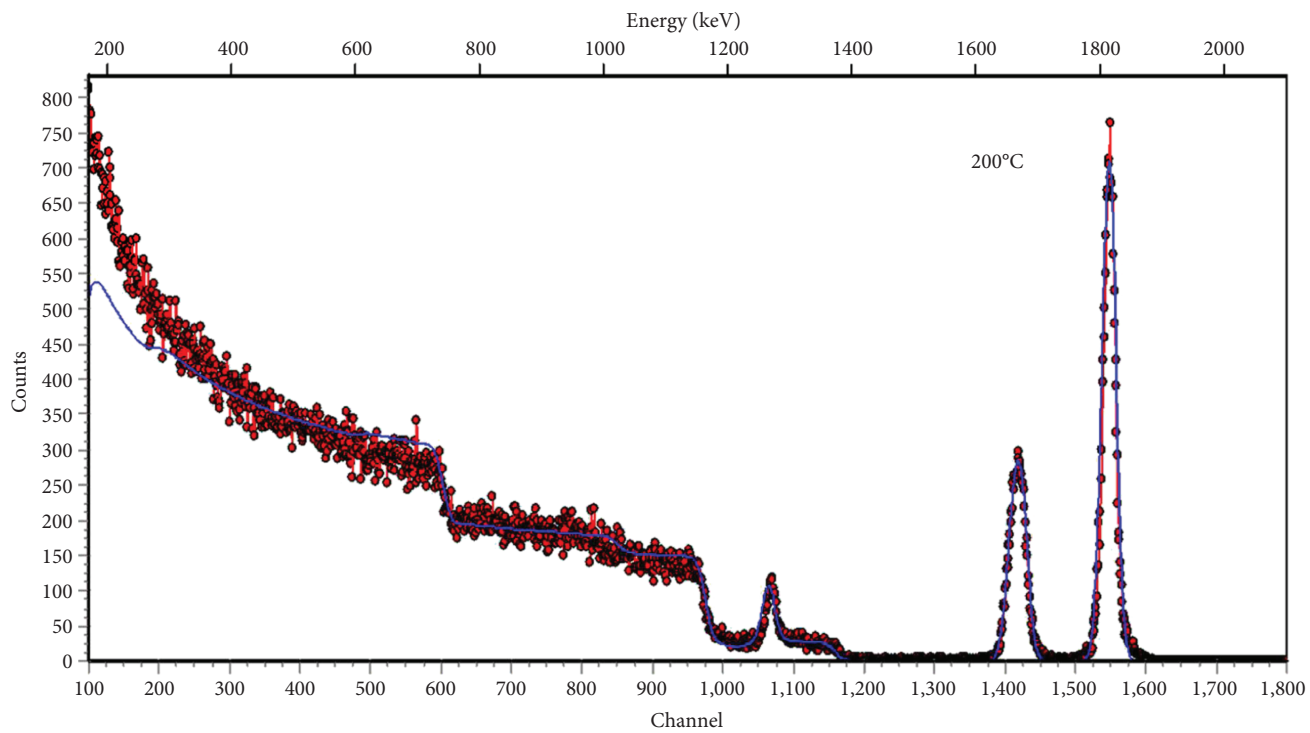


(a)

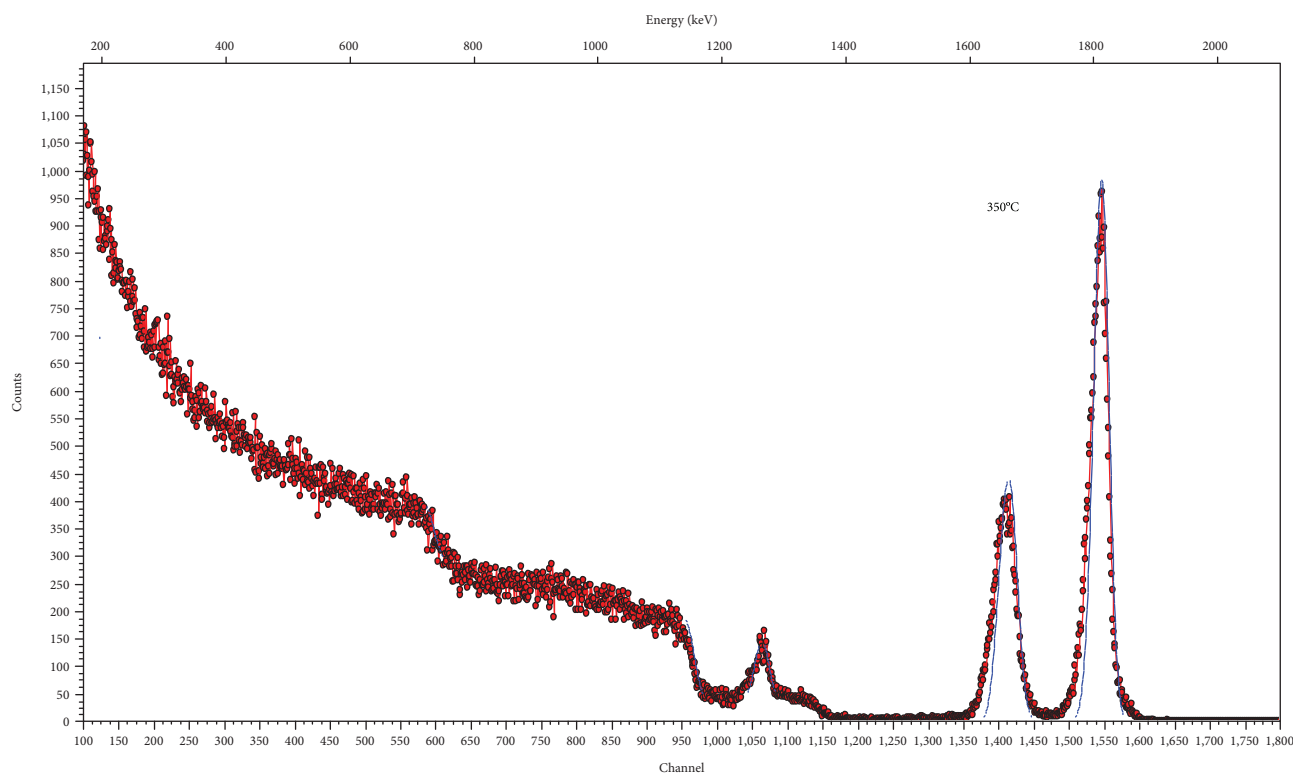


(b)

FIGURE 8: Continued.



(c)



(d)

FIGURE 8: Continued.

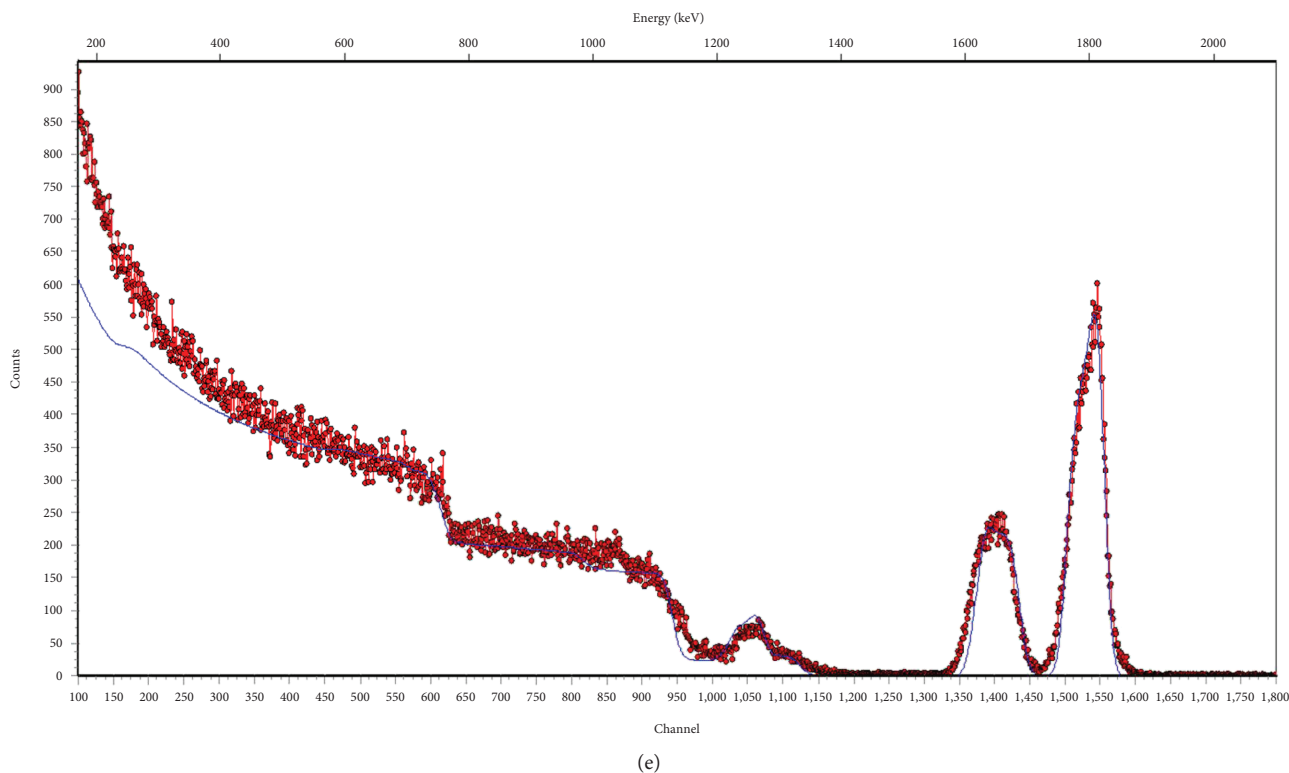


FIGURE 8: (a-e) Simulated curves of all the samples for RBS analysis. The Copper-Silver reference was used.

Figures 4(a)–4(d) show the surface morphology of bilayer Ge and CdS system. The surface roughness was found to increase more rapidly, i.e., from 20.3 nm to 24.0 nm, for annealing until 200°C. A further increase of the annealing temperature to 400°C was found to influence the surface roughness by 26.7 nm little as compared to 200°C. This can be attributed to the oxidation of the surface at 400°C. The observed changes in the surface roughness can be possibly due to an increase in the crystallite size and improved film uniformity [24].

Figure 5(a) shows the absorption spectra of the annealed samples while Figure 5(b) shows the transmission spectra. The UV/Vis spectroscopy showed two peaks of as-prepared sample, a weak shoulder at around 500 nm and a broader hump peaked at about 640 nm. The weak shoulder was found to become stronger and blueshifted with the increasing annealing temperature while the broader hump was found to disappear for the annealed films. The optical bandgap of the as-prepared and annealed samples was calculated by the Tauc plot and plotted in Figure 6. The bandgap was found to increase with the annealing temperature.

Figure 7 shows the photoluminescence of the thin films at different temperatures. The peak at 396 nm in all the samples corresponds to the electron-hole recombination near the bandgap edge. The peak near 450 nm in the as-prepared sample corresponds to sulfur vacancy, while peak near 530 nm in the heat-treated samples may be assigned to surface trap-induced emission. It can be seen with the increase in temperature that the green emission shift to the red from

450 nm to 525 nm is the result of interlayer diffusion and removal of shallow traps [25].

Figure 8 shows the RBS fittings for as-deposited and annealed samples. The distinct peaks for all of the three possible elements can be marked separately at different energies. The CdS and Ge peaks are marked and well fitted for as-deposited samples confirming the successful deposition of CdS and Ge. Sulfur (S) shows a relatively less intense peak around 1250 KeV which can be attributed to the smaller atomic mass of sulfur. One can see that the prominent effect of annealing appears at 400°C as the broadening of individual peaks with a decrease in their height which confirms the diffusion of both layers as a result of annealing. The composition of mixed phase was found out to be $\text{Cd}_{0.7}\text{Ge}_{0.3}\text{S}$ which can also be observed in the XRD pattern of the samples annealed at 400°C.

4. Conclusions

Bilayer thin films of Ge/CdS have been successfully fabricated. The structure of the conformed films was verified through XRD analysis. The analysis was done at a grazing angle to minimize the contribution from underlying substrate. The major peak at (400°C) can be attributed to the superposition of CdS and Ge films. The XPS analysis confirmed the formation of oxides at temperatures above 350°C. From the SEM analysis, it was found that the grain boundaries of the annealed films keep on growing with the annealing temperature. The surface roughness was found to increase with the annealing temperature attributed to the

formation of bigger grains. The Rutherford Backscattering (RBS) analysis showed that the annealing of the thin films resulted in the interlayer diffusion across the CdS and Ge layers emanating the bandgap narrowing in the case of Ge layer. The presence of different phases was confirmed both by XRD and RBS analysis. The optical bandgap was calculated using the Tauc plot and was found to increase with the annealing temperature. The photoluminescence data showed that the green luminescence increases with the increase in temperature due to the removal of shallow traps. The photoelectron spectroscopy revealed the presence of both surface-adsorbed and oxidized surface which leads to the bandgap widening as expected. However, the phenomenon of diffusion and the development of phases need to be further investigated.

Data Availability

No data were used to support this study.

Conflicts of Interest

No conflict of interest exists and the submitting author is responsible for coauthors declaring their interests.

Acknowledgments

The authors Faheem Amin and Syedah Afsheen Zahra, are thankful to the Higher Education Commission, Pakistan, for providing a Start-up Grant (PD-IPFP/HRD/-HEC/2013/1994) for this research work. Authors Faheem Amin, Syedah Afsheen Zahra, and Muhammad Sultan, are also thankful to the National Center for Physics, Islamabad, for granting access to the research facilities.

References

- [1] M. Yamaguchi and S. Wakamatsu, "Super-high efficiency solar cell R&D program in Japan," in *Proceedings of the 25th IEEE Photovoltaic Specialists Conference*, p. 167, New York, 1996.
- [2] J. Zeitouny, E. A. Katz, A. Dollet, and A. Vossier, "Band gap engineering of multi-junction solar cells: Effects of Series Resistances and Solar Concentration," *Scientific Reports*, vol. 7, no. 1, article 1766, 2017.
- [3] M. Hosenuzzaman, N. A. Rahim, J. Selvaraj, M. Hasanuzzaman, A. B. M. A. Malek, and A. Nahar, "Global prospects, progress, policies, and environmental impact of solar photovoltaic power generation," *Renewable and Sustainable Energy Reviews*, vol. 41, pp. 284–297, 2015.
- [4] M. M. Aman, K. H. Solangi, M. S. Hossain et al., "A review of safety, health and environmental (SHE) issues of solar energy system," *Renewable and Sustainable Energy Reviews*, vol. 41, pp. 1190–1204, 2015.
- [5] A. W. Czanderna, "Stability of interfaces in solar energy materials," *Solar Energy Materials*, vol. 5, no. 4, pp. 349–377, 1981.
- [6] W. Shockley and H. J. Queisser, "Detailed balance limit of efficiency of *p-n* junction solar cells," *Journal of Applied Physics*, vol. 32, no. 3, pp. 510–519, 1961.
- [7] L. C. Hirst and N. J. Ekins-Daukes, "Fundamental losses in solar cells," *Progress in Photovoltaics: Research and Applications*, vol. 19, no. 3, pp. 286–293, 2011.
- [8] T. B. Leijtens, K. A. Pasanna, R. McGehee, and D. E. "Opportunities and challenges for tandem solar cells using metal halide perovskite semiconductors," *Nature Energy*, vol. 3, no. 10, pp. 828–838, 2018.
- [9] R. S. Bauer and J. C. Mikkelsen Jr., "Surface processes controlling MBE heterojunction formation: GaAs (100)/Ge interfaces," *Journal of Vacuum Science and Technology*, vol. 21, no. 2, pp. 491–497, 1982.
- [10] A. D. Katnani, N. G. Stoffel, R. R. Daniels, T.-X. Zhao, and G. Margaritondo, "Heterojunction interface formation: Si on Ge, GaAs, and CdS," *Journal of Vacuum Science and Technology A*, vol. 1, no. 2, pp. 692–694, 1983.
- [11] D. W. Niles, M. Tang, J. McKinley, R. Zannoni, and G. Margaritondo, "Schottky-like correction terms in heterojunction band lineups," *Physical Review B*, vol. 38, no. 15, pp. 10949–10952, 1988.
- [12] W. Zi, X. Ren, X. Ren, Q. Wei, F. Gao, and S. Liu, "Perovskite/germanium tandem: a potential high efficiency thin film solar cell design," *Optics Communications*, vol. 380, pp. 1–5, 2016.
- [13] S. Hu, M. McDaniel, D. Posadas et al., "Monolithic integration of perovskites on Ge(001) by atomic layer deposition: a case study with $\text{SrHf}_x\text{Ti}_{1-x}\text{O}_3$," *MRS Communications*, vol. 6, no. 3, pp. 125–132, 2016.
- [14] C. Paorici, C. Pelosi, G. Bolzoni, and G. Zuccalli, "Epitaxial growth of cadmium sulphide on (111) germanium substrates," *Journal of Materials Science*, vol. 10, no. 12, pp. 2117–2123, 1975.
- [15] Q. Wu, J. Hou, H. Zhao et al., "Charge recombination control for high efficiency CdS/CdSe quantum dot co-sensitized solar cells with multi-ZnS layers," *Dalton Transactions*, vol. 47, no. 7, pp. 2214–2221, 2018.
- [16] D. Kathirvela, N. Suriyanarayanan, S. Prabakar, and S. Srikanth, "Structural, Electrical and Optical Properties of CdS Thin Films by Vacuum Evaporation Deposition," *Journal of Ovonic Research*, vol. 7, no. 4, pp. 83–92, 2011.
- [17] T. Torimoto, S. Nagakubo, M. Nishizawa, and H. Yoneyama, "Photoelectrochemical properties of size-quantized CdS thin films prepared by an electrochemical method," *Langmuir*, vol. 14, no. 25, pp. 7077–7081, 1998.
- [18] N. Romeo, A. Bosio, R. Tedeschi, A. Romeo, and V. Canevari, "A highly efficient and stable CdTe/CdS thin film solar cell," *Solar Energy Materials and Solar Cells*, vol. 58, no. 2, pp. 209–218, 1999.
- [19] N. Memarian, S. M. Rozati, I. Concina, and A. Vomiero, "Deposition of Nanostructured CdS Thin Films by Thermal Evaporation Method: Effect of Substrate Temperature," *Materials*, vol. 10, no. 7, p. 773, 2017.
- [20] M. A. Islam, M. S. Hossain, M. M. Aliyu et al., "Growth of Wide Bandgap CdS Thin Films as Window Layers of Ultra-Thin CdTe Solar Cells," in *The 22nd International Photovoltaic Science and Engineering Conference*, Hangzhou, China, November 2012.
- [21] D. B. Khadka and J. Kim, "Band gap engineering of alloyed $\text{Cu}_2\text{ZnGe}_x\text{Sn}_{1-x}\text{Q}_4$ (Q = S, Se) films for solar cell," *Journal of Physical Chemistry C*, vol. 119, no. 4, pp. 1706–1713, 2015.
- [22] G. Gu, M. Burghard, G. T. Kim et al., "Growth and electrical transport of Ge nanowires," *Journal of Applied Physics*, vol. 90, no. 11, pp. 5747–5751, 2001.

- [23] L. V. Titova, T. B. Hoang, H. E. Jackson et al., “Low-temperature photoluminescence imaging and time-resolved spectroscopy of single CdS nanowires,” *Applied Physics Letters*, vol. 89, no. 5, article 053119, 2006.
- [24] W.-D. Park, “Structural and optical properties of thermally annealed Nanocrystalline CdS thin films,” *Journal of the Korean Physical Society*, vol. 54, no. 5, pp. 1793–1797, 2009.
- [25] L. Saravanan, S. Diwakar, R. Mohankumar, A. Pandurangan, and R. Jayavel, “Synthesis, Structural and Optical Properties of PVP Encapsulated CdS Nanoparticles,” *Nanomaterials and Nanotechnology*, vol. 1, no. 2, pp. 17–48, 2011.

Research Article

Improving Electrochemical Activity in a Semi-V-I Redox Flow Battery by Using a C-TiO₂-Pd Composite Electrode

Tsung-Sheng Chen,¹ Shu-Ling Huang ,¹ Mei-Ling Chen,² Tz-Jiun Tsai,¹
and Yung-Sheng Lin ¹

¹Department of Chemical Engineering, National United University, Miaoli 360, Taiwan

²Department of Electrical Engineering, National United University, Miaoli 360, Taiwan

Correspondence should be addressed to Shu-Ling Huang; simone@nuu.edu.tw and Yung-Sheng Lin; linys@nuu.edu.tw

Received 2 July 2018; Revised 29 October 2018; Accepted 8 November 2018; Published 20 January 2019

Guest Editor: Zhengping Zhou

Copyright © 2019 Tsung-Sheng Chen et al. This is an open access article distributed under the Creative Commons Attribution License, which permits unrestricted use, distribution, and reproduction in any medium, provided the original work is properly cited.

This study developed composite electrodes used in a semi-vanadium/iodine redox flow battery (semi-V-I RFB) system and designed semi-V-I RFB stacks to provide performance comparable to that of an all-vanadium redox flow battery (all-VRFB) system. These electrodes were modified using the electroless plating method and sol-gel process. The basic characteristics of the composited electrodes, such as the surface structural morphology, metal crystal phases, and electrochemical properties, were verified through cyclic voltammetry, field emission-scanning electron microscopy, energy-dispersive X-ray spectrometry, and X-ray diffraction. The results show that the sintering C-TiO₂-Pd electrode improved the electrocatalytic activity of the semi-V-I RFB system, thereby effectively increasing the energy storage ability of the system. The C-TiO₂-Pd electrode was used as a negative electrode in a single semi-V-I RFB and exhibited excellent cyclic performance in a charge-discharge test of 50 cycles. The average values for coulomb efficiency, voltage efficiency, and energy efficiency were approximately 96.56%, 84.12%, and 81.23%, respectively. Moreover, the semi-V-I RFB stacks were designed using series or parallel combination methods that can effectively provide the desired operating voltage and linearly increase the power capacity. The amount of vanadium salt required to fabricate the semi-V-I RFB system can be reduced by combining large stack modules of the system. Therefore, this system not only reduced costs but also exhibited potential for applications in energy storage systems.

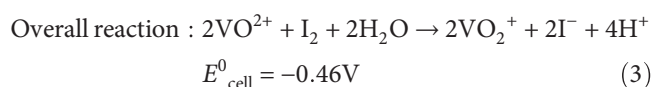
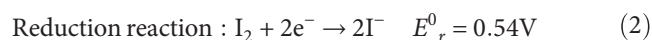
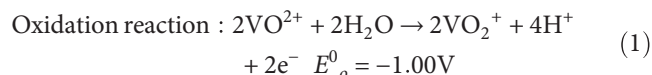
1. Introduction

The energy of a redox flow battery (RFB) is stored in separated positive and negative electrolytes, which provide the driving force that initiates the oxidation-reduction reaction [1]. The use of energy stored in the form of chemical energy, a mode of storage that does not entail any geographical restrictions, is expected to facilitate large-scale energy storage and has significant environmental and socioeconomic advantages. RFBs have been utilized as large-scale energy storage systems in the last decade [2–5]. The all vanadium RFB (all-VRFB) is one of the most promising technologies for mid-to-large-scale (kilowatt-megawatt) energy storage and was first proposed by Skyllas-Kazacos in 1985 [6, 7]. The power output of a vanadium RFB increases with the size of the cell stack and the active electrode surface area, whereas

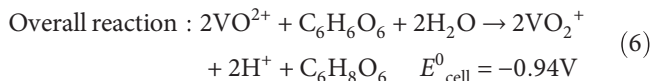
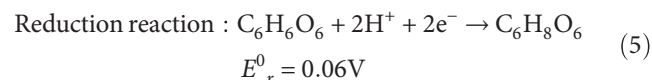
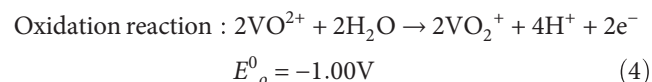
its energy storage capacity increases with the volume of the storage tanks and the electrolyte concentrations [8–10]. The all-VRFB can be modified for use in specific large-scale utility applications; however, these batteries are more expensive than secondary batteries. Consequently, the technologies of the all-VRFB system should be further advanced to realize low-cost fabrication and to improve performance and durability, thus enabling their widespread application. The key materials of the all-VRFB system include an ion exchange membrane, electrodes, electrolyte, and a flow channel. The battery's energy density is determined not only by the characteristics of these key materials but also by their intimate interrelationships. An ideal electrode is one that exhibits low resistance, high conductivity, and acid-resisting property. Many studies have focused on modifying electrode materials, such as increasing their electrocatalytic activity or developing

a new, low-cost electrode with more robust mechanical strength in concentrated acid solutions [11–15]. In our previous research, we developed a novel semi-vanadium-iodine RFB (semi-V-I RFB) [16]. This battery has a high coulomb efficiency and significantly reduces the fabrication cost; however, its voltage efficiency is low (68%). The overall reactions of vanadium-iodine, iodine-vitamin C ($C_6H_8O_6$), and vanadium-vitamin C oxide ($C_6H_6O_6$) can be expressed as shown in equations (1)–(6) on the charging mode.

1.1. Vanadium-Iodine.



1.2. Vanadium-Vitamin C.



A study demonstrated that the reversibility of the oxidation-reduction reaction can be effectively increased if vitamin C is added to the iodine solution [17]. Therefore, the standard electromotive forces of the semi-V-I RFB system are between 0.46 to 0.94 V on the discharging mode.

This study focused on developing composite electrodes that can be used as the negative electrode of the semi-V-I RFB system to effectively improve the voltage efficiency of the system. Furthermore, we designed semi-V-I RFB stacks and compared the charge-discharge performance of the stacks with that of the all-VRFB system.

2. Experimental

2.1. Fabrication of Composite Electrodes. Graphite carbon paper electrodes (C-electrodes; Shenhe Carbon Fiber Materials Co. Ltd., Liaoning, China) were modified by depositing palladium (Pd) through electroless plating. The effective exposed surface area of the electrodes was $5 \times 5 \text{ cm}^2$. $SnCl_2$ and $PdCl_2$ were used as sensitized and active reagents in the deposition of the C-Pd electrode. The composition of the plating solution was 19 g/L $Na_2C_4H_4O_4 \cdot 6H_2O$, 10 g/L $PdCl_2$, 8.5 g/L HCl, and 25.6 g/L $C_2H_4(NH_2)_2$. The C-Pd, C-Pd-TiO₂, and C-TiO₂-Pd electrodes were prepared through electroless metal deposition by using the composition of the

plating solution [18–21]. Among them, the C-TiO₂ electrode was fabricated using the following steps: tetrabutryric acid was mixed with EtOH/HCl (pH = 1) aqueous solution at a tetrabutryric acid:EtOH:HCl molar ratio of 1:8:4 in a flask and mechanically stirred to carry out the hydrolysis reaction at room temperature. Then, carbon paper was added to the pre-mixed tetrabutryric acid solution under vigorous stirring for 1 h. Finally, it was completely dried in an oven at 60°C, and a C-TiO₂ composite electrode was obtained. The C-Pd-TiO₂ and C-TiO₂-Pd electrodes were fabricated using a two-step deposition method. In the first step, the sol-gel route was employed to prepare the C-TiO₂-electrode, following which the Pd was redeposited on the C-TiO₂ electrode through the electroless technique to form the C-TiO₂-Pd modified electrode. The C-Pd-TiO₂ electrode was fabricated under the same conditions, but with the process reversed. The plating solution had a pH in the range of 4.8–5.1 at 80°C. Finally, the modified electrodes were heat treated at 400°C in an oven for 1 h. All chemicals used were of analytical reagent grade.

2.2. Morphology and Composition of Composite Electrodes.

The surface morphologies and components of the composite electrodes were characterized through scanning electron microscopy coupled with energy dispersive X-ray analysis (JSM-6700F, JEOL, Tokyo, Japan). The composition of the electrode was identified through X-ray diffraction (XRD) with a filtered Cu-K α radiation source (X'Pert PRO, PANalytical, Almelo, the Netherlands), and diffraction patterns were collected from 20° to 90°.

2.3. Measurement of the Electrochemical Properties.

Cyclic voltammetry (CV) experiments were conducted in a three-electrode cell and by using an electrochemical analyzer (CHI 6273 C, CH Instruments Inc., US). The composition of the cell was as follows: an Ag-AgCl electrode was used as the quasireference electrode, the reference electrode and the platinum gauze were used as the counter electrode, and the C-Pd or C-TiO₂-Pd modified electrode with a surface area of $1 \times 1 \text{ cm}^2$ was used as the working electrode. The positive electrolyte was a solution of 0.01 M I_2 with a variable amount of vitamin C. The scan rate was varied from 1 to 10 mV·s⁻¹. Electrochemical properties, such as the potential interval (ΔE_p), ratio of the anodic-cathodic current (I_{pa}/I_{pc}), diffusion coefficient (D_o), and double-layer charged capacity (C_d), were obtained from the CV experimental data.

2.4. Charge-Discharge Test.

We used the iodine-vitamin C solution as a cathode electrolyte and vanadium ion (V^{4+} - V^{5+}) solution as an anodic electrolyte to set up a single cell. The (V^{4+} - V^{5+}) vanadium solutions were prepared by dissolving 1 M $VOSO_4$ in 2 M H_2SO_4 aqueous solution. Multiple electrodes, that is, C and C-TiO₂-Pd electrode, were used. The electrodes were separated by a cationic exchange Nafion 117 membrane (DuPont, USA). In addition, the charge-discharge test was conducted on two cell stacks—series and parallel.

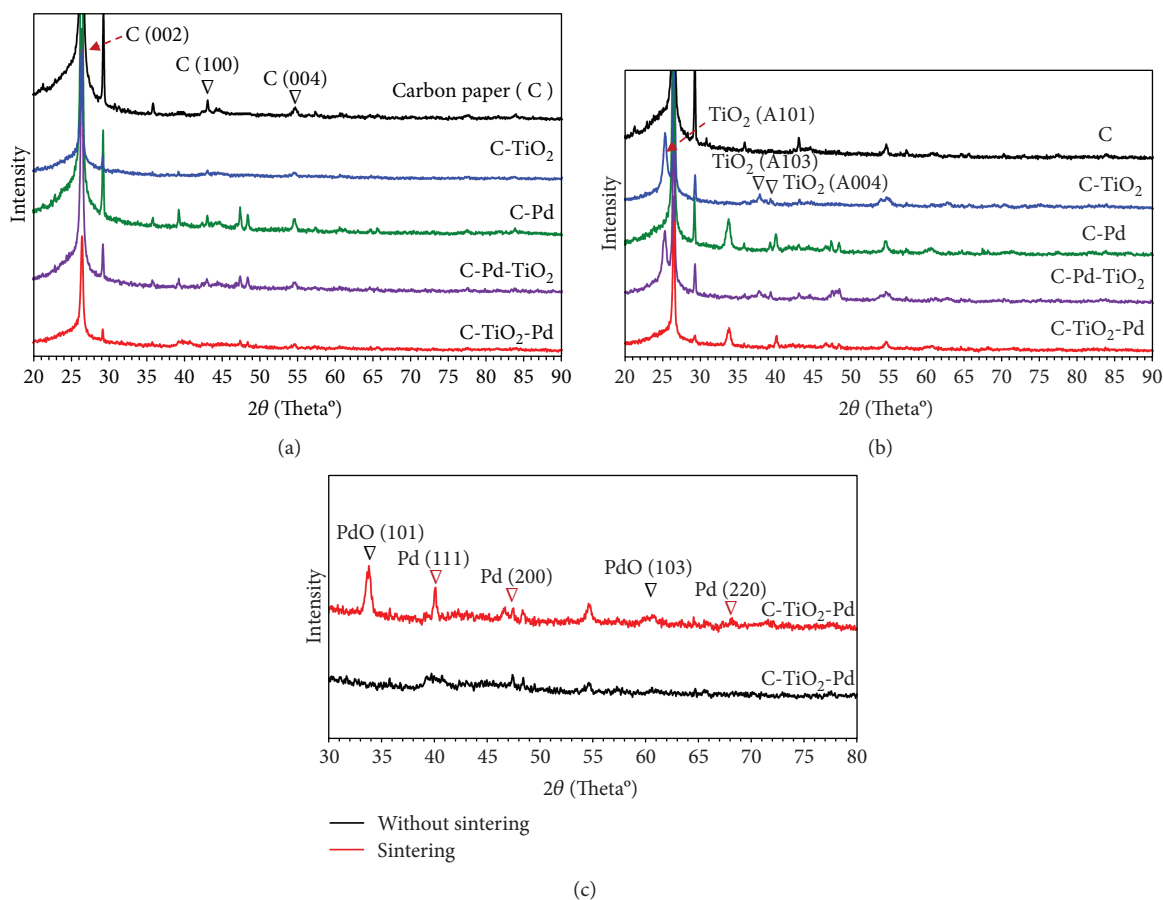


FIGURE 1: XRD patterns of various electrodes (a) without sintering for all electrodes, (b) sintering for all electrodes, and (c) without and with sintering for the C-TiO₂-Pd electrode.

3. Results and Discussion

3.1. Crystal Structure Identification of Composite Electrodes.

The XRD diffraction patterns of all the composite electrodes, including C, C-TiO₂, C-Pd, C-Pd-TiO₂, and C-TiO₂-Pd with and without 400°C sintering, are shown in Figure 1. The diffraction pattern in Figure 1 reveals that (1) before sintering, C (002) possessed two sharp diffraction peaks at 27°–29° and two weak peaks, C (100)/C (004), at 43° and 54°, respectively. TiO₂ in the C-TiO₂ region was amorphous; thus, the diffraction patterns were similar to those of C. The (111), (200), and (220) facets of Pd with a face-centered cubic lattice structure were assigned to the diffraction peaks at 40°, 47°, and 68°, respectively. Three regions (i.e., C-Pd, C-Pd-TiO₂, and C-TiO₂-Pd) can verify a part of the Pd crystal structure (111, 200); nevertheless, the intensity of the peaks was weak in the C-TiO₂-Pd regions, as depicted in Figure 1(a). (2) After sintering, the C electrode's diffraction patterns remained unchanged. The C-TiO₂ electrode exhibited a strong diffraction peak at 25°, which was the anatase lattice structure of TiO₂ (A101), and a relatively weak diffraction peak at 38°–39° for TiO₂ (A103) and TiO₂ (A004). In the C-Pd-TiO₂ region, fingerprint peaks similar to those of TiO₂ were observed; however, these were not

observed in the C-TiO₂-Pd region. In particular, in the C-Pd and C-TiO₂-Pd regions, a strong new diffraction peak appeared at 34°, which is the diffraction characteristic peak of PdO (101), implying that Pd oxidized to form PdO, as presented in Figure 1(b). (3) A significant difference was observed between the diffraction peaks of C-TiO₂-Pd crystal structures with and without sintering. The intensity of the diffraction peaks of Pd (111) and Pd (200) for the sintering C-TiO₂-Pd electrode was stronger and more stable, and the diffraction pattern of Pd (220) was more apparent than without sintering. Moreover, a strong new PdO (101) diffraction peak was observed at 34° in the C-TiO₂-Pd regions but not in the C-Pd-TiO₂ region, as shown in Figure 1(c). Thus, the experimental results demonstrate that the stable Pd metals and PdO crystal structures for the C-TiO₂-Pd electrode could be formed through high-temperature sintering. These may affect electrocatalytic activity and generate different electrochemical properties [22–24].

3.2. Surface Morphology Analysis of Composite Electrodes.

The scanning electron microscopy (SEM) images of the composite electrodes are presented in Figure 2. The Pd particles with white spots were deposited onto the carbon

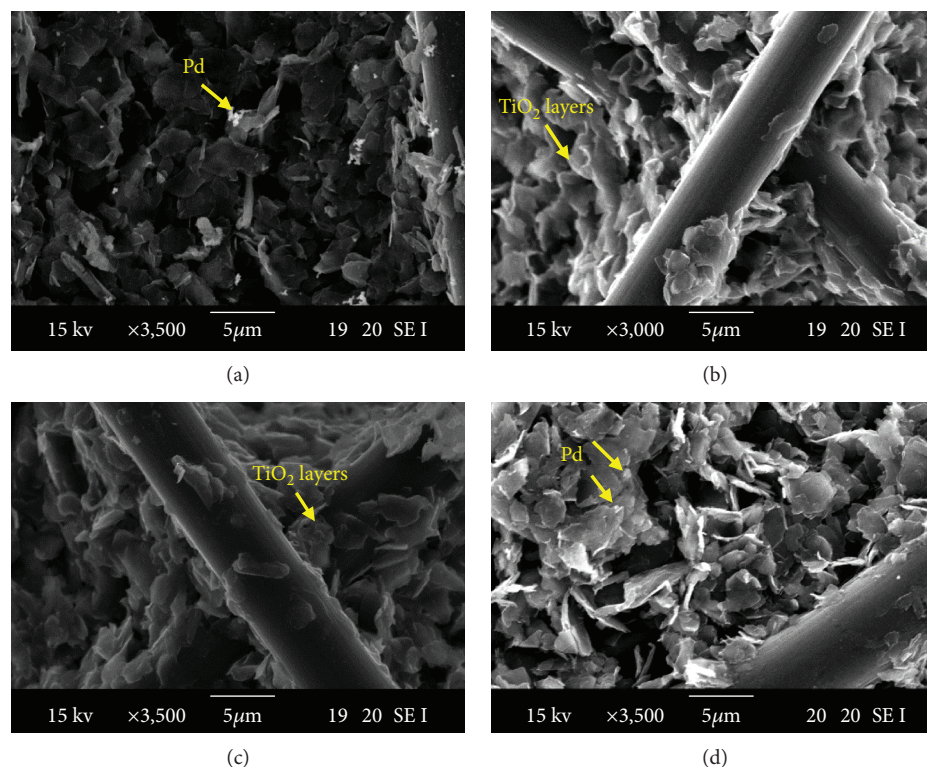


FIGURE 2: SEM images of composite electrodes. (a) C-Pd, (b) C-TiO₂, (c) C-Pd-TiO₂, and (d) C-TiO₂-Pd.

fiber layers of the C-Pd electrode and onto the TiO₂ layers of the C-TiO₂-Pd electrode, as shown in Figures 2(a) and 2(d). Nevertheless, we did not observe the Pd particles in the C-Pd-TiO₂ electrode in Figure 2(c), implying that the inner Pd particles are covered by the outer TiO₂ layers. Additionally, we observed that the growth in TiO₂ was derived from the inner layer and layer-by-layer stacking of TiO₂, and a significant number of TiO₂ grains were uniformly embedded into the carbon paper network matrix through the sol-gel method, as presented in Figure 2(b). Furthermore, to identify the component of the C-TiO₂-Pd electrode, we performed energy-dispersive spectrometry (EDS) analysis of the C-TiO₂-Pd electrode with sintering, as depicted in Figure 3. The spectrum and element analysis presented in Figure 3(a) reveals that the elements of the sintering C-TiO₂-Pd electrode included C (47.58 wt%), Ti (17.64 wt%), Pd (2.71 wt%), and O (32.07 wt%). O elements exhibited a high wt% under a low wt% Ti element, implying that Pd was oxidized to form PdO. These results were confirmed because the PdO (101) facet was assigned to the diffraction peak at 34°, as presented in Figure 1(c). In addition, the Pd particles were deposited uniformly on the TiO₂ layers, as illustrated in the mapping analysis of Figures 3(b)–3(f). The deposition of Pd and PdO particles on the TiO₂ layers reduced the aggregation of Pd particles and increased the active area of the C-TiO₂-Pd composite electrode.

3.3. Electrochemical Characteristics of Various Electrodes.

The CV curves of various electrodes in 10 mL of 0.01 M

iodine with 1 wt% vitamin C solution at a 10 mV/s scanning rate in the range of 0–1 V are shown in Figure 4, and the data are summarized in Table 1. The oxidation pattern of electrolyte solutions is referred to as an oxidized or anodic current peak (I_{pa}) on a tested electrode, corresponding to the anodic voltage (E_{pa}) when CV is scanned from a low to high potential. Conversely, if it is scanned from a high to low potential, then the electrolyte is reduced to obtain a reduced or cathodic current peak (I_{pc}) and a cathodic voltage (E_{pc}). The I_{pa}/I_{pc} ratio tended to unity, revealing that the quasireversible redox reactions occurred because of the effects of the iodine electrolyte solutions on the tested electrodes. The values of I_{pa} and I_{pc} were low, meaning that the redox efficiency of the composite electrodes in the iodine solutions was poor. The I_{pa} values were in the following order: C-TiO₂-Pd > C-Pd > C-Pd-TiO₂ > C > C-TiO₂. Moreover, the potential interval (ΔE_p) was in the following order: C-TiO₂ > C-Pd-TiO₂ > C-Pd > C > C-TiO₂-Pd, as listed in Table 1. The low ΔE_p value demonstrated that the energy barriers of redox reactions were lower because of the effects of the iodine electrolyte solutions on the tested electrodes. These results imply that the C-TiO₂-Pd electrode has higher redox currents and lower ΔE_p than other electrodes. Moreover, the C-TiO₂-Pd electrode had a symmetric I_{pa}/I_{pc} value, which was close to unity, meaning that this is a reversible redox reaction for the iodine solutions. In addition, the outer TiO₂ layer of the C-Pd-TiO₂ electrodes could not improve the redox kinetic reaction of the iodine solution; thus, the redox current of the C-Pd-TiO₂ electrode was lower

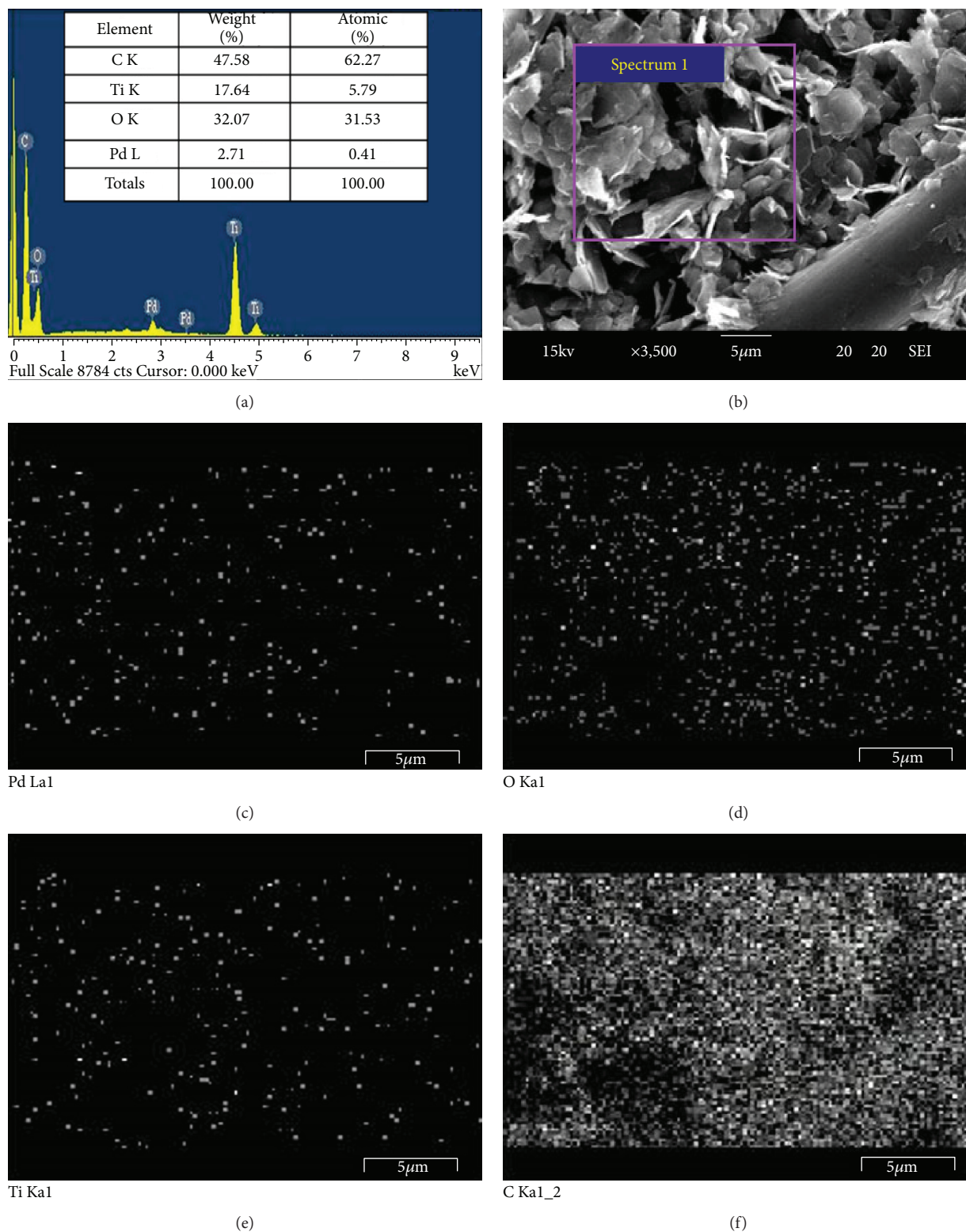


FIGURE 3: Analysis of energy-dispersive spectrometry (EDS) for the C-TiO₂-Pd electrode with sintering. (a) EDS spectrum and element analysis, (b) EDS mapping electron image, (c) Pd element, (d) O element, (e) Ti element, and (f) C element.

than that of the C-TiO₂-Pd electrode. Therefore, TiO₂ particles between a carbon matrix and Pd metal layers increase the active surface area of an electrode and can enhance

the electrocatalytic effect of the electrode [19, 22]. Consequently, the C-TiO₂-Pd electrode performed better in the redox kinetic reaction than the others.

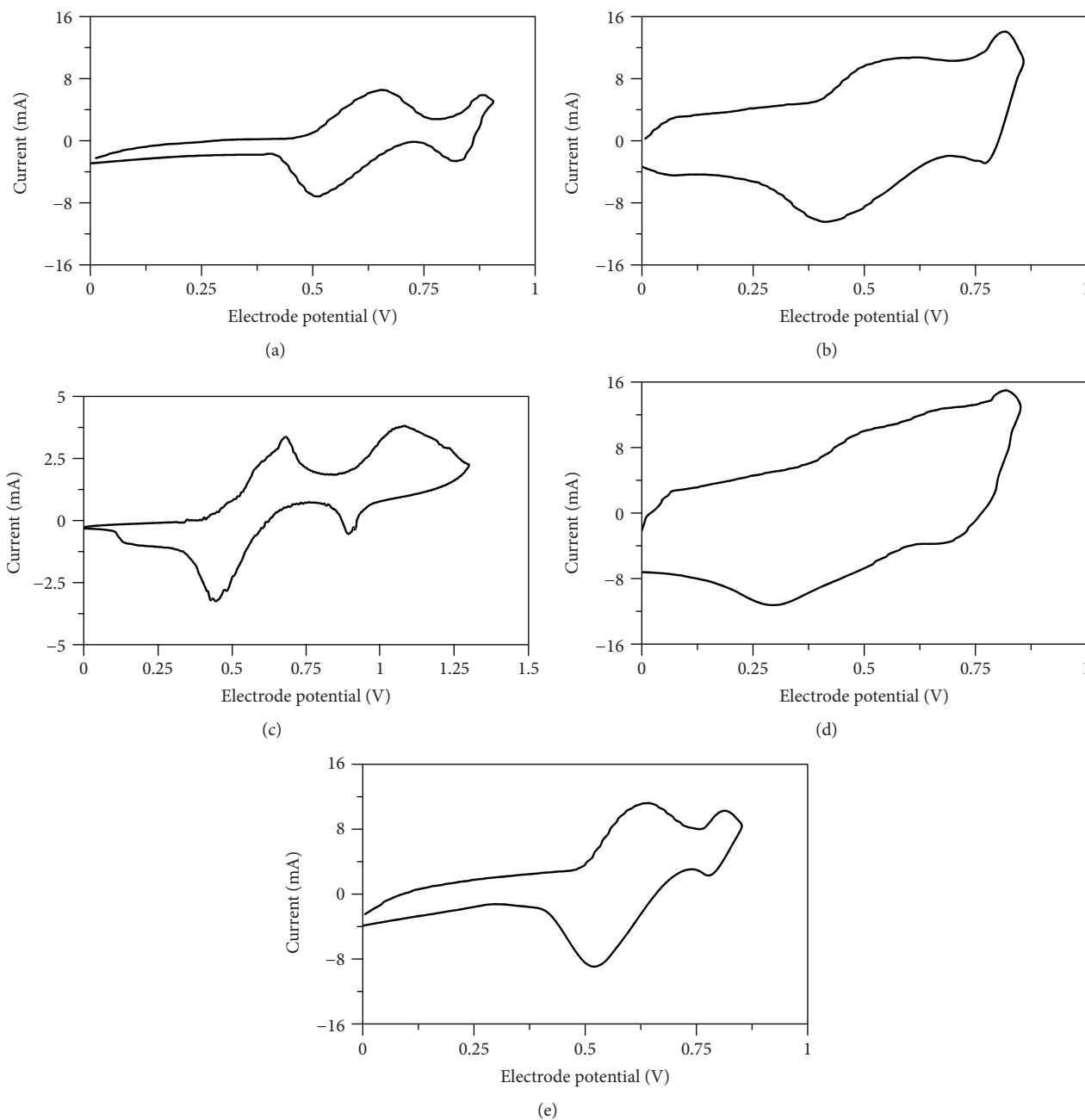


FIGURE 4: Cyclic voltammograms for 0.01 M iodine solution with 1 wt% of vitamin C on different electrodes: (a) C, (b) C-Pd, (c) C-TiO₂, (d) C-Pd-TiO₂, and (e) C-TiO₂-Pd.

3.4. Kinetic Reactions of Composite Electrodes. A reversible redox equation (7) can be obtained on the basis of the Randles-Sevcik equations [25, 26]:

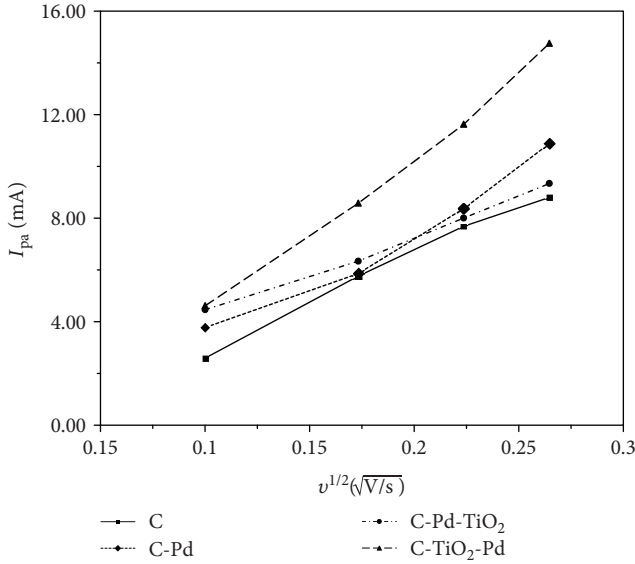
$$i_p = (2.69 \times 10^5) n^{3/2} A C D_o v^{1/2}, \quad (7)$$

where i_p , n , A , C , D_o , and v are the peak current, electron mobility number, reaction area (cm²), concentration of reactants (mole/cm³), diffusion coefficient (cm²/s), and scan rate (V/s), respectively. The kinetic reactions of iodine with

vitamin C electrolyte solutions on various electrodes were studied through a series of CV experiments at different scan rates. The relationship between I_{pa} and $v^{1/2}$ was plotted in Figure 5, and the value of D_o was obtained using the slope of I_{pa} and $v^{1/2}$ and Randles-Sevcik equations [16]. As shown in Table 2, the modified C-TiO₂-Pd electrode increased the overall mass transfer and iodide ion electrochemical activity. The D_o value of iodine-vitamin C species was enhanced by approximately 60% compared with that of the C-electrode, from 12.8×10^{-6} to 20.4×10^{-6} cm²/s, on the C-TiO₂-Pd electrode.

TABLE 1: Cyclic voltammograms of 0.01 M iodine solutions with 1 wt% of vitamin C on different electrodes.

Electrodes	E_{pa} (V)	E_{pc} (V)	ΔE_p (V)	Anodic peak, I_{pa} (mA)	Cathodic peak, I_{pc} (mA)	I_{pa}/I_{pc}
C electrode	0.67	0.50	0.17	5.76	7.08	0.81
C-Pd electrode	0.61	0.42	0.19	5.86	8.27	0.71
C-TiO ₂ electrode	0.68	0.46	0.22	3.35	3.78	0.89
C-Pd-TiO ₂ electrode	0.50	0.29	0.21	6.34	7.44	0.85
C-TiO ₂ -Pd electrode	0.64	0.52	0.12	8.58	9.23	0.92

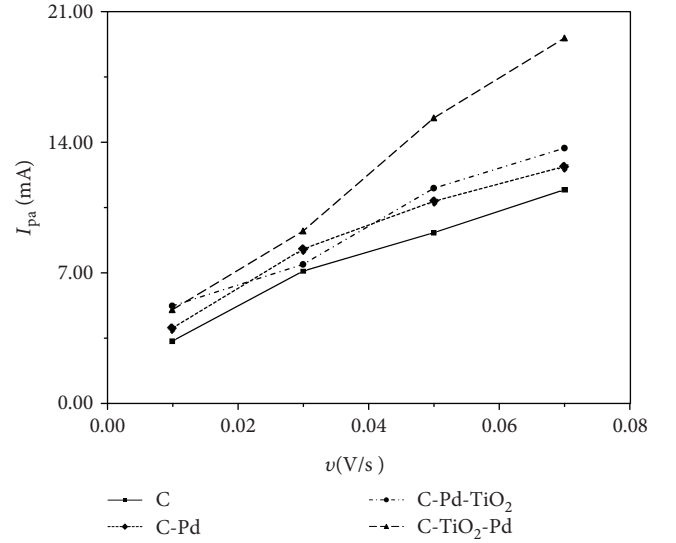
FIGURE 5: Plots of the anodic peak current (I_{pa}) versus the square root of scan rates ($v^{1/2}$) for the iodine-1 wt% vitamin C electrolyte for different electrodes.TABLE 2: D_0 and C_d of the iodine-vitamin C electrolyte solution on various electrodes.

Electrodes	$D_0 \times 10^6$ (cm ² /s)	C_d (F/cm ²)
	Iodine/1 wt% vitamin C electrolytes	Iodine/1 wt% vitamin C electrolytes
C electrode	12.8	0.132
C-Pd electrode	14.3	0.143
C-Pd-TiO ₂ electrode	9.9	0.148
C-TiO ₂ -Pd electrode	20.4	0.249

An electric double layer exists between the electrode and electrolyte. The electric double layer capacitor can be represented by equation (8).

$$i_{cd} = AC_d v, \quad (8)$$

where i_{cd} , A , C_d , and v are the electric double layer charging current, reaction area (cm²), electric double layer capacitor

FIGURE 6: Plots of the anodic peak current (I_{pa}) versus the scan rate (v) for the iodine-vitamin C electrolyte for various electrodes.

value (F/cm²), and scan rate (V/s), respectively. On the basis of our previous research [16], the relationship between i_{cd} and v can be derived by forming a straight line with the slope proportional to C_d in Figure 6 for the iodine-vitamin C electrolyte for the different electrodes. Table 2 summarizes the C_d data for comparison. C_d was the highest for the C-TiO₂-Pd electrode in the iodine-vitamin C electrolyte. Moreover, C_d increased from 0.132 to 0.249 F/cm², 89% higher than the C_d for the C-electrode.

3.5. Charge-Discharge Performance. Battery energy storage systems entail numerous design requirements, such as high voltage, current, power, and capacity. The capacity units of a large-scale energy storage battery system should meet the commercial operation requirements of the unit cells. Ordinarily, these batteries are fabricated in series or parallel to increase the storage capacity of the battery module and supply voltage group for achieving commercial requirements. In this section, we fabricated the C-TiO₂-Pd composite electrode as a negative electrode in the semi-V-I RFB system to design a single cell and series and parallel cell stacks and to evaluate the charge-discharge performance of the cell and stacks.

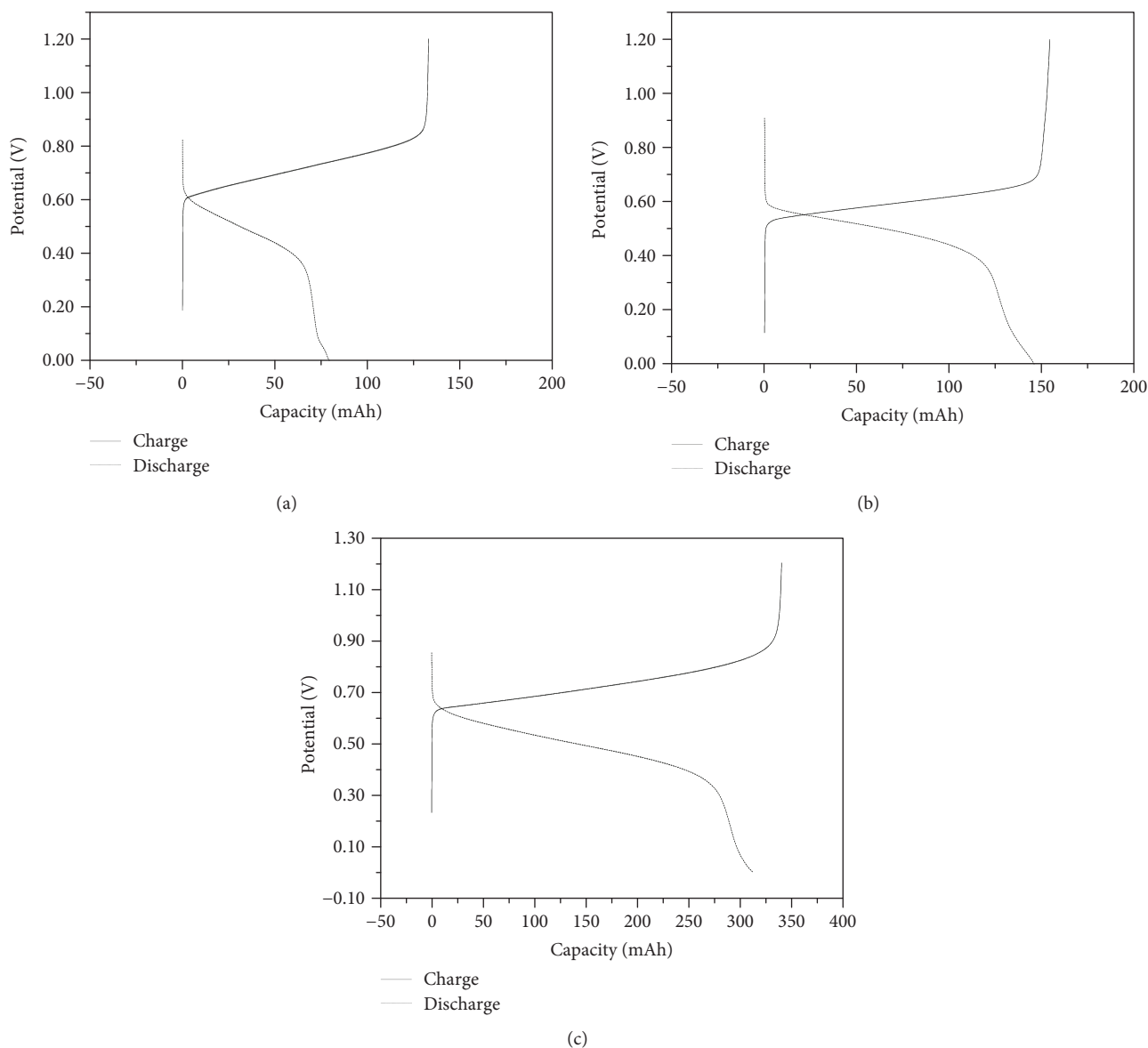


FIGURE 7: Charge-discharge diagrams of a semi-V-I RFB system with Nafion 117 as a separated membrane, C-TiO₂-Pd composite electrode as a negative electrode, and carbon paper as a positive electrode at different electrolyte concentrations. The volume of the electrolytic solution in each half cell was 10 mL. (a) 0.5 M I₂; (b) 1 M I₂; and (c) 2 M I₂.

3.5.1. Single Cell. The RFB energy storage capacity is proportional to the volume and concentration of the electrolyte. The C-TiO₂-Pd composite electrode is employed as a negative electrode in the semi-V-I RFB system with various concentrations of the electrolyte to conduct the charge-discharge tests. The charge-discharge curves are displayed in Figure 7, and performance of a single semi-V-I RFB is detailed in Table 3. The data in Table 3 verify that the energy storage capacity of the semi-V-I RFB system increases with the concentration of iodine-vitamin C solutions. The system exhibited optimal performance in the 1 M iodine solution; the coulomb efficiency (CE), voltage efficiency (VE), and energy efficiency (EE) were 96%, 81%, and 77%, respectively.

TABLE 3: Charge-discharge performance of the semi-V-I RFB system at different electrolyte concentrations.

Iodine concentration (M)	Capacity (mAh)	CE (%)	VE (%)	EE (%)
0.5	70	60	66	39
1	130	96	81	77
2	280	92	67	62

As specified in the literature [19, 23, 24], crystal structures of metals or alloys have different effects on the catalytic electrode. In our study, we observed that C-TiO₂-Pd

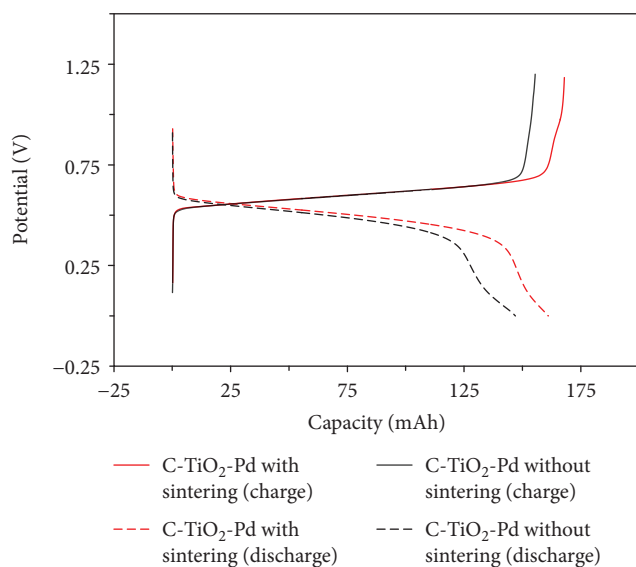


FIGURE 8: Charge-discharge diagram of the C-TiO₂-Pd electrodes by heat treatment for a semi-V-I RFB system.

TABLE 4: Charge-discharge performance of the C-TiO₂-Pd electrode by heat treatment for the semi-V-I RFB system.

Electrodes	Capacity (mAh)	CE (%)	VE (%)	EE (%)
C-TiO ₂ -Pd without sintering	130	96	81	77
C-TiO ₂ -Pd with sintering	150	96	87	83

electrodes with or without sintering at a high temperature affect the battery energy storage efficiency. Figure 8 displays the charge-discharge diagram of C-TiO₂-Pd electrodes with or without sintering in a semi-V-I RFB system, and the charge-discharge performance of the electrodes is detailed in Table 4; these data confirm that when the C-TiO₂-Pd electrode is sintered at high temperatures, the intensity of crystalline lattice conformations of Pd (111) and Pd (200) is stronger than that without sintering; additionally, a new PdO (101) crystal compound appeared, as shown in Figure 1(c). The formation of Pd (111), Pd (200), and PdO may contribute to the electrocatalytic activity in semi-V-I-RFB systems, in turn causing the VE to increase from 81% to 87% and EE from 77% to 83%. Furthermore, a series of continued charge-discharge tests of the semi-V-I RFB system was performed at a current density of 20 mA cm⁻² and is presented in Figure 9, which plots CE, VE, and EE as a function of cycle number. The average CE, VE, and EE values of the semi-V-I RFB system for 50 cycles illustrated in Figure 9 are approximately 96.52%, 84.12%, and 81.22%, respectively, revealing that the cyclic performance is excellent.

3.5.2. Battery Stacks. To facilitate large-scale commercial applications, the stacks of the RFB system are often fabricated in series and parallel cross combinations for increasing the storage capacity and operating voltage of the battery module.

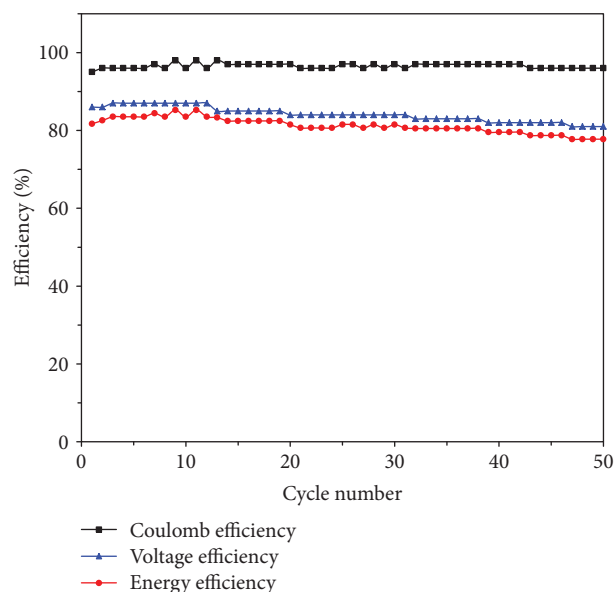


FIGURE 9: Cyclic efficiency diagram for a semi-V-I RFB system with Nafion 117 as a separated membrane, a C-TiO₂-Pd composite electrode as a negative electrode, and carbon paper as a positive electrode with a 1 M iodine/1 wt% vitamin C negative electrolyte and a 1 M VOSO₄/2 M H₂SO₄ positive electrolyte, and a current density of 20 mA cm⁻².

In the series configuration, the current supplied to the circuit is equal to the current across all elements in series ($I = I_1 = I_2 = \dots = I_N$), the total voltage is equal to the sum of each element voltage ($E = V_1 + V_2 + \dots + V_N$), and the total resistance is equal to the sum of each element resistance ($R_t = R_1 + R_2 + \dots + R_N$). In the parallel configuration, the total current is equal to the sum of each element current ($I_t = I_1 + I_2 + \dots + I_N$), the voltage supplied to the circuit is equal to the voltage across all elements in parallel ($V_t = V_1 = V_2 = \dots = V_N$), and the reciprocal of the total resistance is equal to the sum of the reciprocal of each element resistance ($1/R_t = 1/R_1 + 1/R_2 + \dots + 1/R_N$).

The charge and discharge curves of the all-VRFB stacks and the semi-V-I RFB stacks were composed of two cells in series and parallel, as shown in Figures 10(a) and 10(b), and the performances of the cells are summarized in Table 5. The results revealed that the charging voltage in the series stacks effectively increased from 1.8 to 3.6 V for the all-VRFB stacks, and the CE of the all-VRFB stacks significantly reduced to 73%. In the semi-V-I RFB system, a linear increase in the charging voltage from 1.2 to 2.4 V was observed. Moreover, the CE of the stacks remained at 92%, but the storage capacity of both systems was reduced. By comparison, in the series configuration, the overall efficiency value of the semi-VRFB system is higher than that of the all-VRFB system. In the parallel configuration, the capacity of the all-VRFB and semi-V-I RFB systems were altered from 139 to 137 mAh and from 147 to 162 mAh, respectively. The capacity of the semi-V-I RFB system improved slightly, but capacity of the all-VRFB system reduced. The charge-discharge performances of both systems attenuated significantly.

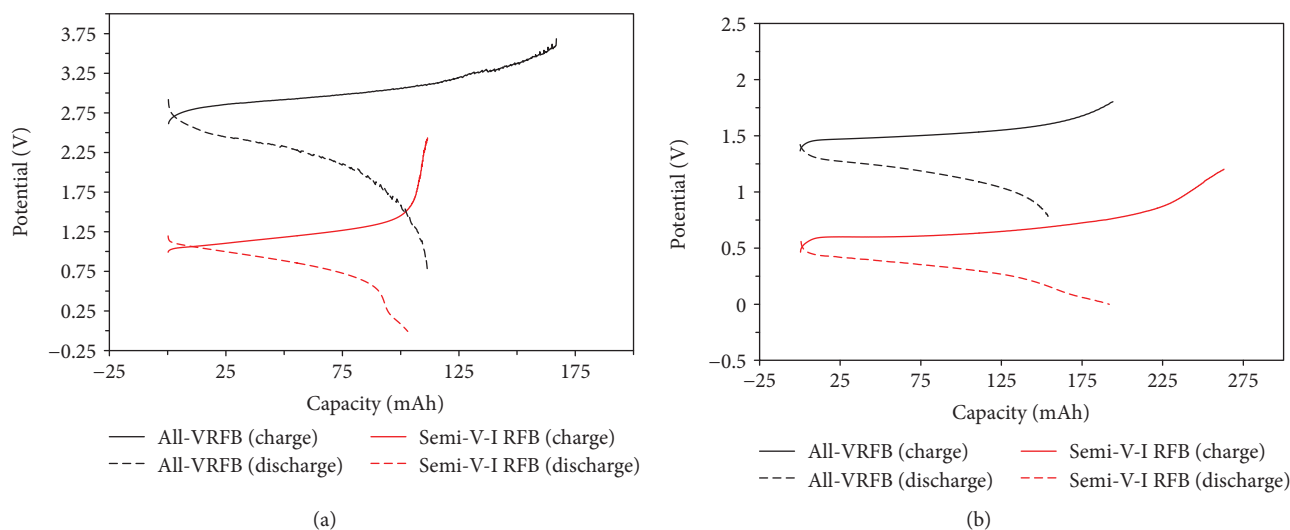


FIGURE 10: Charge-discharge diagram of all-VRFB and semi-V-I RFB stacks: (a) two cells in series and (b) two cells in parallel.

TABLE 5: Charge-discharge performance of all-VRFB and semi-V-I RFB stacks.

Types of battery		CE (%)	VE (%)	EE (%)	Capacity (mAh)	Charge voltage (V)
Single cell	All-VRFB	79	78	62	139	1.80
	Semi-V-I RFB	96	87	83	147	1.20
Series of two cells	All-VRFB	73	57	41	100	3.60
	Semi-V-I RFB	92	73	67	100	2.40
Parallel of two cells	All-VRFB	65	69	45	137	1.80
	Semi-V-I RFB	73	57	41	162	1.20

The capacity of the battery with the parallel combination cannot be increased; this may be due to the flow channel differences of the two batteries or due to an external line loss. If the voltage, inherent resistance, or current of the battery stacks are different, then a small voltage or battery resistance forms an electricity load and consumes part of the energy of another battery, thus decreasing the overall efficiency.

4. Conclusions

The C-TiO₂-Pd composite electrode was fabricated using carbon paper as a substrate that was coated with titanium dioxide and palladium metal in sequence. The C-TiO₂-Pd composite electrode exhibited superior electrochemical activity after high-temperature sintering. Moreover, the D_o value of the iodine-vitamin C electrolyte solutions increased by approximately 60% more than that of the C-electrode. The use of C-TiO₂-Pd as a negative electrode for the semi-V-I RFB system effectively enhanced the VE, thus improving the overall EE to 83%. In the series configuration, the charge voltage of the all-VRFB and semi-V-I RFB battery stacks linearly increased. However, performance of the all-VRFB battery stacks was significantly attenuated, and the EE decreased from 62% to 41%. By comparison, the semi-V-I RFB stacks can still be maintained at 67%. If we can use the design and assembly technology to enhance

and improve the flow channel of the battery, the overall efficiency can be effectively improved. For series and parallel combinations obtained by stacking large modules, the proposed semi-V-I RFB system has high application potential to meet commercial requirements.

Data Availability

Previously reported experiment system was used to support this study and is available at <https://www.hindawi.com/journals/jchem/2017/4590952/>. This prior study is cited within the text as reference [4].

Conflicts of Interest

The authors declare no conflicts of interest.

Acknowledgments

The authors are grateful for the financial support by the Ministry of Science and Technology, Taiwan.

References

- [1] P. Alotto, M. Guarnieri, and F. Moro, "Redox flow batteries for the storage of renewable energy: a review," *Renewable and Sustainable Energy Reviews*, vol. 29, pp. 325–335, 2014.

- [2] A. Cunha, J. Martins, N. Rodrigues, and F. P. Brito, "Vanadium redox flow batteries: a technology review," *International Journal of Energy Research*, vol. 39, no. 7, pp. 889–918, 2015.
- [3] J. Xi, S. Xiao, L. Yu, L. Wu, L. Liu, and X. Qiu, "Broad temperature adaptability of vanadium redox flow battery—part 2: cell research," *Electrochimica Acta*, vol. 191, pp. 695–704, 2016.
- [4] S. L. Huang, H. F. Yu, and Y. S. Lin, "Modification of Nafion® membrane via a sol-gel route for vanadium redox flow energy storage battery applications," *Journal of Chemistry*, vol. 2017, Article ID 4590952, 10 pages, 2017.
- [5] L. F. Arenas, C. P. León, and F. C. Walsh, "Mass transport and active area of porous Pt/Ti electrodes for the Zn-Ce redox flow battery determined from limiting current measurements," *Electrochimica Acta*, vol. 221, pp. 154–166, 2016.
- [6] M. Skyllas-Kazacos, M. Rychcik, R. G. Robins, A. G. Fane, and M. A. Green, "New all-vanadium redox flow cell," *Journal of the Electrochemical Society*, vol. 133, no. 5, pp. 1057–1058, 1986.
- [7] A. Parasuraman, T. M. Lim, C. Menictas, and M. Skyllas-Kazacos, "Review of material research and development for vanadium redox flow battery applications," *Electrochimica Acta*, vol. 101, pp. 27–40, 2013.
- [8] J. Maruyama and T. Shinagawa, "Catalyst layer structures for enhancement of redox reactions of V(IV/V) ions," *Electrochimica Acta*, vol. 210, pp. 854–861, 2016.
- [9] L. Wei, T. S. Zhao, G. Zhao, L. An, and L. Zeng, "A high-performance carbon nanoparticle-decorated graphite felt electrode for vanadium redox flow batteries," *Applied Energy*, vol. 176, pp. 74–79, 2016.
- [10] D. Lloyd, T. Vainikka, M. Ronkainen, and K. Kontturi, "Characterisation and application of the Fe(II)/Fe(III) redox reaction in an ionic liquid analogue," *Electrochimica Acta*, vol. 109, pp. 843–851, 2013.
- [11] J. W. Lim and D. G. Lee, "Carbon fiber/polyethylene bipolar plate-carbon felt electrode assembly for vanadium redox flow batteries (VRFB)," *Composite Structures*, vol. 134, pp. 483–492, 2015.
- [12] C. Yang, H. Wang, S. Lu et al., "Titanium nitride as an electrocatalyst for V(II)/V(III) redox couples in all-vanadium redox flow batteries," *Electrochimica Acta*, vol. 182, pp. 834–840, 2015.
- [13] K. Oh, S. Won, and H. Ju, "Numerical study of the effects of carbon felt electrode compression in all-vanadium redox flow batteries," *Electrochimica Acta*, vol. 181, pp. 13–23, 2015.
- [14] G. Nikiforidis, L. Berlouis, D. Hall, and D. Hodgson, "An electrochemical study on the positive electrode side of the zinc-cerium hybrid redox flow battery," *Electrochimica Acta*, vol. 115, pp. 621–629, 2014.
- [15] J. Melke, P. Jakes, J. Langner et al., "Carbon materials for the positive electrode in all-vanadium redox flow batteries," *Carbon*, vol. 78, pp. 220–230, 2014.
- [16] M. L. Chen, S. L. Huang, C. L. Hsieh, J. Y. Lee, and T. J. Tsai, "Development of a novel iodine-vitamin C/vanadium redox flow battery," *Electrochimica Acta*, vol. 141, pp. 241–247, 2014.
- [17] M. H. Pournaghi-Azar and H. Razmi-Nerbin, "Electrocatalytic characteristics of ascorbic acid oxidation at nickel plated aluminum electrodes modified with nickel pentacyanonitrosylferate films," *Journal of Electroanalytical Chemistry*, vol. 488, no. 1, pp. 17–24, 2000.
- [18] V. M. Dubin, "Electroless Ni-P deposition on silicon with Pd activation," *Journal of the Electrochemical Society*, vol. 139, no. 5, pp. 1289–1294, 1992.
- [19] B. M. Praveen and T. V. Venkatesha, "Electrodeposition and properties of Zn-nanosized TiO₂ composite coatings," *Applied Surface Science*, vol. 254, no. 8, pp. 2418–2424, 2008.
- [20] J. R. Henry, "Electroless (autocatalytic) plating," *Metal Finishing*, vol. 97, no. 1, pp. 424–435, 1999.
- [21] K. Cheng, D. X. Cao, F. Yang, L. L. Zhang, Y. Xu, and G. L. Wang, "Electrodeposition of Pd nanoparticles on C@TiO₂ nanoarrays: 3D electrode for the direct oxidation of NaBH₄," *Journal of Materials Chemistry*, vol. 22, no. 3, pp. 850–855, 2012.
- [22] F. Hu, F. Ding, S. Song, and P. K. Shen, "Pd electrocatalyst supported on carbonized TiO₂ nanotube for ethanol oxidation," *Journal of Power Sources*, vol. 163, no. 1, pp. 415–419, 2006.
- [23] M. G. Hosseini and I. Ahadzadeh, "A dual-chambered microbial fuel cell with Ti/nano-TiO₂/Pd nano-structure cathode," *Journal of Power Sources*, vol. 220, pp. 292–297, 2012.
- [24] Y. N. Wu, S. J. Liao, H. F. Guo, and X. Y. Hao, "High-performance Pd@PtRu/C catalyst for the anodic oxidation of methanol prepared by decorating Pd/C with a PtRu shell," *Journal of Power Sources*, vol. 224, pp. 66–71, 2013.
- [25] A. J. Bard and L. R. Faulkner, *Electrochemical Methods—Fundamentals and Applications*, Wiley, 2nd edition, 2001.
- [26] S. Li, K. Huang, S. Liu et al., "Effect of organic additives on positive electrolyte for vanadium redox battery," *Electrochimica Acta*, vol. 56, no. 16, pp. 5483–5487, 2011.

Research Article

Mesoporous Nickel-Based Zeolite Capsule Complex with Fe_3O_4 as Electrode for Advanced Supercapacitor

Lili Song,¹ Yinghui Han ,^{1,2,3} Feng Guo,⁴ Yunpeng Jiao,^{1,2} Yujuan Li,¹ Yunpeng Liu ,³ and Feng Gao²

¹Department of Mathematics & Physics, North China Electric Power University, Baoding, Hebei 071003, China

²Energy Internet Research, Tsinghua University, Beijing 100084, China

³Hebei Key Laboratory of Distributed Energy Storage and Micro-grid, North China Electric Power University, Baoding, Hebei 071003, China

⁴Department of Chemical Engineering, University of Wyoming, Laramie 82072, USA

Correspondence should be addressed to Yinghui Han; yinghuihan@ncepu.edu.cn and Yunpeng Liu; gylyp@263.net

Received 30 June 2018; Revised 20 September 2018; Accepted 27 September 2018; Published 19 December 2018

Guest Editor: Zhengping Zhou

Copyright © 2018 Lili Song et al. This is an open access article distributed under the Creative Commons Attribution License, which permits unrestricted use, distribution, and reproduction in any medium, provided the original work is properly cited.

A new kind of zeolite capsule complex with ferriferrous oxide (Fe_3O_4) materials was prepared in this work. Its morphology was characterized via the scanning electron microscope (SEM), the high-resolution transmission electron microscopy (HRTEM), N_2 adsorption analysis, and X-ray powder diffraction, respectively. The mesoporous nickel-based complex electrodes using substrate coating exhibited excellent energy storage properties through electrochemical testing. The high specific capacitance of 739.8 F g^{-1} was achieved at the current density of 1 A g^{-1} in a 6M KOH solution. The good capacitance retention can retain 72.8% after 1000 cycles in a current density of 1 A g^{-1} . The energy storage mechanism of the nickel-based complex electrodes was also analyzed. Furthermore, the asymmetrical supercapacitors (ASCs) were fabricated using the zeolite capsule complex with Fe_3O_4 as positive electrodes and the AC as negative electrodes, which performs high specific capacitance, outstanding energy density, superb power density, excellent cycle life, and small internal impedance. Those results suggest that the mesoporous nickel-based zeolite capsule complex with Fe_3O_4 as an electrode would be an ideal candidate material for supercapacitor applications.

1. Introduction

In recent years, the ecological environment has been deteriorating day by day. The development of new energy and renewable energy has aroused widespread concern. However, new energy and renewable energy have some disadvantages, such as instability and indirectness. Therefore, developing energy storage technology is an important guarantee for the popularization and application of new energy and renewable energy. As a power storage technology, supercapacitors have attracted much attention in terms of its high power density, fast charge and discharge rate, and long cycle life [1–5]. According to different energy storage mechanisms, the supercapacitors can be divided into double-layer capacitors (EDLCs) and pseudocapacitors [6, 7]. The supercapacitors

consist of three parts, i.e., the electrolyte, the electrode, and the diaphragm. The electrode and the electrolyte play the core role in improving the performance of the supercapacitors. The development of the electrode material has become one of the main research directions, and the trend of electrode materials has two main aspects of nanoscale and composite at present.

Mesoporous materials have become one of the research hotspots in the world because of their large specific surface area, regular pore structure, and excellent controllability. The research on mesoporous materials as electrodes is widely paid attention. Saravanakumar et al. [8] prepared vanadium pentoxide (V_2O_5)/nitrogen-containing mesoporous carbon spheres (n-MPC) nanocomposite without the use of expensive organic vanadium precursors and

sophisticated instruments. The optimal specific capacity was 410 F g^{-1} . Lv et al. [9] developed the NiO/graphene composites. The electrochemical results showed that the NiO/graphene composites exhibited very high specific capacitance 1062 F g^{-1} at 1 A g^{-1} . The mesoporous structure of Ni(OH)₂ and NiO was synthesized using twelve alkyl sodium sulfate as a template, and its specific capacitance was about 106 F g^{-1} [10]. However, among the reported materials, either the cost is too high or the performance is not good enough to meet the needs of the large-scale industrial application. In addition, it is still a challenge to design an electrode material allied with both high specific capacitance and excellent cycle life.

In this work, a new kind of cost-effective complex materials would be prepared via internal template method and suspension polymerization. The structure and morphology will be characterized using SEM, HRTEM, BET, and XRD. Finally, the electrochemical performance test of the asymmetrical supercapacitors (ASCs) in a three-electrode system will be performed by an electrochemical workstation. Those results aim at providing a reference and basic data for the preparation of industrial supercapacitor.

2. Experiment

2.1. Materials and Reagents. All starting chemicals were commercially available reagents with analytical grade and used without further purification, and all solutions were prepared with distilled water. Nickel foam (Tianjin Beichen Reagent Co. Ltd., China) was rinsed four times with distilled water and ethanol, respectively. Beer yeast was from Bozhou Baohua Pharmaceutical Co. Ltd., China. All the other reagents were from Baoding Huaxin Reagent Co. Ltd., China.

2.2. Preparation of Zeolite Template and the Nickel-Based Complex Electrode. In order to obtain the electrode with high performance for advanced supercapacitor, the zeolite template, the complex materials, and the nickel-based complex electrode were prepared, respectively.

Firstly, the beer yeast, as an auxiliary template, was immersed in hydrochloric acid by ultrasonic cleaning. The pretreatment went through repeated filtration, washing, and drying.

Secondly, the amount of sodium hydroxide was added into deionized water. After the dissolution, dropwise add a certain amount of sodium aluminate (NaAlO₂). The directing agent was prepared by maintaining at the reaction temperature (25°C) and stirring for 24 h.

Thus, a certain amount of auxiliary template was dissolved into distilled water and then a certain volume of directing agent was added. After mixing evenly, hydrochloric acid was dropwise to adjust the pH value of the reaction system until white floc appeared. Further, the mixed solution was transferred to a Teflon-lined heated reactor, reacted at 80°C for 5 hours, then suction filtered and dried at 50°C overnight. After grinding in a muffle furnace calcined at 150°C for 2 hours, the temperature was raised to 550°C calcined for 4 hours. In this case, the zeolite template was obtained.

A given amount of Fe₃O₄ ultrasonic mixing dissolved in a certain water. Subsequently, the zeolite template, a certain amount of iron ions, pyrimidine, and hydrogen peroxide solution were added into the solution successively. The mixture was stirred for 12 hours. Finally, the material of the zeolite capsule complex with Fe₃O₄ was synthesized after filtration, washing, and drying.

To prepare the electrodes for electrochemical measurements, the active materials, including the pure Fe₃O₄ and the zeolite capsule complex with Fe₃O₄, polytetrafluoroethylene (PTFE), and acetylene black were mixed with a mass ratio of 80:10:10 in anhydrous ethanol to form a homogeneous slurry. The working electrode was made by coating the viscous slurry onto nickel foam and then dried at 120°C to evaporate the solvent. After this process, the foam nickel loaded with the complex materials was directly sliced and pressed into circular electrodes of supercapacitors.

2.3. Characterizations. The morphologies were observed using a scanning electron microscope (SEM) equipped with a rapid energy dispersive X-ray spectrometer (EDS) research on a FEI Nova NanoSEM 450 microscope. The high-resolution transmission electron microscopy (HRTEM) images were analyzed through a HRTEM (JEOLJEM2100). The specific surface area was calculated using the Brunauer-Emmett-Teller (BET) model based on the N₂ adsorption branch within the relative pressure range of 0.05–0.35, and the pore size distribution was obtained from the N₂ desorption branch by the Barrett-Joyner-Halenda (BJH) method. The phase purity and crystallinity of the products were analyzed by X-ray powder diffraction (XRD, Rigaku, Japan) which were recorded on a RINT 2500 V X-ray diffractometer with Cu K α radiation ($\lambda = 1.5406 \text{ \AA}$) at a scan rate $6^\circ/\text{min}$ in the 2θ range from 10° to 80° .

2.4. Electrochemical Measurement. The measurements of cyclic voltammetry (CV) and galvanostatic charge-discharge (GCD) were carried out in a 6 M KOH solution by electrochemical workstation (Chenhua CHI760E, Shanghai). Electrochemical impedance spectroscopy (EIS) was introduced to estimate the pseudocapacitor performance. An AC voltage with 5 mV amplitude in a range of 0.01 Hz– 10^5 Hz was used to estimate internal resistance of the electrode.

In order to achieve a comparison of the performance of different electrode materials, the specific capacitance was calculated, and the energy density and power density were estimated, respectively. For the CV curve, the charge of the electric potential between φ_1 and φ_2 can be obtained by integrating the volt-ampere curve with the rate $s = d\varphi/dt$ scanning:

$$Q = \int_{\varphi_1}^{\varphi_2} i(\varphi) dt \equiv \int_{\varphi_1}^{\varphi_2} \frac{i(\varphi) d\varphi}{s}, \quad (1)$$

where φ (V) is the electric potential, s (V s^{-1}) is the scanning rate, and t (s) is the scanning time [11].

Therefore, the specific capacitance is calculated according to the following equation [12, 13]:

$$C = \frac{Q}{2\Delta V \times m}, \quad (2)$$

where Q is the charge integrated from the whole voltage range, ΔV (V) is the whole voltage difference, and m (g) is the mass of active material in a single electrode.

In addition, the galvanostatic charge-discharge-specific capacities were calculated from the following equations [14–16]:

$$C = \frac{2i_m \int v dt}{(v_f - v_i)^2}, \quad (3)$$

where C (F g^{-1}) is specific capacitance, i_m (A g^{-1}) is applied discharge current density, $\int v dt$ is the integral current area of the galvanostatic charge-discharge curve, and v_f and v_i (V) are the potential with initial and final values, respectively.

Measurements of electrochemical performance of mesoporous complex materials and active carbon (AC) asymmetric supercapacitors were carried out via electrochemical workstation using 6 M KOH as the electrolyte. The preparation of the negative electrode directly applied activated carbon, acetylene black, and PTFE (80 wt%, 10 wt%, and 10 wt%) mixture onto the foam nickel, which was similar to the synthesis of nickel-based complex electrode.

In terms of the charge balance of asymmetric supercapacitors (ASCs), the principle $q^+ = q^-$ should be satisfied, where q^+ is the positive charges and q^- is the negative charges. The voltammetric charges (q) were obtained by the following equation [17, 18]:

$$q = C \times \Delta V \times m, \quad (4)$$

where C is the specific capacitance (F g^{-1}) of each electrode, ΔV is the potential windows (V), and m is the mass loading (g). So the mass ratio of the positive and negative electrode followed equation as [19]:

$$\frac{m_+}{m_-} = \frac{C_- \times \Delta V_-}{C_+ \times \Delta V_+}. \quad (5)$$

The energy density and power density of the ACSs were calculated by the following equations, respectively:

$$E = \frac{1}{2 \times 3.6} C (\Delta V)^2, \quad (6)$$

$$P = \frac{E \times 3600}{\Delta t}, \quad (7)$$

where E is the specific energy (Wh kg^{-1}), C is specific capacitance (F g^{-1}), Δt is discharge time (s), P is the specific power

(W kg^{-1}), and ΔV (V) is operating potential window of the ASCs [18, 20].

3. Results and Discussion

3.1. Structural and Morphological Study. Generally, the preparation process and growth conditions will directly affect the morphology and microstructure of complex materials. As the above section mentioned, the whole process of preparation is illustrated in Figure 1.

The morphology and structures of pure Fe_3O_4 , zeolite template, the complex material, and the nickel-based complex electrode on nickel foam are characterized in Figure 2, respectively. The pure Fe_3O_4 exhibits an excellent bulk structure and single crystal form, as shown in Figures 2(a) and 2(b), respectively. The structures of zeolite template show the great sheet-like pore structure (Figures 2(c)–2(e)). The EDS analysis (Figure 2(k)) of the zeolite template, revealing the presence of C, O, Al, Si, and Cl, and the atomic ratio of C to O, is approximately estimated to be 19.33:58.92. Comparing the SEM of the zeolite template (Figures 2(c)–2(e)) with that of the complex material (Figures 2(f)–2(h)), the complex material exhibits smaller particles and more porous structure for better storage of electrolyte ions and reducing the ion diffusion distance [21]. Furthermore, the EDS (Figure 2(l)) spectra of the complex materials showed the presence of C, N, O, and Fe, and the atomic ratio of C, N, and O to Fe is approximately estimated to be 11.86:3.04:41.56:43.55. The SEM images of the nickel-based complex electrodes (Figures 2(i) and 2(j)) with the magnification $40 \mu\text{m}$ and 500 nm , respectively, showed that the complex material is well attached to the nickel film. Meanwhile, the uniform hole distribution and structures were observed; that is probably one of the reasons why it has the excellent electrochemical performance for the supercapacitor electrode.

Furthermore, the HRTEM images of the nickel-based complex electrode at different magnifications in the range of 5 nm – 200 nm are depicted in Figure 3. The dark area in Figures 3(a) and 3(b) were supposed to be the aggregates of Fe_3O_4 and zeolite template agent in the dry state. The transparent short rods in Figure 3(c) showed the capsuling-like structure of the sample [22]. In addition, a clearly visible nanostave microstructure was observed in Figure 3(d), which would significantly reduce the ion diffusion distance and improve the charge transfer [23, 24].

Because surface and pore-size distribution are two key parameters for electroactive materials in energy conversion/storage applications [25], the N_2 adsorption analyses were carried out. From Figure 4, it is clearly seen that the complex materials have typical IV isotherms with H_3 -type hysteresis loop in the relative pressure (P/P_0) range of 0.6–1.0, indicating the presence of a mesoporous structure, while the zeolite template exhibits typical II isotherms that is characteristic for nonporous/macro porous materials. Furthermore, the pore-size distribution (inset of Figure 3) of the complex materials possesses mesoporous with a relative narrow size distribution in the range from 2 nm to

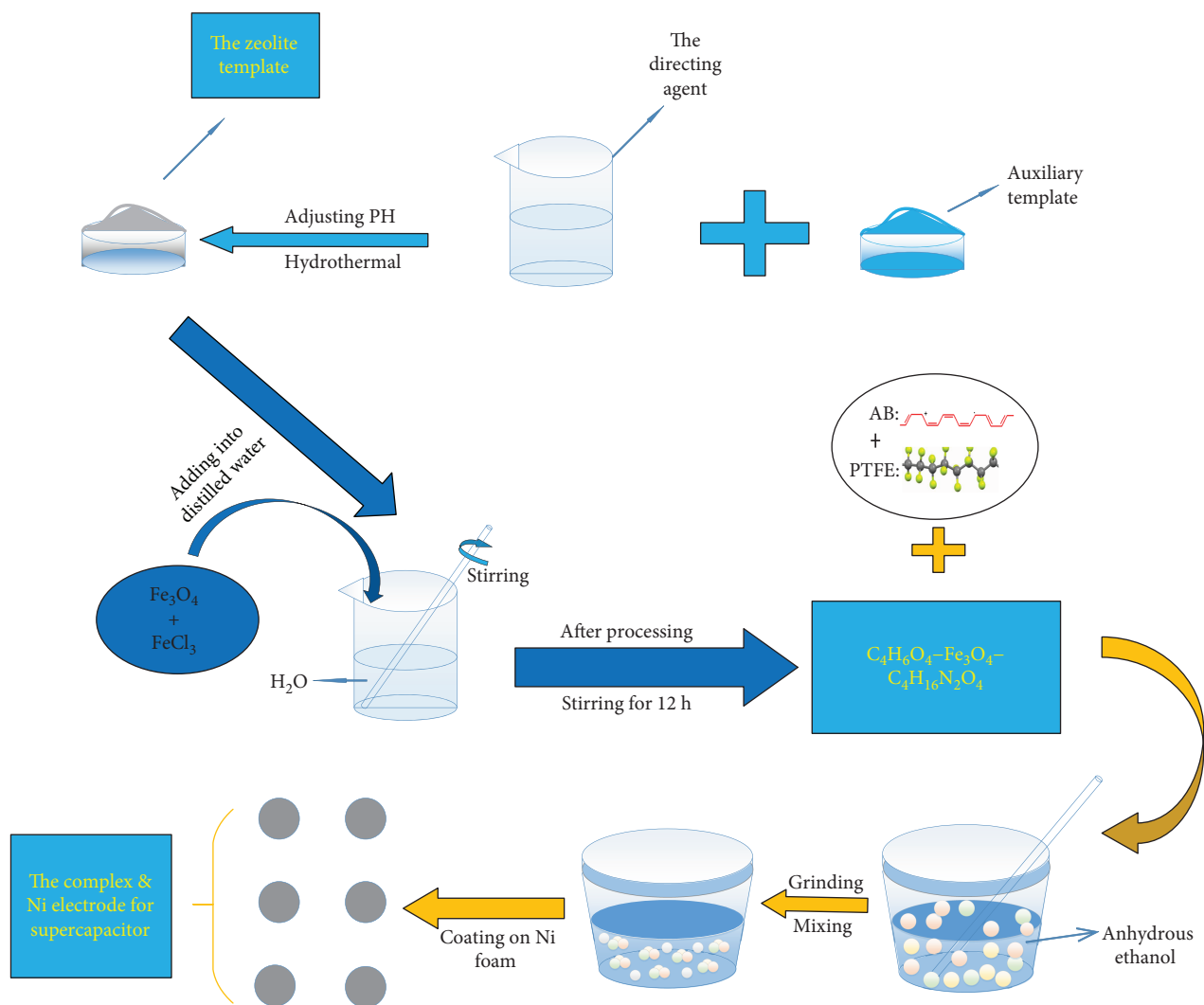


FIGURE 1: The schematic diagram of nickel-based supercapacitor electrode via the zeolite capsule complex with Fe_3O_4 .

10 nm by Barrett-Joyner-Halenda (BJH) method. Compared with the zeolite template, the complex materials reveal a relatively good specific surface area ($13.437\text{m}^2\text{g}^{-1}$) and total pore volume ($0.052\text{cm}^3\text{g}^{-1}$) calculated via Brunauer-Emmett-Teller (BET). Relatively good specific surface area and pore structure should enhance the electrode reaction kinetics [26–28], leading to better electrochemical performance.

To further identify the crystal structure and phase composition of all the samples, X-ray diffraction (XRD) analyses were carried out. As shown in Figure 5, those are the X-ray diffraction patterns of the pure Fe_3O_4 , the zeolite template, and the complex materials, respectively. It is obtained that the diffraction peaks of the pure Fe_3O_4 are in good agreement with those in the PDF standard card (JCPDS card NO.19-0629), and any peaks for the other secondary phases were not observed. It demonstrates that the pure Fe_3O_4 crystallizes in a pure phase. According to the PDF standard cards NO.44-0704 and NO.43-1522, it can be clearly seen that the zeolite template and the complex materials are marked unnamed zeolite (the chemical formula

is $\text{C}_3\text{H}_6\text{O}_2 \cdot 6\text{SiO}_2$) and magnetite-tartrate-quadrol complex (the chemical formula is $\text{C}_4\text{H}_6\text{O}_6\text{-Fe}_3\text{O}_4\text{-C}_{14}\text{H}_{16}\text{N}_2\text{O}_4$), respectively. The pure Fe_3O_4 , the zeolite template, and the composite materials occur most commonly in the crystal structure of cubic I-43m, cubic Fd-3m, and cubic I-43m, respectively. The good matching peaks indicate that the zeolite template and the complex materials belong to a crystal form.

The morphological specific surface area and crystal structure were detected by SEM, HRTEM, N_2 adsorption analyses, and XRD, respectively. It can be well prepared for further analysis of the energy storage mechanism of the sample.

3.2. Electrochemical Performance. In order to study the electrochemical energy storage performance of the nickel-based complex electrodes for supercapacitors, the CV, GCD, and EIS were measured, respectively, in a three-electrode cell (vs. SCE) by electrochemical workstation (Chenhua CHI760E, Shanghai).

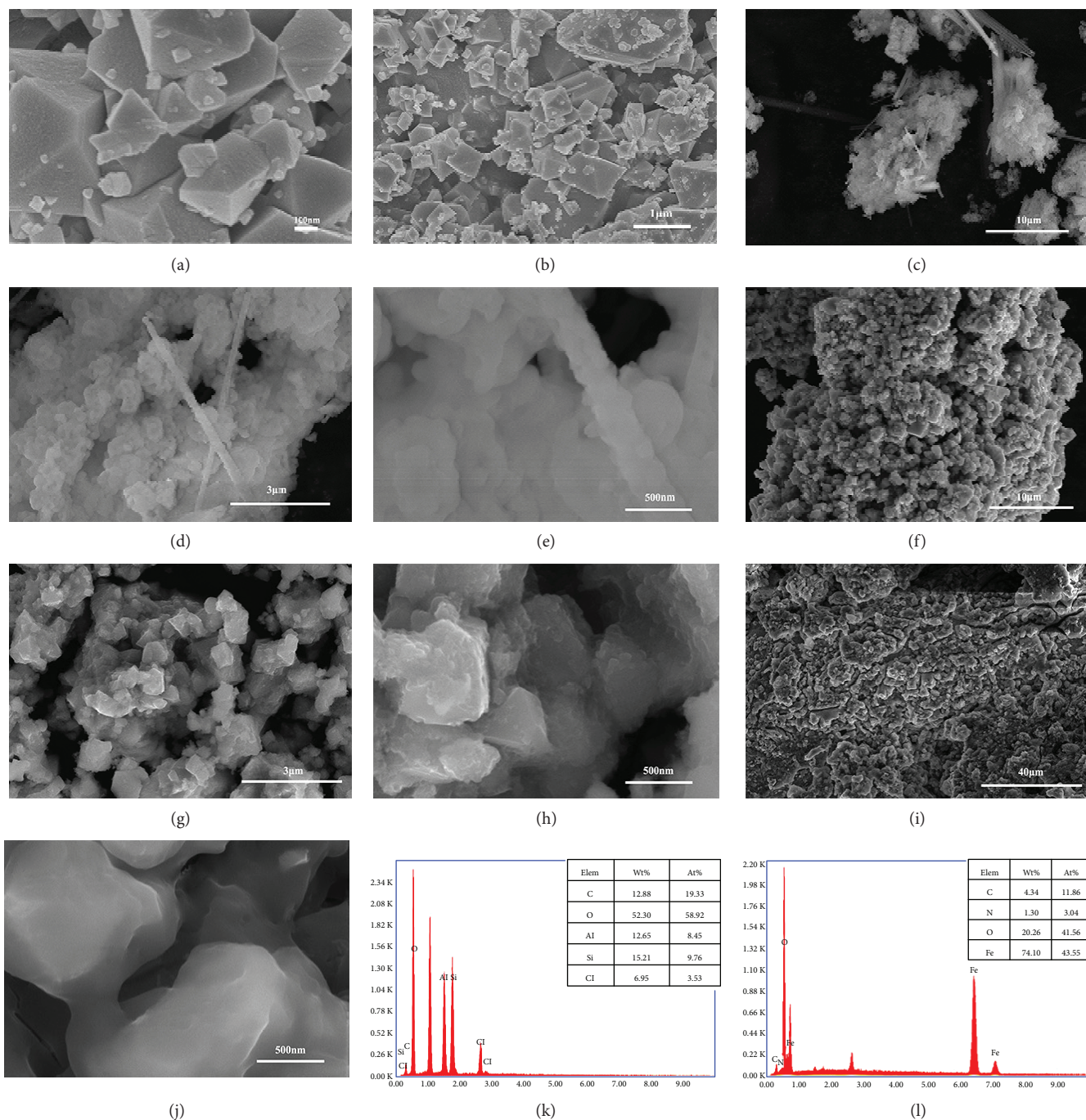


FIGURE 2: The SEM images at different magnification of the pure Fe_3O_4 (a–b), the zeolite template (c–e), the complex materials (f–h), and the nickel-based complex electrode (i–j), respectively. The EDS spectra of the zeolite template (k) and the complex materials (l).

Figure 6(a) shows the CV curve of the nickel-based complex electrodes and the pure nickel-based Fe_3O_4 electrodes at a scan rate of 10 mV s^{-1} . For the nickel-based complex electrodes of supercapacitors, one pair of redox peaks exhibited in CV curves in the range from -0.1 to 0.3 V , demonstrating that it stores energy through Faraday redox reaction. It has a pseudopotential characteristic, while the CV curve of the pure Fe_3O_4 electrodes is close to a smooth line. According to (1) and (2), the CV curve of the

nickel-based complex electrodes exhibits a larger integral area than that of the pure nickel-based Fe_3O_4 electrodes, indicating that the nickel-based complex electrode has a larger capacitance than that of the pure nickel-based Fe_3O_4 electrodes. To further contrast the electrochemical performance difference between the two electrodes, the GCD tests of both (Figure 6(b)) were conducted at current densities of 1 A g^{-1} . The longer discharge time of the nickel-based complex electrodes revealed that it has the higher

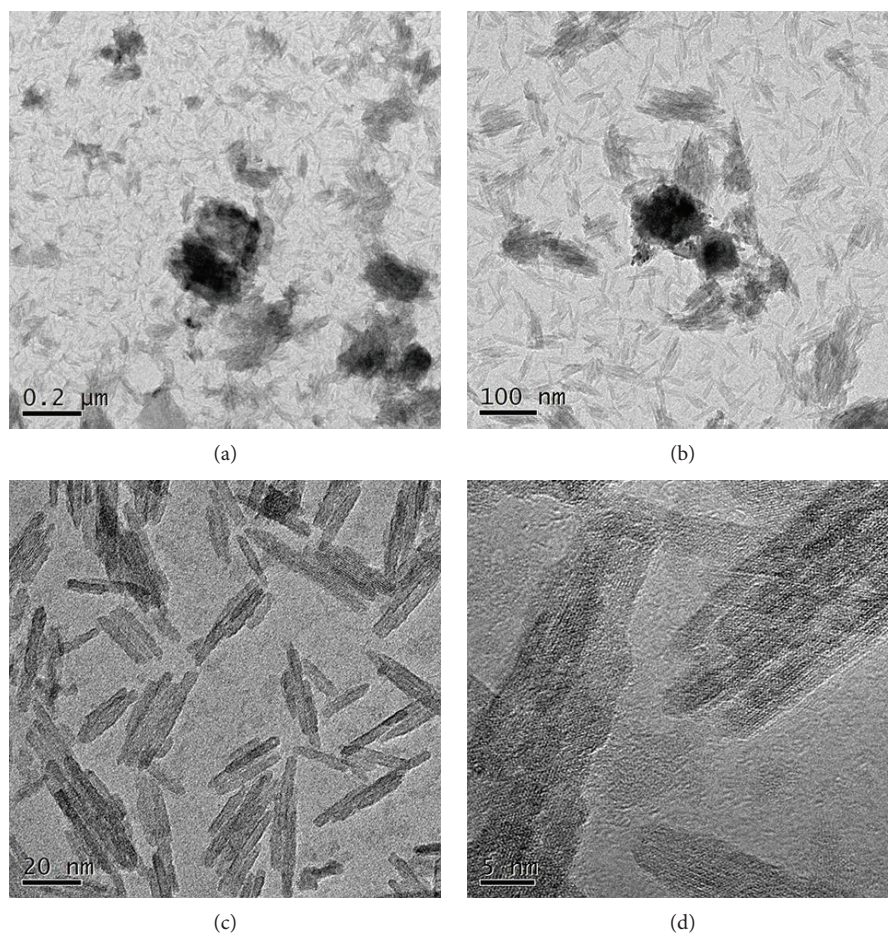


FIGURE 3: HRTEM images of the nickel-based complex electrode at different magnification.

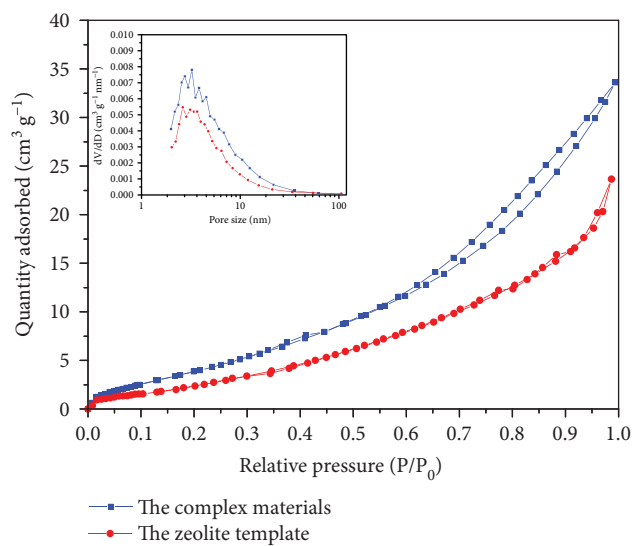


FIGURE 4: N_2 adsorption isotherms (inset: the curve of pore-size distribution).

electrochemical performance, which was similar to the CV results. Figures 6(c) and 6(d) showed the rate performance at different scanning rates and current densities. Along with

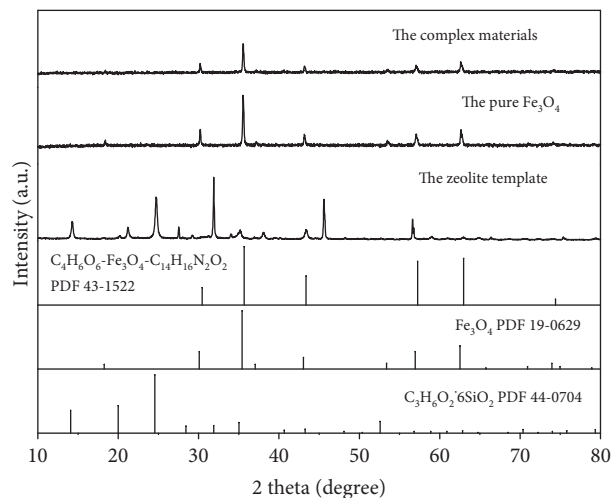


FIGURE 5: X-ray diffraction patterns of the pure Fe_3O_4 , the zeolite template, and the complex materials, respectively.

the increase of scanning rate, the position of the anodic peaks shifted to higher potential, in consistency with Randles-Sevcik rules [29]. With the increase of current density, the discharge time becomes shorter. The anodic

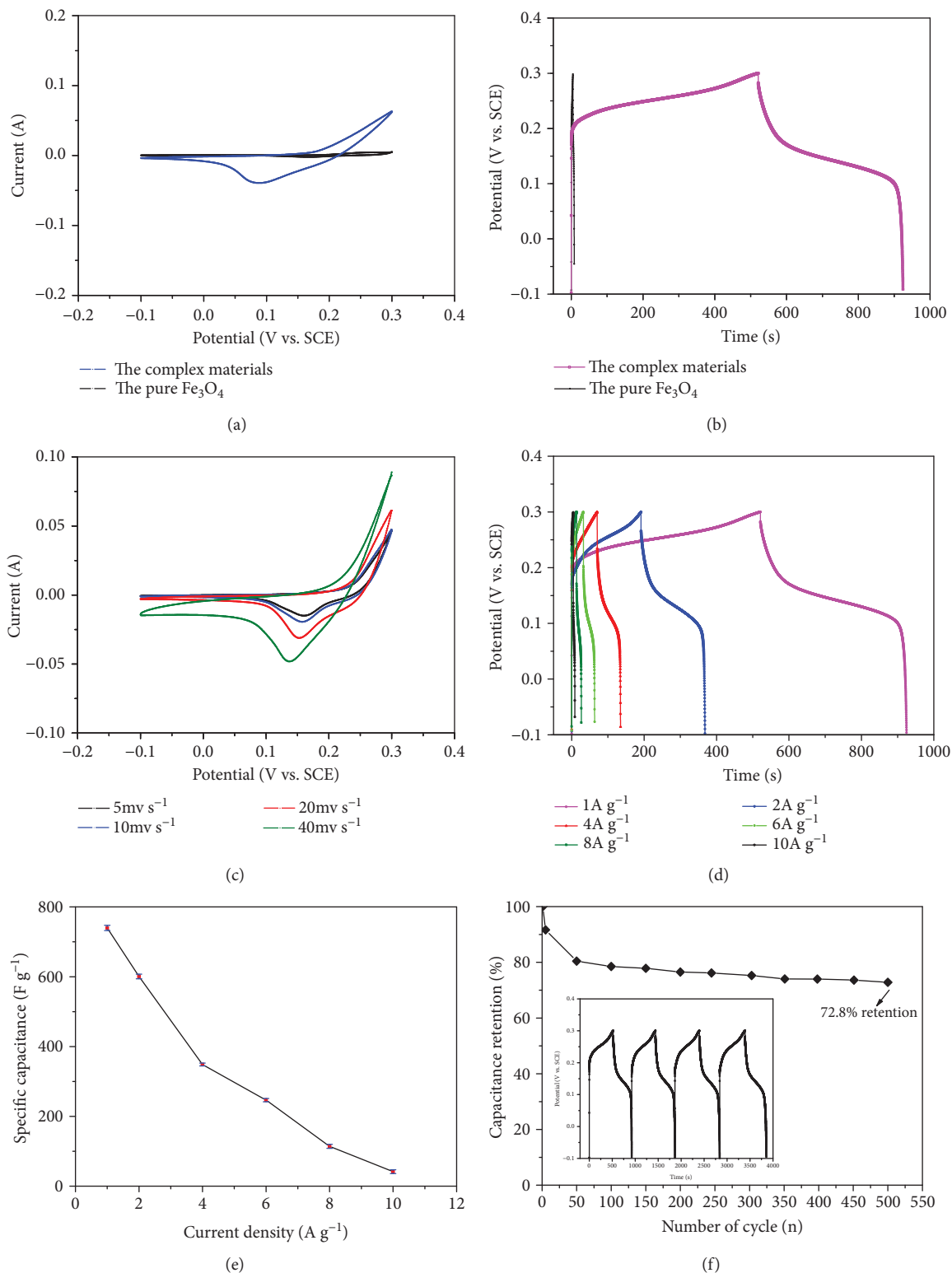


FIGURE 6: (a) CV curves of the nickel-based complex electrodes and the pure nickel-based Fe_3O_4 electrodes at a scan rate of 10 mV s^{-1} ; (b) GCD curves of the nickel-based complex electrodes and the pure nickel-based Fe_3O_4 electrodes at current densities of 1 A g^{-1} ; (c) CV curves of the nickel-based complex electrodes at different scanning rates; (d) GCD curves of the nickel-based complex electrodes at various current densities; (e) specific capacitance of the nickel-based complex electrode discharge curves at various current densities; and (f) cycling performance of the nickel-based complex electrodes measured at a voltage window of -0.1 V to 0.3 V .

peak shift probably results from polarization [30–32]. It clearly manifests that the nickel-based complex electrodes have excellent rate characteristics.

In order to observe the different current scanning rates of special capacitance changes, the specific capacitance of the nickel-based complex electrode at various current densities is calculated by (3) (Figure 6(e)). It is obvious that the specific capacitance decreases gradually with the increase of discharge current density. It can be seen that the specific capacitances of the nickel-based complex electrodes at the current density of 1, 2, 4, 6, 8, and 10 A g⁻¹ are 739.8, 600.8, 348.4, 246.5, 114, and 41.5 F g⁻¹, respectively. As the current density increases, the specific capacitance becomes smaller. This indicates both high specific capacitance and good capacitance retention at high rate.

Long-term cyclic stability is an important requirement for its applications in supercapacitors [33, 34]. As shown in Figure 6(f), the curve that the capacitance retention follows the number of the charge-discharge cycles is observed. And the inset is a partial GCD curve that was used to calculate the specific capacitance retention according to the following equations [35]:

$$\Delta C = |C_{\text{low}} - C_{\text{high}}|, \quad (8)$$

$$\alpha = \frac{\Delta C}{C_{\text{high}}} \times 100\%, \quad (9)$$

$$\beta = 1 - \alpha, \quad (10)$$

where C_{high} and C_{low} are the values of specific capacitance at -0.1 V and 0.3 V calculated by (3). β is the capacitance retention.

The capacitance retention reduced with the increase of the number of cycle because of consumption of active materials during energy storage. In the cycle number of 1 to 100, the capacity retention sharply drops due to the activation of the electrode material, while the capacity retention slows down after the cycle number of 100. The favorable capacitance retention retained 72.8% after 1000 cycles in a current density of 1 A g⁻¹. The good stability of the long-term cycle shows that it has considerable application prospects of electrodes for advance supercapacitor.

To evaluate the resistance of the nickel-based complex electrodes, an electrochemical impedance spectroscopy (EIS) was utilized. Figure 7 exhibits the Nyquist plots extracted from the EIS measurement on the nickel-based complex electrode in the frequency range of 0.01 Hz–10⁵ Hz. The inset image shows a Randles equivalent circuit and an enlarged picture of high-frequency curve, respectively. The impedance characteristics were simulated by ZsimpWin software. From the fitting data, it can be clearly obtained that the values of solution resistance (R_s) and charge-transfer resistance (R_{ct}) are 0.741 Ω and 0.0027 Ω , respectively, indicating a very low internal resistance charge-transfer resistance of the nickel-based complex electrode [36, 37].

3.3. Reaction Mechanism. From the electrochemical test results, the electrode is driven by a reversible Faraday

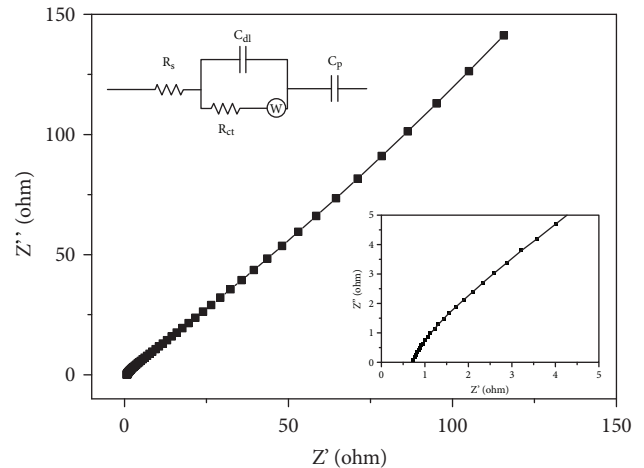


FIGURE 7: Complex plane impedance plots (Nyquist plots) of the nickel-based complex electrodes (inset: a Randles equivalent circuit, where R_s and R_{ct} are the solution and charge-transfer resistance, respectively. W , C_{dl} , and C_p are the Warburg resistance, electric double layer capacitance, and pseudocapacitive element; and an enlarged picture of high-frequency curve).

oxidation-reduction reaction. According to previous work [38–41], the mechanism might base on the following reactions:

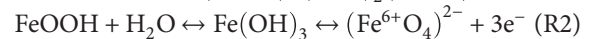
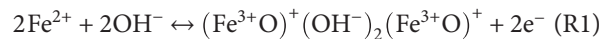


Figure 8 shows a conjecture diagram of the nickel-based complex electrode redox reaction. The nickel foam, as a good substrate material, is very suitable as the electrode of supercapacitors. In addition, the advantage of porous structure of the complex materials contains not only promoting electrolyte access and ion transport but also improving the contact opportunities between electrode material and electrolyte ion [42]. The synergy between the two materials might be one of the important reasons for the high electrochemical performance. The reasons mentioned above are the factors accounting for the high performance of the nickel-based complex electrode for the supercapacitor.

3.4. Performance Analysis of Asymmetrical Supercapacitors.

In order to obtain the complex materials in supercapacitor applications, the asymmetrical supercapacitors (ASCs) were fabricated using the zeolite capsule complex with Fe_3O_4 as positive electrodes and the AC as negative electrodes. Figure 9(a) shows the CV curve of the ASCs at different working cell potentials including 0 to 0.8, 0 to 1.0, 0 to 1.2, 0 to 1.4, and 0 to 1.5 V at 10 mV s⁻¹. Fortunately, there is an obvious H₂ or O₂ evolution switching potential indicating the excellent voltage range. As shown in Figure 9(b), this presents the CV curve of the cell at different scan rates from 5 to 100 mV s⁻¹ within a 0–1.5 V potential window. It can be clearly obtained that the energy storage was contributed via both capacitive (0–0.6 V) and faradaic (0.6–1.5 V) behavior. And it illustrates the good electrochemical reversibility and low internal resistance of the device [43]. The specific

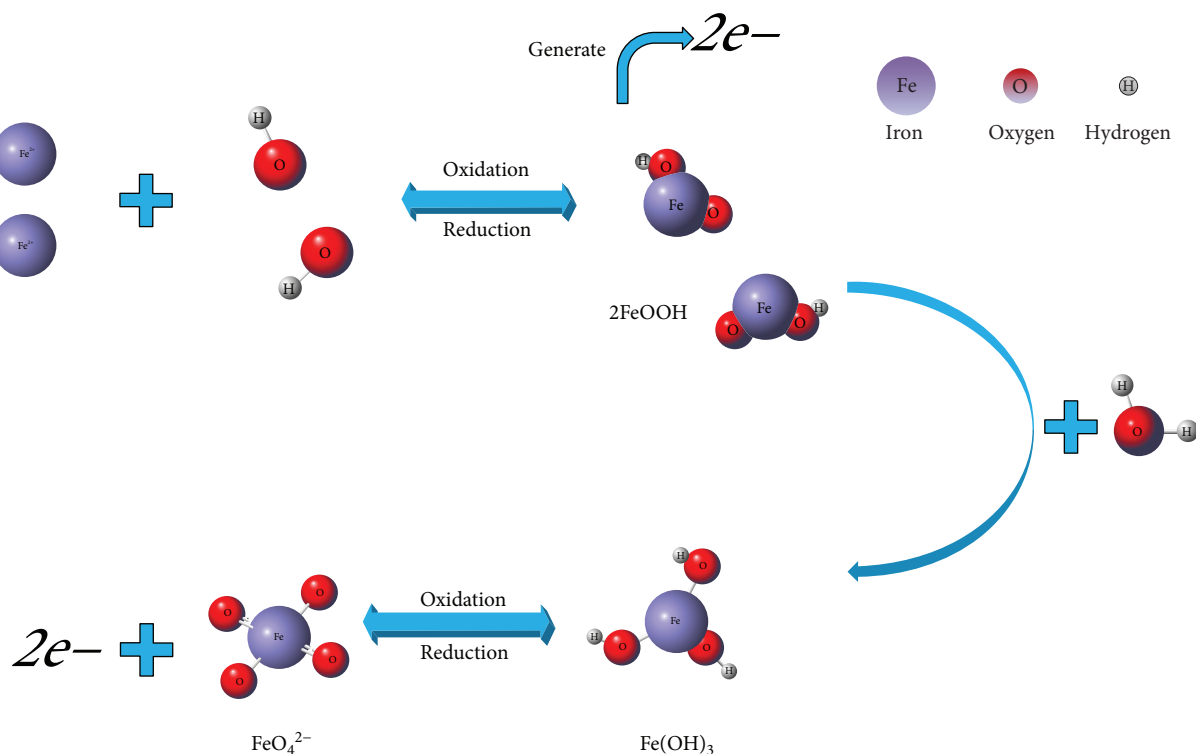


FIGURE 8: The conjecture mechanism of the Faraday oxidation-reduction reaction.

capacitance of the device was calculated using (1) and (2) at different scan rates in Figure 9(c). It can be seen that the ASCs exhibit a specific capacitance of about 105.9 F g^{-1} at 5 mV s^{-1} .

Figure 9(d) presents the GCD curve of the Ni-based complex//AC ASCs with cell voltage from 0 to 1.5 V at various current densities ($1\text{--}10 \text{ A g}^{-1}$). During the charge/discharge steps, the smaller IR or potential drop shows that the ASCs have less energy loss [44]. Unfortunately, the discharge time of the asymmetrical supercapacitor is slightly lesser than charge time. To observe the different current scanning rates of special capacitance changes, the mass specific capacitance of the nickel-based complex//AC ASCs at various current densities was calculated by (3) (Figure 9(e)). The specific capacitances of the ASCs at the current density of 1, 2, 3, 5, 8, and 10 A g^{-1} are 117.2, 97.1, 85.2, 69.5, 53.4, and 45.6 F g^{-1} , respectively. Further, the energy and power densities were calculated by (6) and (7), respectively. Figure 9(f) represents the variation of power density with energy density. The device transmits maximum energy density and power density of 36.6 Wh kg^{-1} and 916.1 W kg^{-1} , respectively.

Furthermore, the cyclic stability (Figure 10(a)) was carried up to 1000 cycles at current density of 1 A g^{-1} using 2 M KOH as the electrolyte. It is observed that the ASCs can keep 80.3% of initial capacitance over 1000 cycles, and the specific capacitance retention can remain stable after 550 cycles, which suggests that the ASCs display excellent stability. Finally, Figure 10(b) shows the impedance Nyquist plot of the ASC device from the fitted EIS data (the equivalent

circuit is the same as Figure 6). R_s and R_{ct} are 0.8046Ω and 0.05924Ω , respectively, indicating the low internal resistance and charge transfer resistance of the ASC device.

4. Conclusions

In this work, the mesoporous complex materials (the zeolite capsule complex with Fe_3O_4) with zeolite template capsule as the electrodes for supercapacitors were synthesized through suspension polymerization composite method and internal template method, respectively. The results showed that the high specific capacitance of the nickel-based complex electrode reaches as high as 739.8 F g^{-1} , and capacitance still retains 72.8% after 1000 cycles at current density of 1 A g^{-1} in 6 M KOH solution, indicating that the electrode materials have excellent electrochemical performances including high specific capacitance, excellent charge-discharge stability, good long-term cycling life, and small impedance. Moreover, the asymmetrical supercapacitors (ASCs) were fabricated using the zeolite capsule complex with Fe_3O_4 as positive electrodes and the AC as negative electrodes. It reveals high specific capacitance, outstanding energy density, and superb power density up to 117.2 F g^{-1} , 36.6 Wh kg^{-1} , and 916.1 W kg^{-1} at the current density of 1 A g^{-1} using 6 M KOH solution as electrolyte, respectively. Finally, the specific capacitance retains 80.3% after 1000 cycles at current density of 1 A g^{-1} in 2 M KOH solution, and the smaller internal impedance is obtained. It can be used as a promising electrode material for advanced supercapacitor.

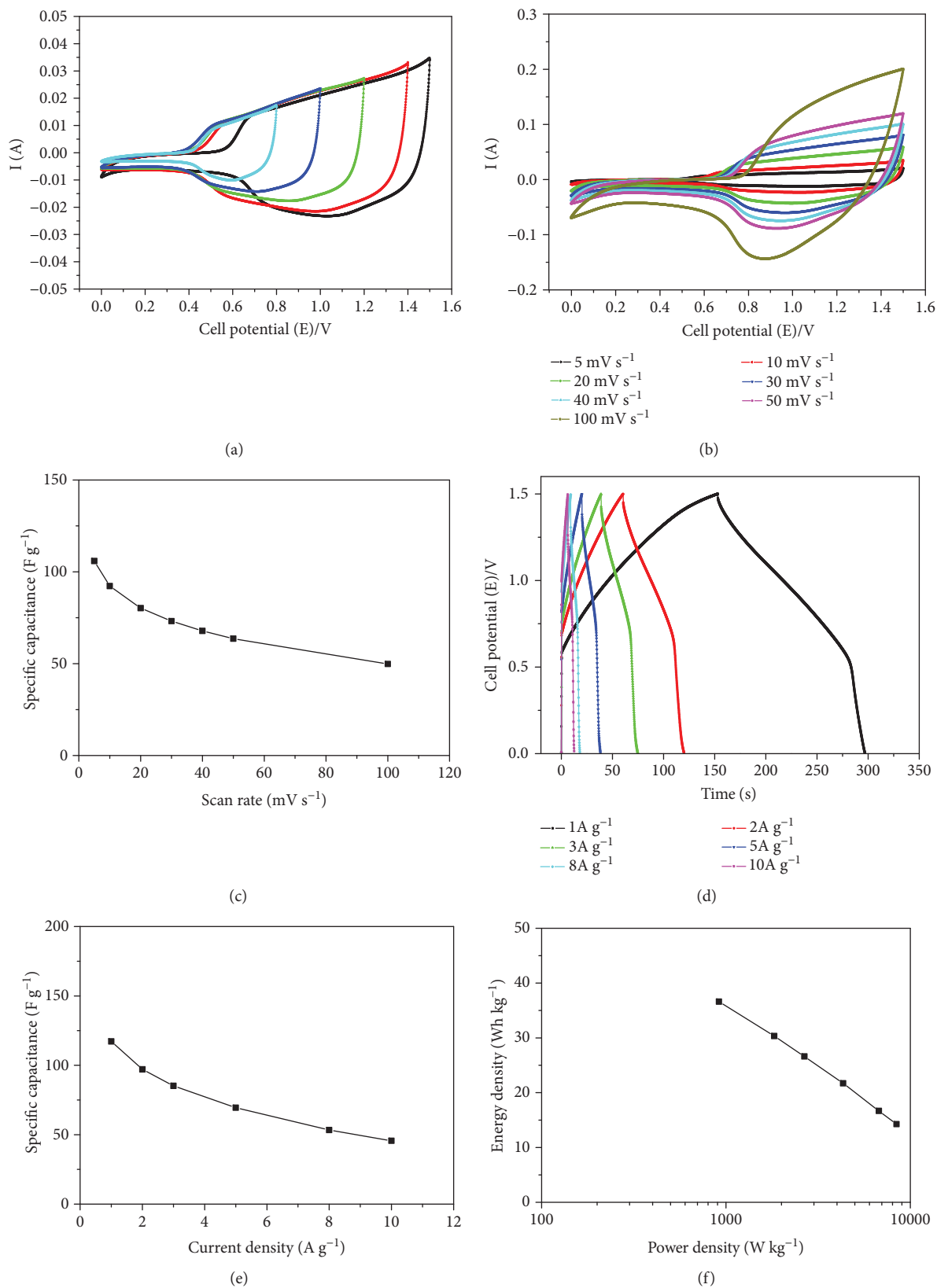


FIGURE 9: CV curve of the device (a) at different working potential window at 10 mV s^{-1} , (b) different scan rates, (c) variation of capacitance with scan rates, (d) GCD curves of the cell at various current densities, (e) specific capacitance at various current densities, and (f) Ragone plots of the energy and power densities of the device at various charge/discharge rates.

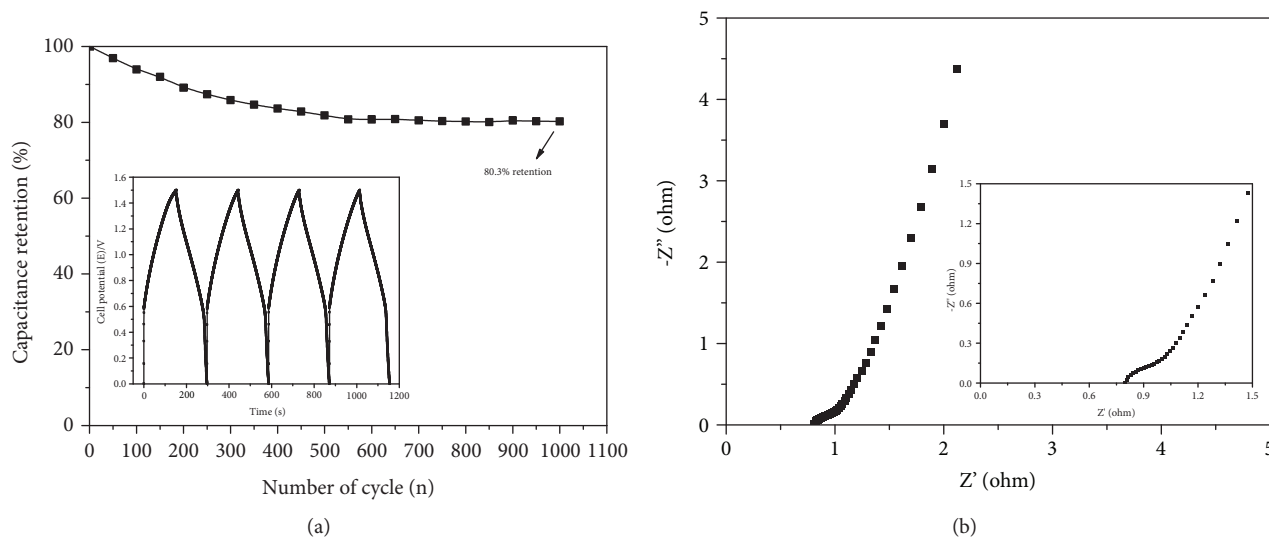


FIGURE 10: (a) The cycling performance of the device at 1 A g^{-1} for 1000 cycle and (b) Nyquist plots of the asymmetrical device.

Data Availability

The data used to support the findings of this study are available from the corresponding author upon request.

Conflicts of Interest

The authors declare no conflict of interest.

Authors' Contributions

LS was responsible for the original draft preparation and experimental implementation. YH was responsible for research ideas and scheme design. FG was responsible for review writing and grammar editing. YH and YL were responsible for the funding support. YJ and YL were responsible for characterization, and FG was responsible for the visualization. Lili Song and Yinghui Han contributed equally to this work.

Acknowledgments

This research was supported by the National Key R&D Plan (no. 2017YFC0210202-1), the Fundamental Research Funds for the Central Universities of China (no. 2015ZZD3), and the National Natural Science Foundation of China (no. 51308212).

References

- [1] N. Konikkara and L. J. Kennedy, "Electrochemical properties of solid leather wastes based supercapacitor electrodes using H_2SO_4 electrolyte," *Materials Letters*, vol. 205, pp. 56–61, 2017.
- [2] A. Eftekhari, "Supercapacitors utilising ionic liquids," *Energy Storage Materials*, vol. 9, pp. 47–69, 2017.
- [3] Y. Han, L. Li, Y. Liu, X. Li, X. Qi, and L. Song, "Fabrication of strontium bismuth oxides as novel battery-type electrode materials for high-performance supercapacitors," *Journal of Nanomaterials*, vol. 2018, Article ID 5078473, 10 pages, 2018.
- [4] P. Zhou, L. Fan, J. Wu, C. Gong, J. Zhang, and Y. Tu, "Facile hydrothermal synthesis of NiTe and its application as positive electrode material for asymmetrical supercapacitor," *Journal of Alloys and Compounds*, vol. 685, pp. 384–390, 2016.
- [5] G.-S. Jang, S. Ameen, M. S. Akhtar, and H.-S. Shin, "Cobalt oxide nanocubes as electrode material for the performance evaluation of electrochemical supercapacitor," *Ceramics International*, vol. 44, no. 1, pp. 588–595, 2018.
- [6] Y.-P. Gao, K.-J. Huang, H.-L. Shuai, and L. Liu, "Synthesis of sphere-feature molybdenum selenide with enhanced electrochemical performance for supercapacitor," *Materials Letters*, vol. 209, pp. 319–322, 2017.
- [7] Z. Wang, C. Ma, H. Wang, Z. Liu, and Z. Hao, "Facilely synthesized Fe_2O_3 -graphene nanocomposite as novel electrode materials for supercapacitors with high performance," *Journal of Alloys and Compounds*, vol. 552, no. 1, pp. 486–491, 2013.
- [8] B. Saravanakumar, K. K. Purushothaman, and G. Muralidharan, " V_2O_5 / nitrogen enriched mesoporous carbon spheres nanocomposite as supercapacitor electrode," *Microporous and Mesoporous Materials*, vol. 258, pp. 83–94, 2018.
- [9] J. Lv, Z. Wang, and H. Miura, "Facile synthesis of mesoporous NiO nanoflakes on graphene foam and its electrochemical properties for supercapacitor application," *Solid State Communications*, vol. 269, pp. 45–49, 2018.
- [10] W. Xing, F. Li, Z. Yan, and G. Q. Lu, "Synthesis and electrochemical properties of mesoporous nickel oxide," *Journal of Power Sources*, vol. 134, no. 2, pp. 324–330, 2004.
- [11] M.-J. Deng, J.-K. Chang, C.-C. Wang et al., "High-performance electrochemical pseudo-capacitor based on MnO_2 nanowires/Ni foam as electrode with a novel Li-ion quasi-ionic liquid as electrolyte," *Energy & Environmental Science*, vol. 4, no. 10, pp. 3942–3946, 2011.
- [12] L. Jiang, J. Yan, L. Hao, R. Xue, G. Sun, and B. Yi, "High rate performance activated carbons prepared from ginkgo shells for electrochemical supercapacitors," *Carbon*, vol. 56, no. 56, pp. 146–154, 2013.

- [13] H.-L. Jiang, B. Liu, Y.-Q. Lan et al., "From metal-organic framework to nanoporous carbon: toward a very high surface area and hydrogen uptake," *Journal of the American Chemical Society*, vol. 133, no. 31, pp. 11854–11857, 2011.
- [14] H. Li, L. McRae, C. J. Firby, M. al-Hussein, and A. Y. Elezzabi, "Nanohybridization of molybdenum oxide with tungsten molybdenum oxide nanowires for solution-processed fully reversible switching of energy storing smart windows," *Nano Energy*, vol. 47, pp. 130–139, 2018.
- [15] L.-Q. Mai, A. Minhas-Khan, X. Tian et al., "Synergistic interaction between redox-active electrolyte and binder-free functionalized carbon for ultrahigh supercapacitor performance," *Nature Communications*, vol. 4, no. 1, 2013.
- [16] X. Xiong, D. Ding, D. Chen et al., "Three-dimensional ultrathin Ni(OH)₂ nanosheets grown on nickel foam for high-performance supercapacitors," *Nano Energy*, vol. 11, pp. 154–161, 2015.
- [17] K. N. Hui, K. S. Hui, Z. Tang, V. V. Jadhav, and Q. X. Xia, "Hierarchical chestnut-like MnCo₂O₄ nanoneedles grown on nickel foam as binder-free electrode for high energy density asymmetric supercapacitors," *Journal of Power Sources*, vol. 330, pp. 195–203, 2016.
- [18] X. Qi, W. Zheng, G. He, T. Tian, N. Du, and L. Wang, "NiCo₂O₄ hollow microspheres with tunable numbers and thickness of shell for supercapacitors," *Chemical Engineering Journal*, vol. 309, pp. 426–434, 2017.
- [19] K. Vijaya Sankar and R. Kalai Selvan, "Fabrication of flexible fiber supercapacitor using covalently grafted CoFe₂O₄/reduced graphene oxide/polyaniline and its electrochemical performances," *Electrochimica Acta*, vol. 213, pp. 469–481, 2016.
- [20] C.-S. Dai, P.-Y. Chien, J.-Y. Lin et al., "Hierarchically structured Ni₃S₂/carbon nanotube composites as high performance cathode materials for asymmetric supercapacitors," *ACS Applied Materials & Interfaces*, vol. 5, no. 22, pp. 12168–12174, 2013.
- [21] D. Xiang, L. Yin, C. Wang, and L. Zhang, "High electrochemical performance of RuO₂-Fe₂O₃ nanoparticles embedded ordered mesoporous carbon as a supercapacitor electrode material," *Energy*, vol. 106, pp. 103–111, 2016.
- [22] W. Yang, Z. Gao, N. Song, Y. Zhang, Y. Yang, and J. Wang, "Synthesis of hollow polyaniline nano-capsules and their supercapacitor application," *Journal of Power Sources*, vol. 272, pp. 915–921, 2014.
- [23] Y. Obukuro, S. Matsushima, K. Obata et al., "Effects of La doping on structural, optical, electronic properties of Sr₂Bi₂O₅ photocatalyst," *Journal of Alloys and Compounds*, vol. 658, pp. 139–146, 2016.
- [24] Y. C. Zhang, H. Yang, W. P. Wang et al., "A promising supercapacitor electrode material of CuBi₂O₄ hierarchical microspheres synthesized via a coprecipitation route," *Journal of Alloys and Compounds*, vol. 684, pp. 707–713, 2016.
- [25] X. Li, J. Zhou, X. Li et al., "Bifunctional petaloid nickel manganese layered double hydroxides decorated on a freestanding carbon foam for flexible asymmetric supercapacitor and oxygen evolution," *Electrochimica Acta*, vol. 252, pp. 275–285, 2017.
- [26] J. Zhao, J. Chen, S. Xu et al., "Hierarchical NiMn layered double hydroxide/carbon nanotubes architecture with superb energy density for flexible supercapacitors," *Advanced Functional Materials*, vol. 24, no. 20, pp. 2938–2946, 2014.
- [27] W. Lu, R. Hartman, L. Qu, and L. Dai, "Nanocomposite electrodes for high-performance supercapacitors," *Journal of Physical Chemistry Letters*, vol. 2, no. 6, pp. 655–660, 2011.
- [28] M. Liu, J. Li, W. Han, and L. Kang, "Simple synthesis of novel phosphate electrode materials with unique microstructure and enhanced supercapacitive properties," *Journal of Energy Chemistry*, vol. 25, no. 4, pp. 601–608, 2016.
- [29] R. Holze, "Piero Zanello: inorganic electrochemistry: theory, practice and applications," *Journal of Solid State Electrochemistry*, vol. 10, no. 7, pp. 512–513, 2006.
- [30] D. Han, P. Xu, X. Jing et al., "Trisodium citrate assisted synthesis of hierarchical NiO nanospheres with improved supercapacitor performance," *Journal of Power Sources*, vol. 235, no. 4, pp. 45–53, 2013.
- [31] M. Yu, J. Chen, J. Liu et al., "Mesoporous NiCo₂O₄ nanoneedles grown on 3D graphene-nickel foam for supercapacitor and methanol electro-oxidation," *Electrochimica Acta*, vol. 151, pp. 99–108, 2015.
- [32] H. Chen, Y. Ai, F. Liu et al., "Carbon-coated hierarchical Ni-Mn layered double hydroxide nanoarrays on Ni foam for flexible high-capacitance supercapacitors," *Electrochimica Acta*, vol. 213, pp. 55–65, 2016.
- [33] L. Li, P. Gao, S. Gai et al., "Ultra small and highly dispersed Fe₃O₄ nanoparticles anchored on reduced graphene for supercapacitor application," *Electrochimica Acta*, vol. 190, pp. 566–573, 2016.
- [34] H. Xiao, S. Yao, H. Liu, F. Qu, X. Zhang, and X. Wu, "NiO nanosheet assembles for supercapacitor electrode materials," *Progress in Natural Science: Materials International*, vol. 26, no. 3, pp. 271–275, 2016.
- [35] J.-Y. Shieh, S.-Y. Tsai, B.-Y. Li, and H. H. Yu, "High-performance flexible supercapacitor based on porous array electrodes," *Materials Chemistry and Physics*, vol. 195, pp. 114–122, 2017.
- [36] T.-S. Hyun, H.-G. Kim, and I.-D. Kim, "Facile synthesis and electrochemical properties of conducting SrRuO₃-RuO₂ composite nanofibre mats," *Journal of Power Sources*, vol. 195, no. 5, pp. 1522–1528, 2010.
- [37] H. Yang, Z. Yang, X. Wen, and L. Liu, "The in-situ growth of zinc-aluminum layered double hydroxides on graphene and its application as anode active materials for Zn-Ni secondary battery," *Electrochimica Acta*, vol. 252, pp. 507–515, 2017.
- [38] X. Lv, G. Li, Z. Pang et al., "Fabricate BC/Fe₃O₄@PPy 3D nanofiber film as flexible electrode for supercapacitor application," *Journal of Physics and Chemistry of Solids*, vol. 116, pp. 153–160, 2018.
- [39] J. Chen, J. Qiu, B. Wang, H. Feng, K. Ito, and E. Sakai, "Fe₃O₄/biocarbon composites with superior performance in supercapacitors," *Journal of Electroanalytical Chemistry*, vol. 804, pp. 232–239, 2017.
- [40] S. G. Mohamed, S. Y. Attia, and H. H. Hassan, "Spinel-structured FeCo₂O₄ mesoporous nanosheets as efficient electrode for supercapacitor applications," *Microporous and Mesoporous Materials*, vol. 251, pp. 26–33, 2017.
- [41] A. Pendashteh, J. Palma, M. Anderson, and R. Marcilla, "Nanostructured porous wires of iron cobaltite: novel positive electrode for high-performance hybrid energy storage devices," *Journal of Materials Chemistry A*, vol. 3, no. 32, pp. 16849–16859, 2015.

- [42] Y. Zhang, S. Yu, G. Lou et al., "Review of macroporous materials as electrochemical supercapacitor electrodes," *Journal of Materials Science*, vol. 52, no. 19, pp. 11201–11228, 2017.
- [43] K. Vijaya Sankar and R. Kalai Selvan, "Improved electrochemical performances of reduced graphene oxide based supercapacitor using redox additive electrolyte," *Carbon*, vol. 90, pp. 260–273, 2015.
- [44] Q. X. Xia, K. San Hui, K. N. Hui et al., "Facile synthesis of manganese carbonate quantum dots/Ni(HCO₃)₂-MnCO₃ composites as advanced cathode materials for high energy density asymmetric supercapacitors," *Journal of Materials Chemistry A*, vol. 3, no. 44, pp. 22102–22117, 2015.

Research Article

Study of a Microbistable Piezoelectric Energy Harvesting

Li Hua Chen , Shou Jie Cui , Shuo Yang , and Wei Zhang 

College of Mechanical Engineering, Beijing University of Technology, Beijing 100124, China

Correspondence should be addressed to Li Hua Chen; lihuachenli@yahoo.com

Received 6 June 2018; Revised 30 August 2018; Accepted 17 September 2018; Published 16 December 2018

Guest Editor: Zhengping Zhou

Copyright © 2018 Li Hua Chen et al. This is an open access article distributed under the Creative Commons Attribution License, which permits unrestricted use, distribution, and reproduction in any medium, provided the original work is properly cited.

A microbistable piezoelectric energy harvester has been developed. The harvester was based on a center-fixed and quadrilateral-free microbistable plate with mass blocks placed at the four corners. Considering the thermoelectromechanical coupling effect, a nonlinear oscillation differential equation was established by Hamilton's principle. Strain gradient theory was applied to consider the size effect, and von Karman theory was used to consider the large deformation effect. The influences of the laying position and area of the piezoelectric layer on the efficiency of energy capture were investigated. The voltage-frequency response of the nonlinear system was investigated, and the snap-through behavior of the bistable plate results in energy harvesting achieving the ideal broaden frequency range before the resonance region.

1. Introduction

Piezoelectric energy harvesters are devices that convert ambient environmental vibration into electrical energy by absorbing ambient vibrations. The bistable plate can trigger snap-through by overcoming the critical load to realize large amplitude oscillations. Therefore, piezoelectric energy harvesting with the characteristics of a bistable plate can improve the energy harvesting efficiency [1]. With the development of microelectromechanical system (MEMS) technology, the size of wireless sensors is simultaneously becoming smaller. To cope with the trend of miniaturization, piezoelectric energy harvesters that provide energy for wireless sensors often tend to be miniaturized [2].

In recent years, bistable piezoelectric energy harvesting has been widely explored. The nonlinear behavior of the bistable plate, such as chaos and the transition between the two steady states, is used to drive the piezoelectric plate to achieve broadband vibration in the nonresonant frequency environment. In 2010, Arrieta et al. [1] proposed a bistable composite laminate with four attached piezoelectric patches and an asymmetric set-up to capture energy in broadband frequency. They found that high energy conversion can be obtained with snap-through between the stable states. In 2012, Betts et al. [3] used an electrical function to study the effects of the aspect ratio, thickness, stacking sequence, and

piezoelectric area on the efficiency of energy capture. In 2013, Betts et al. [4] continued their previous experimental work to understand the dynamic response of the structure, and they used high-speed digital image correlation to identify the dynamic modes and study the energy capture characteristics. Experiments showed that the large deformation caused by snap-through improves the efficiency of energy capture. In 2015, Syta et al. [5] experimentally identified the dynamics of the system response by generated voltage time series, and the frequency spectrum, bifurcation diagrams, and phase portraits were investigated. In 2016, Syta et al. [6] used nonlinear time series analysis methods of the Fourier spectrum and recurrence quantification analysis to experimentally investigate the dynamic response of energy harvesting and relational capturing energy generation.

With the development of MEMS technology, the microbistable structure has been widely investigated. In 2010, Andò et al. [7] considered the nonlinear behavior of a bistable cantilever beam to broaden the spectrum and lower the frequency. They then performed a numerical study based on stochastic differential equations to evaluate the behavior of a MEMS device. In 2016, Medina et al. [8, 9] demonstrated dynamic snap-through of micromechanically initially curved beam structures under electrostatic actuation. Experimental and theoretical results showed that snap-through motion can be achieved by tailored time-dependent electrostatic

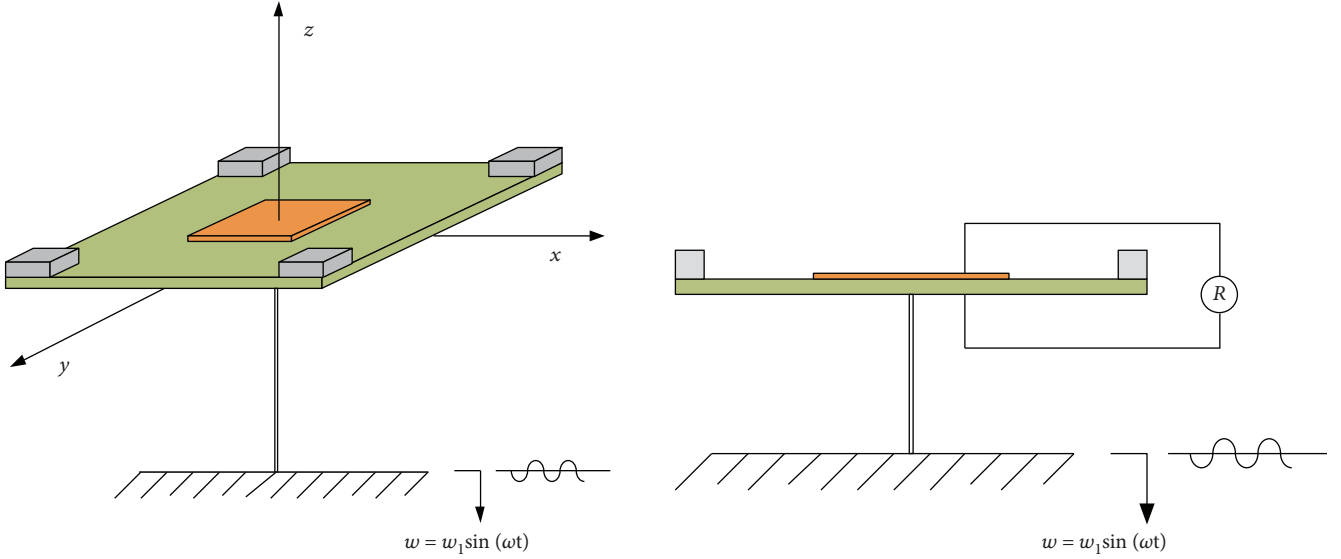


FIGURE 1: The energy harvesting structure diagram.

actuation. In the same year, this group constructed a model of a microscale circular curved bistable plate and investigated its reliability, accuracy, and suitability. By applying reasonable low voltages, the actuation feasibility of a microbistable plate with realistic dimensions was demonstrated.

Most reports have discussed triggering of snap-through in macroscale bistable plates. However, few studies have described the snap-through behavior in microscale plates for energy harvesting. In this study, we investigated the effects of the laying position, area, and thickness of the piezoelectric layer on the efficiency of piezoelectric energy harvesting for microbistable piezoelectric energy harvesting. The unique snap-through behavior of the bistable plate was investigated, and several wide frequency ranges were discovered.

2. Device Modeling

With the aim of microbistable piezoelectric energy harvesting, the four corners of the base layer were covered with mass blocks and the pedestal provides harmonic excitation: $w = w_1 \cdot \sin(\omega t)$, where w_1 is the amplitude and ω is the vibration frequency, as shown in Figure 1.

The displacements of any point in the x , y , and z directions are

$$\begin{aligned} u(x, y, z, t) &= u_0(x, y, t) - z \cdot \frac{\partial w}{\partial x}, \\ v(x, y, z, t) &= v_0(x, y, t) - z \cdot \frac{\partial w}{\partial y}, \\ w(x, y, t) &= w_0(x, y, t) + w_1 \sin(\omega t), \end{aligned} \quad (1)$$

where u_0 , v_0 , and w_0 are the displacements of any point on the neutral surface in the x , y , and z directions.

According to von Karman's large deformation theory, the nonlinear strain expressions are given by

$$\begin{aligned} \varepsilon_{xx} &= \frac{\partial u}{\partial x} + \frac{1}{2} \left(\frac{\partial w}{\partial x} \right)^2, \\ \varepsilon_{yy} &= \frac{\partial v}{\partial y} + \frac{1}{2} \left(\frac{\partial w}{\partial y} \right)^2, \\ \gamma_{xy} &= \frac{\partial u}{\partial y} + \frac{\partial v}{\partial x} + \frac{\partial w}{\partial x} \cdot \frac{\partial w}{\partial y}. \end{aligned} \quad (2)$$

The stress expressions for the base layer are obtained from the constitutive relation:

$$\begin{aligned} \sigma_{xx}^S &= \frac{E_S}{1 - \nu_S^2} ((\varepsilon_{xx} - \alpha_S \cdot \Delta T) + \nu_S (\varepsilon_{yy} - \alpha_S \cdot \Delta T)), \\ \sigma_{yy}^S &= \frac{E_S}{1 - \nu_S^2} ((\varepsilon_{yy} - \alpha_S \cdot \Delta T) + \nu_S (\varepsilon_{xx} - \alpha_S \cdot \Delta T)), \\ \tau_{xy}^S &= \frac{E_S}{2(1 + \nu_S)} \cdot \gamma_{xy}. \end{aligned} \quad (3)$$

Similarly, the piezoelectric layer stress expressions are defined as

$$\begin{aligned} \sigma_{xx}^P &= \frac{E_P}{1 - \nu_P^2} ((\varepsilon_{xx} - \alpha_P \cdot \Delta T) + \nu_P (\varepsilon_{yy} - \alpha_P \cdot \Delta T)), \\ \sigma_{yy}^P &= \frac{E_P}{1 - \nu_P^2} ((\varepsilon_{yy} - \alpha_P \cdot \Delta T) + \nu_P (\varepsilon_{xx} - \alpha_P \cdot \Delta T)), \\ \tau_{xy}^P &= \frac{E_P}{2(1 + \nu_P)} \cdot \gamma_{xy}, \end{aligned} \quad (4)$$

where E is the elastic modulus, ν is Poisson's ratio, α is the thermal expansion coefficient, h_p is the thickness of the piezoelectric layer, e_{31} and e_{32} are the piezoelectric coefficients,

V is the electric potential, superscript S represents the base layer, subscript P represents the piezoelectric layer, and ΔT is the temperature change between the processing and normal operating temperatures. All of the MEMS manufacturing processes, such as sputtering [10], deposition [11], and the sol-gel [12] method, involved high-temperature processing. The difference between the thermal expansion coefficients of the piezoelectric layer and base layer leads to the generation of the original thermal stress.

Suppose that displacements at any point in the middle plane were expressed by

$$\begin{aligned} u_0(x, y) &= d_1x + d_2xy^2 + d_3x^3 + d_4xy^4 + d_5x^3y^2 + d_5x^5, \\ v_0(x, y) &= d_7y + d_8xy^2 + d_9x^3 + d_{10}xy^4 + d_{11}x^3y^2 + d_{12}x^5, \\ w_0 &= \frac{1}{2}(ax^2 + by^2), \end{aligned} \quad (5)$$

where d_i ($i = 1, 2, \dots, 12$) are undetermined coefficients with time t and a and b are the curvatures along the x and y directions, respectively.

The total strain energy within the microplate is composed of two parts. One part is based on the classical continuum mechanics theory and can be expressed as

$$\begin{aligned} U_S^h &= \iiint_{V_S} \frac{1}{2} \left(\sigma_{xx}^S \cdot \varepsilon_{xx} + \sigma_{yy}^S \cdot \varepsilon_{yy} + \tau_{xy}^S \cdot \gamma_{xy} \right) dx dy dz, \\ U_P^h &= \iiint_{V_P} \frac{1}{2} \left(\sigma_{xx}^P \cdot \varepsilon_{xx} + \sigma_{yy}^P \cdot \varepsilon_{yy} + \tau_{xy}^P \cdot \gamma_{xy} \right) dx dy dz. \end{aligned} \quad (6)$$

Based on the strain gradient theory proposed by Mindlin, η_{ijk} ($i, j, k = x, y, z$), and the other part can be expressed as

$$\begin{aligned} U_S^w &= \iiint_{V_S} \left(L_1^S \cdot \eta_{iik} \cdot \eta_{kjj} + L_2^S \cdot \eta_{ijj} \cdot \eta_{ikk} + L_3^S \cdot \eta_{iik} \cdot \eta_{jjk} \right. \\ &\quad \left. + L_4^S \cdot \eta_{ijk} \cdot \eta_{ijk} + L_5^S \cdot \eta_{ijk} \cdot \eta_{kji} \right) dx dy dz, \\ U_P^w &= \iiint_{V_P} \left(L_1^P \cdot \eta_{iik} \cdot \eta_{kjj} + L_2^P \cdot \eta_{ijj} \cdot \eta_{ikk} + L_3^P \cdot \eta_{iik} \cdot \eta_{jjk} \right. \\ &\quad \left. + L_4^P \cdot \eta_{ijk} \cdot \eta_{ijk} + L_5^P \cdot \eta_{ijk} \cdot \eta_{kji} \right) dx dy dz, \end{aligned} \quad (7)$$

where L_i^ξ ($i = 1, 2, \dots, 5$) are the material parameters. The reference value for each material parameter has been obtained by Ramezani [13]:

$$\begin{aligned} L_2^\xi &= \frac{1}{2} l_\xi^2 \lambda_\xi, \\ L_4^\xi &= l_\xi^2 \mu_\xi, \\ L_1^\xi &= L_3^\xi = L_5^\xi = 0, \\ \xi &= S, P, \end{aligned} \quad (8)$$

where l_ξ is the internal length scale parameter depending on the specific material and λ_ξ and μ_ξ are the common Lamé constants:

$$\begin{aligned} \lambda_\xi &= \frac{E_\xi \nu_\xi}{(1 - 2\nu_\xi)(1 + \nu_\xi)}, \\ \mu_\xi &= \frac{E_\xi}{2(1 + \nu_\xi)}, \\ \xi &= S, P. \end{aligned} \quad (9)$$

The potential energy of the system U consists of two parts:

$$U = U_S^h + U_P^h + U_S^w + U_P^w. \quad (10)$$

Because the kinetic energies in the x and y directions are small compared with that in the z direction, they can be ignored [4]. The kinetic energy expression of the structure is

$$T_1 = \iiint_{V_S} \frac{\rho_S}{2} \dot{w}^2 dV_S + \iiint_{V_P} \frac{\rho_P}{2} \dot{w}^2 dV_P, \quad (11)$$

where ρ_S and ρ_P are the densities of each layer of material.

The kinetic energy of the mass block is

$$T_2 = \frac{1}{2} (M_1 \dot{w}_{c1}^2 + M_2 \dot{w}_{c2}^2 + M_3 \dot{w}_{c3}^2 + M_4 \dot{w}_{c4}^2), \quad (12)$$

where \dot{w}_{ci} ($i = 1, \dots, 4$) are the displacement of the four corner points and M_i is the mass of the mass block.

The total kinetic energy of the system is

$$T = T_1 + T_2. \quad (13)$$

The virtual work done by the damping force is

$$\delta W = -\iiint_{V_S} r_S \dot{w} \delta w dV_S - \iiint_{V_P} r_P \dot{w} \delta w dV_S, \quad (14)$$

where r_S and r_P are the damping coefficients.

Because the sizes of the piezoelectric layer in the length and width directions are much larger than those in the thickness direction and the polarization direction is along the thickness direction, the electric displacement D_3 in the thickness direction is much larger than the electric displacement in the other two directions (D_1 and D_2). Thus, D_1 and D_2 can be ignored and D_3 can be expressed as

$$D_3 = e_{31} \varepsilon_{xx} + e_{32} \varepsilon_{yy} - \varepsilon_{33} \frac{V}{h_p}, \quad (15)$$

where V is the electric potential and ε_{33} is the dielectric constant.

Because the electric displacement D_3 does not change with the thickness, the above equation is subjected to homogenization in the thickness direction:

$$\tilde{D}_3 = \frac{\int_{h/2}^{h/(2+h_p)} (e_{31}\varepsilon_{xx} + e_{32}\varepsilon_{yy} - \varepsilon_{33}(V/h_p)) dz}{h_p}. \quad (16)$$

The charge on the electrode can be obtained as follows:

$$Q = -\iint_{\Omega_p} \tilde{D}_3 dx dy = -\frac{1}{h_p} \int_{V_p} \left(e_{31}\varepsilon_{xx} + e_{32}\varepsilon_{yy} - \varepsilon_{33} \frac{V}{h_p} \right) dV_p. \quad (17)$$

According to the generated charge, the current can be obtained by

$$I = -\frac{\partial Q}{\partial t} = \frac{1}{h_p} \int_{V_p} \left(e_{31}\dot{\varepsilon}_{xx} + e_{32}\dot{\varepsilon}_{yy} - \varepsilon_{33} \frac{\dot{V}}{h_p} \right) dV_p. \quad (18)$$

When the external resistance is set to R , the current is

$$I = \frac{V}{R}. \quad (19)$$

From Eqs. (18) and (19), we can obtain

$$-\frac{\partial Q}{\partial t} = \frac{V}{R}. \quad (20)$$

That is,

$$\frac{1}{h_p} \int_{V_p} \left(e_{31}\dot{\varepsilon}_{xx} + e_{32}\dot{\varepsilon}_{yy} - \varepsilon_{33} \frac{\dot{V}}{h_p} \right) dV_p = \int_{V_p} \frac{V}{RV_p} dV_p. \quad (21)$$

The electric equation can be obtained by

$$\dot{V} = \frac{(e_{31}\dot{\varepsilon}_{xx} + e_{32}\dot{\varepsilon}_{yy} - (h_p V/RV_p))h_p}{\varepsilon_{33}}. \quad (22)$$

Substituting the variation of the kinetic energy and potential energy and the virtual force of the damping force into Hamilton's principle gives

$$\int_{T_0}^{T_1} (\delta U - \delta T + \delta W) dt = 0, \quad (23)$$

where t_1 and t_2 are the initial and final moments of the system movement, respectively. The equations about a , b , and d_i can be obtained by Eq. (23). d_i is about the algebraic equation of a and b , which can be expressed in terms of a

and b . By substituting d_i into the first two equations, the system dynamics differential equation can be obtained:

$$\begin{aligned} \ddot{a} = & -m_1 a + m_2 b - m_3 a^2 + m_4 b^2 + m_5 ab + m_6 a^2 b - m_7 ab^2 \\ & + m_8 a \Delta T - m_9 b \Delta T - m_{10} a V + m_{11} b V_1 - m_{12} \Delta T \\ & + m_{13} V - m_{14} r_p \omega \cos(\omega t) - m_{15} r_s \omega \cos(\omega t) \\ & - m_{16} r_p \dot{a} - m_{17} r_s \dot{a} + m_{18} r_p \dot{b} + m_{19} r_s \dot{b} + m_{20} \omega^2 \sin(\omega t), \\ \ddot{b} = & n_1 a - n_2 b + n_3 a^2 - n_4 b^2 + n_5 ab - n_6 a^2 b + n_7 ab^2 \\ & - n_8 a \Delta T + n_9 b \Delta T + n_{10} a V - n_{11} b V + n_{12} \Delta T - n_{13} V \\ & - n_{14} r_p \omega \cos(\omega t) - n_{15} r_s \omega \cos(\omega t) + n_{16} r_p \dot{a} + n_{17} r_s \dot{a} \\ & - n_{18} r_p \dot{b} - n_{18} r_p \dot{b} - n_{19} r_s \dot{b} + n_{20} \omega^2 \sin(\omega t), \end{aligned} \quad (24)$$

where m_i ($i = 1 - 20$) and n_i ($i = 1 - 20$) are the coefficients determined by the material and size parameters.

Equation (24) is connected to electrical Eq. (22) to form a dynamic model for microbistable piezoelectric energy harvesting.

3. Study on the Efficiency of Capturing Energy

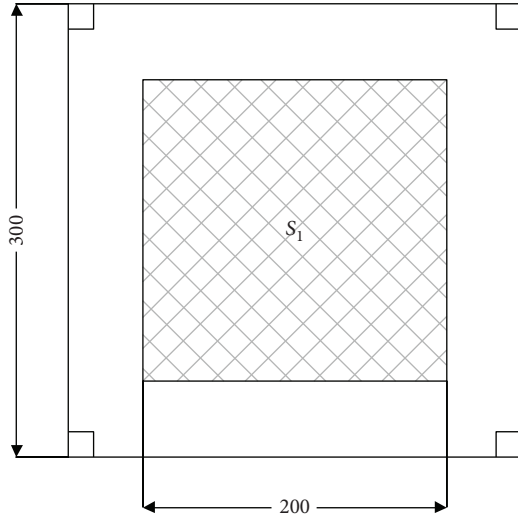
To improve the efficiency of energy capture, the effects of the laying position, area, and thickness on the efficiency of the piezoelectric energy were investigated.

3.1. Selection of Layout Location. In this section, we discuss the generated voltage of two types of laying positions. Piezoelectric layers of type I and type II are shown in Figure 2. The size of the base layer is $300 \mu\text{m} \times 300 \mu\text{m} \times 0.7 \mu\text{m}$, and the size of the piezoelectric layer is $200 \mu\text{m} \times 200 \mu\text{m} \times 0.7 \mu\text{m}$, where $S_1 = S_{2-1} + S_{2-2} + S_{2-3} + S_{2-4}$.

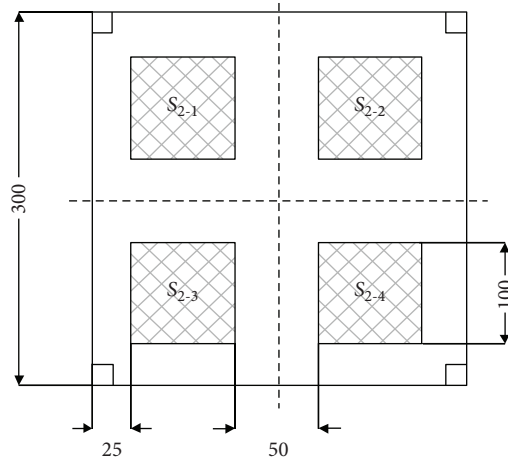
The material parameters of the two layers are given in Table 1. The piezoelectric layer material is polyvinylidene fluoride, whose elastic modulus is much smaller than that of the base layer. In scanning the vibration frequency of the pedestal ω , the variation of the voltage with the frequency is obtained (Figure 3).

From Figure 3, for the same excitation and laying area, the natural frequency of type I is lower than that of type II and the peak value of the capturing voltage under the natural frequency is about twice as high as that of type II. This is because under the boundary conditions of center-fixed quadrilateral free, the closer to the center, the greater the strain. To clearly observe the elliptical part of the graph, a local enlarged plot is shown in Figure 3. Therefore, the laying position in the middle has better energy capturing efficiency than at the four sides. Thus, we select type I for the ideal laying position.

3.2. Influence of Thickness and Area of Piezoelectric Layer. In this section, the thickness and area of the piezoelectric layer are discussed for type I when the temperature decreases from the high MEMS processing temperature to room temperature; that is, $\Delta T = -400^\circ\text{C}$. Using I and II laying types, we investigated the influence of the piezoelectric layer area on



(a) Type I



(b) Type II

FIGURE 2: Type I and type II piezoelectric laying position.

TABLE 1: Material coefficients.

Physical quantity	Value
E_S	190 Gpa
E_P	2.1 Gpa
ν_S	0.2788
ν_P	0.31
α_S	$3 \cdot 10^{-5} / ^\circ C$
α_P	$2.5 \cdot 10^{-6} / ^\circ C$
e_{31}	$2C \cdot m^2$
e_{32}	$2C \cdot m^2$
ϵ_{33}	$6500\epsilon_0$
ρ_S	2300 kg/m^2
ρ_P	5670 kg/m^2

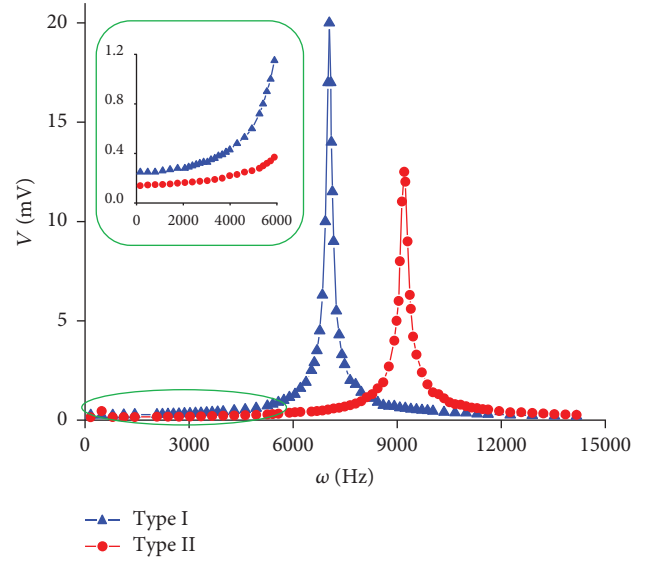


FIGURE 3: Type I and type II capture voltage versus stimulated frequency.

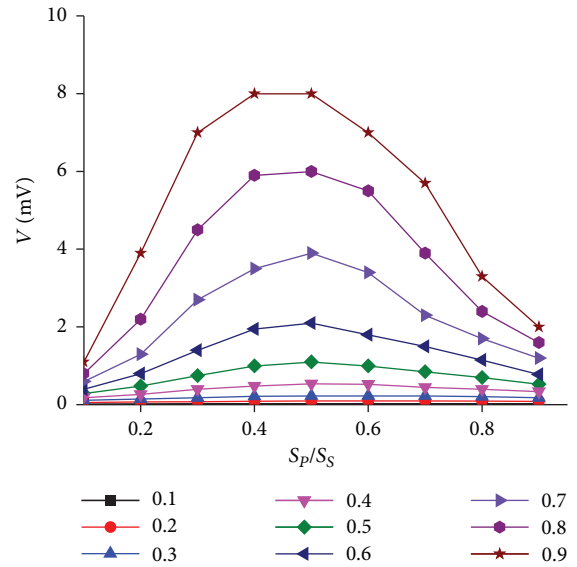


FIGURE 4: The thickness effect of the layout area on device efficiency.

the energy efficiency of the piezoelectric layer thickness in the range of 0.1–0.9 (Figure 4).

From Figure 4, for the same piezoelectric layer area, the efficiency of energy capture increases with increasing thickness. This is because a thicker piezoelectric layer results in more charge generation and higher capturing voltage. For the same piezoelectric layer thickness, the efficiency of energy capture first increases and then decreases with the increasing area of the piezoelectric layer. In this study, the elastic modulus of the piezoelectric layer is much smaller than that of the base layer. In the initial stage of the increase of the piezoelectric layer area ($0.1 < S_p/S_s < 0.5$), the thermoelectromechanical coupling effect is greater than the effect of

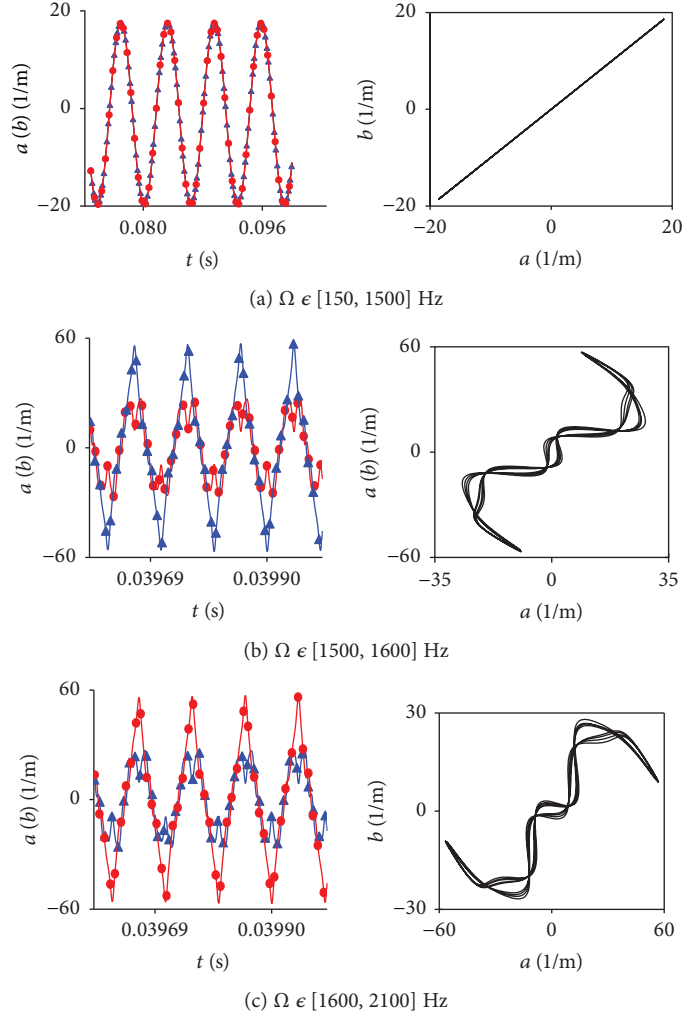


FIGURE 5: Waveform and phase diagrams of a (red circle) and b (blue triangle) in case of no snap-through.

the increased stiffness. As the area increases in the range ($0.5 < S_p/S_S < 0.9$), the increased stiffness effect becomes dominant, system deflection begins to decrease, and the capturing energy efficiency decreases.

4. Nonlinear Frequency Responses

From the above results, type I energy harvesting is best when the area of the piezoelectric patch is 0.5 times the base area and $\Delta T = -400^\circ\text{C}$. Although the efficiency of energy capture increases with the increasing thickness of the piezoelectric layer, the layer cannot be too thick because the stiffness of the structure will increase and deflection will decrease, ultimately leading to lower efficiency of energy capture and snap-through being difficult to achieve. Thus, the thickness is set at $0.7 \mu\text{m}$.

In this section, we discuss the effect of the snap-through behavior of the bistable plate on the efficiency of energy capture. By fixing the excitation amplitude and scanning the frequency, we obtained the waveforms and phase diagrams of a and b (the curvatures in the x and y directions). These waveforms and phase diagrams reveal that the various snap-through behaviors existing in different frequency

regions allow the system to obtain multiple wide-band energy capture regions before the resonant region.

From Figure 5(a), when the excitation frequency is between 150 and 1500 Hz, the curvatures of the plate in the x and y directions are always the same ($a = b$) and no snap-through behavior occurs. When the frequency is between 1500 and 1600 Hz, the plate is in the state $b > a$ (Figure 5(b)), no snap-through occurs, and the amplitude is small. No snap-through also occurs in the frequency range 1600–2100 Hz, and the plate is in the state $a > b$, as shown in Figure 5(c). However, with increasing frequency, two types of snap-through behavior occur. (1) The states $a > b$ and $a < b$ alternately appear, and there is continuous snap-through behavior, as shown in Figure 6(a). (2) Successive conversion of the two stable states $a = 0$ and $b = 0$ causes large amplitude vibration and enhances the efficiency of energy harvesting, as shown in Figure 6(b). When the excitation frequency is between 2200 and 3100 Hz, no snap-through behavior occurs. The waveform and phase diagram are shown in Figure 5(a).

For microscale energy harvesting, the fundamental frequency is so high that the frequency of vibration in the ambient environment cannot reach the natural frequency

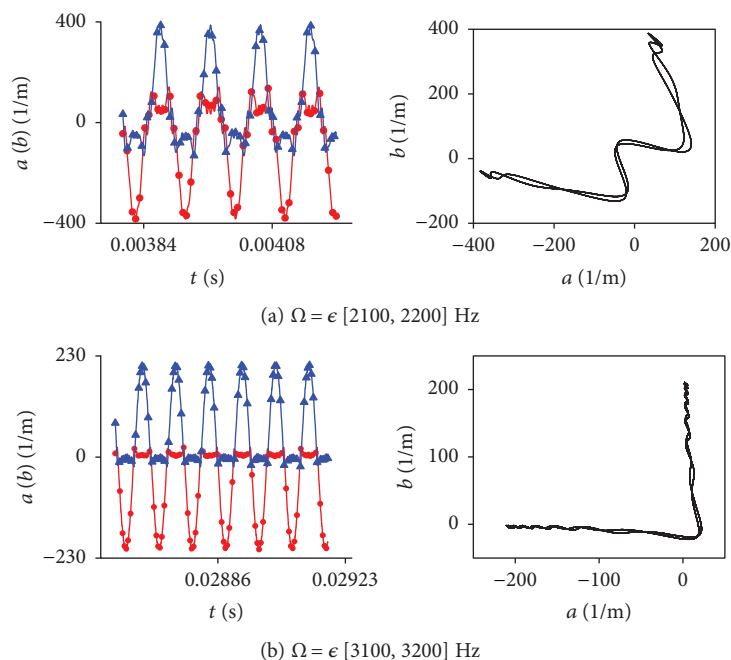


FIGURE 6: Waveform and phase diagrams of a (red circle) and b (blue triangle) in case of snap-through.

and excite resonance. For bistable energy harvesting with the mass block proposed in this paper, although the mass block reduces the natural frequency of the structure, the resonant frequency (6.3 kHz) is also too high compared with the ambient vibration frequency. Therefore, in this study, we make use of the characteristic of large amplitude vibration caused by the snap-through behavior to capture high voltage in several wide frequency ranges far from the resonance region.

To describe the influence of the snap-through behavior of the microbistable plate on the captured voltage, the frequency is plotted against the voltage in Figure 7. The figure shows that $1/3$ and $1/2$ subharmonic resonances occur when the ambient vibration frequency ω is close to $1/3$ and $1/2$ times the natural frequency of the microscale bistable energy harvester. There are two types of snap-through phenomena: (1) in the $1/3$ subharmonic resonance region (\times), continuous snap-through behavior occurs, as shown in Figure 6(a). (2) In the $1/2$ subharmonic resonance region (\bullet), the two stable states $a=0$ and $b=0$ alternatively occur, as shown in Figure 6(b). The snap-through behavior can produce a higher output voltage and wider bandwidth at a lower frequency, which is crucial for a microscale bistable energy harvester.

5. Conclusion

Considering the size effect, the strain gradient theory is extended to the nonlinear problem of microbistable piezoelectric energy harvesting. Based on the dynamic model established in this paper, a microbistable energy harvester structure was obtained by theoretical analysis. With increasing ambient vibration frequency, the snap-through phenomenon occurs for the microscale bistable energy harvester. Furthermore, the effect of the snap-through behavior on the

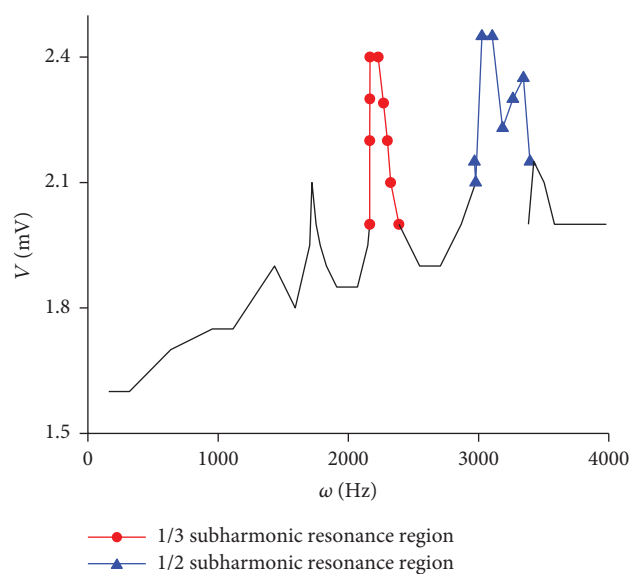


FIGURE 7: Voltage frequency response curve.

capturing energy efficiency was investigated, and the aim of capturing more energy in several wide frequency ranges far from the resonance region was realized.

Data Availability

The data used to support the findings of this study are available from the corresponding author upon request.

Conflicts of Interest

The authors declare that they have no conflicts of interest.

Acknowledgments

The authors wish to express their gratitude for the supports provided by the National Natural Science Foundation of China under Grant no. 11472019 for this research work.

References

- [1] A. F. Arrieta, P. Hagedorn, A. Erturk, and D. J. Inman, "A piezoelectric bistable plate for nonlinear broadband energy harvesting," *Applied Physics Letters*, vol. 97, no. 10, article 104102, 2010.
- [2] M. W. Hyer, "Some observations on the cured shape of thin unsymmetric laminates," *Journal of Composite Materials*, vol. 15, no. 2, pp. 175–194, 1981.
- [3] D. N. Betts, H. A. Kim, C. R. Bowen, and D. J. Inman, "Optimal configurations of bistable piezo-composites for energy harvesting," *Applied Physics Letters*, vol. 100, no. 11, article 114104, 2012.
- [4] D. N. Betts, C. R. Bowen, H. A. Kim, N. Gathercole, C. T. Clarke, and D. J. Inman, "Nonlinear dynamics of a bistable piezoelectric-composite energy harvester for broadband application," *The European Physical Journal Special Topics*, vol. 222, no. 7, pp. 1553–1562, 2013.
- [5] A. Syta, C. R. Bowen, H. A. Kim, A. Rysak, and G. Litak, "Experimental analysis of the dynamical response of energy harvesting devices based on bistable laminated plates," *Meccanica*, vol. 50, no. 8, pp. 1961–1970, 2015.
- [6] A. Syta, C. R. Bowen, H. A. Kim, A. Rysak, and G. Litak, "Responses of bistable piezoelectric-composite energy harvester by means of recurrences," *Mechanical Systems and Signal Processing*, vol. 76–77, pp. 823–832, 2016.
- [7] B. Andò, S. Baglio, C. Trigona, N. Dumas, L. Latorre, and P. Nouet, "Nonlinear mechanism in MEMS devices for energy harvesting applications," *Journal of Micromechanics and Microengineering*, vol. 20, no. 12, article 125020, 2010.
- [8] L. Medina, R. Gilat, B. R. Ilic, and S. Krylov, "Experimental dynamic trapping of electrostatically actuated bistable micro-beams," *Applied Physics Letters*, vol. 108, no. 7, article 073503, 2016.
- [9] L. Medina, R. Gilat, and S. Krylov, "Bistable behavior of electrostatically actuated initially curved micro plate," *Sensors and Actuators A: Physical*, vol. 248, no. 208, pp. 193–198, 2016.
- [10] A. Toprak and O. Tigli, "MEMS scale PVDF-TrFE-based piezoelectric energy harvesters," *Journal of Microelectromechanical Systems*, vol. 24, no. 6, pp. 1989–1997, 2015.
- [11] C. T. Pan, Z. H. Liu, Y. C. Chen, and C. F. Liu, "Design and fabrication of flexible piezo-microgenerator by depositing ZnO thin films on PET substrates," *Sensors and Actuators A: Physical*, vol. 159, no. 1, pp. 96–104, 2010.
- [12] J. Lueke, A. Badr, E. Lou, and W. Moussa, "Microfabrication and integration of a sol-gel PZT folded spring energy harvester," *Sensors*, vol. 15, no. 6, pp. 12218–12241, 2015.
- [13] S. Ramezani, "Nonlinear vibration analysis of micro-plates based on strain gradient elasticity theory," *Nonlinear Dynamics*, vol. 73, no. 3, pp. 1399–1421, 2013.

Research Article

The Effects of Power Levels/Time Periods for Sputtering Cobalt onto Carbon Nanotubes/Graphene Composites and Cobalt Annealed on the Characteristics of Anode Materials for Lithium-Ion Batteries

Chuen-Chang Lin ¹, You-Lun Shen,² and An-Na Wu¹

¹Department of Chemical & Materials Engineering, National Yunlin University of Science and Technology, 123 University Road Sec. 3, Douliu, Yunlin 64002, Taiwan

²Dalin Plant, Refining Business Div., CPC Corporation, 50 Yanhai 4th Rd., Siaoqiang Dist., Kaohsiung 81261, Taiwan

Correspondence should be addressed to Chuen-Chang Lin; linchuen@yuntech.edu.tw

Received 24 April 2018; Accepted 27 August 2018; Published 16 October 2018

Academic Editor: Zhengping Zhou

Copyright © 2018 Chuen-Chang Lin et al. This is an open access article distributed under the Creative Commons Attribution License, which permits unrestricted use, distribution, and reproduction in any medium, provided the original work is properly cited.

Carbon nanotubes/graphene composites are directly grown on nickel foil without additional catalysts by chemical vapor deposition (CVD). Next, the cobalt is deposited on carbon nanotubes/graphene composites by radio frequency (RF) sputtering with different power levels and time periods. Then, the cobalt is transformed into cobalt oxide by annealing. A longer time period of sputtering leads to higher specific capacity. Furthermore, the electrochemical stability of cobalt oxide/carbon nanotubes/graphene composites is higher than that of cobalt oxide.

1. Introduction

The applications of lithium-ion batteries include portable electronic devices, electric vehicles, and hybrid electric vehicles. Lithium-ion batteries compared to other batteries (such as Ni-Cd, lead-acid, and Ni-MH) possess higher energy densities (100–150 Wh kg⁻¹), higher voltage, and lower maintenance [1]. The energy density and performance of lithium-ion batteries mainly depend on the properties of anode and cathode materials. In this research, we focused on anode materials of lithium-ion batteries.

Wang et al. [2] have reported that hybrid carbon nanotubes (CNTs) and graphene nanostructures applied in lithium-ion batteries were directly grown by ambient pressure CVD; methane was introduced to form graphene on copper foils at 950°C, and then Fe catalysts were deposited on graphene/copper foils by e-beam evaporation, and ethylene was next introduced to grow pillar CNTs on graphene/copper foil at 750°C. Wang et al. [3] also demonstrated that to increase the accessible specific surface area and the stability as well as conductivity between the carbon nanotube

bundles and the nickel foam, three-dimensional few layer graphene/multiwalled carbon nanotube architectures were fabricated on oxygen plasma-treated nickel foam coated with Fe catalysts by e-beam evaporation through a one-step ambient pressure CVD process using a mixture of acetylene and hydrogen. In our previous study [4], to control the packing density of CNTs and the number of graphene layers, carbon nanotube/graphene composites were directly grown on cobalt catalyst-coated nickel foam by one-step CVD at different temperatures and times.

Han et al. [5] reported that a cobalt oxide-modified porous carbon was synthesized via a solvothermal method followed by a simple thermal treatment process and its high electrochemical performances (enhanced reversible capacity, excellent cyclic stability, high Coulomb efficiency, and good rate capability) were attributed to the interconnection networks of electrically conductive porous carbon and cobalt oxide nanoparticles, which could provide accessible route for electrolyte diffusion as well as intercalation of Li ions into the active sites, efficiently prevent volume expansion/contraction of cobalt oxide during discharge/charge process,

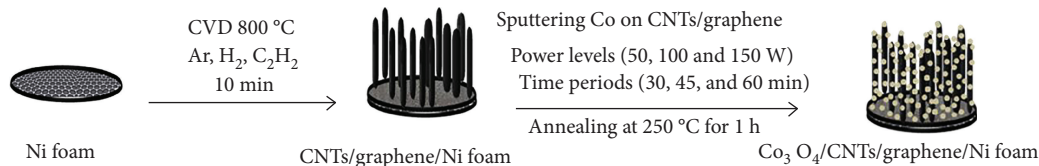


FIGURE 1: Schematic illustration of the fabrication process of $\text{Co}_3\text{O}_4/\text{CNTs}/\text{graphene}$ composites.

and decrease its inner resistance. Yoon and Park [6] demonstrated that a CNTs/cobalt oxide-blended anode was prepared by cobalt oxide nanoparticles and CNTs mixed with Super P as conductive carbon and poly-vinylidene fluoride (PVDF) as a binder; its cyclic ability and rate capability in comparison with a cobalt oxide anode were probably improved by the high electronic conductivity and mechanical flexibility of CNTs, respectively. Abbas et al. [7] also reported that mesoporous Co_3O_4 nanoparticles anchored on CNTs by a chemical coprecipitation method exhibited high capacity as well as rate capability and good capacity retention due to the intimate interaction between the CNTs and Co_3O_4 nanoparticles. Li et al. [8] have demonstrated that cobalt oxide/graphene nanostructured composites were prepared by cobalt oxide nanoparticles homogeneously dispersed onto graphene sheets through a chemical deposition method and possessed large reversible capacity in the initial cycle and excellent cyclic stability due to improving the structure stability by the interactions between high conductive graphene sheets and cobalt oxide nanoparticles anchored on the graphene sheets. Wang et al. [9] have reported that cobalt oxide/graphene nanocomposites synthesized by an in situ solution-based method exhibited initial reversible lithium storage capacity and the high conductive graphene was used as a buffer medium to allow volume expansion/contraction of cobalt oxide reacted with lithium by lithium-ion insertion/extraction. Qiu et al. [10] also demonstrated that mesoporous cobalt oxide/graphene nanocomposites synthesized by one-step in situ growth of cobalt oxide on a graphene matrix and the volume expansion/contraction of cobalt oxide nanoparticles could be confined by graphene with large sizes to prevent electrode pulverization during the lithium-ion insertion/extraction process. Lou et al. [11] reported that ultrasmall cobalt oxide nanoparticles/reduced graphene oxide nanocomposites were prepared by a facile solution-based synthesis and exhibited good rate capability, excellent Coulomb efficiency, and high reversible capacity since cobalt oxide was anchored on graphene which provided a high electronic conductivity as well as an elastic buffer medium. Yang et al. [12] demonstrated that binder free 3D hierarchical graphene nanosheets/cobalt oxide fibers composite papers were synthesized by graphene nanosheets deposited onto electrospun cobalt oxide fibers and possessed good rate capability, very high reversible capacity, and excellent cyclic ability due to high electronic conductivity as well as flexible structure of graphene, large electrode/electrolyte contact area, and short path length for lithium transportation. Yang et al. [13] reported that sandwich-like ultrathin cobalt oxide nanosheet/graphene hybrids were prepared by a layer-by-layer self-assembly and low-temperature annealing method; they

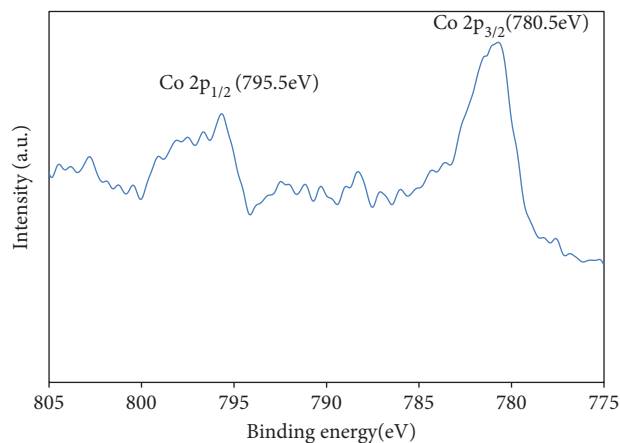


FIGURE 2: XPS spectra in Co 2p region for cobalt oxide/carbon nanotubes/graphene composites.

possessed very high rate capability and excellent reversible capacity. Wu et al. [14] also reported that $\text{Co}_3\text{O}_4/\text{graphene}$ nanocomposites prepared by solution-phase dispersion of $\text{Co}(\text{OH})_2$ on graphene followed transformation of $\text{Co}(\text{OH})_2$ into Co_3O_4 by annealing treatment exhibited excellent cyclic stability and high rate capability because of graphene being beneficial for allowing large volume expansion of Co_3O_4 without the severe cracking or crumbling of electrode materials during discharge/charge cycles. Li et al. [15] have demonstrated that Co_3O_4 mesoporous nanostructures directly grown on a graphene membrane by hydrothermal treatment and then annealing possessed excellent capacity retention due to mesoporous nanostructures with enough space being beneficial to strain buffer of Co_3O_4 during discharge/charge process. Hu et al. [16] have reported that porous cobalt oxide nanofibers coated with reduced graphene oxide (rGO) by hydrothermal reaction showed good rate capability as well as enhanced cyclic stability for a half cell and possessed high stable capacity with operation potential (2 V) for a full cell (the cathode electrode (LiMn_2O_4)) assembled with the anode electrode ($\text{Co}_3\text{O}_4/\text{rGO}$).

The main aim of this research was to improve the characteristics of anode materials of lithium-ion batteries through depositing cobalt on carbon nanotubes/graphene composites by sputtering with different power levels as well as time periods and transforming cobalt into cobalt oxide by annealing.

2. Materials and Methods

Nickel foam with three-dimensional conductive network structure working as template for the growth of graphene

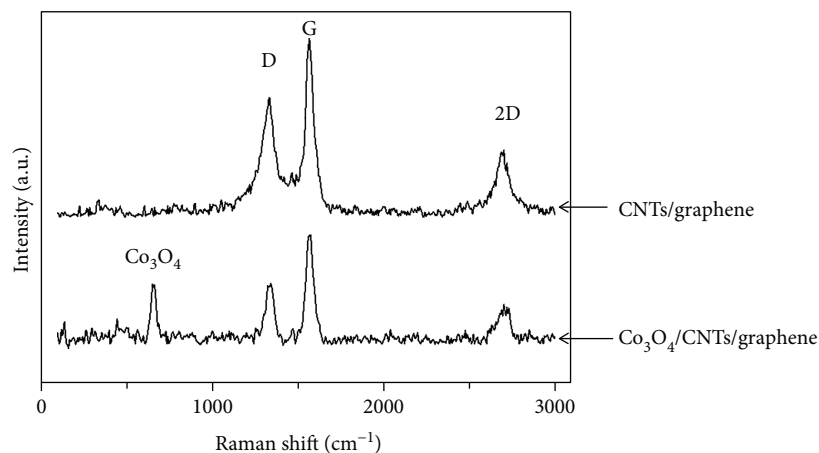


FIGURE 3: Raman spectra of carbon nanotubes/graphene composites and cobalt oxide/carbon nanotubes/graphene composites.

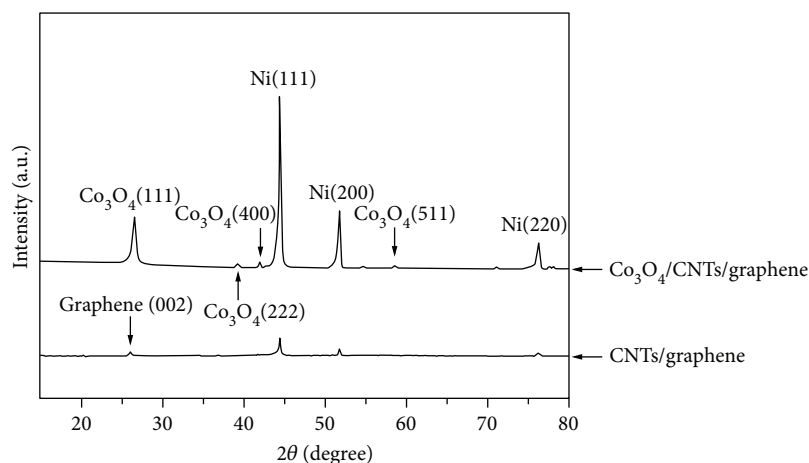


FIGURE 4: X-ray diffraction patterns of carbon nanotubes/graphene composites and cobalt oxide/carbon nanotubes/graphene composites (power = 100 W and time = 60 min for sputtering cobalt on carbon nanotubes/graphene composites).

facilitated easy access of electrolyte ions to the electrode surface [17, 18]. The use of Ni foam is known to increase the active material utilization of the electrode, and thus, the specific capacitance of the electrode with the Ni foam current collector was higher than that with the Ti mesh current collector [17, 18]. The nickel foam ($1 \times 2 \times 0.1 \text{ cm}^3$) was degraded ultrasonically (40 kHz) in acetone for 15 min. Next, it was rinsed ultrasonically (40 kHz) with pure deionized water for 15 min and then oven-dried in air (50°C) to constant weight.

First, the pretreated nickel foam substrate was heated at 1000°C in H₂ (100 sccm) and Ar (250 sccm) for 10 min to reduce the surface oxide layer. Next, carbon nanotubes/graphene composites were directly and simultaneously synthesized on the annealed nickel foam without additional catalysts using one-step ambient pressure thermal CVD with a gas mixture of C₂H₂ (15 sccm), H₂ (100 sccm), and Ar (250 sccm) for 10 min at 800°C and then cooled to ambient temperatures in Ar with the same volume flow rate as carbon nanotubes/graphene composites grown. Finally, the carbon nanotubes/graphene composites were weighed.

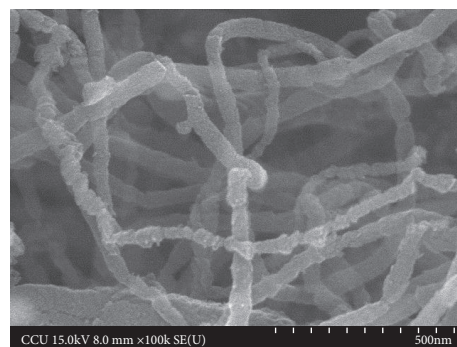


FIGURE 5: The FESEM images of carbon nanotubes/graphene composites.

The cobalt was deposited on the carbon nanotubes/graphene composites by RF magnetron sputtering from a 3-inch disk Co target (purity: 99.9%, purchased from SCM, INC) in a vacuum chamber with a background

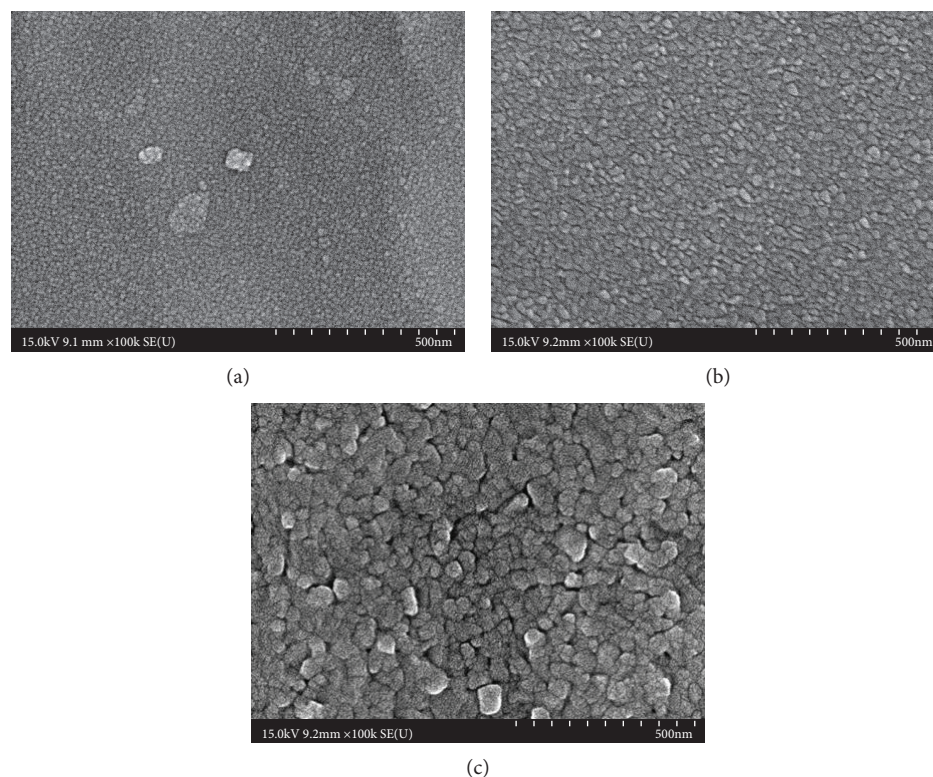


FIGURE 6: The FESEM images of cobalt oxide/carbon nanotubes/graphene composites with time period (60 min) and different power levels (a) 50 W, (b) 100 W, and (c) 150 W for sputtering cobalt onto carbon nanotube/graphene composite.

pressure of 7×10^{-6} torr. The distance between the target and the substrate was 10 cm. The pressure and volume flow rate of argon were maintained at 5 mtorr and 15 sccm, respectively. The power levels (50, 100, and 150 W) and time levels (30, 45, and 60 min) were varied. Then, the cobalt was transformed into cobalt oxide by annealing at 250°C in air for 1 h.

A solution of 1 M LiPF_6 dissolved in 1 : 1 : 1 (v/v/v) ethylene carbonate (EC)-ethyl methyl carbonate (EMC)-dimethyl carbonate (DMC) from Ubiq Technology was used as the electrolyte. The anode electrode (Li metal: 99.9%, 0.3 mm thick, Ubiq Technology) was assembled with the cathode electrode (cobalt oxide or cobalt oxide/carbon nanotubes/graphene composites) into a coin cell battery by using a coin cell manual crimping machine (CR2032, Taiwan) in an Ar-filled glovebox. The electrochemical cycling tests were performed at 0.1–2 C using a cycler (PEX 2011, Kikusui, Japan).

The Co 2p peaks of Co_3O_4 for the Co_3O_4 /carbon nanotubes/graphene composites were explored by XPS (Fison VG. ESCA210, England). The D peak, G peak, 2D peak, and Co_3O_4 peak for the carbon nanotubes/graphene composites and Co_3O_4 /carbon nanotubes/graphene composites were investigated by microscopic Raman spectrometer (inVia, Renishaw, England). XRD (D8 Discover Bruker, Germany) with low angle of incidence was used to characterize the crystalline structure of carbon nanotubes/graphene composites and cobalt oxide/carbon nanotubes/graphene composites (power = 100 W and time = 60 min for sputtering cobalt on carbon nanotubes/graphene composites). Furthermore, the structure or the chemical composition of carbon nanotubes/graphene composites and cobalt oxide/carbon

nanotubes/graphene composites for cobalt being sputtered onto carbon nanotubes/graphene composites at different power levels was conducted by field emission scanning electron microscope (FESEM) combined with energy-dispersive X-ray (EDX) (JEOL JSM-6700F, Japan). Additional information on the surface roughness (root mean square (rms) got by running NanoScope Analysis using original AFM data as input) of cobalt oxide/carbon nanotubes/graphene composites for cobalt being sputtered onto carbon nanotubes/graphene composites at different power levels and time periods was obtained by atomic force microscope (Dimension Icon, Bruker, USA). Moreover, impedance measurement was performed using an electrochemical analyzer (CH Instruments CHI 608B, USA) at 5 mV AC amplitude with a frequency range between 100 kHz and 0.01 Hz to measure the charge-transfer resistance for cobalt oxide (power = 100 W and time = 60 min for sputtering cobalt on nickel foam) and cobalt oxide/carbon nanotubes/graphene composites (power = 100 W and time = 60 min for sputtering cobalt on carbon nanotubes/graphene composites). Cyclic voltammetry tests for cobalt oxide (power = 100 W and time = 60 min for sputtering cobalt on nickel foam), cobalt oxide/carbon nanotubes/graphene composites (power = 100 W and time = 60 min for sputtering cobalt on carbon nanotubes/graphene composites), and the lithium-ion battery (full cell) for cobalt oxide/carbon nanotubes/graphene composites (power = 100 W and time = 60 min for sputtering cobalt on carbon nanotubes/graphene composites) were performed using an electrochemical analyzer (CH Instruments CHI 608B, USA) at a scan rate of 0.1 mV s^{-1} .

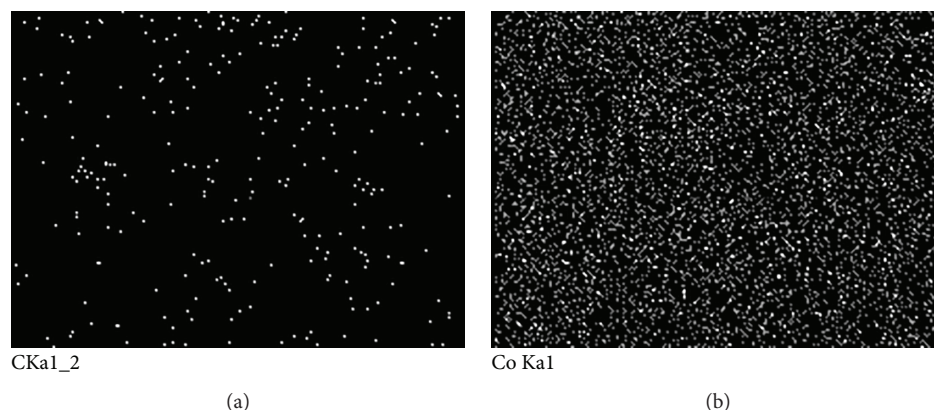


FIGURE 7: The EDX element distributions of (a) C and (b) Co in cobalt oxide/carbon nanotubes/graphene composites (power = 100 W and time = 60 min for sputtering cobalt on carbon nanotubes/graphene composites).

2.1. Results and Discussion. Figure 1 illustrates cobalt oxide prepared by sputtering Co on CNTs/graphene grown on Ni foil by CVD and subsequent transformation of cobalt into cobalt oxide by annealing. The Co 2p XPS spectrum (Figure 2) of the Co_3O_4 /carbon nanotubes/graphene composites shows two peaks located at 780.5 eV (Co $2p_{3/2}$) and 795.5 eV (Co $2p_{1/2}$), and the spin-energy separation is 15 eV with the characteristic of Co_3O_4 [5, 8], which demonstrate the existence of Co_3O_4 in the composites. Furthermore, the Raman spectra (Figure 3) for the carbon nanotubes/graphene composites and Co_3O_4 /carbon nanotubes/graphene composites have three same peaks positioned at 1355 cm^{-1} (D), 1583 cm^{-1} (G), and 2679 cm^{-1} (2D) which can be assigned to carbon nanotubes and graphene; however, the additional peak at 667 cm^{-1} in the Raman spectrum for Co_3O_4 /carbon nanotubes/graphene composites can be attributed to Co_3O_4 which is in good agreement with the previous literatures [5, 8]. Furthermore, X-ray diffraction patterns of carbon nanotubes/graphene composites and cobalt oxide/carbon nanotubes/graphene composites (power = 100 W and time = 60 min for sputtering cobalt on carbon nanotubes/graphene composites) are shown in Figure 4. The peaks for CNTs/graphene in Figure 4 are identified as coming from the (111), (200), and (220) planes of face-centered cubic Ni metal (JCPDS card no. 04-0850) which originated from the Ni foam substrate. The peaks for Co_3O_4 /CNTs/graphene in Figure 4 are the same as those for CNTs/graphene in Figure 4 except the peaks for Co_3O_4 /CNTs/graphene in Figure 4 from the (111) diffraction plane of Co_3O_4 (JCPDS card no. 76-1802) [19], (222) and (400) crystal planes of Co_3O_4 (JCPDS card no. 73-1701) [20], and (511) plane of Co_3O_4 (JCPDS card no. 42-1467) [21]. Moreover, Co_3O_4 coated on CNTs/graphene was also confirmed by comparing the FESEM image in Figure 5 with the FESEM image in Figure 6(b) and from the EDX element distributions in Figure 7.

Figure 8 shows the effects of power levels and time periods for sputtering cobalt onto carbon nanotubes/graphene composites on the specific capacity (0.1 C) of cobalt oxide/carbon nanotubes/graphene composites. It shows that the longer the time period of sputtering, the higher the specific capacity. The reason behind this may be that a longer

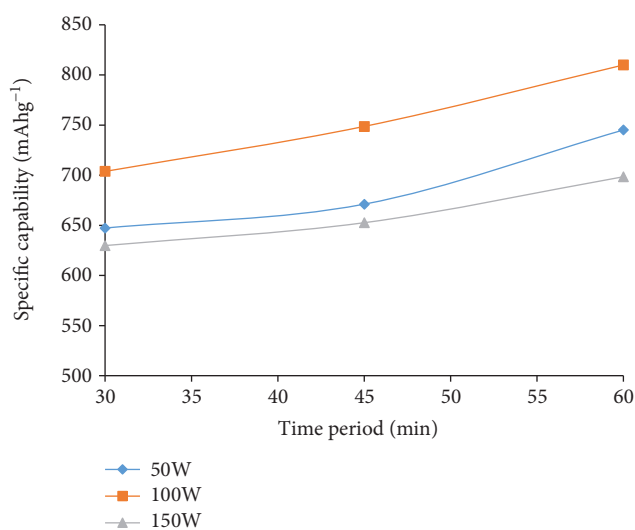


FIGURE 8: The effects of power levels and time periods for sputtering cobalt onto carbon nanotubes/graphene composites on the specific capacity (0.1 C) of cobalt oxide/carbon nanotubes/graphene composites.

time period of sputtering led to higher surface roughness (Figures 9 and 10), thus leading to higher specific capacity since a highly rough surface should possess large surface area [22]. Furthermore, the specific capacity increased at power levels in the range 50–100 W. This picture may be explained as follows. The higher the power level, the higher the sputtering yield, thus enhancing the deposition rate. Then, particles falling on the carbon nanotubes/graphene composite surface do not have enough time to rearrange and resputter themselves; thus, more uniform particles are homogeneously deposited (Figures 6(a) and 6(b)), which leads to increasing surface roughness (Figures 9 and 10) and specific capacity (Figure 8). However, the specific capacity decreased with power levels in the range 100–150 W. This illustrates that an overly high power level leads to an overly strong ion and reflected neutral bombardment of the carbon nanotubes/graphene composite surface, which only causes more damages and then increases the pore size (Figures 6(b) and 6(c)) and

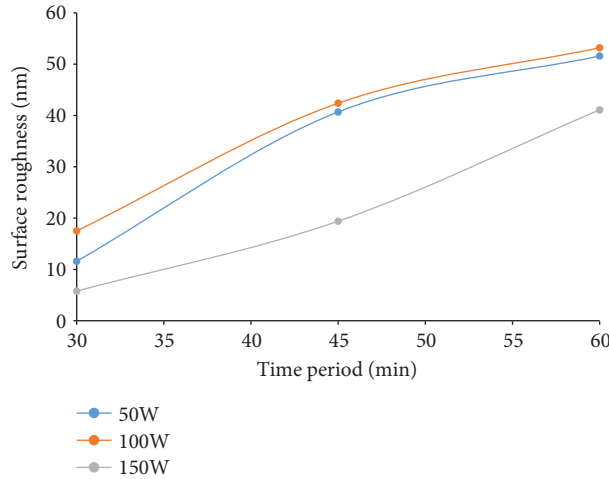


FIGURE 9: The effects of power levels and time periods for sputtering cobalt onto carbon nanotubes/graphene composites on the surface roughness of cobalt oxide/carbon nanotubes/graphene composites.

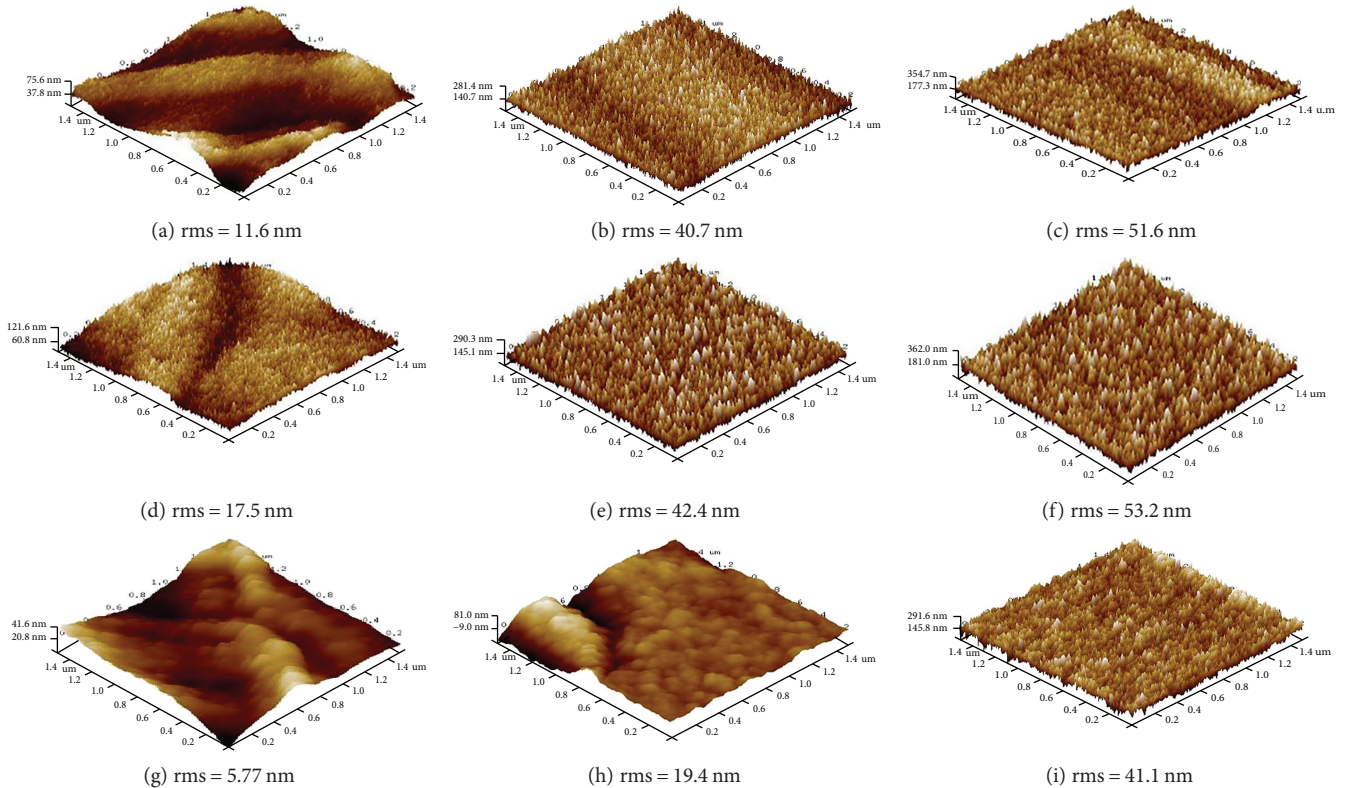


FIGURE 10: AFM micrograph of cobalt oxide/carbon nanotubes/graphene composites with different power levels and time periods (a) 50 W and 30 min, (b) 50 W and 45 min, (c) 50 W and 60 min, (d) 100 W and 30 min, (e) 100 W and 45 min (f) 100 W and 60 min, (g) 150 W and 30 min, (h) 150 W and 45 min, and (i) 150 W and 60 min for sputtering cobalt onto carbon nanotube/graphene composite.

thus decreases surface roughness (Figures 9 and 10) as well as specific capacity (Figure 8).

The discharge/charge profiles (0.1 C) of cobalt oxide (power = 100 W and time = 60 min for sputtering cobalt on nickel foam) and cobalt oxide/carbon nanotubes/graphene composites (power = 100 W and time = 60 min for sputtering cobalt on carbon nanotubes/graphene composites) are shown in Figures 11(a) and 11(b). The potential plateau in the

first discharge curves of cobalt oxide/carbon nanotubes/graphene composites is not more obvious than that of cobalt oxide since the crystallinity of cobalt oxide decreases by adding the poorly crystal carbon nanotubes/graphene composites and a cathode peak (about 0.6 V) in the first cycle of cobalt oxide is sharper than a cathode peak (about 0.7 V) in the first cycle of cobalt oxide/carbon nanotubes/graphene composites (Figures 12(a) and 12(b)).

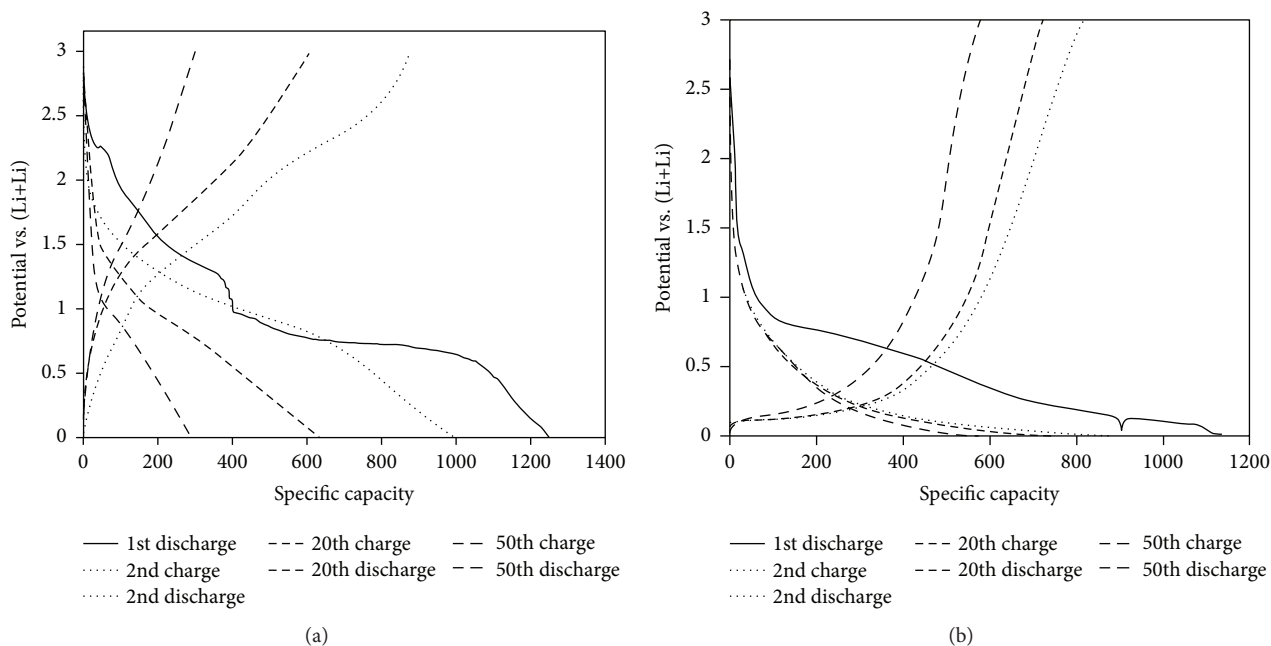


FIGURE 11: The discharge/charge profiles (between 0.01 V and 3 V at 0.1 C) of (a) cobalt oxide (power = 100 W and time = 60 min for sputtering cobalt on nickel foam) and (b) cobalt oxide/carbon nanotubes/graphene composites (power = 100 W and time = 60 min for sputtering cobalt on carbon nanotubes/graphene composites).

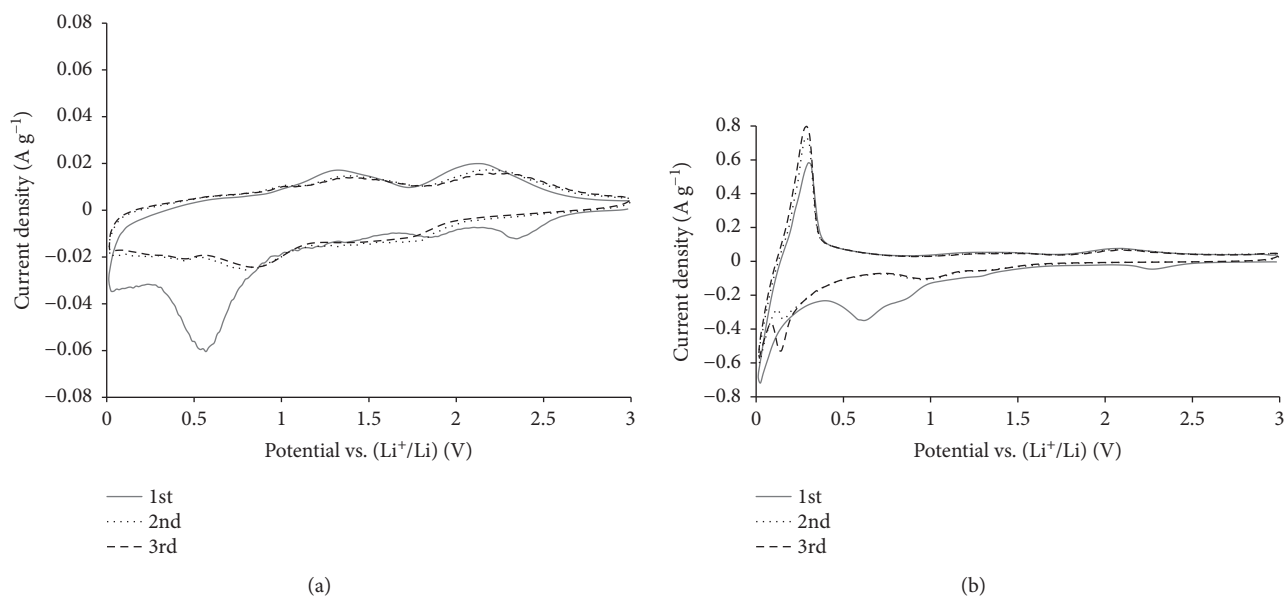


FIGURE 12: Cyclic voltammograms (between 0.01 V and 3 V from the 1st cycle to the 3rd cycle) of (a) cobalt oxide (power = 100 W and time = 60 min for sputtering cobalt on nickel foam) and (b) cobalt oxide/carbon nanotubes/graphene composites (power = 100 W and time = 60 min for sputtering cobalt on carbon nanotubes/graphene composites).

The presence of the plateaus in the first discharge curve can be attributed to the formation of a solid electrolyte interface (SEI) film on the surface of electrodes [23] and the discharge plateaus disappear in the subsequent cycles (Figures 11(a) and 11(b)) which also is confirmed by the cathode peaks (about 0.6 V–0.7 V) occurring during the first discharge scan and disappearing in the following cycles (Figures 12(a) and 12(b)). Furthermore, if discharge specific capacity (200 mAh g^{-1}) at the 2nd cycle is the

same, it occurs at higher potential (about 1.3 V) for cobalt oxide and at lower potential (about 0.4 V) for cobalt oxide/carbon nanotubes/graphene composites (Figures 11(a) and 11(b)). Moreover, if charge specific capacity (400 mAh g^{-1}) at the 2nd cycle is the same, it occurs at higher potential (about 1.5 V) for cobalt oxide and at lower potential (about 0.4 V) for cobalt oxide/carbon nanotubes/graphene composites (Figures 11(a) and 11(b)). Therefore, the cathode electrode (LiCoO_2) was assembled with the anode electrode

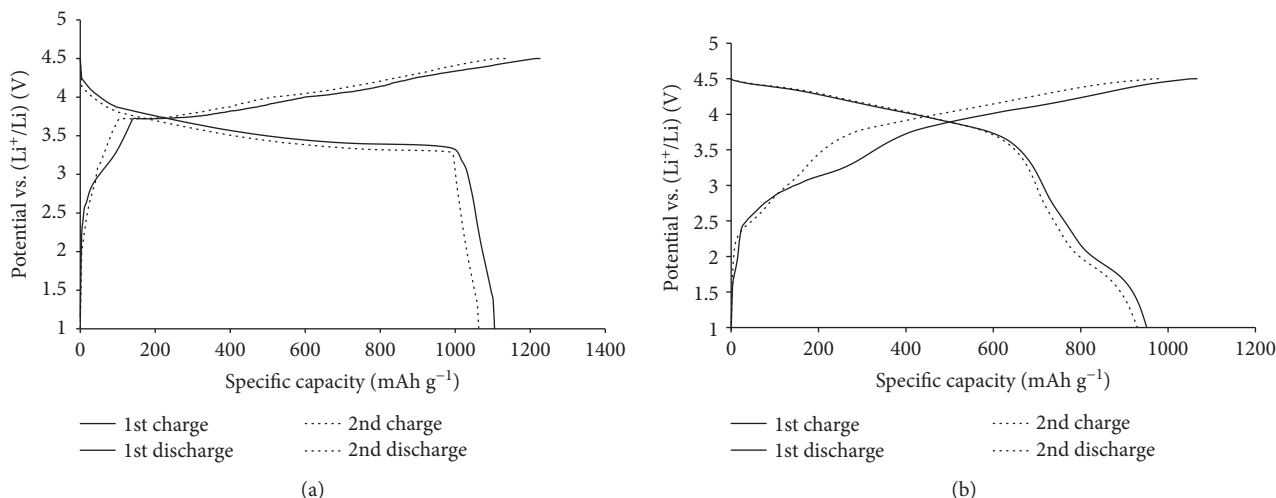


FIGURE 13: The discharge/charge profiles (between 1 V and 4.5 V at 0.1 C) of the lithium-ion battery (full cell) for (a) cobalt oxide (power = 100 W and time = 60 min for sputtering cobalt on nickel foam) and (b) cobalt oxide/carbon nanotubes/graphene composites (power = 100 W and time = 60 min for sputtering cobalt on carbon nanotubes/graphene composites).

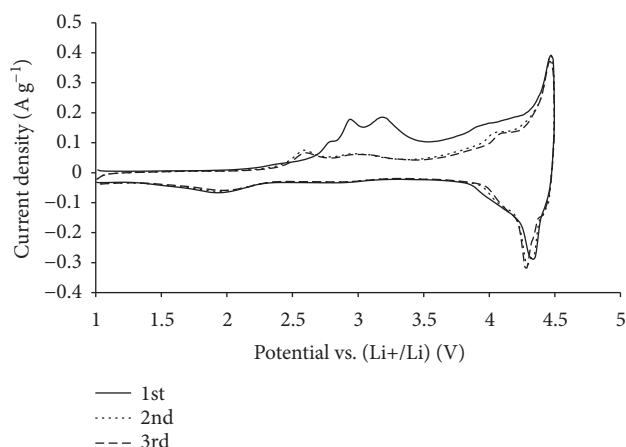


FIGURE 14: Cyclic voltammograms (between 1 V and 4.5 V from the 1st cycle to the 3rd cycle) of the lithium-ion battery (full cell) for cobalt oxide/carbon nanotubes/graphene composites (power = 100 W and time = 60 min for sputtering cobalt on carbon nanotubes/graphene composites).

(Co_3O_4 or Co_3O_4 /carbon nanotubes/graphene composites) into a lithium-ion battery (full cell) and the potential plateau (about 3.5–4.5 V) in the discharge curves (0.1 C) of the lithium-ion battery (full cell) for cobalt oxide/carbon nanotubes/graphene composites is not more obvious than that (about 3.25–4.25 V) for cobalt oxide since the crystallinity of cobalt oxide decreases by adding the poorly crystal carbon nanotubes/graphene composites; however, the discharge processes of the lithium-ion battery (full cell) for cobalt oxide/carbon nanotubes/graphene composites occur at higher voltage (Figures 13(a) and 13(b)) for the benefit of merchantable lithium-ion batteries. Finally, the cyclic voltammograms of the lithium-ion battery (full cell) for cobalt oxide/carbon nanotubes/graphene composites are shown in Figure 14. The peaks were seen ranging from 2.9 V to 3.2 V (Figure 14) which can be attributed to the lithiation of

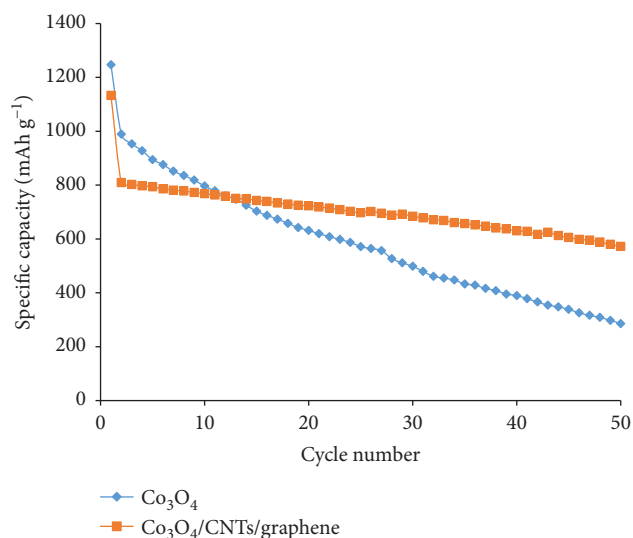
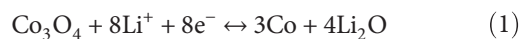


FIGURE 15: The effects of cobalt oxide (power = 100 W and time = 60 min for sputtering cobalt on nickel foam), cobalt oxide/carbon nanotubes/graphene composites (power = 100 W and time = 60 min for sputtering cobalt on carbon nanotubes/graphene composites), and different charge/discharge cycles on the specific capacity (0.1 C).

Co_3O_4 as well as delithiation of LiCoO_2 during the charge processes, and the peak was observed at about 2 V (Figure 14) which can arise from the lithiation of $\text{Li}_{1-x}\text{CoO}_2$ as well as delithiation of $\text{Co/Li}_2\text{O}$ during the discharge processes [16, 24]. The charge/discharge reactions of Co_3O_4 , carbon nanotubes/graphene composites, and LiCoO_2 can be described by 1, 2, and 3, respectively [5, 25, 26].



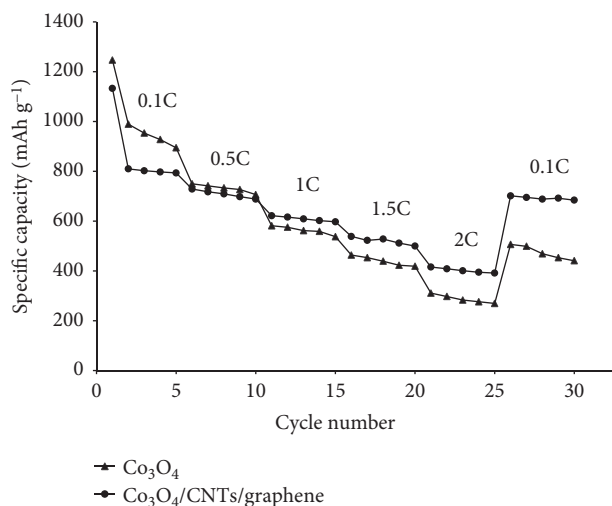


FIGURE 16: Rate capability (between 0.01 V and 3 V) for the cobalt oxide (power = 100 W and time = 60 min for sputtering cobalt on nickel foam) and cobalt oxide/carbon nanotubes/graphene composites (power = 100 W and time = 60 min for sputtering cobalt on carbon nanotubes/graphene composites).

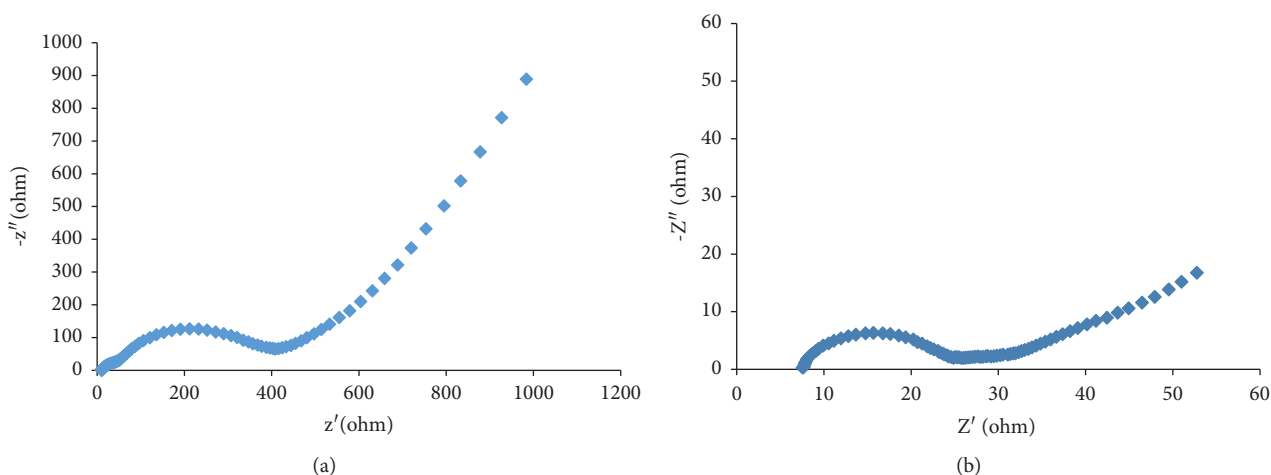


FIGURE 17: Nyquist diagrams of (a) cobalt oxide (power = 100 W and time = 60 min for sputtering cobalt on nickel foam) and (b) cobalt oxide/carbon nanotubes/graphene composites (power = 100 W and time = 60 min for sputtering cobalt on carbon nanotubes/graphene composites).

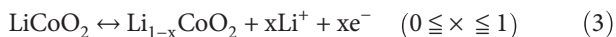


Figure 15 shows the effects of cobalt oxide (power = 100 W and time = 60 min for sputtering cobalt on nickel foam), cobalt oxide/carbon nanotubes/graphene composites (power = 100 W and time = 60 min for sputtering cobalt on carbon nanotubes/graphene composites), and different charge/discharge cycles on the specific capacity (0.1 C). The reason for the large specific capacity fading after the first cycle (Figure 15) could possibly be the irreversible lithium loss due to the side reaction of electrolyte decomposition and then formation of a SEI film [23]. Cobalt oxide/carbon nanotubes/graphene composites possessed a better cycling performance (specific capacity only decreased 29% from the 2nd cycle to the 50th cycle in Figure 15) in comparison to cobalt oxide (specific capacity decreased 71% from the 2nd cycle to the 50th cycle in Figure 15) since the CNTs/G composites could provide

stable support to cobalt oxide and allow volume expansion of cobalt oxide without the severe cracking or crumbling of electrode materials during discharge/charge cycles [5, 9, 10], which also is confirmed by the discharge/charge profiles of cobalt oxide and cobalt oxide/carbon nanotubes/graphene composites (Figures 11(a) and 11(b)). The specific capacity for cobalt oxide/carbon nanotubes/graphene composites is about two-fold of the specific capacity for cobalt oxide after the 50th cycle (Figure 15). Furthermore, cobalt oxide/carbon nanotubes/graphene composites show better rate capability in comparison to cobalt oxide at different C-rates (Figures 16(a) and 16(b)) since the charge-transfer resistance (16.7 ohm) for cobalt oxide/carbon nanotubes/graphene composites is much lower than that (366.6 ohm) for cobalt oxide (Figures 17(a) and 17(b)), hinting that cobalt oxide/carbon nanotubes/graphene composites show faster charge transfer during the lithium-ion insertion/extraction reaction. The cobalt oxide/carbon nanotubes/

graphene composites almost recover its original specific capacity while the C-rate is back to the initial 0.1 C after 25 cycles; however, the cobalt oxide exhibits apparent specific capacity drop.

3. Conclusions

The Co 2p XPS spectrum shows the existence of Co_3O_4 in the composites, which also is confirmed by the Raman spectra. Furthermore, the specific capacity increased at power levels in the range 50–100 W; however, the specific capacity decreased with power levels in the range 100–150 W. Moreover, discharge processes of the lithium-ion battery (full cell) for cobalt oxide/carbon nanotubes/graphene composites occur at higher potential for the benefit of merchandising. Finally, cobalt oxide/carbon nanotubes/graphene composites exhibit better rate capability compared with cobalt oxide at different C-rates.

Data Availability

The data used to support the findings of this study are available from the corresponding author upon request.

Disclosure

Furthermore, the abstract entitled “Synthesis of cobaltic oxide/carbon nanotube/graphene composites for anode materials of lithium-ion batteries” was done in the oral presentation by Chuen-Chang Lin from National Yunlin University of Science and Technology, Taiwan, in the 20th International Conference on Emerging Materials and Nanotechnology during June 25–26, 2018, at Vancouver, British Columbia, Canada.

Conflicts of Interest

The authors declare that there is no conflict of interests regarding the publication of this paper.

Acknowledgments

Financial support by the Ministry of Science and Technology of the Republic of China (under grant no. MOST 106-2221-E-224-042) is gratefully acknowledged.

References

- [1] D. Miranda, C. M. Costa, and S. Lanceros-Mendez, “Lithium ion rechargeable batteries: state of the art and future needs of microscopic theoretical models and simulations,” *Journal of Electroanalytical Chemistry*, vol. 739, pp. 97–110, 2015.
- [2] W. Wang, I. Ruiz, S. Guo et al., “Hybrid carbon nanotube and graphene nanostructures for lithium ion battery anodes,” *Nano Energy*, vol. 3, pp. 113–118, 2014.
- [3] W. Wang, S. Guo, M. Penchev et al., “Three dimensional few layer graphene and carbon nanotube foam architectures for high fidelity supercapacitors,” *Nano Energy*, vol. 2, no. 2, pp. 294–303, 2013.
- [4] C. C. Lin and Y. W. Lin, “Synthesis of carbon nanotube/graphene composites by one-step chemical vapor deposition for electrodes of electrochemical capacitors,” *Journal of Nanomaterials*, vol. 2015, Article ID 741928, 8 pages, 2015.
- [5] Y. Han, L. Dong, J. Feng, D. Li, X. Li, and S. Liu, “Cobalt oxide modified porous carbon anode enhancing electrochemical performance for Li-ion batteries,” *Electrochimica Acta*, vol. 167, pp. 246–253, 2015.
- [6] T. H. Yoon and Y. J. Park, “Electrochemical properties of CNTs/ Co_3O_4 blended anode for rechargeable lithium batteries,” *Solid State Ionics*, vol. 225, pp. 498–501, 2012.
- [7] S. M. Abbas, S. T. Hussain, S. Ali, N. Ahmad, N. Ali, and K. S. Munawar, “Synthesis of carbon nanotubes anchored with mesoporous Co_3O_4 nanoparticles as anode material for lithium-ion batteries,” *Electrochimica Acta*, vol. 105, pp. 481–488, 2013.
- [8] B. Li, H. Cao, J. Shao, G. Li, M. Qu, and G. Yin, “ Co_3O_4 @graphene composites as anode materials for high-performance lithium ion batteries,” *Inorganic Chemistry*, vol. 50, no. 5, pp. 1628–1632, 2011.
- [9] B. Wang, Y. Wang, J. Park, H. Ahn, and G. Wang, “In situ synthesis of Co_3O_4 /graphene nanocomposite material for lithium-ion batteries and supercapacitors with high capacity and supercapacitance,” *Journal of Alloys and Compounds*, vol. 509, no. 29, pp. 7778–7783, 2011.
- [10] D. Qiu, G. Bu, B. Zhao et al., “In situ growth of mesoporous Co_3O_4 nanoparticles on graphene as a high-performance anode material for lithium-ion batteries,” *Materials Letters*, vol. 119, pp. 12–15, 2014.
- [11] Y. Lou, J. Liang, Y. Peng, and J. Chen, “Ultra-small Co_3O_4 nanoparticles–reduced graphene oxide nanocomposite as superior anodes for lithium-ion batteries,” *Physical Chemistry Chemical Physics*, vol. 17, no. 14, pp. 8885–8893, 2015.
- [12] X. Yang, K. Fan, Y. Zhu et al., “Electric papers of graphene-coated Co_3O_4 fibers for high-performance lithium-ion batteries,” *ACS Applied Materials & Interfaces*, vol. 5, no. 3, pp. 997–1002, 2013.
- [13] Q. Yang, J. Wu, K. Huang et al., “Layer-by-layer self-assembly of graphene-like Co_3O_4 nanosheet/graphene hybrids: towards high-performance anode materials for lithium-ion batteries,” *Journal of Alloys and Compounds*, vol. 667, pp. 29–35, 2016.
- [14] Z. S. Wu, W. Ren, L. Wen et al., “Graphene anchored with Co_3O_4 nanoparticles as anode of lithium ion batteries with enhanced reversible capacity and cyclic performance,” *ACS Nano*, vol. 4, no. 6, pp. 3187–3194, 2010.
- [15] L. Li, G. Zhou, X. Y. Shan, S. Pei, F. Li, and H. M. Cheng, “ Co_3O_4 mesoporous nanostructures@graphene membrane as an integrated anode for long-life lithium-ion batteries,” *Journal of Power Sources*, vol. 255, pp. 52–58, 2014.
- [16] R. Hu, H. Zhang, Y. Bu, H. Zhang, B. Zhao, and C. Yang, “Porous Co_3O_4 nanofibers surface-modified by reduced graphene oxide as a durable, high-rate anode for lithium ion battery,” *Electrochimica Acta*, vol. 228, pp. 241–250, 2017.
- [17] T. Xiao, X. Hu, B. Heng et al., “ $\text{Ni}(\text{OH})_2$ nanosheets grown on graphene-coated nickel foam for high-performance pseudocapacitors,” *Journal of Alloys and Compounds*, vol. 549, pp. 147–151, 2013.
- [18] Y. Wang, A. Yuan, and X. Wang, “Pseudocapacitive behaviors of nanostructured manganese dioxide/carbon nanotubes composite electrodes in mild aqueous electrolytes: effects of

- electrolytes and current collectors,” *Journal of Solid State Electrochemistry*, vol. 12, no. 9, pp. 1101–1107, 2008.
- [19] S. R. M. Rusi, “Electrodeposited Mn_3O_4 -NiO- Co_3O_4 as a composite electrode material for electrochemical capacitor,” *Electrochimica Acta*, vol. 175, pp. 193–201, 2015.
- [20] K. Jiao, Y. Jiang, Z. Kang, R. Peng, S. Jiao, and Z. Hu, “Three-dimensional Co_3O_4 @MWNTs nanocomposite with enhanced electrochemical performance for nonenzymatic glucose biosensors and biofuel cells,” *Royal Society Open Science*, vol. 4, no. 12, article 170991, 2017.
- [21] W. Zhang, Y. Fu, and X. Wang, “ Co_3O_4 nanocrystals with exposed low-surface-energy planes anchored on chemically integrated graphitic carbon nitride-modified nitrogen-doped graphene: a high-performance anode material for lithium-ion batteries,” *Applied Surface Science*, vol. 439, pp. 447–455, 2018.
- [22] C. C. Hu and T. W. Tsou, “The optimization of specific capacitance of amorphous manganese oxide for electrochemical supercapacitors using experimental strategies,” *Journal of Power Sources*, vol. 115, no. 1, pp. 179–186, 2003.
- [23] X. M. Liu, Z. D. Huang, S. W. Oh et al., “Carbon nanotube (CNT)-based composites as electrode material for rechargeable Li-ion batteries,” *Composites Science and Technology*, vol. 72, no. 2, pp. 121–144, 2012.
- [24] J. Wang, G. Wang, and H. Wang, “Flexible free-standing Fe_2O_3 /graphene/carbon nanotubes hybrid films as anode materials for high performance lithium-ion batteries,” *Electrochimica Acta*, vol. 182, pp. 192–201, 2015.
- [25] A. D. Roberts, X. Li, and H. Zhang, “Porous carbon spheres and monoliths: morphology control, pore size tuning and their applications as Li-ion battery anode materials,” *Chemical Society Reviews*, vol. 43, no. 13, pp. 4341–4356, 2014.
- [26] X. Li, F. Cheng, B. Guo, and J. Chen, “Template-synthesized LiCoO_2 , LiMn_2O_4 , and $\text{LiNi}_{0.8}\text{Co}_{0.2}\text{O}_2$ nanotubes as the cathode materials of lithium ion batteries,” *The Journal of Physical Chemistry B*, vol. 109, no. 29, pp. 14017–14024, 2005.

Research Article

Template-Free Electrochemical Preparation of Hexagonal CuSn Prism-Structural Electrode for Lithium-Ion Batteries

Xiaona Pan,¹ Haiyan Zhang,² Xiaoyu Wen,¹ Jinqiu Zhang,¹ Maozhong An,¹
and Peixia Yang¹ 

¹MIIT Key Laboratory of Critical Materials Technology for New Energy Conversion and Storage, School of Chemistry and Chemical Engineering, Harbin Institute of Technology, No. 92 West Dazhi Street, Harbin 150001, China

²College of Life Science, Henan University, Kaifeng 475004, China

Correspondence should be addressed to Peixia Yang; yangpeixia@hit.edu.cn

Received 3 May 2018; Revised 30 July 2018; Accepted 5 August 2018; Published 8 October 2018

Academic Editor: Linqin Mu

Copyright © 2018 Xiaona Pan et al. This is an open access article distributed under the Creative Commons Attribution License, which permits unrestricted use, distribution, and reproduction in any medium, provided the original work is properly cited.

A hexagonal prism CuSn alloy was prepared at room temperature from 1-ethyl-3-methylimidazolium dicyanamide ([Emim][DCA]) by the direct template-free electrodeposition method with different concentrations of Cu(I) and Sn(II) at a low current density of 0.04 A dm^{-2} . Moreover, the electrodeposition time was also investigated, and the results indicated that the composition of the CuSn alloy became complex and the structure turned unstable with expanding time. The cycling performance of the hexagonal prism-structural CuSn electrode was investigated, with the first discharge capacity of 345 mAh g^{-1} and a discharge capacity of about 210 mAh g^{-1} after 10 cycles.

1. Introduction

Tin is well investigated as an anode material for lithium-ion batteries (LIB) owing to its high storage capacity (theoretical capacity is 993.3 mAh g^{-1}) [1, 2]. However, during the charge and discharge process, Li intercalation and deintercalation causes the Sn electrode to undergo massive volume expansion and contraction due to the generation of Li_xSn alloy, which causes mechanical disintegration that leads to a poor cycle performance [3].

To stabilize the morphology of Sn anode materials, many efforts have been made to minimize the mechanical stress in the electrodes that cause the volume change. The results of investigations indicate that the Sn alloy [4–6] can effectively buffer the volume expansion during the charge/discharge process, thus improving structural stability and anode material cycle performance. Cu-Sn alloys are studied as anode materials for LIB due to their advantages, such as a stabilized structure, lower cost, environmental friendliness, and especially excellent conductivity. Moreover, the CuSn alloy often is the most commonly formed using template methods by

chemical vapor deposition [7], sol-gel processing [8], and electrodeposition [9]. As known to all, electrodeposition is widely used by industrial production and lab experiments due to its simple process, easy operation, uniform sedimentation, and so on. Furthermore, ionic liquids usually have a wide electrochemical window and show ideal electrolytes for electrodeposition application; it can especially obtain different microstructural platings in ILs [10, 11]. Sun et al. have reported a method that allowed electrochemical growth of metal alloys from ILs, obtaining a nanotube alloy [11] and a nanowire alloy [12].

Herein, we utilized the direct template-free electrodeposition method to synthesize CuSn from 1-ethyl-3-methylimidazolium dicyanamide ([Emim][DCA]). A prism structure of Cu-Sn was obtained, and it could provide a high surface area and a large number of active sites for charge transfer. Hence, this structure can alleviate the large volume change that induces mechanical disintegration during the charge/discharge process. Furthermore, the cycle performance of LIB, which has a hexagonal Cu-Sn prism as the anode, was also investigated.

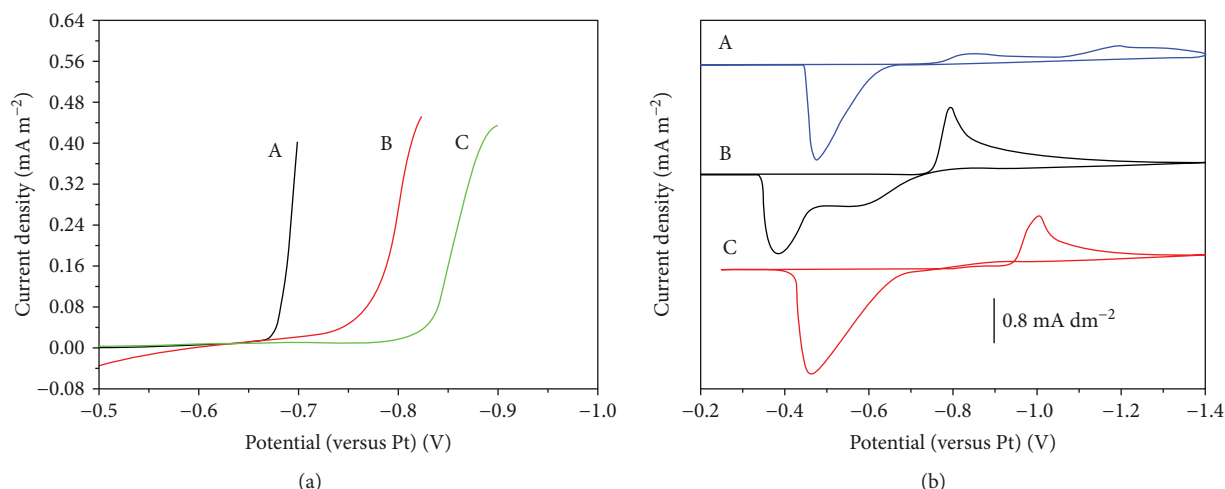


FIGURE 1: (a) Cathodic polarization curves of a Pt electrode for solutions of [Emim][DCA] containing: (A) 0.05 M Sn(II), (B) 0.1 M Cu(I) + 0.05 M Sn(II), and (C) 0.1 M Cu(I) at a scan rate of 0.01 V s^{-1} . (b) Cyclic voltammogram curves of a Pt electrode for solutions of [Emim][DCA] containing: (A) 0.1 M Cu(I), (B) 0.05 M Sn(II), and (C) 0.1 M Cu(I) + 0.05 M Sn(II) at a scan rate of 0.05 V s^{-1} . The scanning direction of CV is shown as an arrow in (b).

2. Experimental

The deposition electrolytes were prepared by the dissolution of various amounts of CuCl and $\text{SnCl}_2 \cdot 2\text{H}_2\text{O}$ ($\geq 99.99\%$, Sigma-Aldrich) into [Emim][DCA] in the glove box. The electrochemical experiments were tested in a three-electrode system using a CHI660E electrochemical workstation. A Pt wire ($\Phi 0.5 \text{ mm}$) was used as the counter electrode and a Pt foil immersed in deposition electrolytes was used as the reference. A Pt wire ($\Phi 0.38 \text{ mm}$) was used as the working electrode for CV measurements, and a Cu foil ($2 \text{ cm} \times 2 \text{ cm}$) was used as a substrate for electrodeposition.

The cell with the CuSn alloy as anode and lithium metal as cathode was assembled on a glovebox filled with argon (H_2O , $\text{O}_2 < 0.5 \text{ ppm}$). The Celgard 2400 was the separator and the electrolyte was 1 M LiPF_6 PC/DEC ($v/v = 1:1$). The cycling performance of the cell was cycled at a current density of $C/10$ at room temperature.

3. Results and Discussion

Figure 1(a) displays the cathodic polarization curves of [Emim][DCA] containing 0.05 M Sn(II), 0.1 M Cu(I) + 0.05 M Sn(II), and 0.1 M Cu(I). The curves have a rising current attributed to the electrodeposition of Sn (-0.66 V versus Pt), Cu-Sn (-0.75 V versus Pt), and Cu (-0.82 V versus Pt). This indicates that the addition of Sn(II) is beneficial to Cu electrodeposition with a Cu and Sn synergy codeposition process. Figure 1(b) shows cyclic voltammogram curves and it reveals that the Sn(II)/Sn couple [13] occur at a potential far more positive than the Cu(I)/Cu couple [14]. Intriguingly, the two redox processes merge together and the potentials are shifted toward each other when the solution contains Cu(I) and Sn(II), suggesting that there is a strong interaction between Cu and Sn. In the CV, the reduction peak at -1.0 V and stripping peak at -0.47 V

(vs. Pt) can correspond to the codeposition and strip of the Cu-Sn alloy, which is evidenced by the XRD spectra displayed in Figure 2. The results of the CV agree with the cathodic polarization.

Figure 2 shows SEM images for a typical Cu substrate electrodeposited with Cu-Sn in different concentrations of Cu(I) and Sn(II) at a current density of 0.04 A cm^{-2} for 1 h. Dendrite-like structures are obtained in the electrolyte with 0.04 M Cu(I) and 0.02 M Sn(II) (Figure 2(a)); with the increase in concentration, the Cu substrate is covered by a large quantity of outward growing Cu-Sn hexagonal prisms with diameters ranging from around $5 \mu\text{m}$ to $10 \mu\text{m}$ (Figure 2(b)). As the concentration continues to increase, uniform Cu-Sn hexagonal prisms are formed and the length of the prisms is about $20 \mu\text{m}$ (Figures 2(c) and 2(d)). The different sizes of the prisms may result from the initial nucleation time which is related to the concentration of Cu(I) and Sn(II). Higher concentration results from nucleation more easily produced and earlier nucleation formed larger prisms because there is a longer time period for the prism to grow [10].

The crystal structure of the as-deposited Cu-Sn prism at different deposition times was tested and shown in Figure 3. As shown in SEM images (Figures 3(a)–3(c)), the diameter of the Cu-Sn prism increases with the increase in deposition time. The tubular hexagonal Cu-Sn with an inner diameter of around $10\text{--}20 \mu\text{m}$ could be observed, but its structure is nonuniform, and its parts have some drawbacks (Figure 3(c)).

The diffraction patterns can be indexed to those of the $\text{Cu}_{10}\text{Sn}_3$, Cu_3Sn , and Cu dominant peaks that resulted from the substrate (Figure 3(d)). As can be seen in Figure 3(d), there are other peaks ($\text{Cu}_{5,6}\text{Sn}$ and Cu_4Sn) when the electrodeposition time is extended to 1.5 h. Moreover, the structure of CuSn is inhomogeneous and unsteady (Figure 3(c)). Furthermore, the ratio of the Cu-Sn alloy is examined with

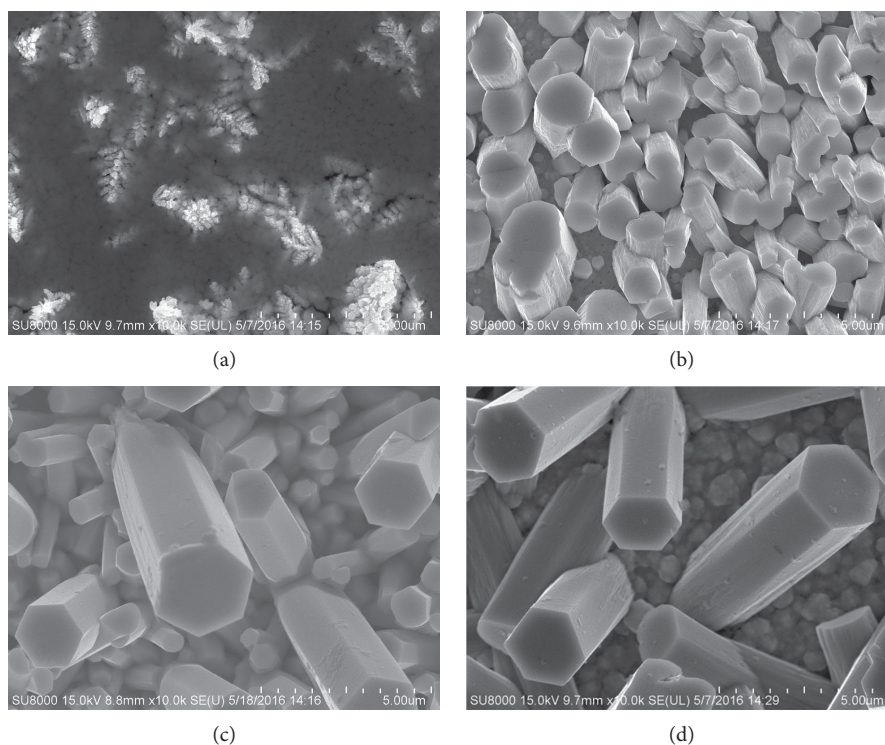


FIGURE 2: SEM images for a typical Cu substrate electrodeposited with Cu-Sn in different concentrations of Cu(I) and Sn(II) at a current density of 0.04 A cm^{-2} for 1 h: (a) $0.04 \text{ M Cu(I)} + 0.02 \text{ M Sn(II)}$, (b) $0.06 \text{ M Cu(I)} + 0.03 \text{ M Sn(II)}$, (c) $0.08 \text{ M Cu(I)} + 0.04 \text{ M Sn(II)}$, and (d) $0.1 \text{ M Cu(I)} + 0.05 \text{ M Sn(II)}$.

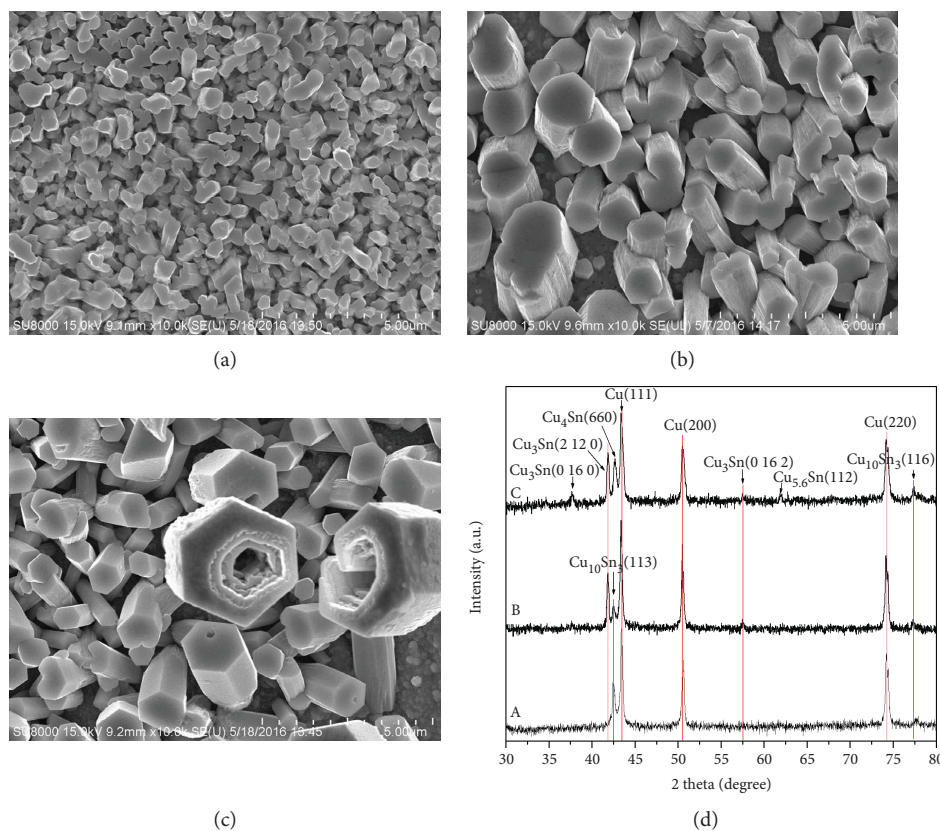


FIGURE 3: SEM images (a, b, and c) and XRD patterns (d) of the as-deposited Cu-Sn in electrolyte with $0.06 \text{ mol L}^{-1} \text{ CuCl}$ and $0.03 \text{ mol L}^{-1} \text{ SnCl}_2$ at a current density of 0.04 A cm^{-2} for different deposition times: (A) 0.5 h, (B) 1 h, and (C) 1.5 h.

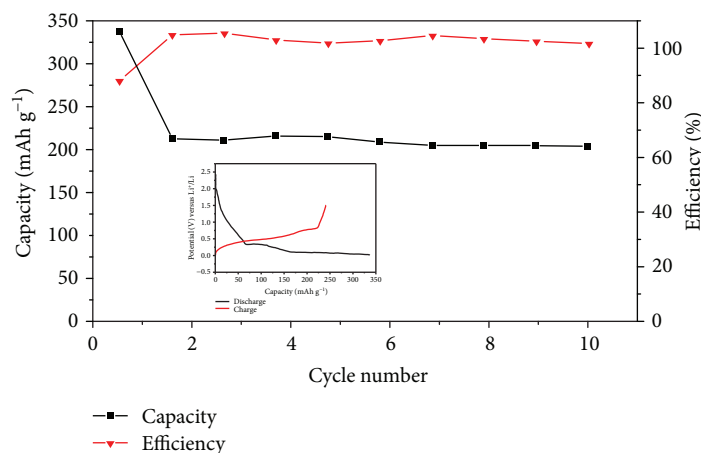


FIGURE 4: Charge-discharge performance and coulombic efficiency of a Cu-Sn cell at a current density of $C/10$ at room temperature.

energy dispersive X-ray analysis (EDS), and the results reveal only Cu and Sn elements in the substrate with a 3.5 : 1 ratio of Cu/Sn, corresponding to the stoichiometry of $\text{Cu}_{10}\text{Sn}_3$. The formation of hexagonal Cu-Sn is unique and the growth mechanism is not very clear. Both the natural environment and the property of Cu and Sn metals provided by the ionic liquid may have an important role in hexagonal prism growth.

Figure 4 displays the cycling performance and coulombic efficiency of the Cu-Sn cell at a current density of $C/10$ at room temperature. The first discharge platform of the Cu-Sn cell is about 0.35 V and the first charge platform is 0.5 V (inset in Figure 4). The initial charge and discharge capacities are about 250 mAh g^{-1} and 345 mAh g^{-1} , respectively. The initial cycle irreversible loss in capacities and lower coulombic efficiency can be seen in Figure 4. It may be attributed to the SEI film formed in the electrode surface and this is an irreversible process [15–17]. After 10 cycles, the discharge capacity stays at 210 mAh g^{-1} and the coulombic efficiency is about 100%. The capacity is lower than the theoretical capacity of Sn due to the Cu-Sn prism still undergoing volume expansion, but the hexagonal prism with Cu-Sn as the anode of LIB has an acceptable cycling performance [1, 18, 19]. Decreasing the size of the Cu-Sn prism or changing the condition during the preparation of nanostructural Cu-Sn probably could improve its capacity and cycle performance [20, 21].

4. Summary

The electrocrystallization of the hexagonal Cu-Sn prism, which is difficult to achieve in an aqueous solution, was obtained for the first time in a [Emim][DCA] ionic liquid at room temperature. Using the hexagonal Cu-Sn prism as the anode for LIB shows that the first discharge capacity is 345 mAh g^{-1} and the discharge capacity stays at 210 mAh g^{-1} after 10 cycles. The cell performance should be improved further; therefore, an in-depth study of this approach will provide a more precise control of the prism size for a synthesis of the nanostructure of the CuSn alloy for LIB.

Data Availability

(1) The cathodic polarization data used to support the findings of this study are included within the article. (2) The cyclic voltammogram data used to support the findings of this study are included within the article. (3) The XRD data used to support the findings of this study are included within the article. (4) The SEM images used to support the findings of this study are included within the article.

Conflicts of Interest

The authors declare that they have no conflicts of interest.

Acknowledgments

This project was supported by the National Natural Science Foundation of China (Grant no. 21276057).

References

- [1] J. W. Park, J. Y. Eom, and H. S. Kwon, "Charge-discharge characteristics of a layered-structure electroplated Cu/Sn anode for Li-ion batteries," *Electrochimica Acta*, vol. 55, no. 5, pp. 1825–1828, 2010.
- [2] X. Chen, J. Guo, K. Gerasopoulos et al., "3D tin anodes prepared by electrodeposition on a virus scaffold," *Journal of Power Sources*, vol. 211, pp. 129–132, 2012.
- [3] J. Hassoun, S. Panero, P. Simon, P. L. Taberna, and B. Scrosati, "High-rate, long-life Ni-Sn nanostructured electrodes for lithium-ion batteries," *Advanced Materials*, vol. 19, no. 12, pp. 1632–1635, 2007.
- [4] H. Y. Lee, S. W. Jang, S. M. Lee, S. J. Lee, and H. K. Baik, "Lithium storage properties of nanocrystalline Ni_3Sn_4 alloys prepared by mechanical alloying," *Journal of Power Sources*, vol. 112, no. 1, pp. 8–12, 2002.
- [5] X. Chen, Q. Ru, Z. Wang, X. Hou, and S. Hu, "Ternary Sn-Sb-Co alloy particles embedded in reduced graphene oxide as lithium ion battery anodes," *Materials Letters*, vol. 191, pp. 218–221, 2017.

- [6] S. D. Beattie and J. R. Dahn, "Single bath, pulsed electrodeposition of copper-tin alloy negative electrodes for lithium-ion batteries," *Journal of the Electrochemical Society*, vol. 150, no. 7, article A894, 2003.
- [7] Y. Wang and K. Wu, "As a whole: crystalline zinc aluminate nanotube array-nanonet," *Journal of the American Chemical Society*, vol. 127, no. 27, pp. 9686-9687, 2005.
- [8] Y. Yu, H. Qiu, X. Wu et al., "Synthesis and characterization of silica nanotubes with radially oriented mesopores," *Advanced Functional Materials*, vol. 18, no. 4, pp. 541-550, 2008.
- [9] L. Comai, J. C. Zomerdijk, H. Beckmann, S. Zhou, A. Admon, and R. Tjian, "Reconstitution of transcription factor SL1: exclusive binding of TBP by SL1 or TFIID subunits," *Science*, vol. 266, no. 5193, pp. 1966-1972, 1994.
- [10] Y. T. Hsieh, T. I. Leong, C. C. Huang, C. S. Yeh, and I. W. Sun, "Direct template-free electrochemical growth of hexagonal CuSn tubes from an ionic liquid," *Chemical Communications*, vol. 46, no. 3, pp. 484-486, 2010.
- [11] M. Armand, F. Endres, D. R. MacFarlane, H. Ohno, and B. Scrosati, "Ionic-liquid materials for the electrochemical challenges of the future," *Nature Materials*, vol. 8, no. 8, pp. 621-629, 2009.
- [12] Y. T. Hsieh and I. W. Sun, "Electrochemical growth of hierarchical CuSn nanobrushes from an ionic liquid," *Electrochemistry Communications*, vol. 13, no. 12, pp. 1510-1513, 2011.
- [13] M. J. Deng, T. I. Leong, I. W. Sun, P. Y. Chen, J. K. Chang, and W. T. Tsai, "Fabrication of porous tin by template-free electrodeposition of tin nanowires from an ionic liquid," *Electrochemical and Solid-State Letters*, vol. 11, no. 11, article D85, 2008.
- [14] T. I. Leong, I. W. Sun, M. J. Deng, C. M. Wu, and P. Y. Chen, "Electrochemical study of copper in the 1-ethyl-3-methylimidazolium dicyanamide room temperature ionic liquid," *Journal of the Electrochemical Society*, vol. 155, no. 4, article F55, 2008.
- [15] M. T. Lawder, P. W. C. Northrop, and V. R. Subramanian, "Model-based SEI layer growth and capacity fade analysis for EV and PHEV batteries and drive cycles," *Journal of the Electrochemical Society*, vol. 161, no. 14, pp. A2099-A2108, 2014.
- [16] H. Ekström and G. Lindbergh, "A model for predicting capacity fade due to SEI formation in a commercial graphite/LiFePO₄ cell," *Journal of the Electrochemical Society*, vol. 162, no. 6, pp. A1003-A1007, 2015.
- [17] M. Sina, R. Thorpe, S. Rangan et al., "Investigation of SEI layer formation in conversion iron fluoride cathodes by combined STEM/EELS and XPS," *Journal of Physical Chemistry C*, vol. 119, no. 18, pp. 9762-9773, 2015.
- [18] M. Winter and J. O. Besenhard, "Electrochemical lithiation of tin and tin-based intermetallics and composites," *Electrochimica Acta*, vol. 45, no. 1-2, pp. 31-50, 1999.
- [19] Y. Xia, T. Sakai, T. Fujieda, M. Wada, and H. Yoshinaga, "Flake Cu-Sn alloys as negative electrode materials for rechargeable lithium batteries," *Journal of the Electrochemical Society*, vol. 148, no. 5, article A471, 2001.
- [20] M. G. Kim, S. Sim, and J. Cho, "Novel core-shell Sn-Cu anodes for lithium rechargeable batteries prepared by a redox-transmetalation reaction," *Advanced Materials*, vol. 22, no. 45, pp. 5154-5158, 2010.
- [21] D. G. Kim, H. Kim, H. J. Sohn, and T. Kang, "Nanosized Sn-Cu-B alloy anode prepared by chemical reduction for secondary lithium batteries," *Journal of Power Sources*, vol. 104, no. 2, pp. 221-225, 2002.

Research Article

UCNPs@Zn_{0.5}Cd_{0.5}S Core-Shell and Yolk-Shell Nanostructures: Selective Synthesis, Characterization, and Near-Infrared-Mediated Photocatalytic Reduction of Cr(VI)

Wan-Ni Wang,¹ Wang Dong,¹ Chen-Xi Huang,¹ Bo Liu,¹ Sheng Cheng ^{1,2}
and Haisheng Qian ^{1,3}

¹School of Food and Bioengineering, Hefei University of Technology, Hefei 230009, China

²Instrumental Analysis Center, Hefei University of Technology, Hefei 230009, China

³Biomedical and Environmental Interdisciplinary Research Centre, Hefei 230010, China

Correspondence should be addressed to Sheng Cheng; chengsh@hfut.edu.cn and Haisheng Qian; shqian@hfut.edu.cn

Received 29 May 2018; Accepted 9 August 2018; Published 13 September 2018

Academic Editor: Zhengping Zhou

Copyright © 2018 Wan-Ni Wang et al. This is an open access article distributed under the Creative Commons Attribution License, which permits unrestricted use, distribution, and reproduction in any medium, provided the original work is properly cited.

Constructing near-infrared-light-mediated core-shell nanostructures incorporating upconversion nanoparticles (UCNPs) and semiconductors is of great importance for potential applications in photocatalysis, nano-biomedical engineering, solar cell, etc. In this work, we have demonstrated a two-step solution process to synthesize UCNPs@Zn_{0.5}Cd_{0.5}S core-shell nanoparticles (CSN). Firstly, a layer of AA-Zn(Cd)[OH]⁴⁻ composites was coated on UCNPs to form UCNPs@AA-Zn(Cd)[OH]⁴⁻ composites, which has been converted to UCNPs@Zn_{0.5}Cd_{0.5}S CSN via sulfidation reaction process using thioacetamide (TAA) as the sulfur source. Moreover, the UCNPs@Zn_{0.5}Cd_{0.5}S yolk-shell nanoparticles (YSN) have been obtained from the UCNPs@Zn_{0.5}Cd_{0.5}S CSN after calcination at 400°C, which show significantly photocatalytic activity for reduction of Cr(VI) under near-infrared light. All these can be attributed to the enhanced crystallization degree, resulting in enhanced energy transfer efficiency and separation efficiency of the photogenerated electrons and holes. An alternative strategy is provided in this study for fabrication of UCNP/semiconductor composites for various applications.

1. Introduction

The photocatalytic technology driven by solar light has become more and more attractive because solar energy is one of the most abundant resources [1–5]. Heterogeneous photocatalytic techniques based on semiconductor materials are widely used in photocatalytic decomposition of water, CO₂ reduction, and organic reactions [6–8]. Semiconductor materials have their unique electronic band structure, which will produce highly reactive electrons and holes when the electron of the valence band transits to the conduction band inspired by the light of appropriate wavelength. Moreover, the photogenerated electrons can reduce Cr(VI) under sunlight or simulated sunlight irradiation [9–12]. However, most of the semiconductor

photocatalysts can only be activated with UV or visible light. In particular, near-infrared (NIR) light occupies more than 40% of the incoming solar energy, which makes it more significant to fabricate and develop photocatalysts driven by NIR light [13–16]. Despite this, the traditional plasmonic nanoparticles which can be absorbed in the NIR region are used in catalysis, bioimaging, and so on [17–19]. However, lanthanide ions doped upconversion nanoparticles (UCNPs), which can convert infrared energy to UV-Vis energy and excite semiconductors to broaden the scope of the spectral response and raise the utilization ratio of solar energy. Up to date, much effort has been devoted to fabricate NIR-light-mediated UCNP-based nanocomposites to fully utilize solar energy [20–26], including UCNPs@CuS [27–30], UCNPs@ZnO [31–33],

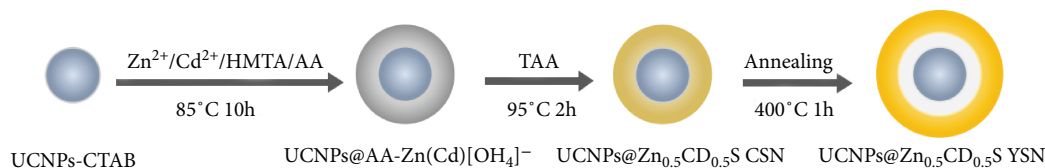


FIGURE 1: Schematic description of selective synthesis of UCNP@Zn_{0.5}Cd_{0.5}S core-shell and yolk-shell nanoparticles.

UCNPs@TiO₂ [34–37], UCNPs@Bi₂WO₆ [38, 39], and UCNPs@Bi₂MoO₆ [40–42]. As for the UCNP/semiconductor composites, the fluorescence energy can be passed from UCNPs (donors) to semiconductors (acceptors) to broaden the scope of the spectral response of the semiconductor effectively. These composite materials exhibit encouraging therapeutic efficacy of photodynamic therapy and the photochemical oxidation of organic matter under irradiation of NIR light [43, 44]. Many synthetic strategies including the epitaxial growth method, chemical assembly method, hydrothermal method, and electrospinning technique have been pioneered to fabricate UCNP-based Förster resonance energy transfer (FRET) nanostructures [45–49]. However, the large lattice mismatch makes it difficult for coating directly a layer of semiconductors on the surface of UCNPs.

Herein, a facile chemical solution process has been proposed to synthesize UCNP@Zn_{0.5}Cd_{0.5}S core-shell nanoparticles (CSN), in which UCNPs@AA-Zn(Cd)[OH]⁴⁻ composites are firstly synthesized and subsequently converted to UCNP@Zn_{0.5}Cd_{0.5}S CSN by liquid sulfidation, as shown in Figure 1(a). UCNP@Zn_{0.5}Cd_{0.5}S yolk-shell nanoparticles (YSN) can be derived from the as-obtained core-shell nanoparticles of UCNP@Zn_{0.5}Cd_{0.5}S after calcination owing to the UCNPs@Zn_{0.5}Cd_{0.5}S CSN incorporated by the surfactant. The optical properties of the samples have been studied carefully, and photochemical reduction tests of Cr(VI) ions are demonstrated.

2. Experimental

All the chemicals are of analytic grade and used as received. Hydrophilic NaYF₄:Yb(30%)/Tm(0.5%)/NaYF₄ (denoted as UCNPs) has been fabricated according to previously reported protocol [50, 51].

2.1. Synthesis of UCNP@AA-Zn(Cd)[OH]⁴⁻ Composites. In a typical process, 262.32 mg hexadecyltrimethylammonium bromide (CTAB) and 4.2 mg l-ascorbic acid (AA) were added into a 100 mL flask and dissolved using 60 mL deionized water to form clear solution. 2 mg as-prepared hydrophilic UCNPs, 25.24 mg hexamethylenetetramine (HMTA), 26.78 mg Zn(NO₃)₂·6H₂O, and 18.66 mg Cd(CH₃COO)₂·2H₂O with an equal mole ratio of Zn/Cd were added into the previous solution with stirring. Subsequently, the mixed solution was heated to 85°C and maintained for 10 h. Finally, the solution was centrifuged after cooling to room temperature at a speed of 9500 rpm to collect the products, then washed with ethanol and deionized

water for three times, and dried naturally. The yield of the UCNP@AA-Zn(Cd)[OH]⁴⁻ composites is about 90%.

2.2. Synthesis of UCNP@Zn_{0.5}Cd_{0.5}S Core-Shell and Yolk-Shell Nanoparticles. Typically, 20 mg previously prepared UCNP@AA-Zn(Cd)[OH]⁴⁻ composites and 3.76 mg TAA were added into a flask, which was dispersed using 15 mL deionized water and stirred for 12 h, then the temperature was raised to 95°C and kept for 2 h. The product in yellow was centrifugally separated (9500 rpm, 5 min) and the precipitate washed with deionized water and ethanol to remove the redundant ions. The as-synthesized UCNP@Zn_{0.5}Cd_{0.5}S core-shell nanoparticles were placed into a muffle furnace and then calcined at 400°C for 1 h to form UCNP@Zn_{0.5}Cd_{0.5}S yolk-shell nanoparticles (UCNP@Zn_{0.5}Cd_{0.5}S YSN). For comparison, UCNPs@ZnS CSN and UCNPs@ZnS YSN have been synthesized according to the same protocol. The yield of products at this stage is up to more than 95%.

2.3. Photocatalytic Activity. In a typical process, 5 mg of the photocatalyst was added under stirring into 50 mL of Cr(VI) solution (20 mg L⁻¹) which were prepared by dissolving K₂Cr₂O₇ into distilled water. The mixture was magnetically stirred for 1 h in the dark till adsorption-desorption equilibrium before irradiation. The solution was under irradiation of a 1500 mW cm⁻² xenon lamp (PLX-300D, Beijing Precise Technology Co. Ltd.) with an emission wavelength of 320 nm–2500 nm. The NIR band (780–2500 nm) was obtained by equipping with an UV-Vis filter. The photocatalyst was centrifugally separated (9500 rpm, 2 min), and the Cr(VI) concentration was determined by diphenylcarbazide (DPC) method.

3. Results and Discussion

In this work, UCNPs with ca. 42 nm in diameter have been prepared and used as NIR light nanotransducers (Figure S1a, in the Supporting Information) [50]. The UCNP@AA-Zn(Cd)[OH]⁴⁻ core-shell composites with 20 nm in shell thickness were synthesized by a modified process [33], as revealed by TEM image shown in Figure S1b (in the Supporting Information). The FESEM and TEM images of the sample, which were obtained from UCNP@AA-Zn(Cd)[OH]⁴⁻ composites and thioacetamide (TAA) at 95°C for 2 h have been shown in Figures 2(a)–2(c), showing the sample consisted of core-shell nanoparticles. The elemental images shown in Figure S2 (in the Supporting Information) confirm the chemical composition of the as-obtained sample. It is interesting to note that the

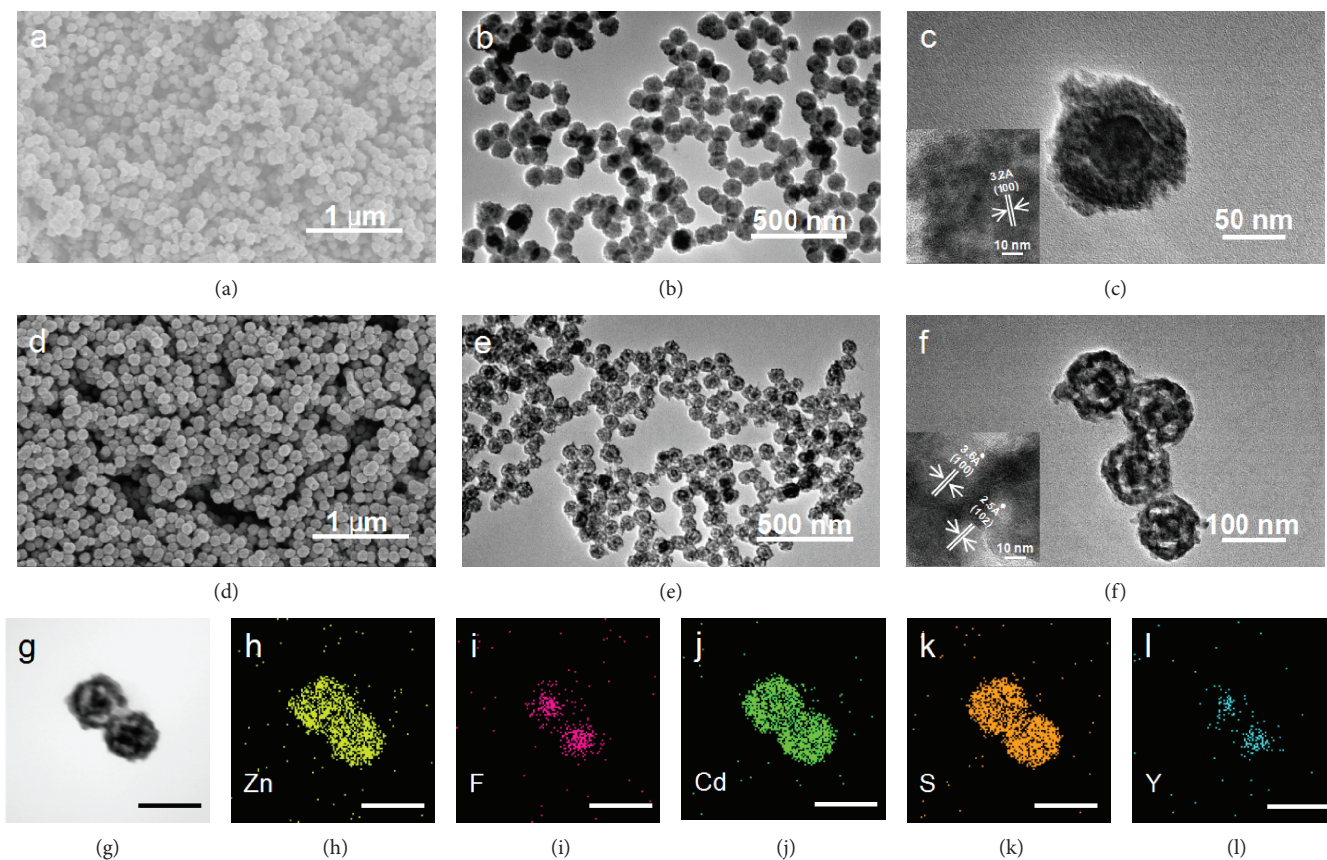


FIGURE 2: (a–c) FESEM, TEM, and HRTEM images of UCNPs@Zn_{0.5}Cd_{0.5}S CSN. (d–f) FESEM, TEM, and HRTEM images of UCNPs@Zn_{0.5}Cd_{0.5}S YSN. (g) STEM image of the UCNPs@Zn_{0.5}Cd_{0.5}S YSN. (h–l) Elemental mapping images; the scale bars are 100 nm.

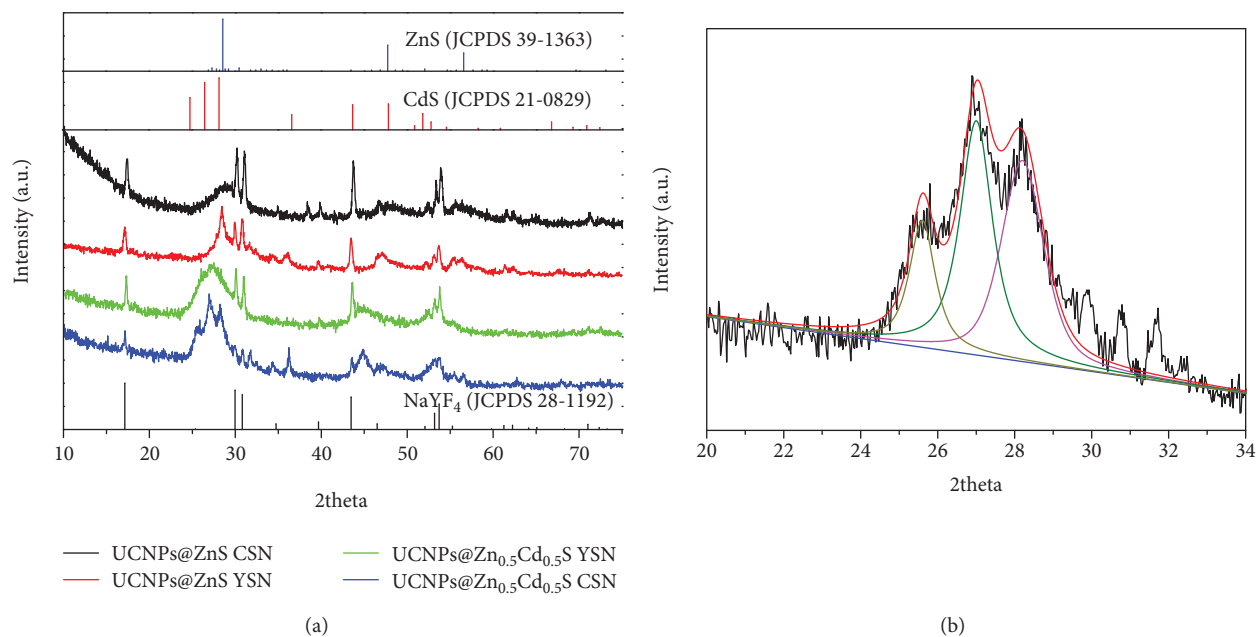


FIGURE 3: XRD patterns of the samples including UCNPs@ZnS CSN, UCNPs@ZnS YSN, UCNPs@Zn_{0.5}Cd_{0.5}S CSN, and UCNPs@Zn_{0.5}Cd_{0.5}S YSN.

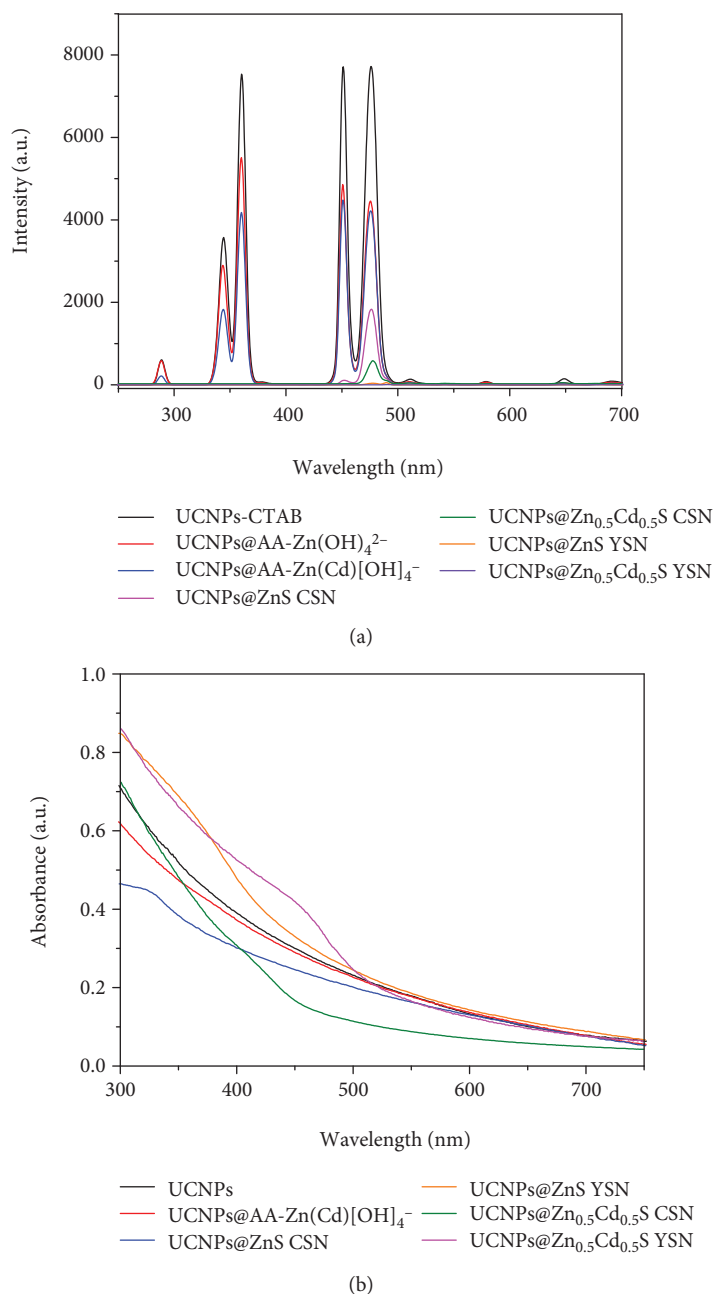


FIGURE 4: Fluorescence spectra (a) and UV-Vis absorbance (b) of different samples.

UCNPs@Zn_xCd_{1-x}S CSN has been converted to the yolk-shell-like nanoparticles obtained after annealing at 400°C for 1 h and the yolk-shell nanoparticles are ca. 80 nm in total diameter and 20 nm in shell thickness (Figures 2(d) and 2(e)). The lattice spacing of 3.6 and 2.5 Å from the shell edge is shown in Figure 2(f), which is a little smaller than that of the (100) and (102) crystal plane of CdS nanostructures [43], confirming that the shell component is alloyed Zn_xCd_{1-x}S. The STEM and elemental mapping images including Zn, F, Cd, and Y are shown in Figures 2(g)–2(l), which further confirm that the yolk-shell nanoparticles with a shell consisted of elements of Zn, Cd, and S. X-ray diffraction (XRD) has been used to characterize the phase of the samples. All the sharper diffraction peaks

(Figure 3(a)) coincide perfectly with the β-NaYF₄ (JCPDS no. 28–1192). On the side, the broad diffraction peak at 27° shown in Figure 3(b) can be derived to three peaks located at 25.6, 27.0, and 28.2° by Gaussian curve, which obviously shifted to higher diffraction angles of CdS (JCPDS no. 41–1049) compared to the pure CdS diffraction peaks at 24.8, 26.5, and 28.1° [52]. The EDX spectrum (Figure S3, in the Supporting Information) and XPS of UCNPs@Zn_xCd_{1-x}S YSN (Figure S4, in the Supporting Information) are also operated to decide the chemical composition of UCNPs@Zn_xCd_{1-x}S YSN. The accurate chemical composition of Zn/Cd in UCNPs@Zn_xCd_{1-x}S is 0.51/0.49, which has been calculated using atomic absorption spectroscopy (AAS). Therefore, all the above analyses

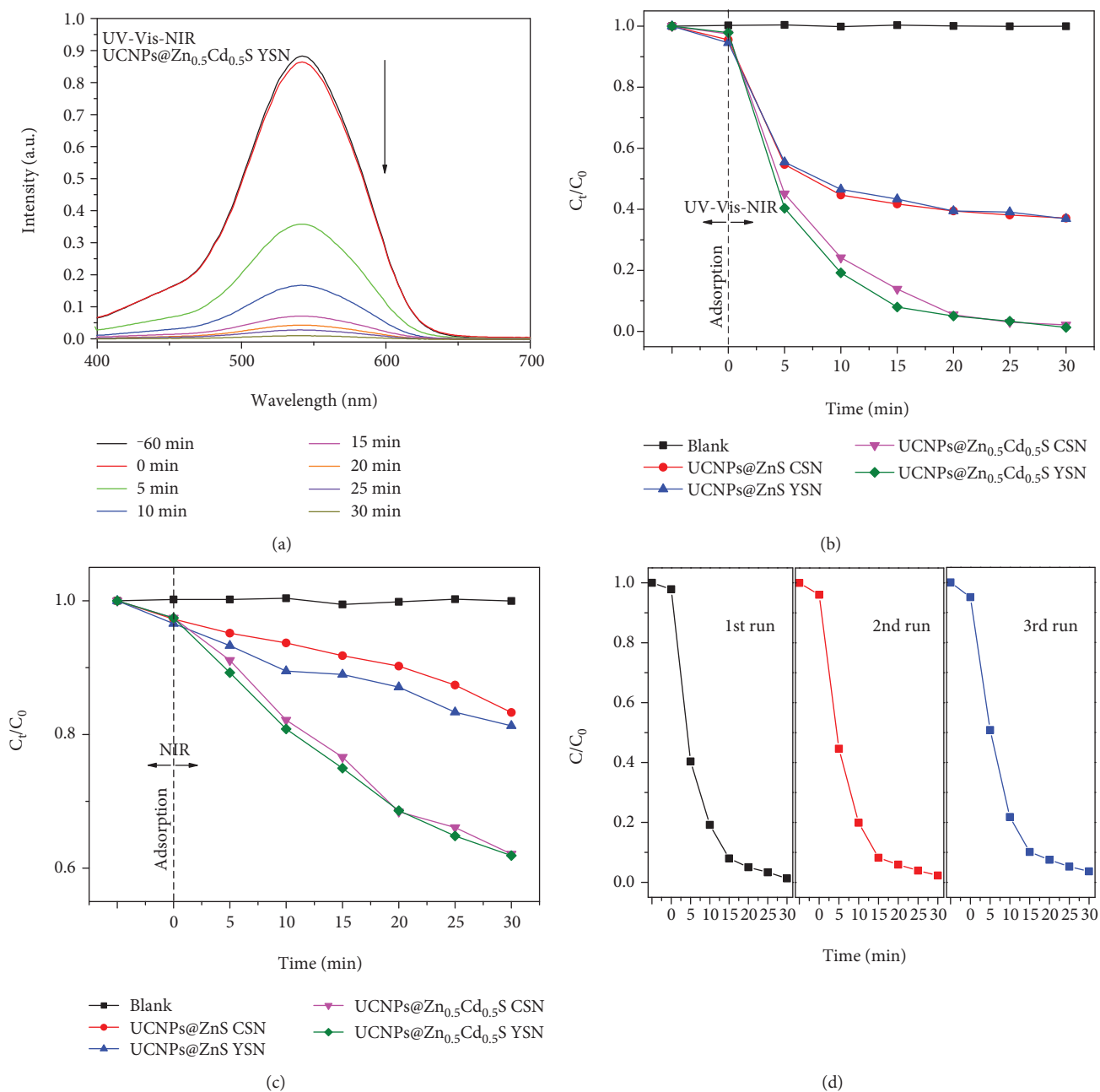


FIGURE 5: (a) UV-Vis spectra of the UV-Vis absorbance spectra of the Cr(VI) complex, showing the photochemical reduction ability of the UCNPs@Zn_{0.5}Cd_{0.5}S YSN towards photocatalytic reduction of Cr(VI) at given irradiation times using a Xe lamp. (b, c) Photochemical reduction kinetic curves of Cr(VI) aqueous solution under irradiation of NIR light and a simulated solar light, respectively. C_0 : the concentration of initial solution, C_t : the concentration at the irradiation time. (d) The three recycling tests of the photochemical reduction of Cr(VI) over the UCNPs@Zn_{0.5}Cd_{0.5}S YSN.

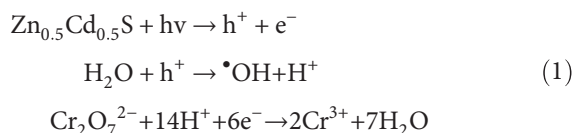
demonstrate successive synthesis of the CSN and YSN of UCNPs@Zn_{0.5}Cd_{0.5}S. Herein, the UCNPs@Zn_{0.5}Cd_{0.5}S CSN can be transferred to yolk-shell nanostructures because the shell (Zn_{0.5}Cd_{0.5}S) is comprised of lots of small nanoparticles stabilized by l-ascorbic acid (AA) molecules, as revealed by the FTIR spectra (Figure S5, in the Supporting Information). Some organic molecules or adsorbed functional group will be removed to form a void between the core and shell components during the annealing process whereas the small nanoparticles of Zn_{0.5}Cd_{0.5}S would be aggregated and the

crystallization degree of Zn_{0.5}Cd_{0.5}S will be improved. As expected, the UCNPs@Zn_{0.5}Cd_{0.5}S YSN show better photocatalytic ability than UCNPs@Zn_{0.5}Cd_{0.5}S CSN.

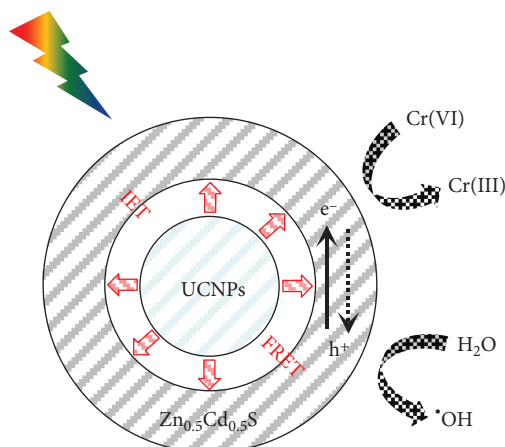
The fluorescence spectra (Edinburgh FLS980, UK) and UV-visible spectra (Hitachi U-5100, Japan) have been used to study the optical properties of the samples. It is worthy to note that the fluorescence emissions at 342, 361, 451, and 476 nm (Figure 4(a)) for UCNPs@Zn_{0.5}Cd_{0.5}S YSN have been quenched and the quenching efficiency is up to 99.90% for all the emissions (342, 361, 476, and 476 nm), confirming

that the yolk-shell nanoparticles show efficiently optical absorption and energy transfer between the yolk and shell. Figure 4(b) shows that the UCNP@Zn_{0.5}Cd_{0.5}S YSN exhibit stronger UV-Vis absorption at 400–600 nm, which overlap well with the fluorescence emissions of the UCNP and will result in an efficient FRET process occurring between UCNP and Zn_{0.5}Cd_{0.5}S. Thus, the as-prepared UCNP@Zn_{0.5}Cd_{0.5}S YSN will efficiently produce a large amount of reactive oxygen species including hydroxyl-free radicals ([•]OH) and photogenerated electrons under irradiation of NIR light or visible light.

In this work, the UCNP can give ultraviolet-visible light emissions under excitation of NIR light, which can activate the shell component (Zn_{0.5}Cd_{0.5}S) via irradiation energy transfer (IET) or FRET process. The electron from the valence band of the excited shell can transit to the conduction band under the appropriate wavelength excitation, then a large amount of photogenerated electrons (e⁻) is produced from the conduction band and positive hole (h⁺) from the valence band [46, 53]. After that, the positive hole (h⁺) can react with Cr(VI), which results in reduction of Cr(VI) to Cr(III). A rationalization mechanism for the photochemical reduction of Cr(VI) has been previously demonstrated as follows [54, 55]:



The terephthalic acid (TA) was used to generate the fluorescent product for detecting [•]OH radicals in solution [56, 57]. The fluorescence intensity of 2-hydroxy-terephthalic acid (TAOH) produced from terephthalic acid (TA) with [•]OH shows a dramatic enhancement with time (Figure S6, in the Supporting Information) in the presence of UCNP@Zn_{0.5}Cd_{0.5}S YSN under irradiation of NIR light, which verified that the YSN has the great ability to produce [•]OH and electrons. Thus, the as-prepared UCNP@Zn_{0.5}Cd_{0.5}S YSN would exhibit good NIR-mediated photochemical reduction or oxidation performance. In the present study, 50 mL (20 μg/mL) Cr(VI) aqueous solution was irradiated using infrared light (IR) or simulated solar light. Before irradiation, mixtures of the as-obtained photocatalysts and K₂Cr₂O₇ aqueous solution were stirred in the dark for 1 h to reach adsorption equilibrium. Diphenylcarbazide (DPC) method has been widely used to analyze the concentration of Cr(VI) [9]. As shown in Figure 5, there is no obvious change in the Cr(VI) concentration in the absence of the photocatalyst after irradiation for 1 h, whereas nearly 38.1% and 98.7% of Cr(VI) have been reduced to Cr(III) in 30 min for UCNP@Zn_{0.5}Cd_{0.5}S YSN under irradiation of a Xe lamp equipped with or without an UV-Vis filter. UCNP@Zn_{0.5}Cd_{0.5}S YSN has better photocatalytic activity property than UCNP@Zn_{0.5}Cd_{0.5}S CSN because of better crystallization during the annealing process and has the highest photocatalytic activity among all of the samples no matter with (Figure 5(b)) or without (Figure 5(c)) UV-Vis filter, indicating that the import of



SCHEME 1: Demonstration the NIR-light-mediated photochemical reduction process.

CdS can enhance the energy transfer efficiency between UCNP with the shell. Additionally, in order to investigate the repeatability and chemical stability of photocatalyst, three uninterrupted cycling tests have been operated and shown in Figure 5(d). Therefore, the as-prepared UCNP@Zn_{0.5}Cd_{0.5}S YSN shows good chemical stability, which has a strong ability for producing [•]OH and electrons for photochemical reduction of Cr(VI). The photocatalytic mechanism has been illustrated and summarized in Scheme 1. The synthetic method described here has demonstrated that it will provide an important strategy for constructing nanocomposite-incorporated UCNP and semiconductors for NIR-mediated photochemical process.

4. Conclusions

In summary, we have synthesized UCNP@Zn_{0.5}Cd_{0.5}S core-shell and yolk-shell nanoparticles by a facile epitaxial growth process. UCNP@AA-[Zn_{0.5}Cd_{0.5}(OH)₄]²⁻ nanocomposites are firstly synthesized via a modified process, which can be converted to UCNP@Zn_{0.5}Cd_{0.5}S CSN via a sulfidation reaction. The UCNP@Zn_{0.5}Cd_{0.5}S YSN can be achieved after calcination of UCNP@Zn_{0.5}Cd_{0.5}S CSN at 400°C. In addition, the crystallization degree for the final UCNP@Zn_{0.5}Cd_{0.5}S YSN has been enhanced during the annealing process. The fluorescence emissions for Tm³⁺ in UCNP@Zn_{0.5}Cd_{0.5}S yolk-shell nanoparticles have been quenched greatly, demonstrating efficient energy transfer between the achieved two components of UCNP and Zn_{0.5}Cd_{0.5}S. The as-obtained UCNP@Zn_{0.5}Cd_{0.5}S YSN exhibit superior photocatalytic activity for reduction of Cr(VI) under no matter simulated solar light or IR light. Therefore, this work should inspire further exploration for alternative nanoparticles with high potential for potential applications in nanomedicine, photocatalytic, energy conversion, etc.

Data Availability

The data used to support the findings of this study are available from the corresponding author upon request.

Conflicts of Interest

There are no conflicts of interest.

Authors' Contributions

W. Wang, F. Zhang, and W. Dong contributed equally to this work.

Acknowledgments

We acknowledge the funding supports from the National Natural Science Foundation of China (Grants 21471043 and 31501576).

Supplementary Materials

Figure S1: (a) transmission electron microscopy (TEM) image of $\text{NaYF}_4\cdot\text{Yb/Tm}@ \text{NaYF}_4$ nanoparticles. (b) Transmission electron microscopy (TEM) image of $\text{UCNPs}@ \text{AA-Zn}[(\text{OH})_4]^{2-}$ nanoparticles. Figure S2: STEM image and elemental imaging of $\text{UCNPs}@ \text{Zn}_{0.5}\text{Cd}_{0.5}\text{S}$ CSN. Figure S3: (a) energy-dispersive X-ray spectra of the as-prepared product shown in Figure 1; (b) element composition of the as-prepared $\text{UCNPs}@ \text{Zn}_{0.5}\text{Cd}_{0.5}\text{S}$ YSN from EDX analyses. Figure S4: X-ray photoelectron spectra of the as-prepared yolk-shell-like nanoparticles of $\text{UCNPs}@ \text{Zn}_{0.5}\text{Cd}_{0.5}\text{S}$ YSN: (a) a general survey; (b) Zn 2p; (c) Cd 3d; (d) S 2p; (e) Na 1s; (f) Y 3d; (g) Yb 4d; and (h) Tm 4d. Figure S5: Fourier transform infrared (FT-IR) spectrum of the as-prepared $\text{UCNPs}@ \text{Zn}_{0.5}\text{Cd}_{0.5}\text{S}$ CSN and $\text{UCNPs}@ \text{Zn}_{0.5}\text{Cd}_{0.5}\text{S}$ YSN. Figure S6: (a) fluorescence spectra of 2-hydroxy-terephthalic acid (TAOH) with the addition of $\text{UCNPs}@ \text{Zn}_{0.5}\text{Cd}_{0.5}\text{S}$ YSN excited by a 980 nm CW laser. (b) Photocatalytic reduction of Cr(VI) in the presence of $\text{UCNPs}@ \text{Zn}_{0.5}\text{Cd}_{0.5}\text{S}$ YSN at given irradiation times under irradiation of a 1500 mW Xe lamp with a UV-Vis filter. (*Supplementary Materials*)

References

- [1] H. Dong, G. Zeng, L. Tang et al., "An overview on limitations of TiO_2 -based particles for photocatalytic degradation of organic pollutants and the corresponding countermeasures," *Water Research*, vol. 79, pp. 128–146, 2015.
- [2] U. I. Gaya and A. H. Abdullah, "Heterogeneous photocatalytic degradation of organic contaminants over titanium dioxide: a review of fundamentals, progress and problems," *Journal of Photochemistry and Photobiology C: Photochemistry Reviews*, vol. 9, no. 1, pp. 1–12, 2008.
- [3] N. Cheng, J. Tian, Q. Liu et al., "Au-nanoparticle-loaded graphitic carbon nitride nanosheets: green photocatalytic synthesis and application toward the degradation of organic pollutants," *ACS Applied Materials & Interfaces*, vol. 5, no. 15, pp. 6815–6819, 2013.
- [4] X. Li, G. Chen, L. Yang, Z. Jin, and J. Liu, "Multifunctional Au-coated TiO_2 nanotube arrays as recyclable SERS substrates for multifold organic pollutants detection," *Advanced Functional Materials*, vol. 20, no. 17, pp. 2815–2824, 2010.
- [5] Z. Li, S. Yang, J. Zhou et al., "Novel mesoporous $\text{g-C}_3\text{N}_4$ and BiPO_4 nanorods hybrid architectures and their enhanced visible-light-driven photocatalytic performances," *Chemical Engineering Journal*, vol. 241, pp. 344–351, 2014.
- [6] M. N. Chong, B. Jin, C. W. K. Chow, and C. Saint, "Recent developments in photocatalytic water treatment technology: a review," *Water Research*, vol. 44, no. 10, pp. 2997–3027, 2010.
- [7] M. Mehrjouei, S. Muller, and D. Moller, "A review on photocatalytic ozonation used for the treatment of water and wastewater," *Chemical Engineering Journal*, vol. 263, pp. 209–219, 2015.
- [8] C. Yu, Z. Wu, R. Liu et al., "Novel fluorinated Bi_2MoO_6 nanocrystals for efficient photocatalytic removal of water organic pollutants under different light source illumination," *Applied Catalysis B: Environmental*, vol. 209, pp. 1–11, 2017.
- [9] X. Gao, H. B. Wu, L. Zheng, Y. Zhong, Y. Hu, and X. W. D. Lou, "Formation of mesoporous heterostructured $\text{BiVO}_4/\text{Bi}_2\text{S}_3$ hollow discoids with enhanced photoactivity," *Angewandte Chemie International Edition*, vol. 53, no. 23, pp. 5917–5921, 2014.
- [10] X. Meng, G. Zhang, and N. Li, " $\text{Bi}_{24}\text{Ga}_2\text{O}_{39}$ for visible light photocatalytic reduction of Cr(VI): controlled synthesis, facet-dependent activity and DFT study," *Chemical Engineering Journal*, vol. 314, pp. 249–256, 2017.
- [11] L. Mao, J. Li, Y. Xie, Y. Zhong, and Y. Hu, "Controllable growth of $\text{SnS}_2/\text{SnO}_2$ heterostructured nanoplates via a hydrothermal-assisted self-hydrolysis process and their visible-light-driven photocatalytic reduction of Cr(vi)," *RSC Advances*, vol. 4, no. 56, pp. 29698–29701, 2014.
- [12] G. M. Shi, B. Zhang, X. X. Xu, and Y. H. Fu, "Graphene oxide coated coordination polymer nanobelt composite material: a new type of visible light active and highly efficient photocatalyst for Cr(vi) reduction," *Dalton Transactions*, vol. 44, no. 24, pp. 11155–11164, 2015.
- [13] Z.-F. Huang, J. Song, L. Pan, X. Zhang, L. Wang, and J.-J. Zou, "Tungsten oxides for photocatalysis, electrochemistry, and phototherapy," *Advanced Materials*, vol. 27, no. 36, pp. 5309–5327, 2015.
- [14] S. Huang, S. Guo, Q. Wang et al., "CaF₂-based near-infrared photocatalyst using the multifunctional CaTiO_3 precursors as the calcium source," *ACS Applied Materials & Interfaces*, vol. 7, no. 36, pp. 20170–20178, 2015.
- [15] D.-X. Xu, Z.-W. Lian, M.-L. Fu, B. Yuan, J.-W. Shi, and H.-J. Cui, "Advanced near-infrared-driven photocatalyst: fabrication, characterization, and photocatalytic performance of $\beta\text{-NaYF}_4\cdot\text{Yb}^{3+}, \text{Tm}^{3+}@ \text{TiO}_2$ core@shell microcrystals," *Applied Catalysis B: Environmental*, vol. 142–143, pp. 377–386, 2013.
- [16] X. Y. Kong, W. L. Tan, B. J. Ng, S. P. Chai, and A. R. Mohamed, "Harnessing Vis-NIR broad spectrum for photocatalytic CO_2 reduction over carbon quantum dots-decorated ultrathin Bi_2WO_6 nanosheets," *Nano Research*, vol. 10, no. 5, pp. 1720–1731, 2017.
- [17] N. R. Jana, L. Gearheart, and C. J. Murphy, "Wet chemical synthesis of high aspect ratio cylindrical gold nanorods," *The Journal of Physical Chemistry B*, vol. 105, no. 19, pp. 4065–4067, 2001.
- [18] A. U. Khan, Z. Zhou, J. Krause, and G. Liu, "Poly(vinylpyrrolidone)-free multistep synthesis of silver nanoplates with plasmon resonance in the near infrared range," *Small*, vol. 13, no. 43, 2017.

- [19] V. Bastys, I. Pastoriza-Santos, B. Rodríguez-González, R. Vaisnoras, and L. M. Liz-Marzán, "Formation of silver nanoprisms with surface plasmons at communication wavelengths," *Advanced Functional Materials*, vol. 16, no. 6, pp. 766–773, 2006.
- [20] J. Ni, C. Shan, B. Li et al., "Assembling of a functional cyclodextrin-decorated upconversion luminescence nanoplat-form for cysteine-sensing," *Chemical Communications*, vol. 51, no. 74, pp. 14054–14056, 2015.
- [21] X. Wu, Y. Zhang, K. Takle et al., "Dye-sensitized core/active shell upconversion nanoparticles for optogenetics and bioimaging applications," *ACS Nano*, vol. 10, no. 1, pp. 1060–1066, 2016.
- [22] D. Lu, S. K. Cho, S. Ahn, L. Brun, C. J. Summers, and W. Park, "Plasmon enhancement mechanism for the upconversion processes in $\text{NaYF}_4:\text{Yb}^{3+}, \text{Er}^{3+}$ nanoparticles: Maxwell versus Förster," *ACS Nano*, vol. 8, no. 8, pp. 7780–7792, 2014.
- [23] V. Muhr, C. Wurth, M. Kraft et al., "Particle-size-dependent Förster resonance energy transfer from upconversion nanoparticles to organic dyes," *Analytical Chemistry*, vol. 89, no. 9, pp. 4868–4874, 2017.
- [24] G. Tian, W. Ren, L. Yan et al., "Red-emitting upconverting nanoparticles for photodynamic therapy in cancer cells under near-infrared excitation," *Small*, vol. 9, no. 11, pp. 1929–1938, 2013.
- [25] L. Wang, R. Yan, Z. Huo et al., "Fluorescence resonant energy transfer biosensor based on upconversion-luminescent nanoparticles," *Angewandte Chemie International Edition*, vol. 44, no. 37, pp. 6054–6057, 2005.
- [26] R. Lv, P. Yang, F. He et al., "A yolk-like multifunctional platform for multimodal imaging and synergistic therapy triggered by a single near-infrared light," *ACS Nano*, vol. 9, no. 2, pp. 1630–1647, 2015.
- [27] R. Lv, P. Yang, B. Hu, J. Xu, W. Shang, and J. Tian, "In situ growth strategy to integrate up-conversion nanoparticles with ultrasmall CuS for photothermal theranostics," *ACS Nano*, vol. 11, no. 1, pp. 1064–1072, 2017.
- [28] B. Liu, C. Li, Z. Xie et al., "808 nm photocontrolled UCL imaging guided chemo/photothermal synergistic therapy with single UCNPs-CuS@PAA nanocomposite," *Dalton Transactions*, vol. 45, no. 33, pp. 13061–13069, 2016.
- [29] G. Yang, R. Lv, F. He et al., "A core/shell/satellite anticancer platform for 808 NIR light-driven multimodal imaging and combined chemo-/photothermal therapy," *Nanoscale*, vol. 7, no. 32, pp. 13747–13758, 2015.
- [30] C. X. Huang, H. J. Chen, F. Li et al., "Controlled synthesis of upconverting nanoparticles/CuS yolk-shell nanoparticles for in vitro synergistic photothermal and photodynamic therapy of cancer cells," *Journal of Materials Chemistry B*, vol. 5, no. 48, pp. 9487–9496, 2017.
- [31] S. Huang, H. Wang, N. Zhu et al., "Metal recovery based magnetite near-infrared photocatalyst with broadband spectrum utilization property," *Applied Catalysis B: Environmental*, vol. 181, pp. 456–464, 2016.
- [32] W. N. Wang, F. Zhang, C. L. Zhang, Y. C. Guo, W. Dai, and H. S. Qian, "Fabrication of zinc oxide composite microfibers for near-infrared-light-mediated photocatalysis," *ChemCatChem*, vol. 9, no. 18, pp. 3611–3617, 2017.
- [33] F. Zhang, W. N. Wang, H. P. Cong, L. B. Luo, Z. B. Zha, and H. S. Qian, "Facile synthesis of upconverting nanoparticles/zinc oxide core-shell nanostructures with large lattice mismatch for infrared triggered photocatalysis," *Particle & Particle Systems Characterization*, vol. 34, no. 2, article 1600222, 2017.
- [34] F. Zhang, C. L. Zhang, H. Y. Peng, H. P. Cong, and H. S. Qian, "Near-infrared photocatalytic upconversion nanoparticles/ TiO_2 nanofibers assembled in large scale by electrospinning," *Particle & Particle Systems Characterization*, vol. 33, no. 5, pp. 248–253, 2016.
- [35] Y. Tang, W. di, X. Zhai, R. Yang, and W. Qin, "NIR-responsive photocatalytic activity and mechanism of $\text{NaYF}_4:\text{Yb}, \text{Er}@\text{TiO}_2$ core-shell nanoparticles," *ACS Catalysis*, vol. 3, no. 3, pp. 405–412, 2013.
- [36] S. Zhuo, M. Shao, and S.-T. Lee, "Upconversion and down-conversion fluorescent graphene quantum dots: ultrasonic preparation and photocatalysis," *ACS Nano*, vol. 6, no. 2, pp. 1059–1064, 2012.
- [37] Y. Zhang and Z. Hong, "Synthesis of lanthanide-doped $\text{NaYF}_4@\text{TiO}_2$ core-shell composites with highly crystalline and tunable TiO_2 shells under mild conditions and their upconversion-based photocatalysis," *Nanoscale*, vol. 5, no. 19, pp. 8930–8933, 2013.
- [38] Z. Zhang, W. Wang, W. Yin, M. Shang, L. Wang, and S. Sun, "Inducing photocatalysis by visible light beyond the absorption edge: effect of upconversion agent on the photocatalytic activity of Bi_2WO_6 ," *Applied Catalysis B: Environmental*, vol. 101, no. 1–2, pp. 68–73, 2010.
- [39] Z. Zhang, W. Wang, J. Xu, M. Shang, J. Ren, and S. Sun, "Enhanced photocatalytic activity of Bi_2WO_6 doped with upconversion luminescence agent," *Catalysis Communications*, vol. 13, no. 1, pp. 31–34, 2011.
- [40] R. Adhikari, G. Gyawali, S. H. Cho, R. Narro-Garcia, T. Sekino, and S. W. Lee, " $\text{Er}^{3+}/\text{Yb}^{3+}$ co-doped bismuth molybdate nanosheets upconversion photocatalyst with enhanced photocatalytic activity," *Journal of Solid State Chemistry*, vol. 209, pp. 74–81, 2014.
- [41] T. Zhou, J. Hu, and J. Li, " Er^{3+} doped bismuth molybdate nanosheets with exposed {0 1 0} facets and enhanced photocatalytic performance," *Applied Catalysis B: Environmental*, vol. 110, pp. 221–230, 2011.
- [42] Y. Sun, W. Wang, S. Sun, and L. Zhang, " $\text{NaYF}_4:\text{Er}, \text{Yb}/\text{Bi}_2\text{MoO}_6$ core/shell nanocomposite: a highly efficient visible-light-driven photocatalyst utilizing upconversion," *Materials Research Bulletin*, vol. 52, pp. 50–55, 2014.
- [43] J. Xu, R. Lv, S. du et al., "UCNPs@gelatin-ZnPc nanocomposite: synthesis, imaging and anticancer properties," *Journal of Materials Chemistry B*, vol. 4, no. 23, pp. 4138–4146, 2016.
- [44] F. Zhang, C. L. Zhang, W. N. Wang, H. P. Cong, and H. S. Qian, "Titanium dioxide/upconversion nanoparticles/cadmium sulfide nanofibers enable enhanced full-spectrum absorption for superior solar light driven photocatalysis," *ChemSusChem*, vol. 9, no. 12, pp. 1449–1454, 2016.
- [45] J. T. Xu, F. He, Z. Y. Cheng et al., "Yolk-structured upconversion nanoparticles with biodegradable silica shell for FRET sensing of drug release and imaging-guided chemotherapy," *Chemistry of Materials*, vol. 29, pp. 7615–7628, 2017.
- [46] W. N. Wang, C. X. Huang, C. Y. Zhang et al., "Controlled synthesis of upconverting nanoparticles/ $\text{Zn}_x\text{Cd}_{1-x}\text{S}$ yolk-shell nanoparticles for efficient photocatalysis driven by NIR light," *Applied Catalysis B: Environmental*, vol. 224, pp. 854–862, 2018.
- [47] W. Su, M. Zheng, L. Li et al., "Directly coat TiO_2 on hydrophobic $\text{NaYF}_4:\text{Yb}, \text{Er}$ nanoplates and regulate their photocatalytic

- activities with the core size,” *Journal of Materials Chemistry A*, vol. 2, no. 33, pp. 13486–13491, 2014.
- [48] W. Wang, M. Ding, C. Lu, Y. Ni, and Z. Xu, “A study on upconversion UV–vis–NIR responsive photocatalytic activity and mechanisms of hexagonal phase $\text{NaYF}_4:\text{Yb}^{3+}, \text{Tm}^{3+}@\text{TiO}_2$ core–shell structured photocatalyst,” *Applied Catalysis B: Environmental*, vol. 144, pp. 379–385, 2014.
- [49] X. Guo, C. Chen, D. Zhang, C. P. Tripp, S. Yin, and W. Qin, “Photocatalysis of $\text{NaYF}_4:\text{Yb}, \text{Er}/\text{CdSe}$ composites under 1560 nm laser excitation,” *RSC Advances*, vol. 6, no. 10, pp. 8127–8133, 2016.
- [50] H. Fan, E. Leve, J. Gabaldon, A. Wright, R. E. Haddad, and C. J. Brinker, “Ordered two- and three-dimensional arrays self-assembled from water-soluble nanocrystal–micelles,” *Advanced Materials*, vol. 17, no. 21, pp. 2587–2590, 2005.
- [51] B. B. Ding, H. Y. Peng, H. S. Qian, L. Zheng, and S. H. Yu, “Unique upconversion core–shell nanoparticles with tunable fluorescence synthesized by a sequential growth process,” *Advanced Materials Interfaces*, vol. 3, no. 3, 2016.
- [52] J. Chen, B. B. Ding, T. Y. Wang et al., “Facile synthesis of uniform $\text{Zn}_x\text{Cd}_{1-x}\text{S}$ alloyed hollow nanospheres for improved photocatalytic activities,” *Journal of Materials Science: Materials in Electronics*, vol. 25, no. 9, pp. 4103–4109, 2014.
- [53] J. Zhang, W.-N. Wang, M.-L. Zhao et al., “Magnetically recyclable $\text{Fe}_3\text{O}_4@\text{Zn}_x\text{Cd}_{1-x}\text{S}$ core–shell microspheres for visible light-mediated photocatalysis,” *Langmuir*, vol. 34, no. 31, pp. 9264–9271, 2018.
- [54] H. Yoneyama, Y. Yamashita, and H. Tamura, “Heterogeneous photocatalytic reduction of dichromate on n-type semiconductor catalysts,” *Nature*, vol. 282, no. 5741, pp. 817–818, 1979.
- [55] S. E. Fendorf and R. J. Zamoski, “Chromium(III) oxidation by δ -manganese oxide (MnO_2). 1. Characterization,” *Environmental Science & Technology*, vol. 26, no. 1, pp. 79–85, 1992.
- [56] Y. Nosaka and A. Y. Nosaka, “Generation and detection of reactive oxygen species in photocatalysis,” *Chemical Reviews*, vol. 117, no. 17, pp. 11302–11336, 2017.
- [57] H. Wang, S. Jiang, W. Shao et al., “Optically switchable photocatalysis in ultrathin black phosphorus nanosheets,” *Journal of the American Chemical Society*, vol. 140, no. 9, pp. 3474–3480, 2018.

Research Article

Effects of Biceramic AlN-SiC Microparticles on the Thermal Properties of Paraffin for Thermal Energy Storage

Arash Badakhsh,^{1,2} Kay-Hyeok An ,³ Chan Woo Park ,² and Byung-Joo Kim ¹

¹Research Laboratory for Multifunctional Carbon Materials, Korea Institute of Carbon Convergence Technology (KCTECH), Jeonju, Jeonbuk 54853, Republic of Korea

²Department of Mechanical Design Engineering, Chonbuk National University, Jeonju, Jeonbuk 54896, Republic of Korea

³Department of Carbon and Nano Materials Engineering, Jeonju University, Jeonju 55069, Republic of Korea

Correspondence should be addressed to Kay-Hyeok An; khandragon@jj.ac.kr, Chan Woo Park; cw-park@jbnu.ac.kr, and Byung-Joo Kim; kimbj2015@gmail.com

Received 23 March 2018; Accepted 28 May 2018; Published 6 September 2018

Academic Editor: Yichen Guo

Copyright © 2018 Arash Badakhsh et al. This is an open access article distributed under the Creative Commons Attribution License, which permits unrestricted use, distribution, and reproduction in any medium, provided the original work is properly cited.

Herein, simplified time-efficient production of AlN-coated SiC (SiC@AlN) ceramic powder was practiced. Short-term vibratory ball milling with high frequency was employed to integrate the microsize particles. Also, paraffin as a significant phase change material (PCM) was reinforced using the manufactured SiC@AlN in order to enhance the thermal conductivity (TC) and stability of the final composite. Various characterization methods were used to clarify the changes in particle size of the biceramic powder as well as the thermal features of the paraffin-based composite. Manufactured SiC@AlN was found to be the most effective in the improvement of interfacial adhesion of composite components and the subsequent enhancement of TC, compared with singular ceramic powders as the reinforcing agents. Also, differential scanning calorimetry (DSC) indicated a very slight increase in latent heat of the fabricated composite PCM.

1. Introduction

Energy can be stored in different forms via a variety of methods. Among these, storage of energy utilizing the latent heat thermal storage (LHTS) and phase change is of interest owing to its simplicity and efficiency and to the abundance of such forms of wasted energy in large quantities. Several characteristics of paraffin wax including suitable melting point, large latent heat (145–240 kJ/kg), chemical stability with regular degradation level, process adaptability, low cost, and low environmental effects present this material as a promising phase change material (PCM) for LHTS purposes. However, engineers still face a significant challenge dealing with paraffin, specifically its intrinsic low thermal conductivity (i.e., below 0.4 W/m·K). To tackle such difficulty and further improve the desired responses in energy storage such as melting/solidification onset temperatures, durability, and chemical inertness, additives have been used to produce a paraffin-based composite PCM [1–7].

Due to their substantially high melting point, chemical stability and durability, and significant high-temperature tolerability, ceramics could also be used as efficient media for energy storage. Dhaidan et al. [8] used CuO for paraffin reinforcement and performed experimental and numerical investigations on the melting behaviour of the resultant composite PCM. Ho and Gao [9] reported the changes in the values of thermal conductivity and effective dynamic viscosity for the paraffin-based PCM loaded with 0, 5, and 10 wt.% of Al₂O₃ as the reinforcing agent. As a result, a rather nonlinear dependence of the thermal conductivity and the effective dynamic viscosity of the PCM on the mass fraction of Al₂O₃ was observed. A maximum increase in thermal conductivity was reported to be 17% by using 10 wt.% of Al₂O₃ measured at 60°C. A comparison between Al₂O₃ and CuO was numerically studied by Valan Arasu et al. [10] on the thermal performance enhancement of paraffin wax. They reported a marginal enhancement with both fillers, where the melting and solidification behaviour of Al₂O₃@paraffin

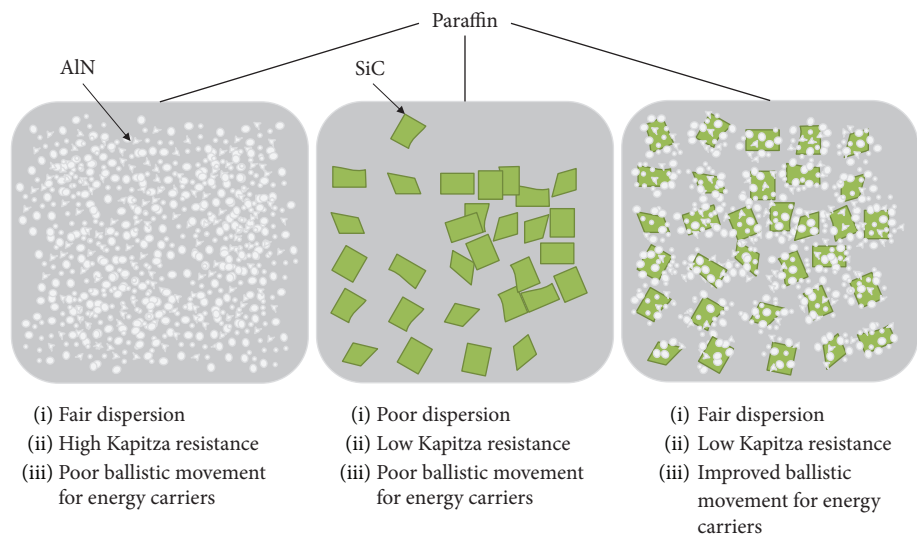


FIGURE 1: Schematic illustration of the formation of the better filler-matrix interface and better pathways for heat conduction in SiC@AlN powder.

was better due to the lower growth in dynamic viscosity compared to the use of CuO as a filler with the same mass fraction. Teng and Yu [11] experimentally studied the effect of different ceramic additives (Al_2O_3 , TiO_2 , SiO_2 , and ZnO) on the LHTS performance of paraffin wax. They concluded that TiO_2 exhibits a better enhancement in thermal energy storage performance as it increases the thermal conduction and solidification onset temperature while reducing the melting onset temperature of paraffin. In the present study, a new series of ceramic fillers were employed to enhance the thermal energy storage behaviour of paraffin. Because of their low density, low thermal expansion, considerably high thermal conductivity, superior thermal shock resistance, and relatively low cost, aluminium nitride (AlN) [12] and silicon carbide (SiC) were selected as the target ceramic fillers. Interface enhancement is the most significant issue in fabrication of composites. Recently, a rather new trend of multiple-filler composite systems has emerged which is aimed at surface enhancement of components to achieve better interactions between the filler and the matrix [13–17]. Herein, to facilitate the encapsulation of SiC particles and subsequent formation of passages for heat conduction within the matrix, a considerable gap was selected between the average sizes of particles for the two ceramic components. The objective is to enhance the adhesion of the paraffin wax to the powder (see Figure 1). For this purpose, production of AlN-coated SiC (SiC@AlN) via time-efficient high-energy ball milling was practiced to unveil the effect of biceramic blend as well as of the singular fillers on the thermal performance of the resultant PCMs. A variety of characterization methods were carried out to thoroughly investigate the fillers and thermal features of the final composite PCMs.

2. Materials and Methods

2.1. Materials. Paraffin wax, aluminium nitride (powder, $\geq 98\%$), and silicon carbide (powder, 200–450 meshes) were all purchased from Sigma-Aldrich Chemicals Company, United

States. All of the mentioned materials were used without any further purification. Some of the physical and thermophysical specifications of as-received materials are shown in Table 1.

2.2. Powder Preparation. The mechanical alloying method via vibratory mini ball mill (Pulverisette 23, Fritsch International, Germany) was used in order to mechanically fuse the AlN on the surface of SiC particles and enhance the particle bonding in the biceramic powder. Also, it likely facilitates the production of a uniformly distributed particle size within the functionally coated SiC, where AlN and SiC particles are 6 and $67.8\ \mu\text{m}$ in diameter, respectively. Accordingly, SiC@AlN powder is expected to enhance the thermal energy storage capacity of paraffin while maintaining the intrinsic low electrical conductivity of the matrix as it could be potentially used as phase change thermal energy storage medium.

Different variables have been considered to optimize the integration and uniformity of the final SiC@AlN powder. 15, 30, and 50 Hz were chosen as the studied milling frequencies, where the milling time and ball-to-powder mass ratio (BPR) vary from 15 to 120 min and 4:1 to 20:1, respectively. The mass fraction of each component in the biceramic powder was kept constant at 50 wt.%. The grinding ball (15 mm in diameter) and the milling vial (10 ml) were both made of zirconia (95% ZrO_2).

For single-filler systems, AlN particles were used as received and pristine (as-received) SiC particles were exposed to the mechanical stress via ball milling for 60 min at 50 Hz to minimize the deposition of powder while moulding and enhance the dispersion of SiC within the matrix. Ball-milled SiC with an average particle diameter of about $28.53\ \mu\text{m}$ will be referred to as “SiC” throughout this report unless otherwise mentioned.

2.3. Composite PCM Preparation. Uniformly mixing the composed biceramic powder with the liquefied paraffin is the next step in the PCM fabrication. A rather simple, but

TABLE 1: Specifications of as-received materials.

Material	Average particle size (μm)	ρ (g/cm^3) at 25°C [18]	k ($\text{W}/\text{m}\cdot\text{K}$) at 25°C	C_p ($\text{J}/\text{kg}\cdot\text{K}$) at 0–100°C	Melting point (°C) [18]
Paraffin wax	—	0.90	<0.4 [19]	2140–2900 [20]	53–57 (ASTM D87)
Aluminium nitride (AlN)	6.0	3.26	320 [21]	819.7 [22]	>2200
Silicon carbide (SiC)	67.8	3.22	270 [21]	675.4 [23]	2700

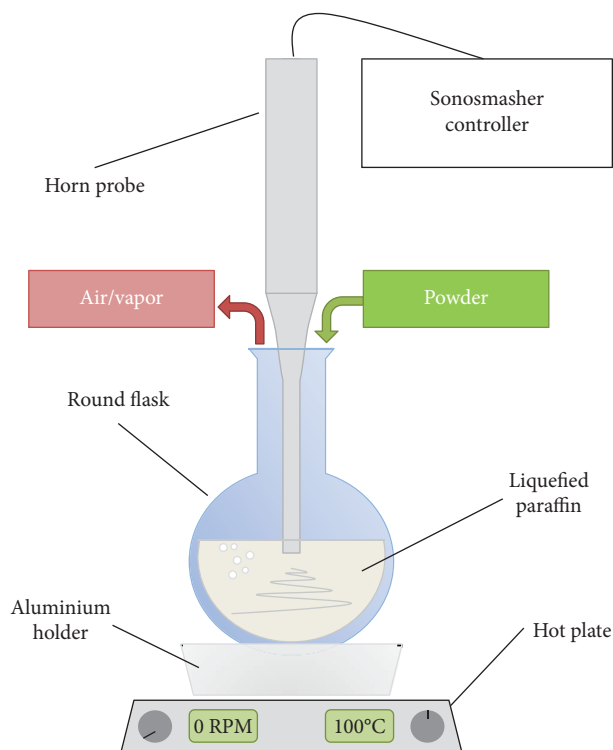


FIGURE 2: Graphic illustration of the mixing process.

effective, method was used employing an ultrasonic generator (Sonosmasher, Ulssco Hitech Co. Ltd., Korea) to increase the dispersion of the solid particles within the melted paraffin wax while reducing the number of trapped bubbles and gaseous impurities in the mixture. This process is graphically shown in Figure 2. During the sonication process, the mixture was regularly monitored to ensure the minimum deposition of the powder by controlling the input power of the ultrasonic generator (10–30%). The hot plate was kept at 100°C, and the mass fraction ratio of the filler to the whole composite PCM is 5 wt.% for all the cases.

3. Results and Discussion

3.1. Particle Morphology. SEM images of the as-received and as-prepared particles are shown in Figure 3. As seen here, AlN particles are physically attached to the surface of the deformed SiC.

3.2. Particle Size Analysis. A step-by-step procedure via a laser diffraction particle size analyzer (Microtrac S3500

integrated with a wet SDC unit, Microtrac Inc., United States) was carried out to individually optimize each parameter leading to the final set of optimum variables. Firstly, the effect of different milling frequencies (15, 30, and 50 Hz) with variations in BPR on the particle size distribution (PSD) was examined, while the ball milling time was kept constant at 15 min. The PSD graphs are illustrated in Figure 4 with respect to changes in the milling frequency. As the ball milling frequency increases, the particle diameter tends to decrease, specifically a dramatic reduction in the highest peak, due to the impact force and shear stress between the particles, ball, and walls of the milling vial. It also indicates that the particle size integration in SiC@AlN powder is possible as multiplex graphs are inclined to unify in a single-peak curve with the increase in frequency. Therefore, the mechanical stress when the milling frequency is at 50 Hz tends to alloy the AlN on SiC particles noting that fracture effects are also at minimum due to the large gap of about 11 times between the particle sizes of as-received powders.

Secondly, following the optimization of milling frequency, further variations of BPR were also undertaken to enhance the integration, while delivering a handful amount of powder for PCM preparation. As shown in Figure 5(a), the rise in BPR gradually flattens the volume distribution of lower peaks which in turn heightens the desired singular peak at a fair SiC@AlN particle size falling between the average sizes for as-received AlN and SiC powders. Given 20:1 as BPR, 0.3301 g of powder was prepared in a single run for PCM reinforcement.

Thirdly, following the optimization of milling frequency and BPR, the milling time was studied to conclude the process. Figure 5(b) displays the PSD graphs with respect to changes in the milling time. Results imply the consistency of the average SiC@AlN particle size after 60 min (up to 120 min) maintaining 33.9 μm in value. The only difference was the slight reduction observed in the number of smaller particles. Hence, according to Figures 4 and 5, the optimum milling conditions for obtaining the largest SiC@AlN particles would be 60 minutes of mechanical alloying while milling frequency and BPR are at 50 Hz and 20:1, respectively.

3.3. XRD Analysis. X-ray diffraction (XRD MAX-2500, Rigaku Corp., Japan) analysis was carried out to establish a better understanding of the powder integration via ball milling. As seen in Figure 6, the crystal structure of singular ceramic powders was barely altered after low-energy milling. High-energy milled powders, however, have responded well



FIGURE 3: SEM images of the as-received and as-prepared particles.

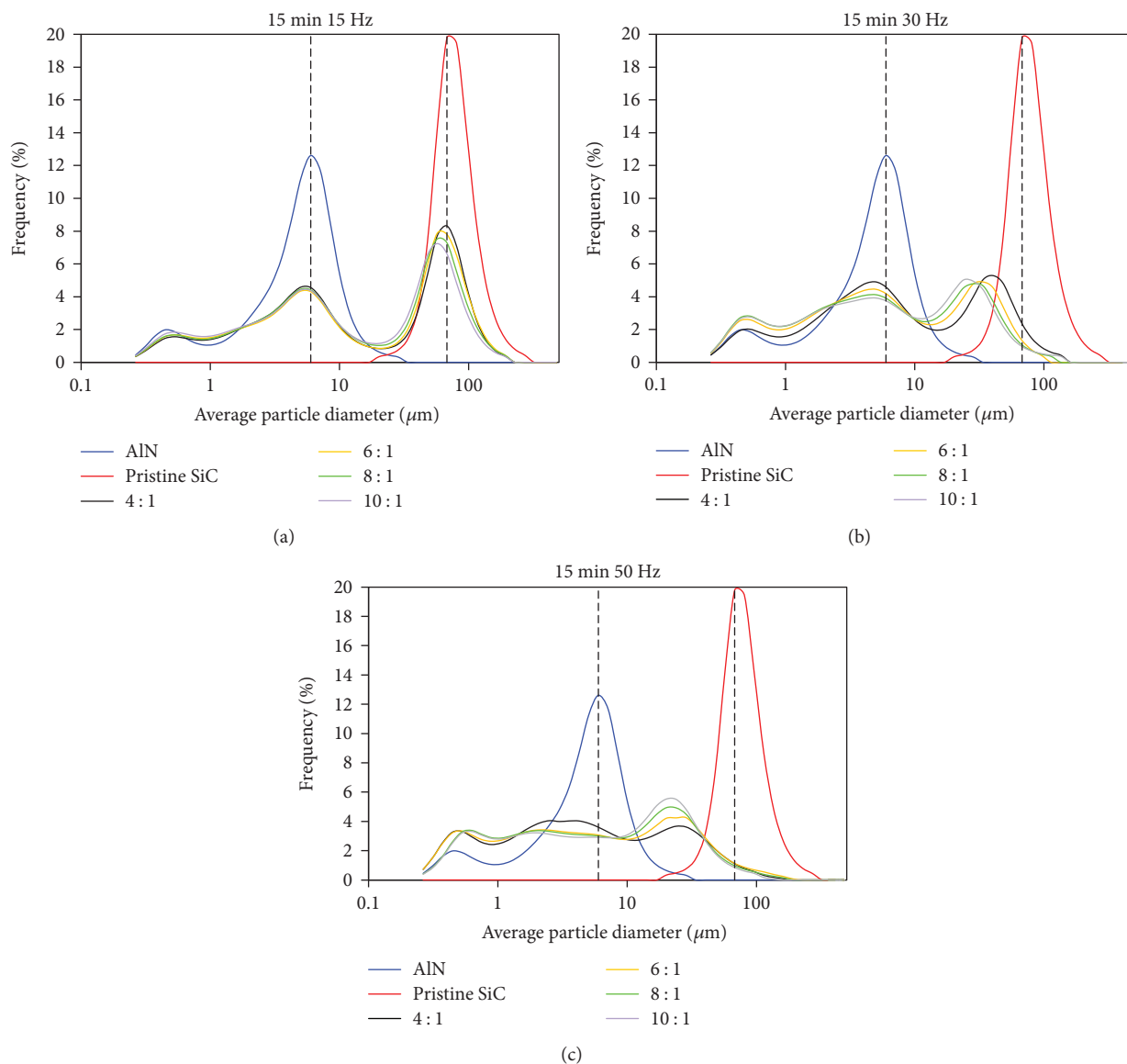


FIGURE 4: PSD graphs of AlN, pristine SiC, and SiC@AlN (50 wt.% AlN/50 wt.% SiC) powders with respect to different milling frequencies and BPRs.

to lattice integration as the peaks for SiC and AlN are merged at $2\theta = 35.5^\circ, 37.6^\circ, 60^\circ, 65^\circ,$ and 71° . This can be attributed to the formation of SiC@AlN particles due to mechanical

stresses and temperature growth in the vial. Also, the increase in milling time will result in Bragg's angle shift implying exertion of higher levels of uniform strains. XRD

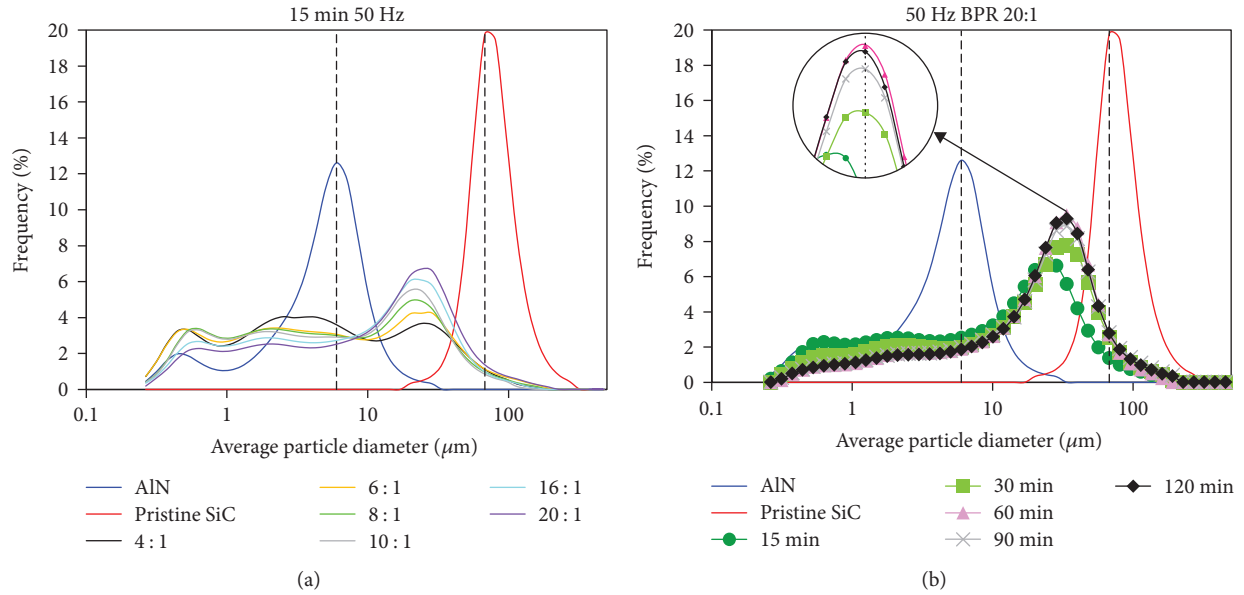


FIGURE 5: PSD graphs of AlN, pristine SiC, and SiC@AlN (50 wt.% AlN/50 wt.% SiC) powders with respect to different BPRs and milling periods.

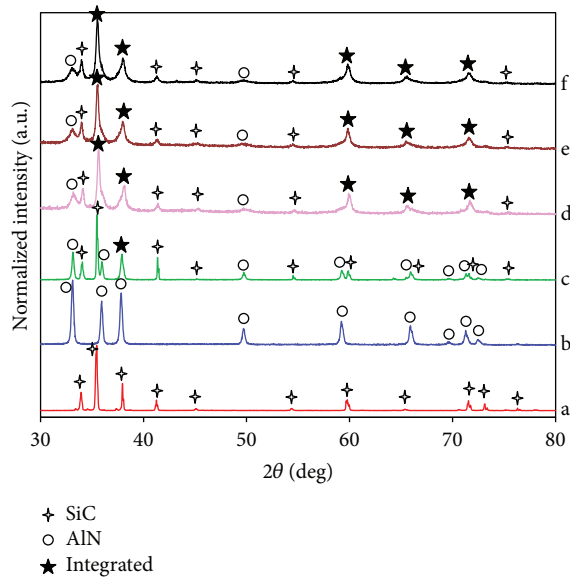


FIGURE 6: XRD patterns of SiC (a), AlN (b), and SiC@AlN powders after low-energy milling ($t_{BM} = 15$ min, $f_{BM} = 15$ Hz, BPR $\equiv 4 : 1$) (c) and high-energy milling ($f_{BM} = 50$ Hz, BPR $\equiv 20 : 1$) where the milling times were 60 (d), 90 (e), and 120 min (f).

then confirms the previous statement claiming that the integration was adequately done by 60 min of milling and a further increase in the time will merely reduce the number of smaller particles.

3.4. Surface Properties. The surface free energy (SFE) of reinforcing powders was analyzed using the sessile drop technique (Tilt Controller, Surface Electro Optics, Korea). Several samples were prepared using uniformly dispersed

powder over adhesive tapes. Distilled water and diiodomethane (Sigma-Aldrich Chemicals Company, United States) were then used as the probe liquids to observe the contact angle for each case of dispersed powder. Measurements were carried out several times to ensure the reliability of contact angle values. Then, to calculate the values of SFE using the obtained average contact angle, the Owens-Wendt theory [24] was employed for the extrapolation of the results through the analysis program (Surfaceware 9, Surface Electro Optics, Korea). As illustrated in Table 2, the SiC powder exhibits greater total SFE compared with AlN and hybrid SiC@AlN particles. The obtained SFE values were then used to calculate the work of adhesion (WA) between the components [25–28]. In thermodynamics, WA is explained as the work required for dividing one surface into two separate surfaces. For composites, this can be defined as the amount of work required to separate the filler from the matrix. Accordingly, a larger value of this surface parameter in a multicomponent system means a greater adhesion between the components (filler and matrix). This parameter is calculated using

$$WA = 2\sqrt{\sigma_M^D \sigma_F^D} + 2\sqrt{\sigma_M^P \sigma_F^P}, \quad (1)$$

where σ_M and σ_F are the SFE values for matrix and filler materials, respectively. Superscripts D and P stand for dispersive and polar components of the SFE.

The respective results for WA of different PCM composite systems are also shown in Table 2. It can be seen that compared to pristine AlN, WA was slightly improved in PCM reinforced with SiC@AlN, which implies improvement of interfacial adhesion between paraffin and the biceramic filler. However, SiC possesses the largest value of WA and it is presumably due to the greater dispersive component of

TABLE 2: Surface free energy of the reinforcing powders.

Sample	Contact angle (deg)		Surface free energy (mJ/m ²)			WA (mN/m)
	Water	Diiodomethane	Dispersive	Polar	Total	
Paraffin	87.44 (± 0.367)	56.08 (± 0.825)	32.688	2.363	35.051	—
AlN	84.63 (± 2.477)	22.28 (± 2.247)	45.797	1.180	46.977	80.722
SiC	14.9 (± 1.103)	9.5 (± 0.408)	43.310	32.383	75.693	92.747
SiC@AlN	74.18 (± 3.207)	13.22 (± 0.545)	47.131	3.763	50.894	84.465

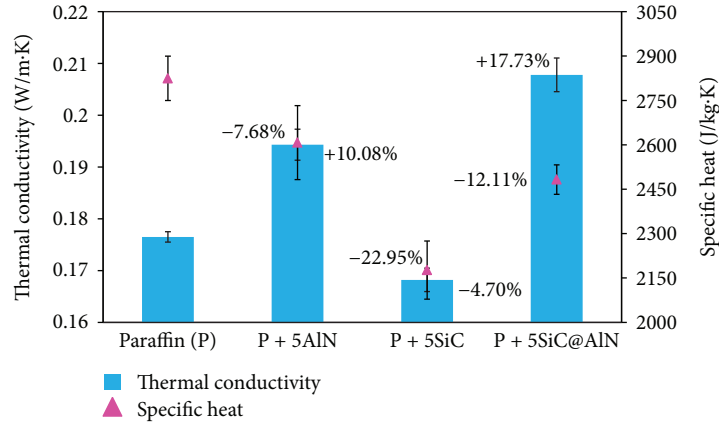


FIGURE 7: Thermal conductivity and specific heat of fabricated composite PCMs compared with those of pure paraffin. Growth and reduction percentages of parameters against pure paraffin are marked by plus (+) and minus (-) signs, respectively.

SFE of the powder. The SiC powder used for this study has a high Si/C ratio which in turn decreases its polarity and gives the powder a mild viridescent colour.

3.5. Thermal Conductivity. Thermal conductivity (TC) and specific heat (SH) of the samples were measured via a transient plane source method using a Hot Disk instrument (Hot Disk, TPS 2500 S, Hot Disk AB, Sweden). A nickel coil wrapped in Kapton with a diameter of 3.2 mm (#5465) was used as the measuring probe for TC. The estimated data reproducibility and accuracy of the equipment provided by the manufacturer are better than 1% and better than 5%, respectively. The SH value of the fabricated composite PCM was also measured using a highly conductive golden cell as the reference. Results are shown in Figure 7 with the percentages of the change in each parameter compared with that of pure paraffin as the reference. Each sample was measured by more than four times, and the standard deviation bars can also be seen. The standard deviation for TC and SH is less than 2% and less than 5%, respectively.

Addition of AlN powder increases the value of TC by more than 10% compared with that of pure paraffin. SiC powder, however, not only does not improve the energy conduction capability of paraffin but also lessens this value by about 4.7% presumably due to the introduction of crystallite impurities and amorphous phases after ball milling. It is assumed that despite the lower Kapitza resistance between SiC and paraffin (see Section 3.4), phonons are scattered via the SiC lattice defects and grain boundaries. Also, the porous structure of SiC may lead to a larger volume of air voids

which in turn reduces the TC. The highest increase in TC was achieved using SiC@AlN biceramic as the filler. This is attributed to the integration of major accommodating characteristics of the two ceramic components resulting in better adsorption of paraffin by the biceramic powder. Also, according to the percolation theory, the percolation threshold of particles decreases by using the mixture of powders with bimodal PSD [29] which in turn increases the chance of formation of longer-range pathways for heat conduction.

This is also evidenced by energy dispersive X-ray spectrometry (EDS, Oxford Instruments, United Kingdom) of composites' cross-sectional area. Samples were linearly notched and submerged under liquid nitrogen for approximately 10 min before the breakage. Figure 8 shows the distribution of elements across the fracture area. It can be easily seen that conductive networks are better formed using the SiC@AlN filler. Comparing all three cases, P + 5SiC@AlN exhibits the larger density of particles across the composite with a higher number of networking bridges, while P + 5AlN falls in the second place pushing the composite reinforced with SiC to the last. This trend properly corresponds to the results obtained for thermal conductivity.

As preceded by the rule of mixture, specific heat of the fabricated blend drops with the use of all types of fillers studied. The largest reduction occurs with SiC as the reinforcing agent. AlN and SiC@AlN on the other hand exhibit better storage capacities of thermal energy in the solid state. Also, this could result from the coarse AlN particles (6 μm) and the larger SiC@AlN particles which are dispersed more uniformly compared with the isotropic scattering of larger SiC particles (28.53 μm).

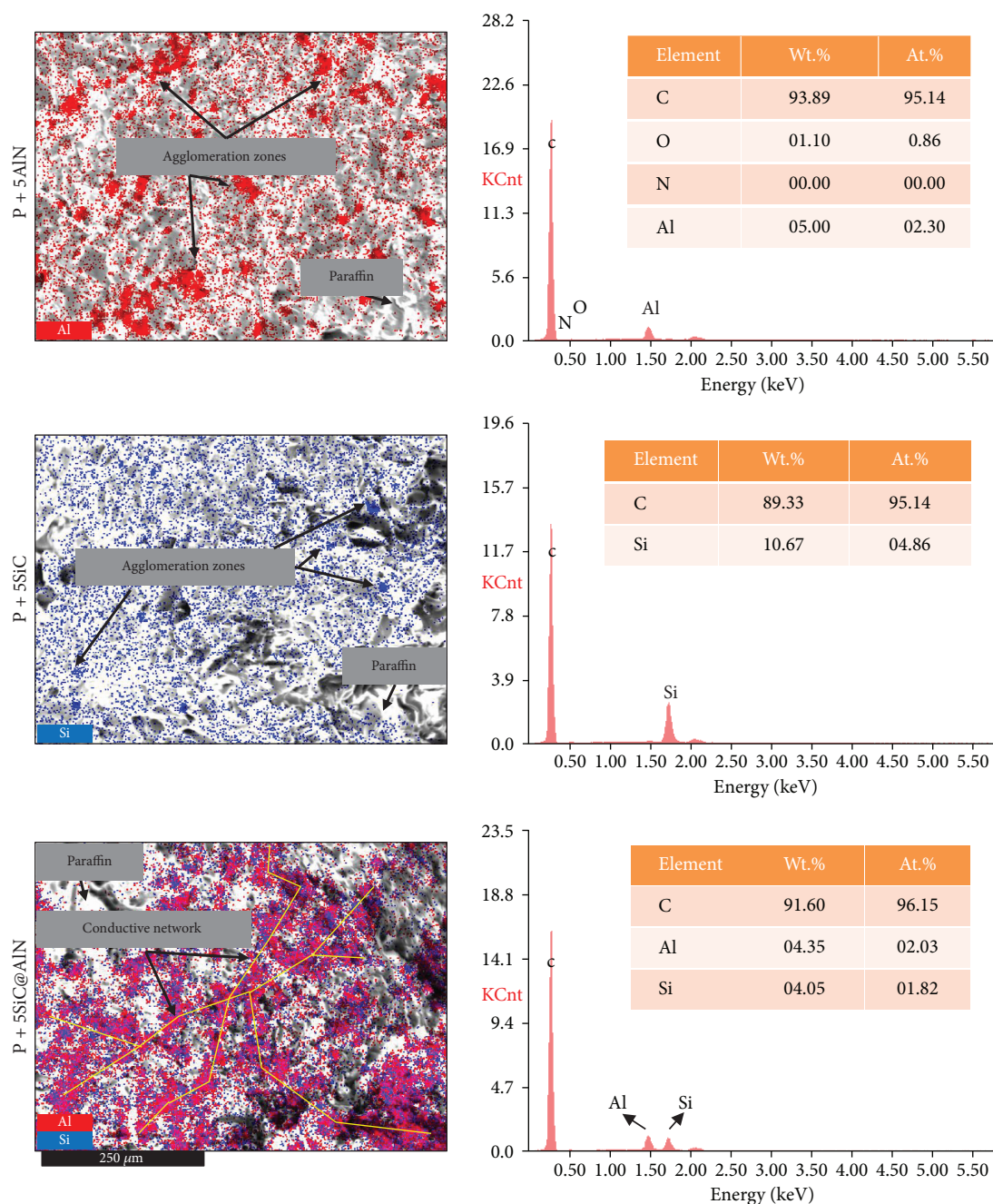


FIGURE 8: EDS mapping of composite cross sections and their respective elemental compositions.

Figure 9 shows the values of thermal conductivity for P + 5SiC@AlN according to different durations of the mechanical alloying process. As seen here, the biceramic filler after 60 min of milling exhibits the highest conductivity which confirms the optimum condition of ball milling obtained in Section 3.2.

3.6. DSC Thermograms of Fabricated PCMs. The final fabricated material is to be ultimately used as a phase change medium under high charge/discharge rates for energy storage and retrieval. Differential scanning calorimetry (DSC-60, Shimadzu Corp., Japan) was employed to explore the behaviour of the fabricated composite PCM under the variation of

temperatures and also to observe the phase change utility of the material by fluctuations in the energy response. A small piece of solidified PCM (7 mg) was placed inside an aluminium hermetic pan (S201-53090, $T_{\text{Max}} = 300^{\circ}\text{C}$, $P_{\text{Max}} = 0.3\text{ M Pa}$; Shimadzu Corp., Japan) and then melted to ensure the uniform distribution of the sample in the holder. Prior to measurement, the sample was cooled down to room temperature to minimize the effect of residual heat within the specimen. Following the insertion of the sample and reference into the measurement chamber, experimental parameters including heating rate and the lowest and highest measurement temperatures for both endothermic and exothermic

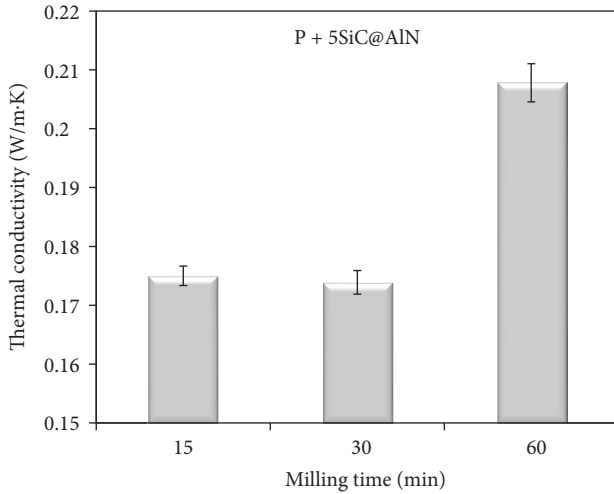


FIGURE 9: Thermal conductivity of paraffin reinforced with 5 wt.% of SiC@AlN powder as a function of milling time.

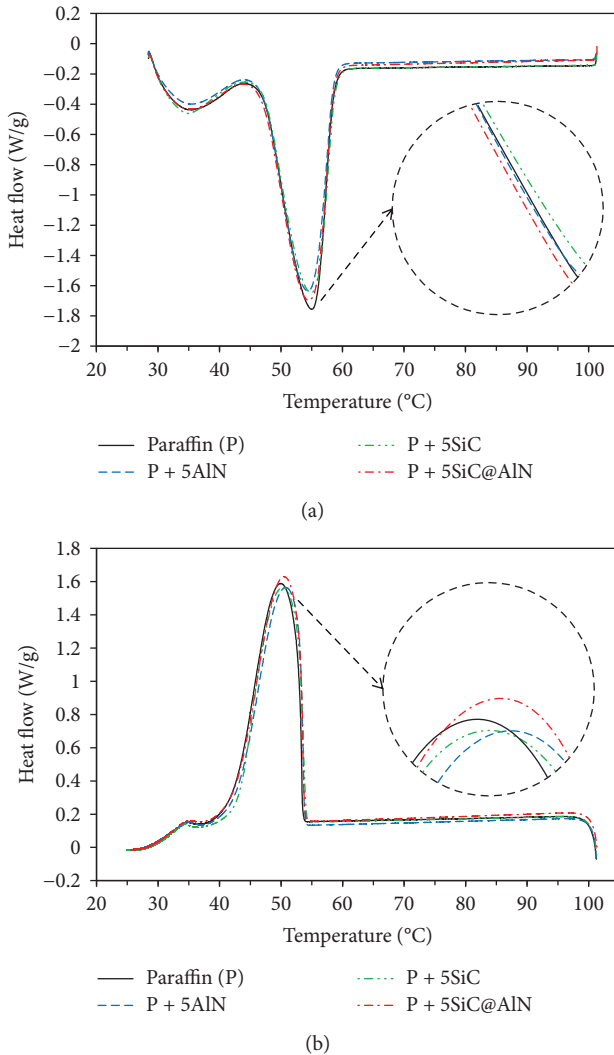


FIGURE 10: DSC thermograms of (a) endothermic and (b) exothermic runs for the fabricated composite PCMs and pure paraffin.

TABLE 3: Experimental values of DSC analysis for the fabricated composite PCMs and pure paraffin.

Sample	Run	Phase change temperature (°C)			Latent heat (J/g)
		T_{Onset}	T_P	T_{Endset}	
Paraffin (P)	Endo	47.22	55	58.21	135.02
	Exo	53.45	49.93	42.81	142.68
P + 5AlN	Endo	47.16	54.39	58.14	131.28
	Exo	53.74	50.74	43.01	139.57
P + 5SiC	Endo	48.17	54.89	58.49	130.2
	Exo	53.98	50.26	43.14	140.57
P + 5SiC@AlN	Endo	47.39	54.5	58.61	137.69
	Exo	53.73	50.48	42.87	146.8

Endo: endothermic run; Exo: exothermic run.

runs were set at 5°C/min and 25 and 100°C, respectively. Resultant thermograms are shown in Figure 10. The DSC patterns of analyzed cases were slightly different. Each case was measured several times (at least three times) to ensure the stability of the analysis. The obtained values for transition temperatures and latent heat are presented in Table 3.

As seen in the values obtained by DSC analysis, the addition of fillers delays the starting temperature of the phase transition in both heating and cooling runs. Among these, SiC due to its higher melting point (~2730°C) exhibits a longer hold-up in phase change onset temperatures. This also could be caused by the lower thermal conductivity of the bulk composite PCM reinforced with SiC (see Section 3.5) which postpones the heat distribution and subsequently transition of the crystal structure. Also, the absence of accommodating porous networks in SiC particles will result in poor integration with paraffin leading to less functionality as a stable and uniform PCM. This is evidenced by the lower phase change differential temperature and latent heat of P + 5SiC at the endothermic run. The use of the AlN coarse particles as the reinforcing agent indicates slightly higher latent heat compared with that of P + 5SiC in the heating run that can be attributed to better dispersion of the particles within the paraffin and higher level of integration with the matrix due to a surface integration. Both of singular fillers, however, decrease the intrinsic higher latent heat of paraffin which is opposed by what is desired from a material for a reliable LHTS.

Comparing the values of latent heat, paraffin reinforced with SiC@AlN presents slightly greater latent heat than all the cases including pure paraffin. This is due to the formation of a particulate structure with a larger surface area, which was improved by the mechanical alloying method, and higher volume fraction of well-dispersed ceramic particles for energy storage.

4. Conclusions

The present study analyzes the effects of ceramic and biceramic powders on the thermal properties of paraffin for the potential use as a PCM in thermal energy storage systems. SiC microparticles were successfully coated with AlN powder

using ball milling with optimized conditions. However, the crystalline structure of SiC seemed to have undergone a negative alteration due to the high intensity of the mechanical stresses. Composite PCMs were fabricated via ultrasonication, and thermal analyses of the samples are presented. The highest increase in thermal conductivity was achieved using the SiC@AlN filler compared with singular ceramic powders. EDS results indicate a better capability of the SiC@AlN filler to conduct energy at the solid state of PCM with higher ballistic movements of phonons compared with AlN or SiC powder as the filler. DSC analysis also indicates a very slight growth in the latent heat of paraffin reinforced with SiC@AlN powder. This increase, however, would not be considered a meaningful enhancement for the fabricated PCM. Further improvement of LHTS must be pursued using the combination of such materials and surface engineering with the enhancement of the paraffin-filler interface as the main objective.

Lastly, according to Sigma-Aldrich catalogues, SiC (Lot #378097; 250 g: 47.90 USD) costs approximately 4.54 times lower than AlN powder (Lot #241903; 250 g: 217.50 USD) [18]. Therefore, production of such a hybrid filler, according to obtained results, not only improves the properties of the final PCM composite but also economically justifies the addition of SiC as a low-cost extender to the AlN powder.

Data Availability

The raw data used to support the findings of this study are available from the corresponding author upon request.

Conflicts of Interest

The authors declare that they have no conflicts of interest.

Acknowledgments

This research was funded by the National Research Foundation (NRF) of Korea (Grant nos. 2015R1A2A2A01005693 and 2015M3A7B4049716) supported by the Ministry of Science, ICT and Future Planning (MSIP), Korea, and by the Korea Institute of Energy Technology Evaluation and Planning (KETEP) (Grant no. 20152020001240) supported by the Ministry of Trade, Industry & Energy (MOTIE), Korea.

References

- [1] K. Chintakrinda, R. D. Weinstein, and A. S. Fleischer, "A direct comparison of three different material enhancement methods on the transient thermal response of paraffin phase change material exposed to high heat fluxes," *International Journal of Thermal Sciences*, vol. 50, no. 9, pp. 1639–1647, 2011.
- [2] S. Y. Wu, H. Wang, S. Xiao, and D. S. Zhu, "An investigation of melting/freezing characteristics of nanoparticle-enhanced phase change materials," *Journal of Thermal Analysis and Calorimetry*, vol. 110, no. 3, pp. 1127–1131, 2012.
- [3] F. Colella, A. Sciacovelli, and V. Verda, "Numerical analysis of a medium scale latent energy storage unit for district heating systems," *Energy*, vol. 45, no. 1, pp. 397–406, 2012.
- [4] Y. Cui, C. Liu, S. Hu, and X. Yu, "The experimental exploration of carbon nanofiber and carbon nanotube additives on thermal behavior of phase change materials," *Solar Energy Materials and Solar Cells*, vol. 95, no. 4, pp. 1208–1212, 2011.
- [5] S. S. Sebti, M. Mastiani, H. Mirzaei, A. Davvand, S. Kashani, and S. A. Hosseini, "Numerical study of the melting of nano-enhanced phase change material in a square cavity," *Journal of Zhejiang University SCIENCE A*, vol. 14, no. 5, pp. 307–316, 2013.
- [6] L. Xia, P. Zhang, and R. Z. Wang, "Preparation and thermal characterization of expanded graphite/paraffin composite phase change material," *Carbon*, vol. 48, no. 9, pp. 2538–2548, 2010.
- [7] E.-B. S. Mettawee and G. M. R. Assassa, "Thermal conductivity enhancement in a latent heat storage system," *Solar Energy*, vol. 81, no. 7, pp. 839–845, 2007.
- [8] N. S. Dhaidan, J. M. Khodadadi, T. A. Al-Hattab, and S. M. Al-Mashat, "Experimental and numerical investigation of melting of phase change material/nanoparticle suspensions in a square container subjected to a constant heat flux," *International Journal of Heat and Mass Transfer*, vol. 66, pp. 672–683, 2013.
- [9] C. J. Ho and J. Y. Gao, "Preparation and thermophysical properties of nanoparticle-in-paraffin emulsion as phase change material," *International Communications in Heat and Mass Transfer*, vol. 36, no. 5, pp. 467–470, 2009.
- [10] A. Valan Arasu, A. P. Sasmito, and A. S. Mujumdar, "Thermal performance enhancement of paraffin wax with Al₂O₃ and CuO nanoparticles – a numerical study," *Frontiers in Heat and Mass Transfer*, vol. 2, no. 4, 2011.
- [11] T.-P. Teng and C.-C. Yu, "Characteristics of phase-change materials containing oxide nano-additives for thermal storage," *Nanoscale Research Letters*, vol. 7, no. 1, p. 611, 2012.
- [12] A. Badakhsh, C. W. Park, and B.-J. Kim, "Preparation and analysis of paraffin-based phase change material using aluminum nitride as the reinforcing agent," in *4th International Conference on Nanotechnology, Nanomaterials & Thin Films for Energy Applications*, pp. 70–72, One Central Press, University of Aalto, Finland, 2017.
- [13] Y.-L. Cho, J.-w. Lee, C. Park, Y.-i. Song, and S.-J. Suh, "Study of complex electrodeposited thin film with multi-layer graphene-coated metal nanoparticles," *Carbon Letters*, vol. 21, pp. 68–73, 2017.
- [14] W.-K. Choi, B.-J. Kim, and S.-J. Park, "Fiber surface and electrical conductivity of electroless Ni-plated PET ultra-fine fibers," *Carbon letters*, vol. 14, no. 4, pp. 243–246, 2013.
- [15] W.-K. Choi, H.-I. Kim, S.-J. Kang, Y. S. Lee, J. H. Han, and B.-J. Kim, "Mechanical interfacial adhesion of carbon fibers-reinforced polarized-polypropylene matrix composites: effects of silane coupling agents," *Carbon letters*, vol. 17, no. 1, pp. 79–84, 2016.
- [16] D.-K. Kim, K.-H. An, Y. H. Bang, L.-K. Kwac, S.-Y. Oh, and B.-J. Kim, "Effects of electrochemical oxidation of carbon fibers on interfacial shear strength using a micro-bond method," *Carbon letters*, vol. 19, pp. 32–39, 2016.
- [17] A. Badakhsh and C. W. Park, "From morphology of attrited copper/MWCNT hybrid fillers to thermal and mechanical characteristics of their respective polymer-matrix composites: an analytical and experimental study," *Journal of Applied Polymer Science*, vol. 134, no. 41, article 45397, 2017.

- [18] Sigma-Aldrich Inc, "Sigma-Aldrich catalog," <http://sigmaaldrich.com>.
- [19] C. X. Guo, X. L. Ma, and L. Yang, "PCM/ graphite foam composite for thermal energy storage device," *IOP Conference Series: Materials Science and Engineering*, vol. 87, no. 1, article 012014, 2015.
- [20] Specific Heat Capacity, *Diracdelta.co.uk Science and Engineering Encyclopedia*, Dirac Delta Consultants Ltd, Warwick, England, 2013.
- [21] D. D. L. Chung, "Materials for thermal conduction," *Applied Thermal Engineering*, vol. 21, no. 16, pp. 1593–1605, 2001.
- [22] J. F. Shackelford and W. Alexander, *CRC Materials Science and Engineering Handbook*, CRC Press, Boca Raton, FL, USA, 3rd edition, 2000.
- [23] Y. S. Touloukian, *Thermophysical Properties of High Temperature Solid Materials*, vol. 5, Part 1, 1967, MacMillan Co., New York, United States, 1967.
- [24] D. K. Owens and R. C. Wendt, "Estimation of the surface free energy of polymers," *Journal of Applied Polymer Science*, vol. 13, no. 8, pp. 1741–1747, 1969.
- [25] O. Sproesser, P. R. Schmidlin, J. Uhrenbacher, M. Eichberger, M. Roos, and B. Stawarczyk, "Work of adhesion between resin composite cements and PEEK as a function of etching duration with sulfuric acid and its correlation with bond strength values," *International Journal of Adhesion and Adhesives*, vol. 54, pp. 184–190, 2014.
- [26] S.-J. Park and B.-J. Kim, "Roles of acidic functional groups of carbon fiber surfaces in enhancing interfacial adhesion behavior," *Materials Science and Engineering: A*, vol. 408, no. 1-2, pp. 269–273, 2005.
- [27] S.-J. Park, B.-J. Kim, D.-I. Seo, K.-Y. Rhee, and Y.-Y. Lyu, "Effects of a silane treatment on the mechanical interfacial properties of montmorillonite/epoxy nanocomposites," *Materials Science and Engineering: A*, vol. 526, no. 1-2, pp. 74–78, 2009.
- [28] K. Jha, E. Anim-Danso, S. Bekele, G. Eason, and M. Tsige, "On modulating interfacial structure towards improved anti-icing performance," *Coatings*, vol. 6, no. 1, p. 3, 2016.
- [29] A. Y. Dovzhenko and P. V. Zhirkov, "The effect of particle size distribution on the formation of percolation clusters," *Physics Letters A*, vol. 204, no. 3-4, pp. 247–250, 1995.